The effect of gas on multi-stage mixed-flow centrifugal pumps

Flow visualisation and modelling

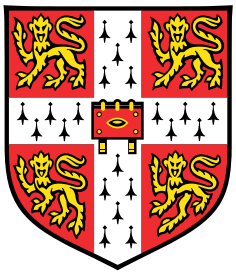

Marine Dupoiron

Department of Applied Mathematics and Theoretical Physics
University of Cambridge

This dissertation is submitted for the degree of
Doctor of Philosophy

Darwin College

November 2017

Declaration

I hereby declare that except where specific reference is made to the work of others, the contents of this dissertation are original and have not been submitted in whole or in part for consideration for any other degree or qualification in this, or any other university. This dissertation is my own work and contains nothing which is the outcome of work done in collaboration with others, except as specified in the text and Acknowledgements. This dissertation contains fewer than 65,000 words including appendices, bibliography, footnotes, tables and equations and has fewer than 150 figures.

Marine Dupoiron
November 2017

Acknowledgements

I am very grateful to Schlumberger Gould Research Centre, and particularly to Gary Oddie and Frank Monmont for giving me the opportunity to start this work, and for supporting me throughout. I am also grateful to my supervisor, Paul Linden for his tactful advice that helped me to formulate my ideas and results, especially writting this thesis.

I was lucky to have enthusiastic and knowledgeable colleagues and managers at SGR, Jon Dusting, Leo Steenson, Peter Johnson, Songming Huang, Andrew Meredith, Carlos Araque and Miriam Archer. I would also like to thanks Stuart Dalziel, Julien Landel and David Page-Croft from the Batchelor Laboratory at Cambridge University who helped me setting up a simplified version of my experiment. Discussions with my colleagues from Schlumberger centres across the world were very insightful and gave me a good understanding of the current and future challenges in Artificial Lift. I would like to particularly acknowledge David Eslinger from Bartlesville (Oklahoma, USA), Kean Wee Cheah from Singapore, Lawrence Camilleri from Paris (France), and Emmanuel Coste and Yves-Marie Subervie from Sugar Land (Texas, USA). Building the ESP rig was the one of the most exciting parts of this work, and I would like to specially thanks Gary Oddie for his very practical advice and help, Tim MacAlinden for putting the drawings together and helping with all sort of mechanical issues, and Pete Woodward and Joe Moore for their good work in setting up the three-axis LDV traverse. I want to particularly thanks Colin Atkinson and Gary Oddie for their constant support and encouragement during the writing-up period.

I could not have gone through the modelling without the help and friendship of Gil-Arnaud Coche. Your moral and scientific qualities support un mot sur deux de cette thèse.

I would like to acknowledge the role CUJC (Cambridge University Judo Club) and its members who have been such an important part of my life during these four years. Friendships have build who I am, and kept me going, so I would like to mention mes amis Marianne Reboul, Audrey Etienne, Flora Bouchacourt, Céline Finas, Christophe Cochet, Adeline Strozza et Sandrine Locret.

Finally, even though a simple acknowledgement seems dérisoire, I would like to mention the support brought by mes parents, mon frère et mes sœurs, and by my partner Andreana Sutherland. They are truly the most important people in my life.

Abstract

The production from an oil reservoir is a mixture of liquids (oil and water) and gas, and is often maintained by using a pump placed in the well to ensure a continuous flow to the surface. Electrical Submersible Pumps consist of stacked centrifugal pump stages, each comprising a bladed impeller (rotating part) and diffuser (stationary part). In multiphase conditions, the gas tends to accumulate in the impeller, severely reducing the pressure produced by the pump. Radial-flow pumps operate in a plane perpendicular to their rotation axis, while mixed-flow pumps are characterised by a lower meridional angle (generally 40 to 80 degrees), and are generally better at handling gas-liquid mixtures.

We first describe the impact of gas on the whole pumping system, from the reservoir to the storage facility, and give context to the subject. The available literature shows that the size of the gas bubbles present in the fluid is critical to the pump performance.

A transparent, full-scale pump was built in order to explore the flow features in single and multiphase flows. Laser Doppler Velocimetry and high speed imaging in single phase flow showed a high turbulence level in the wake of the impeller blades, and recirculation cells at low flow rates. In gas-liquid conditions, we demonstrated that the bubble size varies within a pump stage, as break-up occurs at the impeller tip, and coalescence is dominant in the diffuser, especially because of recirculation. The first impeller acted as a mixer, and at moderate to high gas fractions (10 to 30%), the flow patterns at the stage level alternated between bubbly and radially separated flows.

Finally, a dispersed-gas model was developed to predict the pressure rise in a mixed-flow pump impeller under gas-liquid conditions. This model based on the forces acting on a single spherical gas bubble, was implemented with a simplified, parametric representation of the flow field in a mixed-flow impeller. In the meridional direction, the Coriolis force opposes the centrifugal force and the adverse pressure gradient. Both forces tend to retain the gas bubble within the impeller. The relative magnitude of the drag force strongly depends on the maximal bubble diameter, which was determined as a function of the flow conditions and used to calculate the gas velocity through the impeller. This method resulted in a better agreement with the experimental data than a one-dimensional two-fluid model where the gas phase follows the same path as the liquid. We used the dispersed-gas model to give quantitative evidence that low blade and meridional angles reduce the gas accumulation and the associated performance degradation.

Contents

Nomenclature

Roman Symbols

$\vec{g}$	Gravity,
$\vec{M}$	Angular Momentum,
$\vec{U}$	Circumferential velocity, Undisturbed velocity
$\vec{W}$	Absolute liquid velocity,
$\vec{w}$	Relative liquid velocity,
A	Surface area,
Bo	Bond number,
C_d	Drag coefficient,
C_l	Lift coefficient,
C_M	Added mass coefficient,
D	Impeller tip diameter,
d	Bubble diameter,
f	Pump rotation frequency (Hz),
H	Head,
h	Passage height,
m	meridional coordinate,
M_b	Bubble mass,
N_s	Dimensional specific speed,
P	Pressure,
Q	Volumetric flow rate,

R Impeller tip radius,

Re Reynolds number,

Ri Richardson number,

s spanwise coordinate,

T Torque,

x Mixture quality (mass ratio),

Z Blade number,

Greek Symbols

α Meridional angle or Local gas void fraction

$\bar{\epsilon}$ Average Turbulent Energy Dissipation,

β Flow angle relative to $\vec{U}$,

Δ Difference across the pump,

ϵ Roughness,

γ Laser angle,

λ Gas cut,

μ Fluid dynamic viscosity,

ν Fluid kinematic viscosity,

ω Angular rotation speed,

Φ Flow coefficient,

Ψ Head coefficient,

ρ Fluid density,

σ Interfacial surface tension,

ε Normalised bubble diameter,

ξ Density ratio,

Superscripts

* Non-dimensional,

Subscripts

1 at impeller inlet,

2 at impeller outlet,

a annulus,

b bubble,

bh bottom hole,

f frictional,

g gas,

h hydrostatic,

l liquid,

m meridional,

p passage, pump, pipe

res reservoir,

s system,

w water,

wh well head,

Other Symbols

$\mathcal{M}_{2\phi}$ Head degradation factor,

$\mathcal{Q}$ Thermal energy,

$\mathcal{R}_0$ Stationary frame of reference,

$\mathcal{R}_1$ Rotating frame of reference,

$\mathcal{W}$ Mechanical work,

Acronyms / Abbreviations

API American Petroleum Institute,

BEP Best Efficiency Point,

BM Bubble Motion method,

CFD Computational Fluid Dynamics,

ESP Electrical Submersible Pump,

EV Equilibrium Velocity method,

GVF Gas Volume Fraction,

IFP Institut Francais du Petrole,

LDV Laser Doppler Velocimetry,

MUSIG Multiple Size Groups model,

PID Proportional-Integral-Derivative controller,

PMMA Polymethyl methacrylate,

RANS Reynolds Average Navier-Stokes equations,

TF Two-Fluid model,

Introduction

Producing oil and gas from a reservoir is a long and costly process that requires extensive planning and engineering in order to anticipate potential issues and address them in a safe and economical way. Even if some oil wells flow naturally for years after they have been drilled and put into production, the reservoir pressure generally decreases over time, and sooner or later the natural flow is too low to keep producing. According to the market study by Markets and Markets (2013), more than 90% of the oil producing wells are equipped with some kind of artificial lift. Electrical Submersible Pumps (ESP) are widely used, especially for high volume production.

If there is gas in the reservoir, or if the pressure in the well drops below the bubble point, gas can be ingested into the pump and dramatically degrade its performance. Gas handling in ESPs has been studied since the late 1980's and many technologies and models are available to design ESP installations capable of sustaining up to 95% free gas at the bottom hole, by using gas separators (Rahime et al., 2013) and helico-axial pumps (Camilleri et al., 2009). Because the gas cannot always be vented separately from the liquid, and because helico-axial pumps are more expensive to manufacture and only deliver a small pressure rise compared to conventional designs, gas handling remains a challenge for the oil industry. Even for a low intake gas fraction, the production can be unstable or completely stop, leading to pump failure through overheating or a broken shaft. Takács (2009) describes these phenomena usually referred to as "surging" and "gas locking". They are however not well understood and difficult to predict, let alone to avoid. In this context, we want to gain a better understanding of the physics of the gas-liquid flow through a multi-stage centrifugal pump, in order to design installations that can handle more gas in a more stable way.

Designing a pump that can better handle gas while producing a high head at a high efficiency requires its performance to be characterised in gas-liquid conditions. Even if numerical simulations can be calibrated to match the experimental data (e.g. Zhu and Zhang, 2016), predictive models are still not available. We want to propose a model that can be tested against a variety of designs and give an insight into the effect of geometrical features on the gas handling capabilities.

This thesis consists of experimental and modelling studies. The first chapter is a literature review, not only on the available models and correlations to predict the head of a centrifugal pump in gas-liquid conditions, but also providing some more general

context. In particular, we explain how the pump head curve can have an impact on the system stability. The next three chapters describe the experimental work done to support the subsequent model and analysis. We first describe the methods used (chapter 2), and then the results obtained in single phase, liquid flows (chapter 3) and multiphase, gas-liquid flows (chapter 4). Finally, the fifth chapter presents a simple mixture model for the impeller that can be used with a geometrical description, or with the results of a single phase simulation of the flow. The results are compared with available experimental data for several impeller designs, and are used to highlight general trends.

Chapter 1

Context and Literature Review

An ESP installation is designed for an oil reservoir whose properties (intake pressure, flow rate) will vary slowly with time, but can also present unsteady behaviour on a short time scale. Gas slugging from a horizontal section, variations of the water injection rate or adjustment of the wellhead chokes are examples of events causing unsteadiness. The distance from the bottom hole to the well head can be several kilometres long and couples the reservoir with the processing, transport or storage facilities at surface. Each sub-element needs to be be understood independently in order to provide a robust model for the whole system, which is more complex than the sum of its components. The pump itself is one of these components and typically consists of several geometrically identical stages. Phenomena such as gas compression, shaft loading or gas slug dynamics should be studied with an entire pump, rather than at the stage level. The co-existence of these three scales: system, pump and stage should be kept in mind while conducting modelling or designing experiments. In this chapter, the system is described from the operational viewpoint and the key hardware and physical phenomena are identified. Section 1.1 is dedicated to the system architecture, and the pump performance in single phase flow. Section 1.2 describes the impact of gas on the flow in a centrifugal stage. Finally, Section 1.3 shows the impact of gas on the whole system, and presents the current solutions to producing fluids from a gassy well.

1.1 Electrical Submersible Pumps in Single Phase Flows

Producing oil from a reservoir through an ESP requires a pump, tubing, choke and surface storage (or transport, or processing facility). Figure 1.1 is a simplified representation of the whole system. For fixed reservoir and wellhead pressures, the production rate is limited by the resistance of the porous path through the rock, the hydrostatic head between the bottom of the well and the surface, and the fluid friction in the tubing and the choke. We present below the most common method to design such an installation.

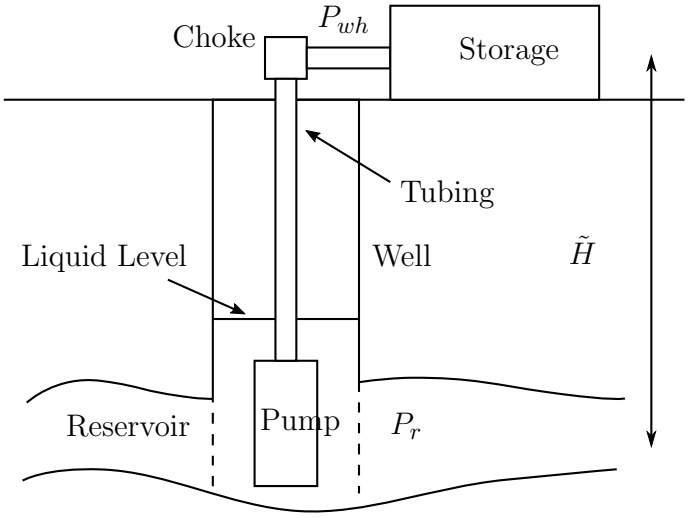

Figure 1.1 Schematics of an oil well produced using an Electrical Submersible Pump (ESP). The pressure in the reservoir is P_r and the pressure in the storage tank is P_{wh}.

1.1.1 Steady-state system analysis

Takács (2009) shows how steady-state system analysis can be used to calculate the operation point of an ESP. This method, also called nodal analysis, consists of calculating the successive pressure drops that the produced fluid has to overcome.

First, the produced fluid is drained from the reservoir to the wellbore. At this stage, the pressure losses are governed by the Darcy equation. The relationship between the flow rate Q and the drawdown $(P_{res} - P_{bh})$ is represented by the so-called Productivity Index PI.

$$Q = PI(P_{res} - P_{bh}), \tag{1.1}$$

where P_{res} is the average reservoir static pressure and P_{bh} the bottom hole pressure.

Assuming a homogeneous, radial, single phase, incompressible flow through the reservoir, the Productivity Index would be constant, solely dependent on the fluid and reservoir properties. Figure 1.2 shows the theoretical relationship between the bottom hole pressure and the liquid flow rate at a constant reservoir pressure (100 % water: dashed straight line). More realistic models for a well producing oil and water, where the flowing pressure can drop below the oil bubble point are also shown for different different water cuts (ratio of water flow rate to total flow rate).

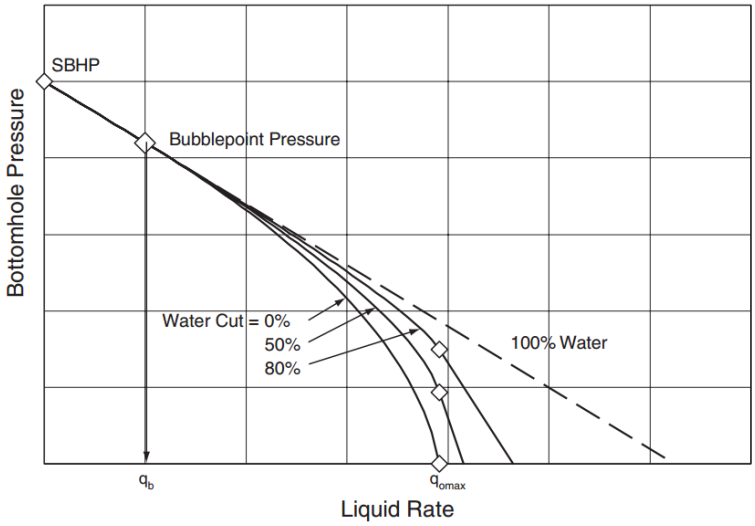

Figure 1.2 Composite inflow performance relationship (IPR) curve, from Takács (2009). The sandface bottomhole pressure (SBHP) is the pressure at the bottom of the well when no liquid is flowing. When the bottomhole pressure is lowered, the reservoir starts flowing, but if it reaches the bubble point pressure, then gas comes out of solution and the Q, P relationship deviates from the linear model. The maximal oil flow rate that can be obtained for 0% water cut is marked as q_{omax}.

The second pressure gradient to overcome is the hydrostatic pressure ΔP_h, due to the height $\tilde{H}$ from the reservoir to the well head. This term is straightforward if the density ρ of the produced fluid is known.

$$\Delta P_h = \rho g \tilde{H}.$$

Finally, the friction through the tubing and choke is likely to be a quadratic function of the flow rate, where the friction coefficient C_f depends on the choke position, tubing diameter d, its roughness ϵ and the physical properties of the fluid being produced.

$$\Delta P_f(d,Q) = \rho \; C_f(d,\epsilon) \; Q^2 \; .$$

The Electrical Submersible Pump provides a pressure increment ΔP_{pump}, which depends on the pump rotation speed ω, or frequency f ($\omega = 2\pi f$) and the total flow rate Q_{tot}. This pressure increment is often expressed in terms of head H_{pump}:

$$\Delta P_{pump}(f,Q) = \rho g H_{pump}(f,Q).$$

Assuming that the reservoir pressure is constant, the pump discharge pressure is computed from the reservoir up and from the surface down:

$$\begin{cases} P_d = P_{bh} + \Delta P_{pump} = P_{bh} + \rho g H_{pump} \\ P_d = P_{wh} + \Delta P_f + \Delta P_h = P_{wh} + \rho \; C_f(d,\epsilon) \; Q^2 + \rho g \tilde{H} \; . \end{cases} \tag{1.2}$$

These two equations determine the pump operating point:

$$H_{pump}(f,Q) = \frac{1}{\rho g}\left(P_{wh} - P_{bh} + \rho\, C_f(d,\epsilon)\, Q^2\right) + \tilde{H}\ . \tag{1.3}$$

This system can also be solved graphically, by looking for the intersection of the "pump curve" (left hand side of (1.3)) and the well performance curve, or "system curve" (right hand side of (1.3)). These are drawn in Figure 1.3 for different pumps speeds and tubing diameters. Each intersection represents a possible operating point.

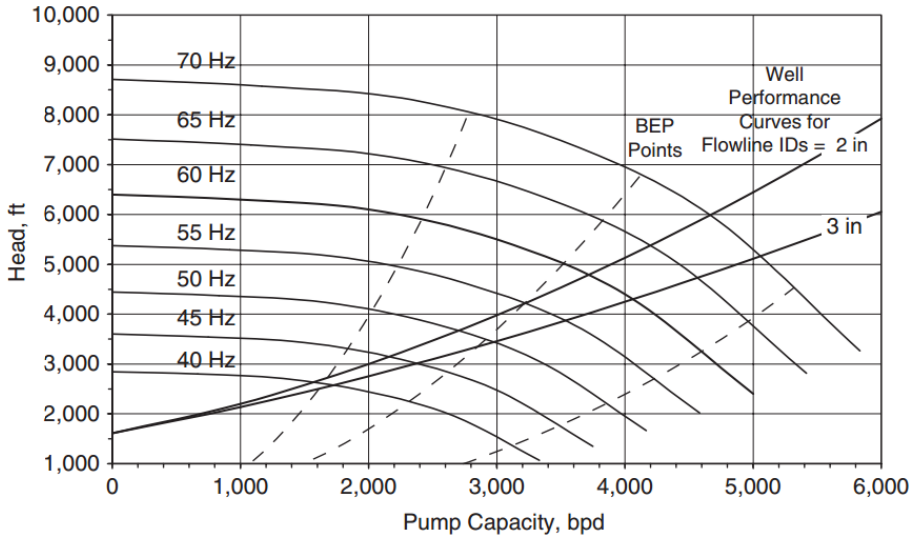

Figure 1.3 ESP head curves and system curves for a single phase well, from Takács (2009). The solid lines numbered with pump speeds are the pump head curves for for one given pump at different speeds. The dashed lines represent, respectively, the lower operating range, Best Efficiency Point (BEP) and higher operating range. The two "well performance curves" (or system curves) represent two possible tubing sizes (different friction loss coefficients).

A correct sizing of the installation ensures that the operating point falls close to the pump Best Efficiency Point (BEP), or at least within the operating range.

1.1.2 Stage Design

Electrical Submersible Pumps are multi-stage pumps, and therefore consist of several stages stacked together in a housing. A housing can contain 8 up to 300 stages. An individual stage consists of an impeller that transmits kinetic energy to the fluid by rotating, and a static diffuser that brings the flow to the next impeller inlet while minimizing the pressure losses. ESP stages can have a radial geometry (Figure 1.4a) where the flow in the impeller goes from the centre outwards, or a so-called mixed flow geometry (Figure 1.4b) lying between radial and axial configurations. For a given diameter, the radial design produces a larger head, while the mixed flow design is better

adapted to higher flow rates and larger gas volume fraction. Axial designs are mainly used for compressors and not pumps, are are not represented here. The helico-axial design (Figure 1.4c) has an axial diffuser and helical impeller blades. It is well suited to gas-liquid flows (up to 90% GVF) but only produces a small head compared to radial or mixed-flow designs.

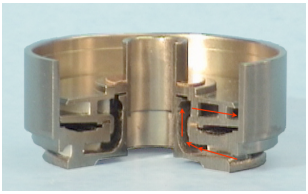

(a) Radial design

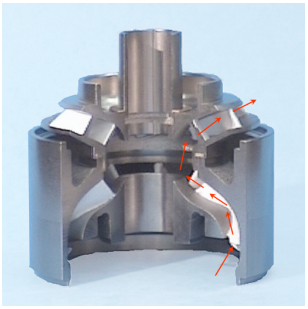

(b) Mixed-flow design

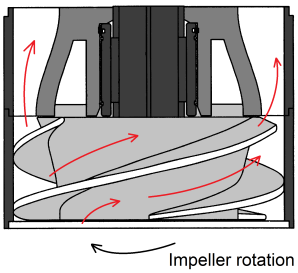

(c) Helico-axial design

Figure 1.4 Stage cross-sections. The classical radial and mixed-flow stages are represented with the diffuser below the impeller. The helico-axial stage drawing (adapted from the patent by Lee (1997)) shows the helicoidal impeller below the axial diffuser. The flow path is indicated in red.

In order to install a pump, the operator needs to know the consumed power and produced pressure for a given flow rate and rotation speed. In incompressible liquid, the pressure and power are proportional to the number of stages, so the properties of a single stage is sufficient to characterise the whole pump. Affinity laws (presented below) are used in order to scale the head and efficiency curves for different rotation speeds and pump diameters for a fixed geometry. Simple models like the Euler equation can be used to estimate the produced head from geometrical parameters, assuming no losses. For a more accurate prediction of the stage performance, numerical simulations are used, along with correlations based on experimental measurements.

1.1.3 Affinity laws

For a single phase flow in a given pump geometry, only seven independent parameters are needed to characterise the pump performance: The pump speed ω, the volumetric flow rate Q, the produced pressure rise ΔP, the torque T, the fluid density ρ, the fluid viscosity μ, and the pump radius R. With three dimensions (length, time, mass), four dimensionless numbers are therefore enough to characterize the whole system, as per Buckingham-Pi theorem. The pump efficiency, defined as the ratio of the hydraulic to the mechanical power, is an alternative to the power coefficient. These numbers are widely used (e.g. Gulich, 2007) and defined as below for a single stage, using the international unit system (SI):

$$\begin{aligned}
\phi &= \frac{Q}{\omega\ R^3} && \text{Flow coefficient} \\
\psi &= \frac{gH}{(\omega R)^2} && \text{Head coefficient} \\
\Pi &= \frac{T\omega}{\rho\omega^3 R^5} && \text{Power coefficient} \\
Re &= \frac{\rho\omega R^2}{\mu} && \text{Reynolds number} \\
\eta &= \frac{Q\ \Delta P}{T\omega} && \text{Hydraulic Efficiency}
\end{aligned} \tag{1.4}$$

Each pump is therefore entirely described by the two relations: $\psi = f_\psi(\phi, Re)$ and $\eta = f_\eta(\phi, Re)$ which are represented on the so-called pump curves, most of the time with the assumption of an inviscid fluid: $Re = +\infty$. We note that in practice, is it difficult to measure the torque applied on a single stage, and the measured torque applies to the whole pump and includes some mechanical friction losses. In this case, the measured efficiency is therefore the product of the mechanical and hydraulic efficiency (see Takács (2009) for more details).

Geometrical parameters are more difficult to list due to the complexity of the impeller and diffuser shapes. The most common features are the pump diameter $D = 2R$, the average passage height h, the number of impeller blades N, the stage length L and the surface roughness ϵ. A pump is also characterized by the number N_s called the specific speed, which represents the rotation speed in rpm necessary to flow 1 gallon per minute while delivering 1 foot head. It is defined using the pump head and flow rate at its design point, also called Best Efficiency Point (BEP, see Figure 1.3). Radial pumps have a specific speed $N_s < 1500$ (low flow rate, high head), axial pumps have a specific number $N_s > 8000$ (large flow rate, low head), and mixed-flow stages lay in-between ($1500 < N_s < 8000$).

$$N_s = \frac{\omega\,[rpm]\ \sqrt{Q_{BEP}\,[gpm]}}{(H_{BEP}\,[ft])^{3/4}} \tag{1.5}$$

This number is unfortunately dimensional although it is widely used in the industry to compare different pump geometries. Its non-dimensional counterpart is noted ω_s. Radial designs are characterised by $\omega_s < 0.5$ and axial designs by $\omega_s > 2.8$.

$$\omega_s = \frac{\omega\sqrt{Q_{BEP}}}{(gH_{BEP})^{3/4}} = \frac{\Phi_{BEP}^{1/2}}{\psi_{BEP}^{3/4}} \tag{1.6}$$

1.1.4 Euler pump and turbine equation

The Euler pump equation derived by Euler (1754), gives an estimate of the total pressure Δp^T produced by a pump impeller, assuming there are no friction losses:

$$\Delta p^T = \rho\ \omega \left(\overline{R}_2 W_{\theta 2} - \overline{R}_1 W_{\theta 1} \right) \ , \tag{1.7}$$

where $\overline{R}_1$ and $\overline{R}_2$ are the inlet and outlet radii, and $W_{\theta 1}$ and $W_{\theta 2}$ the inlet and outlet tangential speed. Appendix A.1 shows the derivation from first principles, and particularly the assumptions that led to the Euler equation, listed below:

- Adiabatic flow
- Uniform density, pressure and velocity at the impeller inlet and outlet
- Constant mass flow rate through the pump
- No thermal, mechanical or hydraulic losses
- Inviscid and incompressible flow

The Euler pump equation (also valid for turbines) is the starting point for building the velocity triangles which is a powerful concept used as a basis for pump design. Schobeiri (2005) describes how the energy brought to the flow by the rotating impeller is converted into a pressure rise.

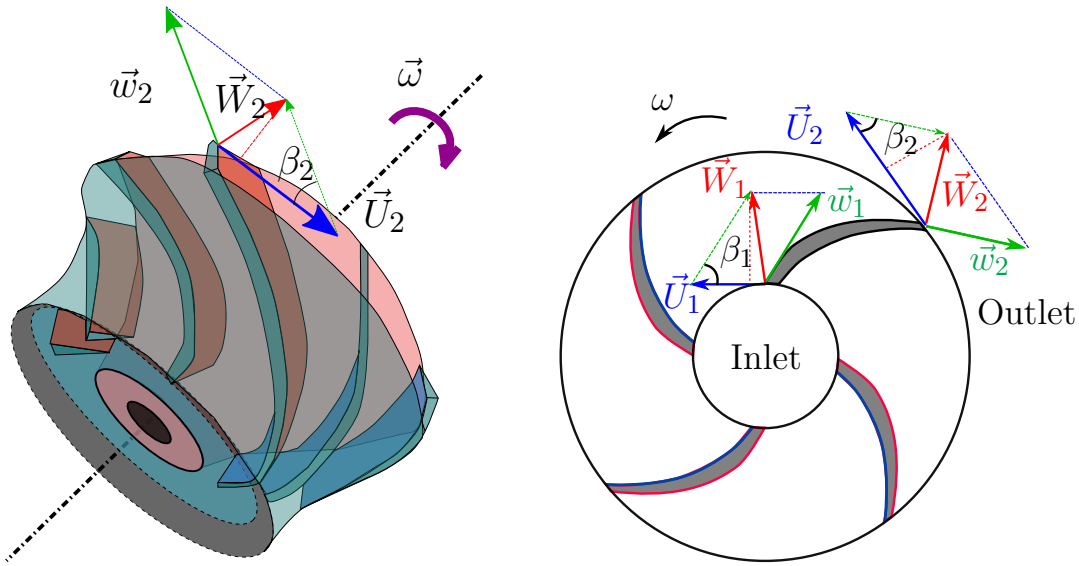

(a) 3D sketch of a mixed-flow impeller (b) Top view of a radial impeller

Figure 1.5 For both impellers, a few blades are shown with the pressure side in red and the suction side in blue. The velocity triangles at the inlet and outlet show the circumferential velocity $\vec{U} = \omega r \vec{e}_\theta$, the relative velocity $\vec{w}$ and the absolute velocity $\vec{W}$.

Velocity triangles

The liquid velocity field in the laboratory frame of reference $\mathcal{R}_0$ is $\vec{W}$ and usually called absolute velocity. It can be expressed in the cylindrical coordinate system (r, θ, z) around the pump rotation axis $\vec{e}_z$. We call relative velocity $\vec{w}$ the flow field expressed in the frame of reference $\mathcal{R}_1$ rotating at ω around the axis $\vec{e}_z$. The so-called "velocity triangles" at the impeller inlet and outlet are shown in Figure 1.6: the projection of the relative flow velocity $\vec{w}$ on the tangential vector $\vec{e_\theta}$ is called the relative tangential speed w_u. Similarly, $W_u = \vec{W} \cdot \vec{e}_\theta$ is the absolute tangential speed.

For an impeller passage of constant height h, we can express the meridional speed ($\vec{W}_m = \vec{W} - W_u\ \vec{e}_\theta$) as a function of the volumetric flow rate Q and flow angle β. The flow angle is defined as the angle between the relative velocity $\vec{w}$ and the tangential direction at this point: $\beta = (\vec{w}, -\vec{e}_\theta)$, as shown in Figure 1.5 (see Figure A.5 for a more detailed 3D drawing). Then,

$$w_m = W_m = \frac{Q \sin\alpha}{2\pi \widetilde{R} h}, \qquad \frac{w_m}{w_u} = \tan\beta \ ,$$

$$W_u = \omega \widetilde{R} - w_m \cot\beta = \widetilde{R}\omega - \frac{Q \sin\alpha}{2\pi \widetilde{R} h} \cot\beta \ .$$

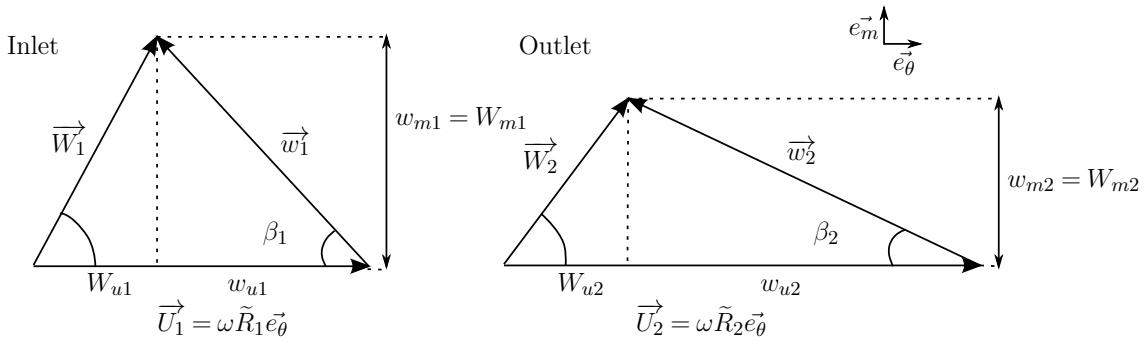

Figure 1.6 Velocity triangles: the absolute velocity $\vec{W}$ is the sum of the relative velocity $\vec{w}$ and the circumferential velocity: $\vec{U}$. $\vec{W} = \vec{w} + \vec{U}$. Figure 1.5 shows these triangles in relation with the impeller geometry.

By comparing the velocity triangles at the impeller inlet and outlet (Figure 1.6) and using the Euler pump equation (1.7) we get the total pressure rise as a function of the operating and geometrical parameters:

$$\Delta p^T = \rho\omega^2 \left(\widetilde{R}_2^2 - \widetilde{R}_1^2\right) + \rho\omega \frac{Q \sin\alpha}{2\pi h} \left(\cot\beta_1 - \cot\beta_2\right).$$

When $W_{u1} = 0$, the incoming flow has no pre-rotation and the total pressure difference is:

$$\Delta p^T = \rho\omega \left(\widetilde{R}_2^2 \omega - \frac{Q \sin\alpha}{2\pi h} \cot\beta_2\right).$$

For a pump with a constant flow angle ($\beta_1 = \beta_2$),

$$\Delta p^T = \rho\, \omega^2 \left(\widetilde{R}_2^2 - \widetilde{R}_1^2 \right) \tag{1.8}$$

These results have the advantage of describing the flow and pressure in an impeller in a very simple way. It shows that the pressure produced by the impeller is proportional to the fluid density, which is an argument that we will use in chapter 5.

The real flow in an impeller is however much more complex, and the next two Sections give a short account of the features that can be encountered and not described in the previous analysis.

1.1.5 Secondary flows and unsteady effects

Two-dimensional secondary flows

The flow in a real impeller does not perfectly follow the impeller blades, nor is perfectly axisymmetric. In fact, the velocities on the blade suction and pressure sides have to be different for this blade to produce a net force on the fluid. The one-dimensional analysis presented in Section 1.1.4 only considers the flow in and out the control volume, ignoring the local flow field. The flow on the pressure side is slower than on the suction side, and the flow angle is therefore smaller than the blade angle. This deviation is referred to as "slip" in the turbomachinery literature (e.g. Gulich, 2007) and depends on the blade shape and number. The slip factor k is defined so that $W_{2u\infty} - W_{2u} = (1-k)\, U_2$, where $W_{2u\infty}$ is the absolute tangential velocity at the impeller outlet in the ideal case where there is no slip ($k = 1$), and W_{2u}, U_2 are defined in the previous Section. Wiesner (1967) gives the empirical approximation

$$k = \frac{\sqrt{\sin \beta_2}}{Z^{0.7}},$$

where β_2 is the blade angle at the impeller outlet, and Z is the number of blades. A typical value for the impeller we study in the next chapters is $k = 0.14$.

The slip factor was analysed for different two-dimensional geometries and flow conditions using potential flows and conformal mapping by Visser (1996), who analytically linked the impeller design parameters with the velocity profiles on the pressure and suction side and the predicted pump performance for an inviscid flow. Hassenpflug (2010) also used the potential flow theory to numerically compute the flow in radial centrifugal impellers, showing recirculation at low flow rates.

The wake following the impeller and diffuser blades also contributes to make the flow non-axisymmetric, and especially complex at the impeller-diffuser interface. This problem is particularly studied in the centrifugal compressor literature, under the name "Rotor-Stator Interaction" but also has implications for centrifugal pumps, as demonstrated by Braun (2009) and Brennen (2011). It can lead to an early stall in the diffuser blades, or to a rotating stall at a frequency lower than the rotation

frequency (sub-synchronous vibrations), which can have a negative impact on the pump mechanical parts, like the shaft and bearings.

Three-dimensional and part-load flow features

The meanline and blade curvature, as well as the centrifugal and Coriolis forces cause vortices to appear in the boundary layer or across the flow passage. Lakshminarayana (1995) describes these secondary flows in detail and underlines their importance for designing elements of turbo-machines. These features can indeed advance or postpone the onset of the boundary layer separation and therefore change the pump, turbine or compressor performance.

For a flow rate less than 80% of the design flow rate, the flow in the impeller and diffuser is no longer parallel to the blades: separation of the boundary layer is likely to occur together with recirculation, and three-dimensional flow features become significant. Gulich (2007) gives a detailed account of these phenomena. As the pressure on the outer diameter is higher than the pressure close to the hub, recirculation cells appear at the blades leading and trailing edges.

Secondary flows are induced by forces that act perpendicularly to the flow. Gulich (2007) defines a Rossby number for radial impellers as the ratio of the centrifugal to Coriolis accelerations:

$$Ro = \frac{||\omega^2 \vec{e}_z \times \vec{r}||}{||2\omega \vec{e}_z \times \vec{w}||}.$$

If this number is near to 1.0, the secondary flow are not noticeable. However if it is lower or higher than one, different secondary flows will take place to balance out the forces. Several Rossby numbers can be formed, based on the decomposition of centrifugal and Coriolis forces, but also the forces arising from the pressure gradients at different points in the pump. They are used to predict the intensity of secondary flows. In practice, these flows all combine together and no pump is exempt from three-dimensional secondary flows.

Unsteady flow effects

Most methods used to predict the head produced by a pump assume that the flow in the impeller is steady in the impeller frame of reference and that the flow in the diffuser is steady in the diffuser (or laboratory) frame of reference. In practice, unless the flow at the impeller outlet is perfectly axisymmetric, which is impossible due to the presence of the blades, this is never the case.

The flow unsteadiness is often maximal at low flow rates, when the flow coming out of the impeller is not well adapted to the diffuser design, as the outlet flow angle has changed. Recirculation cells can fluctuate, changing size and location within the impeller or diffuser passage, and the flow rate through a single passage can vary with time. This can lead to a different average pressure from that predicted when assuming

a steady flow.

An impeller or diffuser blade can "stall" if the angle of attack of the incoming flow is too high: the boundary layer prematurely separates from the pressure side and the force produced by the blade suddenly drops. The flow in the stalled passage is reduced, and this affects the flow angle in the next passage, preventing the next blade from stalling. Depending of the number and arrangement of blades in the impeller and diffuser, a so-called "rotating stall" can be observed, where the impeller or diffuser blades stall and then recover one after the other, often against the rotation direction and at a lower frequency. Brennen (2011) described the onset and conditions of this phenomena, and Braun (2009) experimentally investigated it, using Laser Doppler Velocimetry. This type of instability can trigger mechanical sub-harmonic vibrations, and compromise the pump mechanical integrity.

1.2 Gas-Liquid flow through a pump stage

When a gas-liquid mixture is ingested into a pump impeller, the centrifugal and Coriolis accelerations affect the gas and the liquid differently. As a result, the two phases have different velocities and tend to separate. We first give definitions and orders of magnitude relevant to the gas liquid flow, and then review the experimental and numerical studies on gas-liquid flows in centrifugal pump stages, showing the relationship between the flow pattern in the impeller and its performance, as well as the important role of bubble size.

1.2.1 Definitions

The abbreviation GVF is loosely used in the literature for the ratio of gas flow rate to total flow rate (also called gas cut) going through the pump or at the pump intake (before passing through a gas separator), or the local gas void fraction (mainly used in multiphase numerical simulations). In this thesis, we will use the names and definitions below.

Gas cut at the n-th stage inlet (0 for the pump intake):

$$\lambda_n = \frac{Q_{gn}}{Q_{gn} + Q_{ln}},$$

Gas quality at the n-th stage inlet:

$$x_n = \frac{\dot{m}_{gn}}{\dot{m}_{gn} + \dot{m}_{ln}}, \tag{1.9}$$

Local gas volume fraction in the n-th stage:

$$\alpha_n = \frac{A_{gn}}{A_{gn} + A_{ln}},$$

where Q represents the volumetric flow rate, for gas (subscript g) or liquid (subscript l). $\dot{m}$ is the mass flow rate, and A is the cross-flow area occupied by one or the other phase.

If there is no phase change between the gas and the liquid, x_n is constant through all the stages. In the absence of gas separator, which is sometimes placed upstream of the first pump stage (see Figure 1.13), the gas quality is denoted as x_0.

If there is no gas separator, $\lambda_0 = \lambda_1$. If the gas and liquid travel at the same speed, $\lambda_n = \alpha_n$, and λ is therefore sometimes called the non-slip gas fraction. If the liquid can be considered as incompressible, $Q_{ln} = Q_{l0} = Q_l$. In the following, when we use the abbreviation GVF without further explanation we refer to the gas cut at the first stage inlet, unless the location is otherwise specified.

The geometrical scaling for centrifugal pumps in single phase flows has been presented in Section 1.1.2. For gas-liquid flows, more parameters have to be taken into account. Table 1.1 summarizes the important quantities and their values in a production installation or in a test facility. Using the gas density ρ_g, a characteristic bubble diameter d and gas-liquid surface tension σ, we create three additional dimensionless groups that will be of importance to description the flow.

$$\xi = \frac{\rho_g}{\rho_l} \qquad \text{Density ratio}$$

$$\varepsilon = \frac{d}{R} \qquad \text{Bubble diameter}$$

$$Bo = \frac{\Delta\rho\ \omega^2\ R\ d^2}{\sigma} \qquad \text{Bond number}$$

Table 1.1 List of parameters relevant to gas-liquid flows through an ESP, with their expected range for a real system (Production column) and in a scaled experiment (Test column).

	Production	**Test**	unit
Operating parameters			
Rotation speed ω	3500	1200	rpm
Volumetric flow rate Q	100 - 5000	600-2000	bpd
Pressure rise ΔP	10-100	0.5-2	bar
Head $H = \Delta P/\rho g$	10-100	5- 20	m
Input power $P = \omega T$	100-5000	4.5	kW
Mean passage velocity V_p	5	1.5	m/s
Fluid properties			
Intake pressure P_i	10-200	1-3	bar
Intake temperature T_i	50-250	10-30	°C
Liquid Viscosity μ_l	1 - 1000	1 - 1.8	cP
Gas Viscosity μ_g	0.02	0.01	cP
Liquid Density ρ_l	800 - 1200	800 - 1000	kg/m^3
Gas Density ρ_g	30 - 100	1.2	kg/m^3
Interfacial surface tension σ	5-30	72	mN/m
Bubble diameter d	0.001	0.001	m
Pump geometry			
Pump diameter D	0.1 - 0.2	0.1	m
Passage height h	0.01	0.01	m
Surface roughness ϵ	0.1-0.5	0.01	mm
Specific number N_s	1500-4000	2700	-
Number of blades Z	5-11	8 / 11	-
Number of stages n	8-300	3-5	-
Non-dimensional groups			
Density ratio	0.06	0.001	-
Bond number	500	20	-

1.2.2 Flow regimes in a pump stage

This section is a review of the work done to characterise gas-liquid flows in a centrifugal pump stage, through experimental and numerical studies.

Experimental work

Using high speed imaging, Furukawa et al. (1996) explored radial stage design alterations in order to reduce the impact of gas on the pump head. They found that the gas accumulated on the suction side of the impeller blades. A gas pocket was contained at the impeller outlet for low gas flow rates and progresses toward the inlet while the performance degraded with increasing gas fraction. Based on these observations, they gave some empirical design recommendations to avoid gas accumulation:

1. Leave the impeller tip open to avoid gas accumulation through leakage.
2. Use a vaned diffuser whose vanes are close to the impeller outlet.
3. Keep the impeller outlet blade angle high.
4. Use recirculation holes through the impeller to break up the gas bubbles.

Barrios and Prado (2011a) identified different flow patterns occurring in a single radial impeller and found that gas bubbles were rarely spherical but rather ellipsoidal. At surging conditions (in their case around 0.3% gas volume fraction), the gas bubbles accumulated on the pressure side, coalesced and recirculated in the nearby channel at the impeller outlet, while a gas pocket forms on the suction side at the impeller inlet as shown on Figure 1.7. The gas pocket grew until it blocked the entire channel and triggered "gas lock". We will come back on the definition of this term in Section 1.3.2. Barrios and Prado (2011a) also performed single phase numerical simulations of the same pump geometry and noticed that the gas accumulated in the recirculation areas. The poor tolerance to gas of the pump studied (locking at less than 1% gas fraction) seemed to be due to the recirculation already present in single phase operation.

Schäfer et al. (2015) looked at the gas distribution in a shrouded radial centrifugal impeller, using Gamma-Ray Tomography. The time averaged gas volume fraction $\langle \alpha_1 \rangle$ was always much higher than the inlet gas cut λ, and a large discontinuity was observed at a critical gas fraction ($\lambda_0 = 3\%$) as the local gas volume fraction in the impeller doubled from 24 to 48% when λ_0 increased from 3 to 3.3%. They observed that the gas accumulated in the inlet region of the pump. Like Furukawa et al. (1996), they investigated the effect of a balance hole drilled in the hub and saw that the passage where the hole was drilled presented less gas accumulation as shown in Figure 1.8.

Pirouzpanah et al. (2016) introduced 17 electrodes on the diffuser inner wall of a three-stage Multi-Vane Pump (MVP, commercialised by Centrilift), in order to measure the in-situ gas volume fraction. These measurements confirmed the large difference between the gas cut and the local gas fraction ($\lambda < \alpha$).

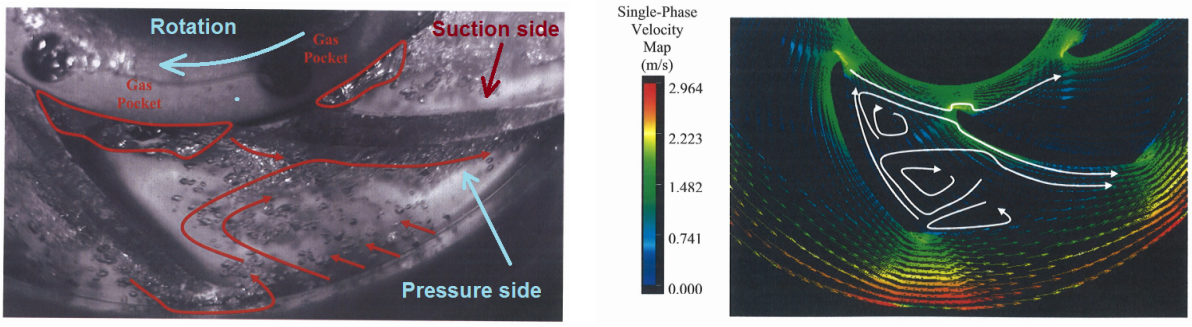

Figure 1.7 Flow visualisation in gas-liquid (left) and CFD single phase results (right) by Barrios and Prado (2011a) of a radial pump running at 900 rpm (clockwise) showing recirculation in both cases.

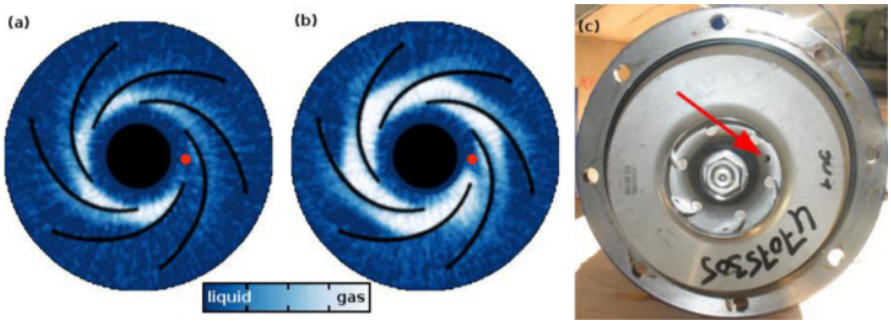

Figure 1.8 Asymmetric gas hold-up distribution caused by a balancing hole in the impeller. rotating at at 1480 rpm, with $\lambda_0 = 1\%$ (a) and $\lambda = 2.6\%$ (b). A picture of the impeller is shown in (c). From Schäfer et al. (2015)

Most of the experiments published in the literature (and all the visualisations) focusing on the flow pattern in a pump stage were carried out using a single radial stage. However, the typical use of these pumps in the oil industry involves several mixed-flow stages. For this work, this motivated the construction of the rig described in chapter 2, that can accommodate more than one stage, in order to assess the potential effect of the adjacent stages on the one under study.

Numerical work

Minemura and Murakami (1980) proposed a finite elements model based on a single bubble in an otherwise single phase liquid flow. Minemura and Uchiyama (1994) later moved to a 3D geometry, with a bubbly flow and a fixed cavity whose size and location was determined by iterating on a critical gas volume fraction above which the cavity was formed. They observed that from the point when a cavity was formed, increasing the gas fraction did not significantly change the performance.

Three-dimensional simulations were carried out by Caridad et al. (2008) for gas-liquid flow in a radial stage and by Ossia and Godeluck (2006) in commercial mixed-flow stages (Schlumberger, model SN8500). Both used a commercial software based on Reynolds-Averaged Navier-Stokes (RANS) equations with embedded turbulence and two-fluid models. Caridad et al. (2008) used a mono-disperse bubbly phase and conducted simulations with different bubble sizes (0.1, 0.3 and 0.5 mm). Ossia and Godeluck (2006) used a population balance model (MUSIG: Multiple Size Groups model) and were able to match the pump experimental degradation curve. Their studies confirmed that the degradation of the pump performance was due to the accumulation of gas bubbles in a "gas pocket" that restricted the passage area for the remaining fluid. Increasing the diameter of the bubbles degraded the performance as larger bubbles experience a larger centrifugal force for a comparable drag force and therefore were more likely to become trapped in the impeller. The location of the gas pocket was however different in both studies: on the pressure side according to Caridad et al. (2008) and on the suction side for Ossia and Godeluck (2006). The difference is likely due to the geometrical features rather than from the method, as similar discrepancies were reported in experiments: Tillack (1998) reported gas bubble accumulation at the inlet on the pressure side, while Barrios and Prado (2011a) reported the bubble accumulation on the suction side.

Zhu et al. (2014) used the commercial package ANSYS to simulate the presence of gas in a three-stage ESP. An Eulerian-eulerian two-fluid model was used, with a fixed bubble size. They reproduced the single phase performance (head, efficiency) within a reasonable accuracy, but the two-phase results depended on the bubble size to the point that no prediction was possible without an a-priori knowledge of the bubble size distribution.

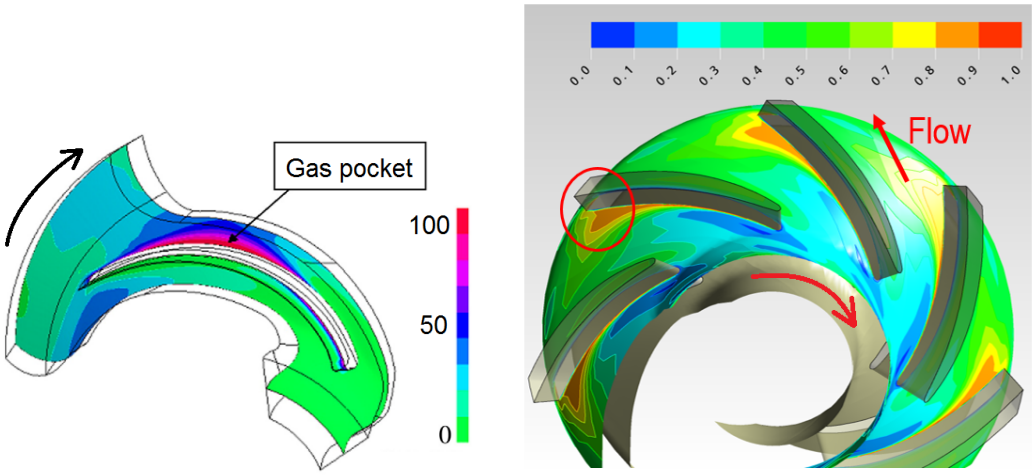

(a) Radial impeller with 10% GVF and 0.5 mm bubbles. A gas pocket appears on the pressure side of the blade.

(b) Mixed-flow impeller with 30% GVF and poly-distributed bubble phase. The gas pocket is on the suction side.

Figure 1.9 Local gas fraction (hold-up) in radial and mixed flow impellers obtained by CFD, from Caridad et al. (2008) (left) and Ossia and Godeluck (2006) (right). The colour scales represent the local gas void fraction.

Bubble size

Minemura and Murakami (1980) showed through an experiment in a radial impeller, that small bubbles (less than 0.1mm) followed the same trajectory as the liquid, while larger ones (about 1mm) are significantly deflected. Barrios and Prado (2011a) measured the bubble size in the radial pump impeller under test, and drawn a correlation fitting the experimental data, based on Hinze (1955) scaling, and dependent on the pump frequency, gas and liquid densities, interfacial surface tension and pump diameter. Zhu and Zhang (2016) improved this correlation, and validated it by using it as an input for CFD simulations, which resulted in a head prediction within 10% error, compared to up to 50% for previous studies. The bubble size is therefore one of the most critical parameters to determine the gas-liquid flow within a pump stage.

1.2.3 Head prediction

For a gas-liquid flow, the total pressure $\Delta p^T_{2\phi}$ produced by the pump is no longer proportional to fluid density. The concept of head is however still used, using the homogeneous mixture density $\rho_m = \rho_l(1-\alpha) + \rho_g\alpha$ as a reference:

$$H_{2\phi} \equiv \frac{\Delta p^T_{2\phi}}{\rho_m g}$$

Correlations based on dimensional analysis and experimental data are put together, in order to predict the pump head curve in these conditions.

Surging boundary

The pump is said to surge, when it is not longer able to provide a steady pressure to the system, leading to fluctuating and/or low flow rates. Knowing the maximal gas fraction allowable in a pump before surging has been the main concern for oil field operators (Lea and Bearden, 1982). For this, it was found useful to have a formula independent of the pump design, which was often kept secret by the manufacturers.

The most widely used criterion was written by Turpin et al. (1986) and was based on the inlet pressure P_i (in psi), and ratio of gas to liquid flow rates Q_g/Q_l. They defined the critical parameter

$$\Phi_c = \left(\frac{2000}{3P_i}\right)\frac{Q_g}{Q_l}.$$

For $\Phi_c < 1$, a degradation factor should be applied to compute the two-phase head and for $\Phi_c > 1$, the pump is surging.

Contrary to single phase flow, the properties in gas-liquid flow change along the pump: the GVF decreases as the fluid progresses through the stages and its pressure increases. Gamboa (2008) therefore instrumented each stage of the pump under test with absolute pressure sensors, in order to study the stage characteristics individually. Gamboa and Prado (2011) list several correlations and underline the discrepancies between them. They tested a 22-stage commercial mixed-flow pump (Centrilift, model GC-6100) using water and nitrogen to determine its head curve (Figure 1.10) in gas-liquid conditions.

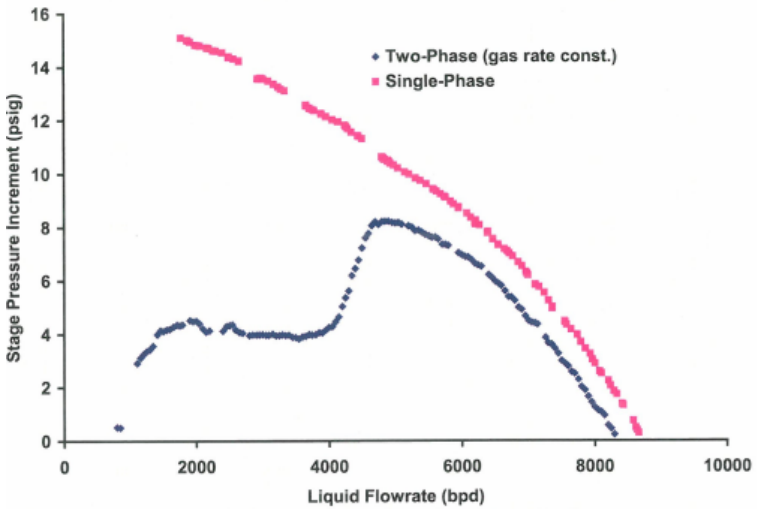

Figure 1.10 Pressure produced by a stage when decreasing the liquid flow rate, for a constant gas flow rate (blue curve), the rapid gradient change of the head curve indicates a surging boundary. From Gamboa (2008).

The authors also proposed drawing several boundaries on a map showing the normalized gas and liquid flow rates, as shown on Figure 1.11. The homogeneous

boundary defined the point where the pump performance started to degrade compared to the single phase prediction. The first surging boundary denoted the highest head achieved for a particular gas flow rate. The second surging boundary was crossed when the head stabilizes at a low value and finally the third surging boundary or gas lock was reached when the pump did not produce any pressure.

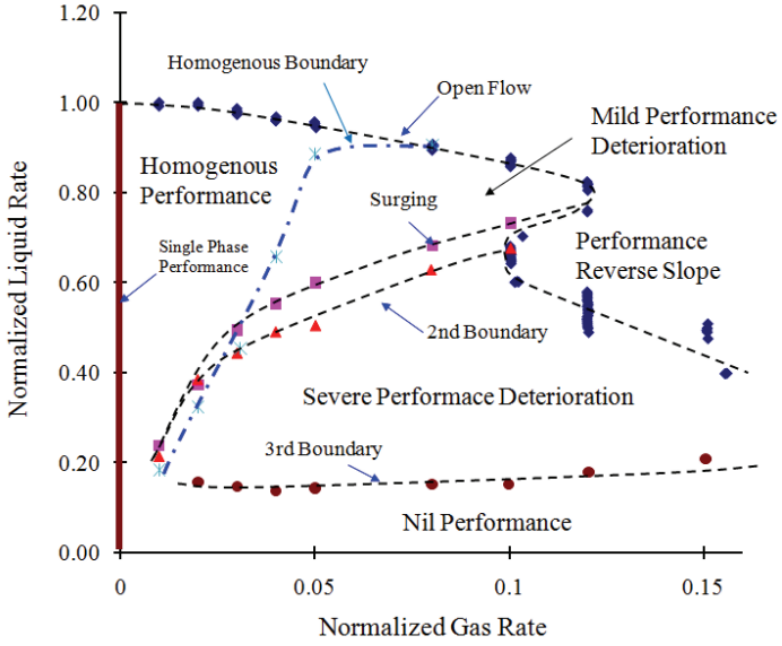

Figure 1.11 Gas-liquid homogeneous and surging boundaries for a commercial pump ($f = 60$ Hz, $Q_{\text{BEP}} = 6480$ bpd, $N_s = 3300$) from Gamboa and Prado (2011).

They propose a new correlation for the surging boundary, based on the phase density ratio ρ_g/ρ_l, normalised liquid and gas flow rate Q_l^* and Q_g^*, rotation speed ω, pump diameter D and liquid viscosity ν. The power coefficients are adjusted to fit the experimental data which leads to a semi-empirical correlation,

$$Q_g^* = \left(\frac{\rho_g}{\rho_l}\right)^{0.2} \left(\frac{\omega D^2}{\nu}\right)^{0.4} (0.1 \exp(Q_l^*))^{4.5} \ .$$

Head degradation

In 2006, in order to improve the correlations and make them specific to the impeller and diffuser geometry, Ossia and Guénégo (2006) tested several pumps. The absolute and differential pressure was measured across several stages at different locations along the pumps that could include from 40 to 100 stages. The results were aggregated together in the form of a head degradation factor

$$\mathcal{M}_{2p} \equiv \frac{\text{Head in two-phase}}{\text{Head in water}} = \frac{\Delta P_{2p}/g\ \rho_m}{\Delta P_{water}/g\ \rho_{water}} \tag{1.10}$$

The two plots on Figure 1.12 represent the head degradation factor for two different mixed-flow stage designs, showing that the details of the geometry have a strong effect on the critical gas fraction.

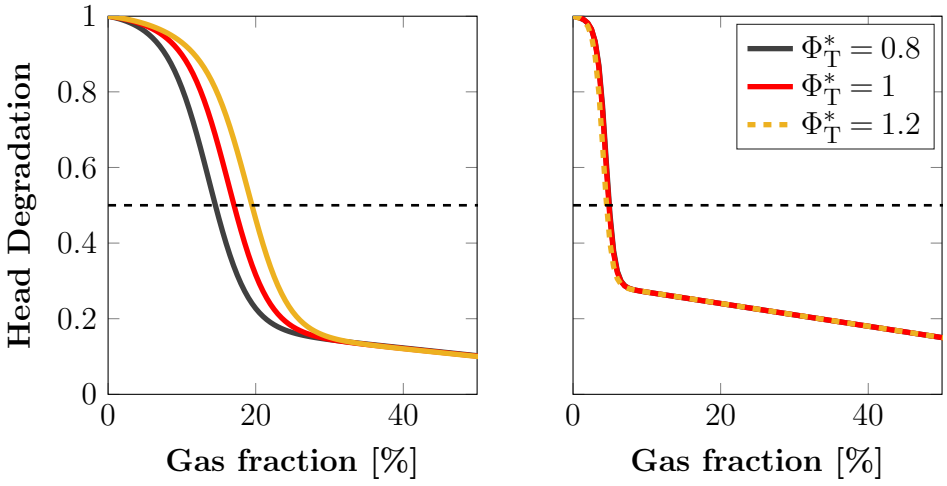

(a) Mixed flow stage A: $\omega_s = 0.6$, Meridional angle $\alpha = 60°$, Blade angle $\beta = 30°$

(b) Mixed flow stage B: $\omega_s = 0.7$, Meridional angle $\alpha = 60°$, Blade angle $\beta = 40°$.

Figure 1.12 Head degradation factor for two mixed-flow stages run in the same conditions with no gas handler. f=50 Hz, P_i = 500 psi, flow rate: 80 to 120 % of BEP ($\Phi_T = 0.8$ to 1.2). The head degradation factor is 1 for single phase flow, and decreases as the gas fraction increases. The impeller geometrical characteristics of the two pumps are similar: outer diameter, and meridional angle, specific speed ω_s and blade angle. The head degradation was however very different. A possible explanation lies in the hydraulic efficiency at the BEP: 60% for the stage A and 70% for the stage B.

Finally, Camilleri et al. (2009) acquired field data (intake and discharge pressures, pump speed and surface gas and liquid flow rates) for two gassy wells equipped with 15 Poseidon stages and 159 mixed-flow stages (Schlumberger, SN8500).

$$P_d - P_i = g \sum_{stage=1}^{174} C_h(\alpha_{stage})\ \rho_m\ H_{\text{single phase}}$$

Both the mixture density ρ_m and the degradation coefficient C_h dependws on the gas fraction α_{stage}. The function $C_h(\alpha)$ was assumed to be a polynomial function fitting the observed pressure rise for the complete string. This method however led to different degradation coefficients for each test well. The authors indicate that the liquid to gas density ratio and water cut, which were not taken into account, could be responsible for this discrepancy.

To summarize, the various correlations found in the literature are pump specific, but share the following characteristics:

- At high liquid flow rate and low gas fraction, there is almost no effect of the gas on the pump head.
- When the flow rate decreases, gas has a larger impact.
- The pump performance improves when the rotation speed increases.
- The intake pressure has an effect through the gas to liquid density ratio (ρ_g/ρ_l). An increase in the intake pressure entails a rise of the density ratio and therefore an improvement of the pump performance.

One-Dimensional Modelling

Minemura et al. (1998) presented a one-dimensional, two-fluid model where the slip between the gas and the liquid phase was only along the streamline direction, and the bubble size was taken from experimental data. Correlations were used for estimating the wall friction, and a critical gas fraction determined the flow regime (bubbly or separated flow). This method provided a head degradation in accordance with the experimental data. Sherwood (2005) implemented a similar model and attempted to compare the performance of two mixed-flow pumps, but concluded that the was not a suitable method to accurately predict the pressure delivered by a mixed-flow pump.

Sterrett et al. (1996) computed the trajectory of a single bubble in a radial impeller with logarithmic blades. The liquid flow was a 2D potential flow based on the superimposition of a source flow and a free vortex flow. He also wrote a 1D model, also using several critical gas fractions to determine the flow regime (bubbly, churn-bubbly and churn-turbulent) with values derived from an existing experimental dataset.

Barrios and Prado (2011b) defined a surging bubble radius from the equation of motion for a single bubble in the impeller. The surging radius was reached when the bubble velocity was zero at a representative pump diameter, chosen between the inlet and outlet diameter.

As part of this work, we have implemented several one-dimensional models, and Chapter 5 is dedicated to finding the simplest possible model that can be used to compare two different pump designs and estimate their performance in a gas-liquid flow.

1.2.4 Gas bubbles in rotating liquid flows

The behaviour (shape, motion, break-up and coalescence) of gas bubbles is fundamental to the study of two-phase flows. Magnaudet and Eames (2000) and Michaelides (2003) wrote comprehensive reviews on the hydrodynamics of particles and bubbles. Appendix B treats the case of high Reynolds bubbles in more depth, while this Section gives a shorter and broader literature review.

We define the bubble (or particle) Reynolds number as

$$Re_b = \frac{2R|V_s|}{\nu},$$

where R is the bubble radius, $|V_s|$ is the difference between the velocity of the bubble centre and the velocity of the undisturbed liquid velocity U at the bubble location. In the bubble frame of reference, $U = V_s$.

Forces on a solid sphere

The equation of motion for a sphere in an incompressible flow is the point of entry to many approaches, as bubbles are often spherical and the contamination of their interface in non-pure liquid can make them behave like a solid in some respect.

D'Alembert formulated in 1752 the paradox that no hydrodynamic force is applied on a stationary solid placed in an inviscid, steady flow. Hydrodynamic forces only emerge out of the transient behaviour of the flow, and its viscosity. Stokes (1851) described the motion of a sphere moving in a viscous stagnant fluid: he found a hydrodynamic force equal to

$$\vec{F} = 6\pi R\mu_l \vec{U},$$

where U is the sphere velocity, R the sphere radius and μ_l the liquid dynamic viscosity. This force can be re-written for a uniform, steady flow as

$$\vec{F} = \frac{1}{2} C_d \pi R^2 \rho_l |U| \vec{U}, \tag{1.11}$$

where $\vec{U}$ is the velocity difference between the sphere and the flow, ρ_l the liquid density and C_d is called the Stokes drag coefficient:

$$C_d = \frac{24}{Re_b}. \tag{1.12}$$

The bubble Reynolds number is defined through the relative flow velocity in relation with the sphere (or bubble), the liquid kinematic viscosity $\nu_l = \mu_l/\rho_l$ and the sphere radius:

$$Re_b = \frac{2R|U|}{\nu_l}.$$

Boussinesq (1885) and Basset (1888) determined the transient hydrodynamic force applied to a sphere in a uniform creeping flow (for $Re_b << 1$) including the Stokes drag, the force due to the existing pressure gradient in the undisturbed flow, the added-mass and the history force. Oseen (1913) formulated an asymptotic correction to the Stokes drag coefficient, valid for $Re_b < 1$. This makes the Boussinesq-Basset-Oseen equation of motion:

$$\begin{aligned}\frac{4\pi}{3}\rho_s R^3\frac{d\vec{v}}{dt} =& \frac{1}{2}C_d\pi R^2\rho_l\left|\vec{v}-\vec{u}\right|(\vec{v}-\vec{u})\\ &-\frac{4\pi}{3}R^3\vec{\nabla}p+\frac{2\pi}{3}\rho_l R^3\frac{d(\vec{u}-\vec{v})}{dt}\\ &+12R^2\sqrt{\pi\rho_l\mu_l}\int_{t_0}^{t_1}\frac{1}{\sqrt{t-\tau}}\frac{d(\vec{u}-\vec{v})}{d\tau}d\tau+\vec{g},\end{aligned}$$

where $\vec{u}$ is the undisturbed liquid velocity field, $\vec{v}$ is the sphere velocity, ρ_s and ρ_l the sphere and liquid density, $\vec{\nabla}p$ the pressure gradient of the undisturbed flow field at the sphere centre, and $\vec{g}$ the acceleration due to gravity. According to Oseen (1913),

$$C_d=\frac{24}{Re_b}\left(1+\frac{3}{8}Re_b\right)$$

Maxey and Riley (1983) gave the equation of motion for a sphere in a unsteady, non-uniform flow for $Re_b << 1$, expressing the undisturbed liquid flow pressure gradient in terms of velocity derivative, using the Navier-Stokes equations.

Even at high Reynolds number, viscous forces are present through the boundary layer. The drag force is created by the shear in the boundary layer, and the pressure drop created at the rear of the sphere when the boundary layer separates from the solid surface.

Auton et al. (1988) studied the effect of unsteady rotational flow on the hydrodynamic force. They introduced the lift force, normal to the relative motion of the sphere and due to the strain present in the undisturbed flow, or the sphere relative rotation (Magnus effect). They give the following expression for the net force on the sphere, for an inviscid flow:

$$\vec{F}=\frac{4\pi}{3}R^3\rho_l\left(\left[(1+C_M)\frac{D\vec{u}}{Dt}-C_M\frac{d\vec{v}}{dt}\right]-C_l(\vec{v}-\vec{u})\times\vec{\omega}\right), \tag{1.13}$$

where $\vec{u}(t)$ is the undisturbed flow velocity at the solid sphere centre, $D\vec{u}/Dt$ is the material derivative of the undisturbed liquid flow field (following a fluid element), $\vec{\omega}$ is the undisturbed liquid flow vorticity, and $\vec{v}$ is the sphere centre velocity. C_M is the added mass coefficient and is 0.5 for a sphere. For a non-spherical body, it is a tensor.

The strain parameter

$$Sr=\frac{2|\vec{\omega}|R}{|\vec{u}|}$$

is used to represent the effect of the liquid strain on the sphere.

Bluemink et al. (2008) used numerical simulations and experimental measurements to analyse the drag and lift forces on a solid particle with a finite Reynolds number, in a rotating flow. For $2\leq Re_b\leq 200$ and $Sr\leq 0.1$, they could express the drag and lift coefficients using dimensionless parameters of the undisturbed flow, giving a good agreement with experimental data.

Forces on a gas bubble

A gas bubble is different from a sphere, as it can deform and/or have an internal flow field. It is also affected by surfactants potentially present in the liquid.

The interfacial tension σ between the gas and the liquid can be affected by the presence of surfactants in the liquid, which accumulate at the surface of the bubble and tend to reduce the interface mobility. The bubble then behaves more like a solid particle, when a critical surfactant concentration is reached, it is less prone to deformation. Its drag coefficient at low Reynolds number decreases, from the expression (1.12) to (1.14), according to Bel Fdhila and Duineveld (1996).

For a clean bubble, the gas-liquid interface is mobile and the boundary condition on the tangential velocity component is better represented by a zero-shear-stress rather than no-slip condition (used for a solid sphere). This results in a different drag coefficient for a fixed spherical bubble in a uniform and steady flow.

For $Re_b > 50$, Moore (1963) gives an estimation of the drag coefficient:

$$C_d = \frac{48}{Re_b}\left(1 - 2.211 Re_b^{-1/2}\right). \tag{1.14}$$

Merle et al. (2005) used large eddy simulations to analyse the forces on a small clean gas bubble in a turbulent pipe flow, for a Reynolds number based on the pipe diameter D_h and liquid velocity $\vec{u}$: $Re = D_h|\vec{u}|/\nu_l = 6000$. The bubble Reynolds number is $Re_b = 500$. They found that Moore's drag law (1.14) and the Auton expression (1.13) for the lift force are suitable for this type of flow.

A bubble can also deform due to the hydrodynamic forces, usually taking an elliptical shape. We use the elliptical factor

$$\chi = \frac{\text{major axis}}{\text{minor axis}},$$

and the Weber number

$$We = \frac{2\rho|U|^2 R}{\sigma} \ ,$$

where $|U|$ is the velocity difference between the bubble centre and the undisturbed flow, and σ the interfacial surface tension between the gas and the liquid.

Moore (1965) found an approximative relationship between the Weber number and the elliptical factor of the bubble for $We << 1$, based on the normal stress at the stagnation point and in the equatorial plane:

$$\chi = 1 + \frac{9}{64} We + \mathcal{O}(We^2). \tag{1.15}$$

Rastello et al. (2011) studied experimentally the force on clean bubbles in a rotating flow, and expressed the drag and lift coefficient as function of the bubble Reynolds number, elliptical factor, and Rossby number: $Ro_b = U/\omega R$.

Finally, path instability is a phenomenon observed for elliptical bubbles, when a gas bubble rising in a quiescent liquid takes a helical or zig-zag path upwards, rather than a straight one. Saffman (1956) looked at the coupled effect of the bubble inertia, surface tension and interface deformation to write a theoretical analysis of this instability. However, Lunde and Perkins (1997) showed that elliptical solid particles can also present a path instability, showing that the interface deformation is not essential in the phenomenon. Wake instability seems to have an important role in this phenomenon, but the complete mechanism leading to path instability is still poorly understood.

Bubbly flow

When more than one bubble are present in a liquid flow, they can interact with each other through break-up and coalescence, and also through the wake they generate.

Many numerical techniques have been developed to model bubbly flows. For example, Tryggvason et al. (2011) used direct numerical simulations with front tracking and mesh refinement methods, to allow the bubbles to be fully deformable. These simulations are however very large and this limits the size of the flow domain and the number of bubbles.

Few experimental studies have been able to simultaneously measure the gas and liquid phases. Ravelet et al. (2011) used fast particle image velocimetry (PIV) and image analysis to study the rise and break-up of bubbles in a turbulent flow. Martinez-Bazan et al. (2010) modelled the break-up frequency and size distribution of the resulting bubble population, using phase Doppler particle sizing (PDPA). Xue (2004) investigated four-point optical probes, as an intrusive measurement system to obtain the bubble sizes and velocities.

Many reviews, for example by Liao and Lucas (2010) and Han et al. (2011) gather experimental and numerical data used to create models and correlations in order to predict the size distribution of a bubbly flow. Coalescence depends on the number of collisions, due to the flow velocity gradients, turbulent eddies or buoyancy, but also on the efficiency of these collisions which is linked to the bubble velocities, and surface chemistry. These population balance equations can be integrated in simulation tools, as demonstrated by Cheung et al. (2013) who compared several models to predict the bubble size distribution in an upflowing bubbly flow, and compared the results to the experiments carried on by Prasser et al. (2002), using an electrode wire-mesh to measure the bubble size in a plane section of the flow.

1.3 Producing a gassy well

The fluid pumped by an ESP generally consists in a mixture of water and hydrocarbon, and the temperature and pressure at which the first bubble of gaseous hydrocarbon is formed is called the bubble point, or boiling point for a single component fluid. Certain reservoirs also have a gas cap which is produced at the same time as the liquid hydrocarbon. From the artificial lift perspective, forming a gas phase above the pump can be beneficial, as the density of the fluid is reduced and so is the hydrostatic pressure gradient. However, this becomes much more problematic when the gas cut is high at the pump inlet. The stability of such systems is widely recognised as critical. For example Bagci et al. (2010) state that the presence of free gas leads to unstable operation of the pump.

Note that the term cavitation is reserved to the phase change and creation of bubbles due to rapid changes of pressure induced by external forces, which is not the subject of our study.

Figure 1.13 represents one possible ESP installation in a well with a horizontal section. It consists of a motor and its protector, a shroud, an intake, a rotary gas separator, pump stages and finally the tubing to carry the fluid to the surface.

1.3.1 Existing multiphase pumping technologies

Lea and Bearden (1982) report early experiments on gas-liquid flows through an ESP and found a surge limit, around 10-15% GVF at pump intake, above which the pump experiences gas lock and the motor has to be shut down to prevent overheating. From the operational perspective, having to deal with gas has many implications on the physical installations as well as on the production strategy. Undesirable effects are: reduced production rates, limited available draw-down, downtime due to gas lock, large variation of the intake pressure (stressing the motor protector) and motor overheating. Frequent starts and stops are also pointed out by Peyramale (2013) as a cause of reduced pump life.

A widely applied guideline to design ESP systems for gassy wells is known as “Avoid, Separate, Handle” as explained by Bedrin et al. (2008). This means to place the pump intake if possible where there is no gas, then to take advantage of gravity separation or add special devices like rotary separators to redirect the gas out to the annulus, and as a last resort, to use pumps stages that are tolerant to high gas fraction.

Kallas and Way (1995) describe techniques to reduce free gas, among which are natural gas separation and venting through the casing annulus or the use of a tail pipe to feed the well from below the perforations. They tested “Advanced Gas Handlers” on depleted oil wells in Texas that would otherwise be too unstable to be produced. Based on recirculation holes and phase mixing, those impellers are placed upstream of the conventional stages and allow an estimated gas fraction of 20 to 30% at the pump inlet.

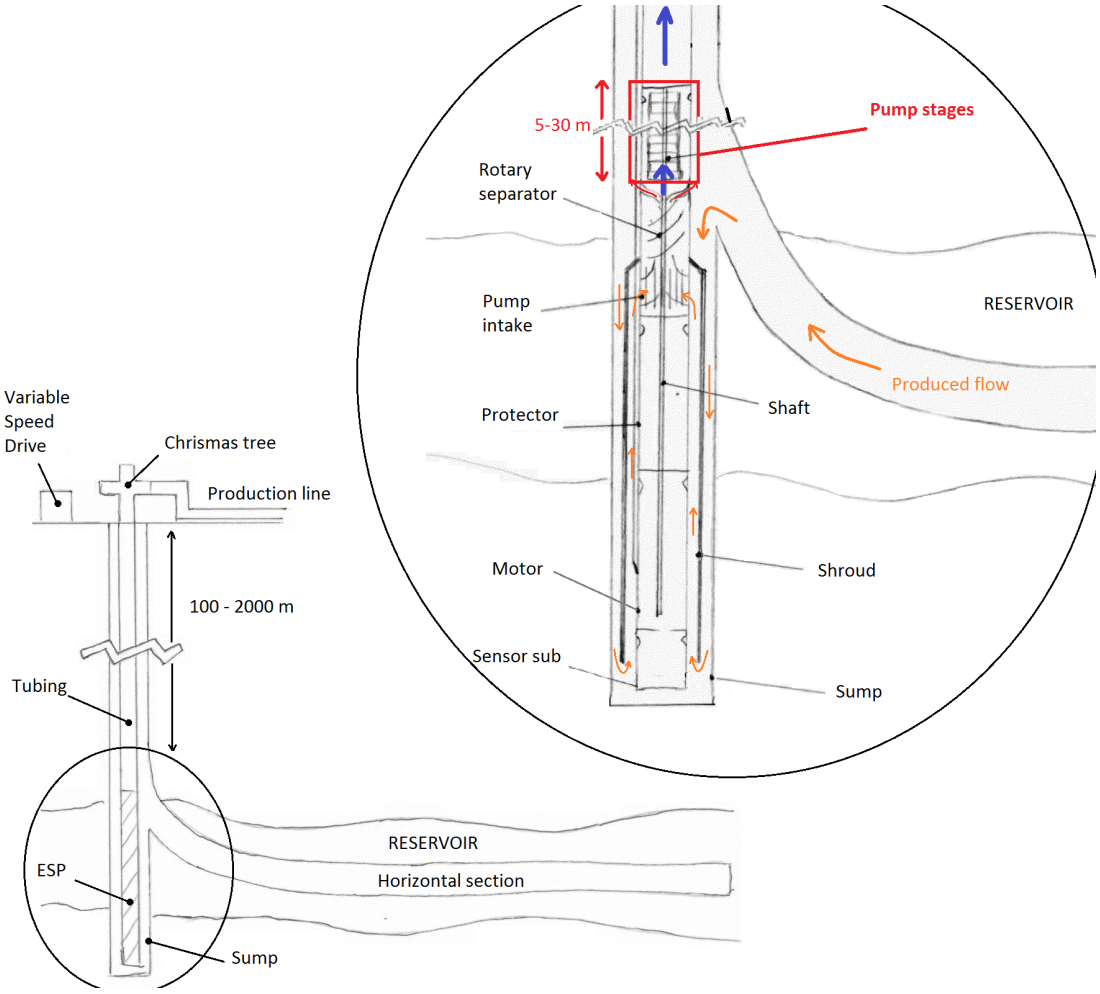

Figure 1.13 Example of ESP installation in a gassy horizontal well. The pump is placed in a vertical section below the reservoir, called the sump, in order to avoid gas entering the system. A rotary separator is added to redirect some of the remaining gas back into the annulus.

In the late 1980's, IFP (Institut Français du Pétrole) together with Total and Statoil started developing a helico-axial multiphase pump (see Figure 1.4c) under the trade mark Poseidon, at first for Onshore and Subsea applications, then extended to ESPs in 1999. Camilleri et al. (2009) show the benefit of these pumps installed upstream of a classical ESP in two wells in Congo. The fields of Kombi and Likalala had formed a secondary gas cap as the water injection had not been initiated early enough to maintain the reservoir pressure above the bubble point. After replacing the gas handlers by Poseidon stages, the production was stabilized, the downtime was reduced and the drawdown could be increased without changing the surface gas to oil ratio (GOR). As both wells had their production permanently monitored by a multiphase flow meter, it was possible to observe the system behaviour in detail.

Hua et al. (2012) give an overview of the current technologies used for multiphase pumping like the IFP helicoaxial pump, the Centrilift Multi Vane Pump (MVP), but also twin-screw pumps as described by MacNeil and Dass (2012) and progressive cavity pumps. These methods and their main features are summarized in Figure 1.14. A more complete patent review of the pumps developed especially for gas handling is presented in Appendix C.

	Pump Type			
	Helico-Axial	Centrifugal	Progressing Cavity	Twin-Screw
Pumping principle	rotating - axial flow	rotating - multivane impeller	Positive displacement	Positive displacement
Main supplier	Schlumberger (Poseidon)	Baker Hughes – Centrilift (MVP™)	PCM	CAN-K (ESTSP, TDTSP)
Maximum GVF	75%	70%	33% (elastomer stator)	98%
Maximum pressure	N/A	N/A	4,930 psi (2,200 m total measured depth maximum setting depth)	Up to 3,500 psi
Total capacity (liquid and gas)	5,000–9,000 BPD	18,000 BPD	Up to 6,200 BPD	Up to 450,000 BPD
Temperature limit	450°F	410°F	248°F	662°F

Figure 1.14 Current commercial downhole multiphase pumps summarized by Hua et al. (2012). Although they can handle significant gas fractions, twin-screw pumps are rarely seen downhole, because of their narrow operating range, and sensitivity to erosion.

A recent method for better gas handling takes advantage of automated control. Brunings and Ramirez (2013) used a closed-loop control of the annulus pressure at the surface. An optimal casing pressure was defined by an expert system to keep the well behaviour as stable as possible, and a simple PID algorithm (Proportional-Integral-Derivative control algorithm, aimed at correcting the inputs to reduce the difference between a measured value and its target set-point) controlled the annulus venting valve to achieve this target pressure.

Many operators also use real-time monitoring to prevent gas lock. If a gas lock is detected or anticipated, action can be taken on the rotation speed to avoid damaging the pump. As reported by Cardona et al. (2014) and Velasquez et al. (2013), the automation of these processes is on-going and seems promising, but the accurate detection as well as appropriate actions to take are still challenging.

1.3.2 Gas Lock

In the multiphase pumping industry "gas lock" is an event where the pump head and liquid flow rate are so low that they require the pump to be shut down because of a severe motor temperature rise. As explained above, this phenomenon can result of the interaction between the pump and the rest of the production system. When the gas volume fraction at the inlet exceeds a critical value, the produced head is not sufficient to maintain the flow through the pump. The head produced by the first stages is close to zero, while the later stages still have enough liquid to maintain some head, only counterbalancing the hydrostatic pressure. This situation can last until the pump is stopped, usually to prevent overheating the motor. If a short gas slug enters the pump inlet, it can progress through the pump stages, reducing the head of a few stages at a time while liquid is entering the first stages again, maintaining the head and ensuring motor cooling. For a steady intake gas fraction, even if the pump can deal with the gas present at the intake, the deformation of the head curve can lead to an instability. A perturbation in the flow can trigger flow rate oscillations that grow exponentially.

All these phenomena (gas lock, gas slugs, gas instability) can be combined, which make the analysis more difficult. From the pump design perspective, they all come from the fact that the head degradation factor depends on the total flow rate and intake gas fraction in a nonlinear way, leading to a threshold effect.

1.3.3 System Instabilities due to Gas

Although Takács (2009) gave a numerical approach for sizing gassy ESP applications, the literature on modelling such systems and their potential instabilities is rather sparse. The pump head curve gradient dH/dQ can be used to predict the stability of the pumping system. Bratu (1995) presented a transient model of a helico-axial pump operation and compared qualitative results with laboratory tests and field data from a surface installation. Using a linear equation to represent the pump two-phase characteristic $p \propto Q$, and neglecting the fluid inertia through the pump, he described the transient multiphase flow with the following parabolic partial differential equation on the pressure p, function of the time t and the location x along the tubing:

$$\frac{\partial^2 p(x,t)}{\partial x^2} = \frac{1}{a^2}\frac{\partial p(x,t)}{\partial t}, \tag{1.16}$$

where a is a parameter which depends on the pump head curve gradient, the pump speed and the mean operating condition (gas and liquid flow rates). This neglects the fluid inertia, and only allows a negative head curve slope which is the case for a helico-axial pump but not for more common mixed-flows or radial stages. This equation is therefore not suitable for predicting potential system instabilities when using mixed-flow pumps.

Stability analysis of a pumping system

Greitzer (1981) examines the static and dynamic stability of pumping systems, and gives a particular example where the pump runs in single phase flows, while gas is present elsewhere in the system. Here we expand the analysis proposed by Greitzer (1981), and explain how it relates to the mechanisms involved in the production stability for an oil well.

A simple system consists of a reservoir A, an inlet pipe of length L and cross-flow area A_p, a pump, a compliance volume V_c, a choke and a reservoir B as shown on Figure 1.15. While the reservoirs A and B have clear equivalents for an oil and gas installation (the oil reservoir and the storage facility), the compliance modelled here is a simplified view of the effect of the gas present in the tubing above the pump or in the annulus, between the well casing and the production tubing. Also for gas-liquid flows, the pump head curve would change dramatically with the gas fraction, as shown in Figure 1.10, which is not the case here, with a pump running in single phase flows.

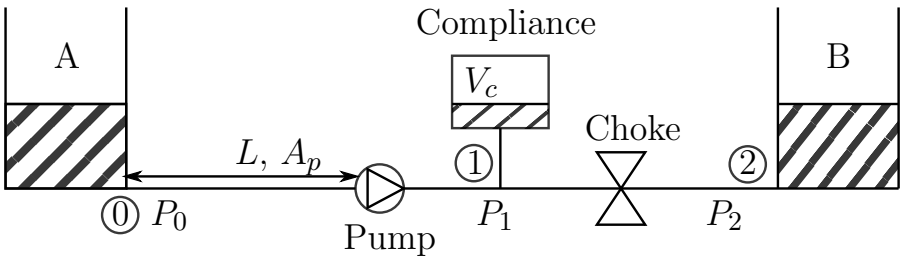

Figure 1.15 Schematics of a simplified pumping system

In the section ⓪ to ①, the mass flow rate through the pump is $\dot{m}_1$ and the fluid mass is $LA_p\rho$. The pump adds the pressure ΔP_p to the flow line. In the section ① to ②, the mass flow rate through the choke is $\dot{m}_2$ and the pressure drop is ΔP_s . The pressures at the system inlet and outlet are constant. For simplicity and without loss of generality, we assume $P_0 = P_2$ and neglect the friction in the inlet pipe and the inertia in the outlet pipe. The integrals of the momentum equations are therefore

$$\begin{cases} P_0 - P_1 = \dfrac{L}{A_p}\dfrac{d\dot{m}_1}{dt} - \Delta P_p(\dot{m}_1), \\ P_1 - P_2 = P_1 - P_0 = \Delta P_s(\dot{m}_2). \end{cases} \tag{1.17}$$

Mass conservation for the compliance gives

$$\dot{m}_1 - \dot{m}_2 = -\rho\frac{dV_c}{dt}. \tag{1.18}$$

In the compliance, the gas is assumed to follow an ideal gas isentropic law: $P_1V_c^\gamma$ is constant, where γ is the heat capacity ratio. This leads to

$$dV = -\frac{dP}{\gamma P}V, \tag{1.19}$$

and therefore

$$\frac{dV_c}{dt} = -\frac{dP_1}{dt}\frac{V_c}{\gamma P_1}. \tag{1.20}$$

Finally

$$\begin{cases} P_0 - P_1 = \dfrac{L}{A_p}\dfrac{d\dot{m}_1}{dt} - \Delta P_p(\dot{m}_1), \\ P_1 - P_0 = \Delta P_s(\dot{m}_2), \\ \dot{m}_1 - \dot{m}_2 = \dfrac{\rho V_c}{\gamma P_1}\dfrac{dP_1}{dt}. \end{cases} \tag{1.21}$$

A steady state solution of this system is

$$\begin{cases} \dot{m}_1 = \dot{m}_2 = \overline{\dot{m}} \\ P_1 = \overline{P}_1 = P_0 + \Delta P_p(\overline{\dot{m}}) = P_0 + \Delta P_s(\overline{\dot{m}}). \end{cases} \tag{1.22}$$

This solution exists if and only if the curves $\Delta P_s(\dot{m})$ and $\Delta P_p(\dot{m})$ intersect.

To assess the stability of the steady state solution, it is possible to linearise the equations (1.22) around $\left(\overline{\dot{m}}, \overline{P}_1\right)$. Using the variables $\delta\dot{m}_1$, $\delta\dot{m}_2$, δP_1 defined as

$$\begin{cases} \delta\dot{m}_1 = \dot{m}_1 - \overline{\dot{m}} \\ \delta\dot{m}_2 = \dot{m}_2 - \overline{\dot{m}} \\ \delta P_1 = P_1 - \overline{P_1}, \end{cases} \tag{1.23}$$

then to first order,

$$\begin{cases} \Delta P_p(\dot{m}_1) = \Delta P_p(\overline{\dot{m}}) + \delta\dot{m}_1 \dfrac{d\Delta P_p}{d\dot{m}}(\overline{\dot{m}}) \\ \Delta P_s(\dot{m}_2) = \Delta P_s(\overline{\dot{m}}) + \delta\dot{m}_2 \dfrac{d\Delta P_s}{d\dot{m}}(\overline{\dot{m}}) \\ \dfrac{\rho V_c}{\gamma P_1}\dfrac{dP_1}{dt} = \dfrac{\rho\overline{V_c}}{\gamma\overline{P_1}}\dfrac{d\delta P_1}{dt}, \end{cases} \tag{1.24}$$

and finally

$$\begin{cases} \delta P_1 = \dfrac{L}{A}\dfrac{d\delta\dot{m}_1}{dt} + \delta\dot{m}_1\dfrac{d\Delta P_p}{d\dot{m}} \\ \delta P_1 = \delta\dot{m}_2\dfrac{d\Delta P_s}{d\dot{m}} \\ \delta\dot{m}_1 - \delta\dot{m}_2 = \dfrac{\rho\overline{V_c}}{\gamma\overline{P_1}}\dfrac{d\delta P_1}{dt}. \end{cases} \tag{1.25}$$

This is a homogeneous linear differential equation with constant coefficients. $Y' = \mathcal{A}Y$, where $Y = (\delta\dot{m}_1, \delta\dot{m}_2)$ and

$$\mathcal{A} = \begin{pmatrix} \dfrac{A_p}{L}\dfrac{d\Delta P_p}{d\dot{m}} & -\dfrac{A_p}{L}\dfrac{d\Delta P_s}{d\dot{m}} \\ \dfrac{\gamma\overline{P_1}}{\rho\overline{V_c}}\Big/\dfrac{d\Delta P_s}{d\dot{m}} & -\dfrac{\gamma\overline{P_1}}{\rho\overline{V_c}}\Big/\dfrac{d\Delta P_s}{d\dot{m}} \end{pmatrix}. \tag{1.26}$$

The solutions are of the form $\alpha e^{s_1 t} + \beta e^{s_2 t}$ where s_1 and s_2 are the roots of the characteristic polynomial $\chi_{\mathcal{A}}(X) = X^2 - tr(\mathcal{A})X + \det(\mathcal{A})$ and the constants α and β depend on the initial conditions $Y(0)$ and $Y'(0)$.

If s_1 and s_2 are real, the system is stable if and only if both roots are negative, that is $s_1 + s_2 = tr(\mathcal{A}) < 0$ and $s_1 s_2 = \det(\mathcal{A}) > 0$. If s_1 and s_2 are complex, the system is stable if and only if $Re(s_{1,2}) = tr(\mathcal{A}) < 0$. With the assumption that the choke characteristic $\Delta P_s(\dot{m})$ always has a positive slope, Table 1.2 summarises the system stability.

Table 1.2 Stability conditions for the pumping system described in Figure 1.15

	If s_1 and s_2 are real ($tr(\mathcal{A})^2 \leq 4\det(\mathcal{A})$)	
A_1	$\dfrac{d\Delta P_p}{d\dot{m}} \leq \dfrac{d\Delta P_s}{d\dot{m}}$ and $\dfrac{A_p}{L}\dfrac{d\Delta P_p}{d\dot{m}} \leq \dfrac{\gamma\overline{P_1}}{\rho\overline{V_c}}\Big/\dfrac{d\Delta P_s}{d\dot{m}}$	Stable
A_2	$\dfrac{d\Delta P_p}{d\dot{m}} > \dfrac{d\Delta P_s}{d\dot{m}}$ or $\dfrac{A_p}{L}\dfrac{d\Delta P_p}{d\dot{m}} > \dfrac{\gamma\overline{P_1}}{\rho\overline{V_c}}\Big/\dfrac{d\Delta P_s}{d\dot{m}}$	Unstable
	If s_1 and s_2 are complex conjugate ($tr(\mathcal{A})^2 > 4\det(\mathcal{A})$)	
B_1	$\dfrac{A_p}{L}\dfrac{d\Delta P_p}{d\dot{m}} < \dfrac{\gamma\overline{P_1}}{\rho\overline{V_c}}\Big/\dfrac{d\Delta P_s}{d\dot{m}}$	Damped oscillations
B_2	$\dfrac{A_p}{L}\dfrac{d\Delta P_p}{d\dot{m}} = \dfrac{\gamma\overline{P_1}}{\rho\overline{V_c}}\Big/\dfrac{d\Delta P_s}{d\dot{m}}$	Sustained oscillations
B_3	$\dfrac{A_p}{L}\dfrac{d\Delta P_p}{d\dot{m}} > \dfrac{\gamma\overline{P_1}}{\rho\overline{V_c}}\Big/\dfrac{d\Delta P_s}{d\dot{m}}$	Unstable oscillations

In conclusion, the compliance introduces the possibility of two different mass flow rates in the pump and choke. When the pump head curve has a positive slope, it brings energy into the system which can lead to instability if this energy is not dissipated by the choke (or any friction in the system). The compliance acts like a mechanical spring, linking the two flow rates, and the onset of instability depends on its magnitude, as well as the inertia of the fluid present in the system, as shown above. A very small compliance would be associated with a very stiff system and a very large compliance corresponds to an open system where the pump and the choke do not interfere.

Stability of a multiphase pumping system

Even if the above conclusions are not directly applicable to an oil well (single phase flow in the pump, isolated compliance), we can compare the pump and system curves gradients with and without gas, for two typical installations. In Figure 1.16, we show a pumping system dominated by friction (blue and green curves), and a system dominated by hydrostatic head (blue and red curves). The solid lines refer to the single phase cases and the dashed lines to a moderate GVF (20 %). The steady-state operating point is the intersection of the corresponding pump curve (blue) and system curve (green or red).

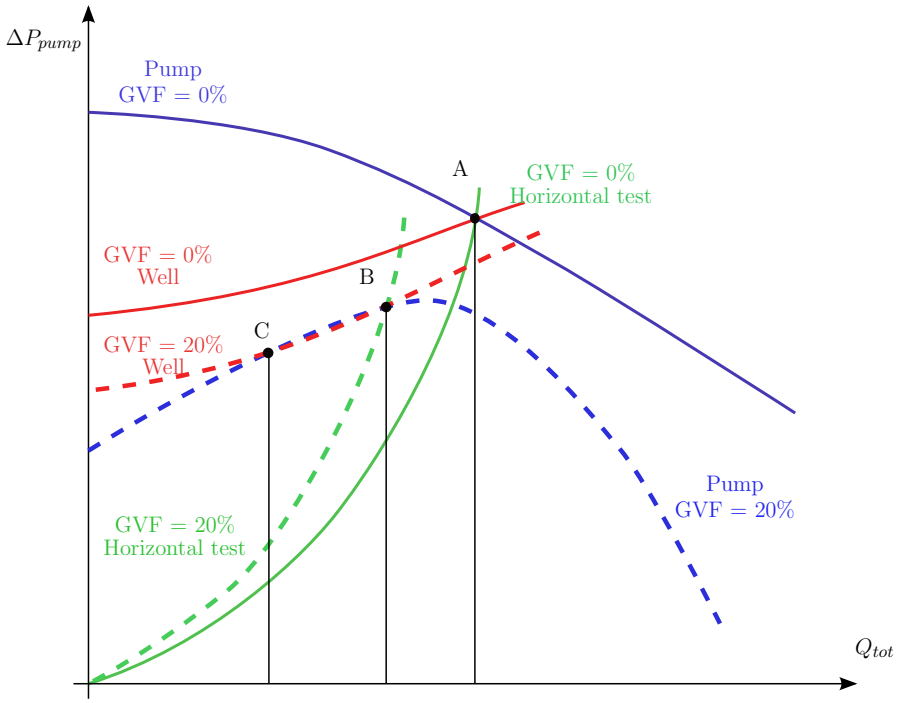

Figure 1.16 Pump head curve (blue) and system curves for two different systems (horizontal test loop -green- and vertical well -red-) in single-phase (solid line) and with 20% gas fraction (dashed line).

In single phase flows, the plain curves intersect at A, where the pump head curve gradient is negative. Therefore the conditions A_1 or B_1 from Table 1.2 are necessarily true and the system is stable. When adding gas, the pump head curve changes to the dashed blue curve, presenting a positive gradient on a large range at low flow rates. The gradients of the system curves slightly increase (higher friction coefficient in multiphase), but the hydrostatic head is also lowered as the fluid density decreases in the vertical section of the well. For the friction dominated system curve (for example in a horizontal test), the operating point is B. Even if $d\Delta P_p/d\dot{m} > d\Delta P_s/d\dot{m}$, the system could be unstable if $d\Delta P_p/d\dot{m} > \rho\overline{V_c}L/(A_p\gamma\overline{P_1}(d\Delta P_s/d\dot{m}))$. This last condition is difficult to assess in a complex system, but we see that the highest values of $d\Delta P_s/d\dot{m}$ are the less likely to produce an unstable system. For the hydrostatic dominated system

curve (for example in oil wells) the red and blue dashed curves have two intersection points: B and C. At the operating point B, the condition A_2 is verified, so the system is likely to be unstable and switch to the point C, where $d\Delta P_p/d\dot{m} > d\Delta P_s/d\dot{m}$. Again, this condition alone does not guarantee a stable system, and high values of $d\Delta P_s/d\dot{m}$ are preferable to achieve stability.

Gulich (2007) gives similar explanations based on potential perturbations from the operating point, but without referring to any quantitative analysis.

To conclude, the presence of gas can destabilise a system that was stable in single phase liquid. Installations driven by hydrostatic head are more sensitive to this phenomena as their system curve is not as steep as in friction dominated cases. To our knowledge, no quantitative stability analysis has been reported on a multiphase pumping system.

Conclusions

We have seen that the head degradation due to the presence of gas has a large impact on oil production, particularly through system instability. This loss of performance is still difficult to predict, and even if the main mechanism is known, the existing numerical and experimental methods have only successfully been applied to a single pump design, resulting in different and sometimes contradicting correlations. From the available literature, the role of Coriolis force on the gas phase remains unclear, as it is sometimes neglected or sometimes pointed out as a cause of separation.

One of the main challenges is to predict the performance of a particular mixed flow design. We will therefore work toward a mechanistic model, in order to give an insight into the forces acting on the gas bubble in a centrifugal pump impeller. The case of radial impellers has already been treated, for example by Sterrett et al. (1996), so we will focus on mixed-flow geometries.

The determination of the bubble size has been shown to be a critical factor in predicting head degradation. It has been studied by Barrios and Prado (2011a) for a single radial stage, but the evolution of the bubble size distribution from one stage to the next has to our knowledge never been investigated. Also, the gas pockets described by Furukawa et al. (1996), Barrios and Prado (2011a) and Caridad et al. (2008) as the triggering mechanism for severe head degradation, appear in different locations within the impeller, depending on the authors and possibly on the pump geometries they studied. Would such gas pockets exist in mixed-flow stages and where would they be located? Is the flow pattern in an impeller affected by the presence of upstream stages? When running the pump at low rotation speed (20 Hz), the segregation times due to gravity and centrifugal force are comparable in the diffuser and only differ by a factor 5 in the impeller. Is the effect of gravity in the pump negligible in these cases? We define in Section 4.3 the head degradation factor that quantifies the performance of a stage in multiphase conditions, and we explore its sensitivity to variations in the

inlet pressure, rotation speed, pump inclination and total volumetric flow rate.

Finally, capturing the single phase flow within the pump will help understanding the behaviour of the gas phase at very low GVF. We will characterise the pump performance in single phase liquid flows, and attempt to relate it to the observed flow features. In single phase liquid flows, mixed-flow stages with a high efficiency at design point tend to have a very flat single phase head curve at low flow rate (see Figure 3.1). Is this related to a particular flow field feature like rotating stall or rotor-stator interaction as suggested by Braun (2009)? Are there any flow instabilities challenging the steady state approach, which is much less costly than transient analysis, and therefore more commonly used for design?

Chapter 2

Experimental methods

A commercial multi-stage pump was used to observe the flow behaviour in single and multi-phase flows. An inclinable rig was built, that can accommodate up to five mixed-flow stages, with Laser Doppler Velocimetry, high speed video and torque, pressure and flow rate measurements capabilities. The objective of this series of experiments was to relate the head delivered by the pump to the observed flow pattern in both single and multiphase conditions. This chapter describes the apparatus and experimental methods used, while Chapters 3 and 4 attempt to answer the questions detailed in the conclusions to the previous chapter, which were not investigated in the surveyed literature.

Finally, we describe an separate attempt at quantitative measurement of the gas phase. A bulk measurement based on the fluid capacitance was implemented in order to obtain a time-resolved measurement of the gas fraction in a particular stage.

2.1 Inclinable ESP Flow Visualisation Rig

This section presents the hardware and methods used to measure the performance of a commercial multi-stage Electrical Submersible Pump (ESP) in single phase and gas-liquid conditions.

The volumetric gas flow rate is expressed in standard m^3/hr (or Sm^3/hr), which is the flow rate corrected for standard conditions of temperature ($T_s = 15^\circ$ C) and pressure ($P_s = 1$ bar).

2.1.1 Flow Loop

The rig, consisting of the tested pump section, its motor and instrumentation, was connected to an existing three-phase flow loop (see Figure 2.1), which can flow oil or water from 0.1 to 25 m^3/hr and gas (nitrogen) from 2 to 200 Sm^3/hr. An independent gas injector was built with a smaller gas controller, for gas flow rates from 0.04 to 20 Sm^3/hr. The gas injection point was located 1 m upstream the first impeller. A fully

transparent ESP was fitted and operated between 20 and 30 Hz, with an inlet pressure of 1.5 to 2.5 bar. The whole rig could be tilted to any inclination, and experiments were carried horizontally (0° from horizontal), quasi-vertically (89°), or tilted (61°), as shown in Figure 2.2.

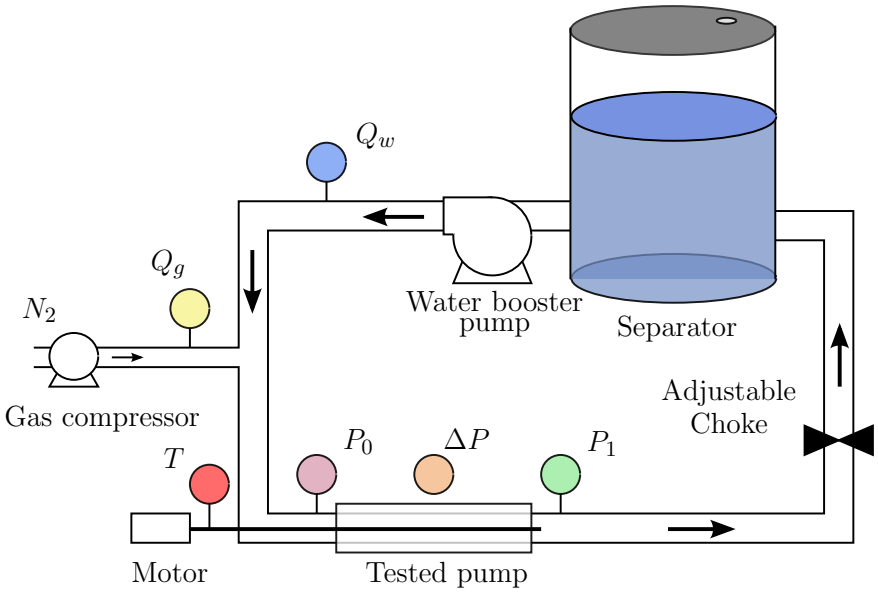

Figure 2.1 Schematics of ESP visualisation rig flow loop with available sensors, represented with a coloured circle and the name of the measured variable: Water flow rate Q_w, Gas (nitrogen, N_2) flow rate Q_g, Torque T, Inlet pressure P_0, Outlet pressure P_1, Pressure difference ΔP.

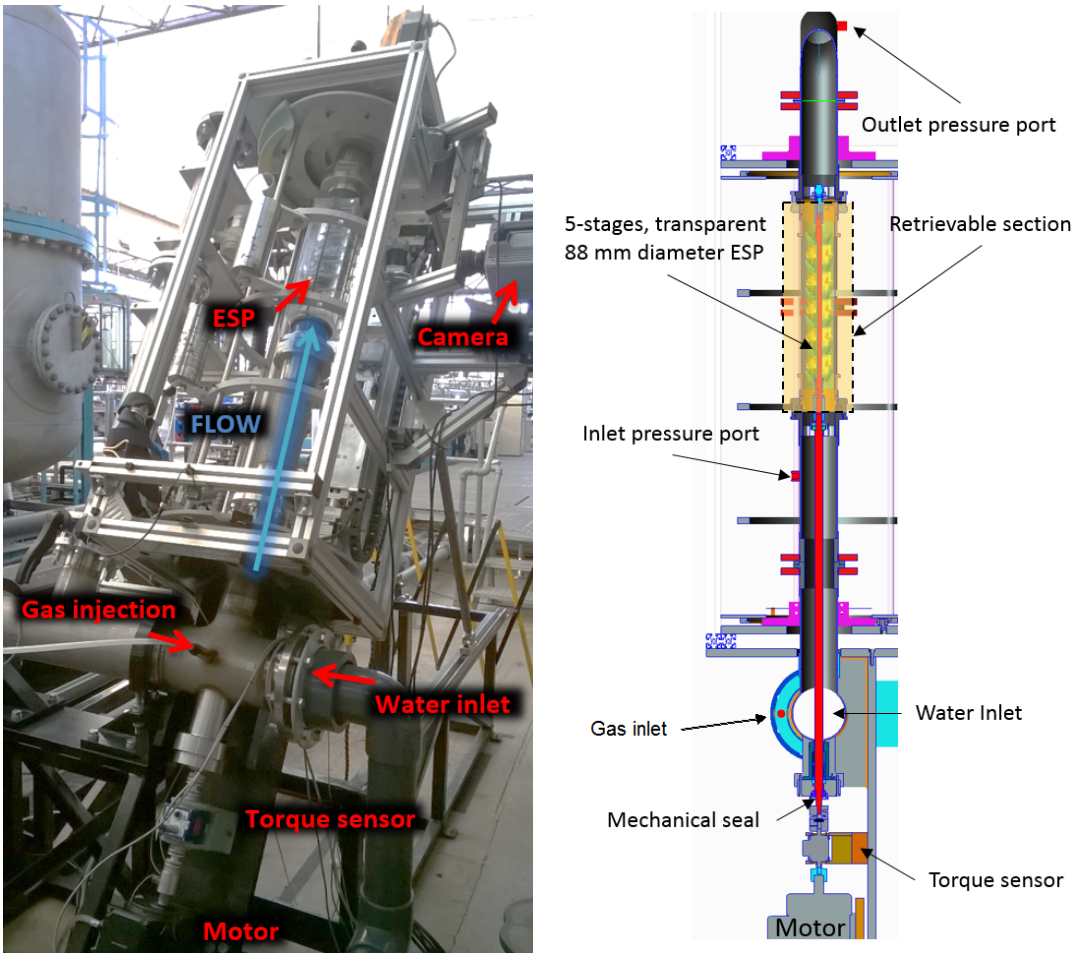

Figure 2.2 Inclinable two-phase ESP visualisation rig. Left: Picture with the ESP at 61 degrees from vertical and high speed camera installed. Right: CAD drawing of the ESP elements and pressure ports, set-up vertically.

2.1.2 Instrumentation and Performance

For single phase tests, the flow loop control system was used. For multiphase tests, at each selected liquid flow rate, the inlet gas cut λ_0, as defined in (1.9), was progressively increased until the pressure across the pump was zero. The position of the downstream choke was manually adjusted to reach the target inlet pressure within 0.1 bar, while the existing flow loop controller maintained the liquid flow rate constant. The data was recorded for 30 to 90 seconds once the flow rate was stable, within 10% of its target value. In some severe cases, the flow loop controller could not maintain a constant flow rate, leading to oscillations in the measured flow rate, as shown in Figure 4.2.

Hardware

Gas and liquid flow rates, shaft torque and rotation speed, inlet, outlet and differential pressure across the pump were measured (see Figure 2.1) and logged using a LabVIEW application. The acquisition rate for the liquid flow rate Q_l was 4 Hz, while all the other measurements were acquired at 500 Hz. The shaft torque and speed were measured using an in-line torque meter (TorqSens RWT420, www.sensors.co.uk) attached to the shaft by two flexible couplings. Two absolute pressure sensors (Gems, 0-4 bara and 1-6 bara) as well as a differential pressure sensor (Honeywell ST3000) were used. The differential pressure sensor was connected to the ports with flexible flow lines. Its response time is therefore of order 0.3 Hz, even if the sampling rate is much higher. This measurement was used to double check the pressure rise obtained by subtracting the two absolute pressures P_0 and P_1.

Measurement accuracy and repeatability

The pressure sensors and flow rate meter have a relative accuracy of $\pm 1\%$ while the torque sensor has an absolute accuracy of 0.02 N.m, which leads to a maximal relative torque accuracy of 2 % on the range that we are interested in. The pump rotation speed is controlled within 0.1 Hz, or 0.5% relative accuracy. This leads to a maximal relative error of 2.5 % for the head coefficient and 5.5 % for the efficiency.

The torque measurement showed poor repeatability. This is likely due to the poor shaft alignment inherent to a plastic set-up, the high friction on the impeller and diffuser washers, and the use of non-lubricated bearings, filled with grease. The grease properties can change with temperature and rotation speed, but also with time when it becomes contaminated with water. The average pressure rise produced by the pump was repeatable (same measurement taken twice in a row) and reproducible (measurement taken on two different days, before and after taking the pump apart).

2.1.3 Transparent stages

The pump stages correspond to a full-scale commercial design, with shrouds made of injection-moulded PMMA (Polymethyl methacrylate, also know as Perspex) and 3D-printed hubs and blades (black acrylic). The first stages that were manufactured (and

used for the LDV measurements) had PMMA blades and hub. Because the injection moulding process results in poor tolerances, this solution resulted in asymmetric geometries, and a gap between the blade and shroud that could be up to 1.5mm. Also, having a fully transparent pump revealed not to be the best solution for flow visualisation, as trapped gas in the non-flowing passages of the hub was interfering with the foreground image. For the 3D-printed solution, the blades were fitted with a thin flexible rubber base in order to prevent any leakage between the blades and the shroud. The two parts (transparent shroud and opaque hub and blades) were glued together with Loctite 770 and 406. The impeller had eight blades and the diffuser had eleven blades. The stages were enclosed in a thin transparent casing, around which a square visualisation box is filled with water.

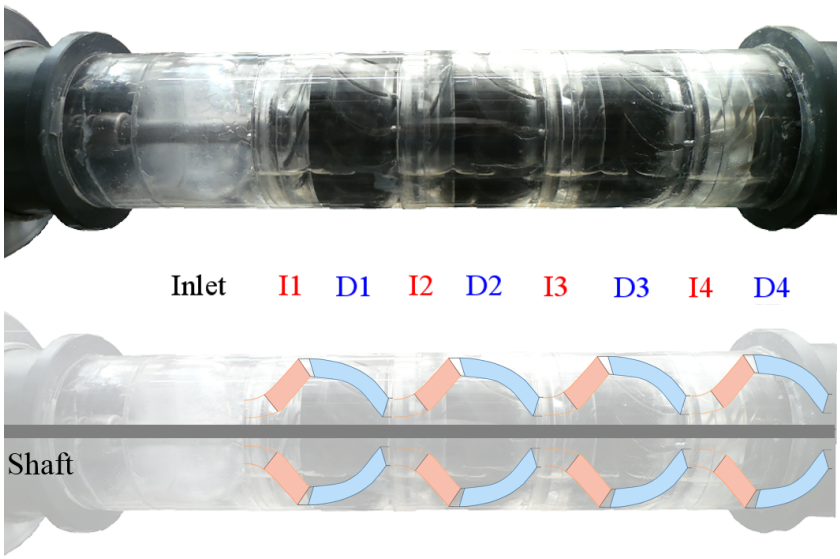

Figure 2.3 Picture of the four-stage arrangement without the visualisation box (top) and superimposed schematic meridional view (bottom). The impellers are in red (I1 to I4) and diffusers in blue (D1 to D4). The flow is from left to right and the shaft rotates anti-clockwise when looking from the outlet.

The meridional view of a typical mixed-flow stage is shown in Figure 2.4. We normalise the radial position using the impeller outer radius, so that $r^* = r/R_2$, and the axial coordinate so that the impeller extends through $z^* = 0$ to 1, and the diffuser from 1 to 2.

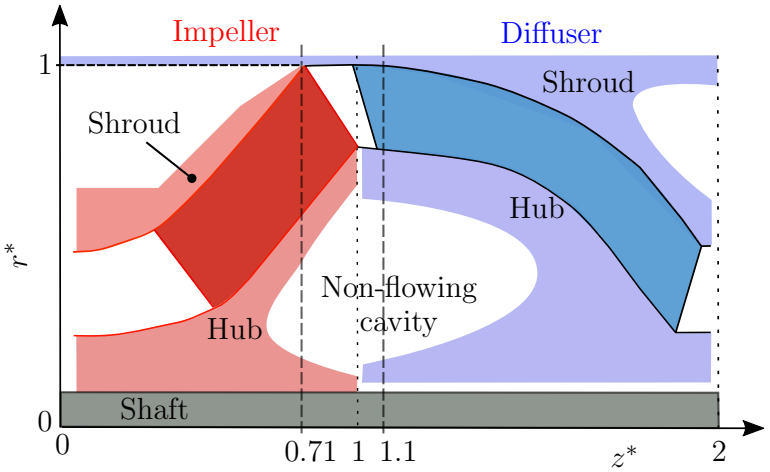

Figure 2.4 Meridional profile of a mixed-flow stage. The rotating surfaces are shown in red, and the blades are filled in.

2.2 Laser Doppler Velocimetry

Non-intrusive velocity measurements were acquired in single phase liquid (water or oil), through Laser Doppler Velocimetry (LDV) for different configurations at various flow rates summarized in Table 2.1.

For these tests, we only used three stages, starting with an impeller. This is one stage less than presented in Figure 2.3. Each impeller was marked with a letter A to C and their arrangement is described in Table 2.1 as a letter sequence. Measurements were taken in the second and third impellers, as well as in the second diffuser. The measured velocities were of order 1 to 2 m/s for the axial component and 2 to 4 m/s for the tangential component. Because of the geometrical configuration of the pump, it was not possible to measure the radial velocity, although the simulation results show that it is not negligible in the investigated area (same order as the axial velocity). In order to compare measurements at different flow rates and rotation speeds, the velocity is normalized using the impeller tip velocity $V_{tip} = \omega R_2$. The flow rate is normalised using the design flow rate, or flow rate at the Best Efficiency Point (BEP): $\Phi^* = Q/Q_{BEP}$.

2.2.1 LDV Principles

The principle of this technique is to create a localized interference pattern using two coherent laser beams, and to measure the Doppler shift of the signal back-scattered by a particle going through the illuminated volume, as shown on Figure 2.5. We used optics and signal processor from Dantec (Flow Explorer and BSA Processor), which comprise two pairs of beams in two perpendicular planes. More information on the laser and geometrical corrections can be found in Appendix D.

Table 2.1 Test matrix in single phase flows. The impellers are marked with a letter and were found not to be perfectly identical (see Appendix E). Impeller B* corresponds to a modification of impeller B, preventing leakages between the blades and the shroud.

Case	Part	Fluid	Seeding	Impeller order	Plane z^*	Flowrate Φ^*
3	D2	Water	Oil	ABC	1, 1.1	0.95
12	I2	Water	Oil	ABC	0.74, 0.77	0.95
13	I2	Water	Gas	ABC	0.77	0.95
14	I2	Water	Gas	ABC	0.77	0.56
15	I2	Water	Oil	ABC	0.77	0.80
16	I2	Water	Gas	ABC	0.77	1.17
21	I2	Water	Gas	CAB	0.74-0.89	0.95
23	I2	Oil	Water	CAB	0.74	0.95
25	I3	Water	Oil	AB*C	0.74	0.95

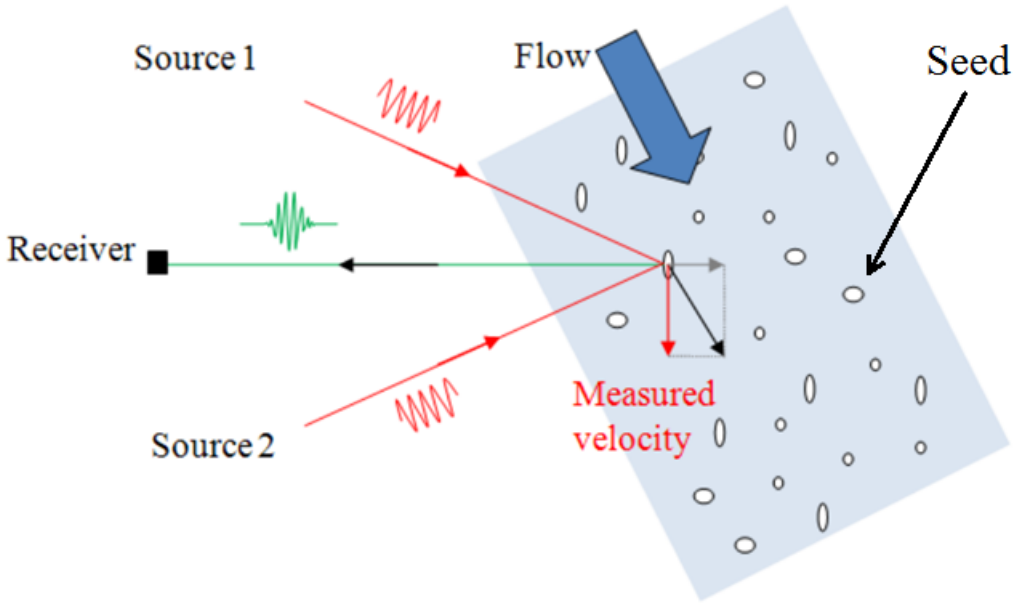

Figure 2.5 Laser Doppler Velocimetry Principle.

This method results in unevenly spaced velocity samples in time which are associated with the impeller angular position through the motor encoder, sending 2500 beats per rotation.

Because LDV is intrinsically a single point measurement, it was necessary to mount the system on a traverse to obtain a velocity field. The visualisation box was not used when measuring the velocity field with the LDV system, as it required to rotate the laser around the pump. As explained in Appendix D and due to the cylindrical geometry of the pump, the measurement locations for axial and tangential velocity component are different when the laser is at a fixed position, so that it was not possible to measure the two components co-located and simultaneously. Also, because of the refraction occurring at the wall/fluid interface, the extent of the measurement was limited to the areas where the shroud is flat, i.e. at the impeller outlet and diffuser inlet. The angular position γ from which the laser beams point at the pump axis was measured with an inclinometer. Finally, the laser axial position was achieved manually by aligning the laser beam with a reference point on the outer pipe. The traverse system therefore enabled three degrees of freedom to move the laser around the pump, and consequently for moving the measurement point within the pump.

2.2.2 Seeding systems

In order to produce a good signal for the LDV system, small neutrally buoyant particles are needed as as tracers. As the flow loop was a shared facility, it was not possible to inject solid particles. Two alternative methods have been used and are described below:

- rapid depressurisation of saturated liquid

This device consists of a high pressure reservoir (4 bar) in which fresh water is circulated in the presence of compressed air. An injection line samples the fluid from the bottom of the reservoir. A needle valve placed a few centimetres before the pump inlet releases a small flow of saturated liquid into the flow, and the sudden pressure drop causes fine gas bubbles to appear. Their size has been visually estimated at 20-100 µm. The advantage of this method for the flow visualisation is that gas bubbles are very bright. The draw-back is the high density difference between the gas and liquid. Because the measurement is taken in the middle stage, relatively far from the bubble injection point, the seeding density is greater at the centre than at the periphery of the impeller.

- Oil-Water shearing system

This device produces small bubbles of oil in water or small bubbles of water in oil. It is made of two peristaltic pumps, a shearing device and a high power pump that mixes both phases vigorously. Again the bubble size has not been measured but is estimated visually to be less than 100 µm. The advantage of this device is a higher bubble concentration than the gas bubble generator and a closer density match (the oil density is 800 kg.m^{-3}). Nevertheless, some of the oil droplets flowing through the

pump stay on the PMMA walls and after a few hours, they impair the transparency of the pump leading to a reduced LDV data rate.

We can use the method described in Section 5.2.2 to estimate the equilibrium velocity of a gas bubble or oil droplet in the flow generated by the impeller, in order to get an order of magnitude for the relative slip velocity, defined as:

$$s = \frac{v - w}{w}$$

where v is the particle velocity and w the working fluid velocity. For a 100 µm particle, with the impeller rotating at 20 Hz, we obtain 9 % relative slip for a gas bubble, and 2.5 % relative slip for an oil droplet. However, the velocity in the impeller is not steady, and since the bubble and droplet sizes were not measured, 100 µm is a conservative estimation. In Appendix E.5, we show that the velocity fields obtained for the two different seeding particles are qualitatively and quantitatively similar, validating the assumption that the gas bubble seeding is appropriate for our purposes, and we will assume a relative error of the order 2.5% for the velocity measurement.

2.2.3 Velocity measurements

When measuring the velocity in the impeller rotating at 20 Hz, the shaft angular position was recorded through the motor encoder and along with the LDV data in order to compute a phase-average velocity field. Depending on the data rate, each phase-average point in the impeller is obtained with 50 to 500 velocity measurements taken within a 2° window, over about a hundred rotations (around 5 seconds). We varied the laser radial position, while the angle γ and axial position z^* were kept constant.

To measure the velocity in the diffuser, the laser had to be moved around the pump in order to measure the blade to blade flow field. The 11 blades divide the diffuser circumference into angular sectors of 32.7° each. Using the full span of the traversing system, a velocity profile was measured every 4 degrees from 4 to 32 degrees. This barely covers one passage and it was not possible to see whether the other passages would have the same velocity profile. Automation of the measurement and increasing the angular position range for the laser head would enable a more accurate study of the rotor-stator interaction in the future.

Velocity fields have been measured in several planes, with z^* varying from 0.71 to 1.1 as shown on Figure 2.4. Axial and tangential velocity are acquired during a minute long measurement (the acquisition stops when the maximal sample number is achieved). The measurements are time-averaged over 100 to 20,000 samples, or phase-averaged using 2° angular bins. With 20,000 samples, it is possible to use statistical tools to explore the velocity time dependence. On the contrary, we considered that the average velocity was not reliable if less than 100 velocity measurements were recorded, given the flow unsteadiness.

2.3 Gas-Liquid flow characterisation

We used a 4-stage mixed-flow pump which was characterised by recording the produced pressure ΔP as a function of the total flow rate $Q_{\text{tot}} = Q_l + Q_g$ and inlet gas fraction λ_0 for 6 different configurations labelled from A to F and shown in Table 2.2 varying the pump inclination, the shaft rotation speed and the inlet pressure.

Table 2.2 Test matrix for the multi-phase characterisation $\Delta P = f(Q_{\text{tot}}, \lambda_0)$ and flow visualisation in the 4-stage pump. The pump inclination is measured from horizontal.

		A	**B**	**C**	**D**	**E**	**F**
Inclination	[deg]	0	0	61	61	61	89
Shaft frequency	[Hz]	20	20	20	25	30	20
Inlet pressure	[bar]	1.5	2.5	1.6	1.6	1.6	1.6

2.3.1 High speed videos

Flow visualisation was carried out for several flow conditions $(Q_{\text{tot}}, \lambda_0)$ in each configuration. A Photron FastCam S1.1 camera was installed on a sliding track parallel to the pump axis, in order to focus on each stage individually. The pump was illuminated using a line LED (CobraMax, 2.5 Amps) placed on the top of the camera, and a square visualisation box was filled with water to minimise the distortion caused by the PMMA interface curvature. A 24-70 mm lens was used to zoom in and out, giving either a full view of all the stages, or a closer view focussed on the impeller passages of a particular stage. At maximal focal length, we achieved a resolution of 9 pixel per millimetre. The frame rate, ranging from 500 to 7200 fps, was chosen depending on the pump rotation speed, the flow regime, and the objective of the video: showing the variation of flow regime with time, or focussing on specific features of a particular flow regime.

A list of all 130 videos is available in Appendix G, and the most relevant ones are presented in Table 2.3, with their main features and characteristics. The total flow rate coefficient is defined as $\Phi_T = (Q_{g0} + Q_w)/Q_{\text{BEP}}$, where Q_{BEP} is the flow rate at the design point for the considered rotation speed, Q_{g0} is the volumetric gas flow rate at the pump inlet, and Q_w is the volumetric water flow rate. The inlet gas fraction is computed as $\lambda_0 = Q_{g0}/(Q_w + Q_{g0})$. Finally, the camera frame rate and the part of the pump visible in the videos are indicated in the two last columns, where 0 corresponds to the inlet, I1 to the first impeller, I2 to the second impeller, etc.

The average bubble size has been estimated visually from the videos, but the results were not accurate enough to observe quantitative trends, apart from the rotation speed dependency, to be presented in Section 4.2.2. More spatial resolution and more complex algorithms are needed to successfully complete and automate this type of analysis.

Automated post-processing has been attempted for the lowest gas fraction, but the low resolution (only 4 to 10 pixels per bubble), bubble shadows and complex geometry

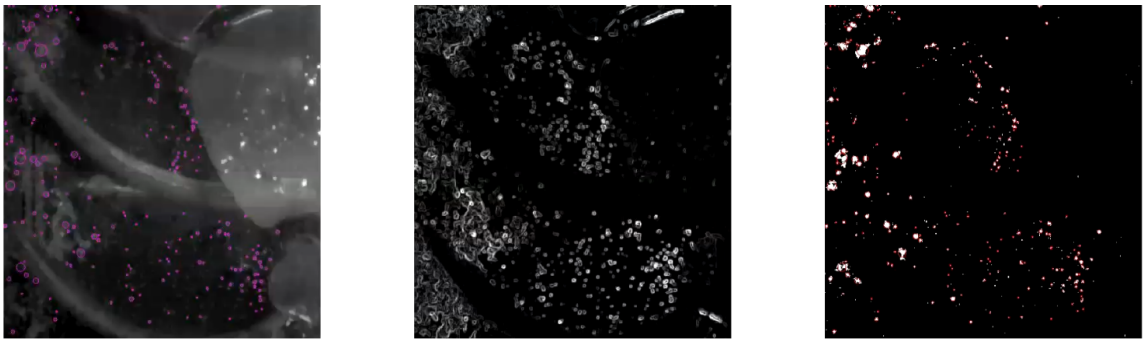

(a) The left picture represents the unprocessed image, the centre one, the result after background removal and edge detection algorithms, and the last one after filling the bubbles and transformation to a binary image. The coloured circles and points show the location (and area) of detected bubbles.

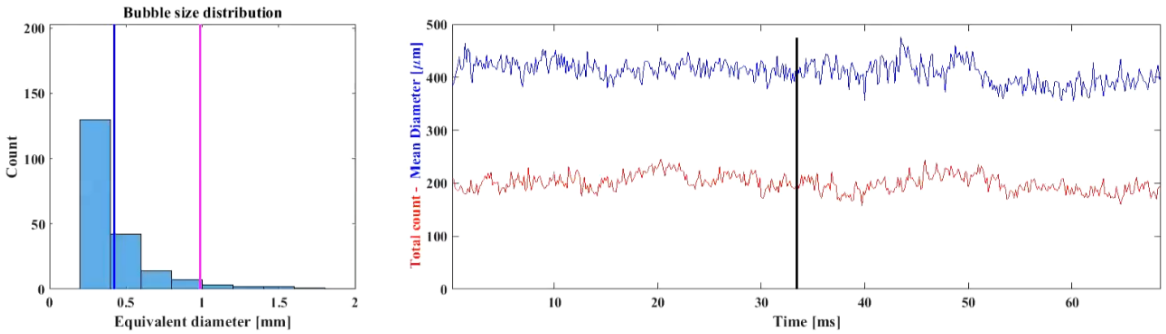

(b) The plot on the left shows the bubble size distribution at a specific time, the chart on the right the evolution with time of the mean diameter and number of detected bubbles.

Figure 2.6 Image processing of a video showing a passage of the third diffuser (D3), when the pump runs at 20 Hz, with a total flow rate coefficient $\Phi^* = 1.5$ and an intake gas fraction of 0.9 % (Case C with reference to Table 2.2, file F10 with reference to Table G.2). We observe on this video that the mean bubble size and total number change with time, while the algorithm only seems to pick up artefacts.

Table 2.3 List of the attached videos, representative of the flow patterns observed in the pump. The column "Case" refers to Table 2.2.

File Name	Case	Φ_T	λ_0	f	**Angle**	**Rate**	**View**
Units	-	-	%	Hz	deg	fps	-
A1	A	1.2	33	20	0	500	0 I1 - I2
Inlet Horizontal	Horizontal slugging and fully separated flow (gas lock)						
A2	C	1	43	20	89	1000	0 - I1 - I2
Inlet Vertical	Taylor bubble, separated flow						
B1	A	1	1	20	0	7200	I3 - I4
BEP Bubbly	Bubbly flow						
B2	A	1	2.5	20	0	7200	I3 - I4
BEP Accumulation	Bubbly flow with accumulation in impeller suction side						
B3	A	1	5	20	0	7200	I3 - I4
BEP GasPocket	Bubbly flow with intermittent gas pockets in impeller						
C1	D	1.54	9.5	25	0	7200	I1 - I2
HighFlow Slug	Flow features, short slugs with separation in diffuser						
D1	A	0.62	2.5	20	0	6000	0 - I1 - I2
LowFlow LowGVF	Bubbly flow with recirculation in diffusers.						
D2	A	0.57	15	20	0	5400	I3 - I4
LowFlow HighGVF	Very large bubbles in diffuser, gas pocket in impeller.						

made it impossible to get significant results. Figure 2.6 represents the post-processing used in Matlab to compute the bubble size distribution from a close-up video of a diffuser passage, but the technique used unfortunately picks up as much artefacts as bubbles. More complex algorithms are being developed and are very promising, for example by Karn et al. (2015) or Besagni and Inzoli (2016) in order to capture the bubbles size when bubbles are not spherical and/or overlap. Using them and higher resolution videos would be a good way to go forward for future work.

2.3.2 Gas phase quantitative measurement

The high speed videos indicate that the local gas fraction in the pump could be higher than the inlet gas cut computed with the respective flow rates. Section 4.3.1 shows how to use the pressure or torque measurement as an indirect measurement of the gas fraction.

In-situ gas fraction measurement has been realised in a diffuser passage using a Electrical Resistance Tomography, by Pirouzpanah et al. (2016). The local gas fraction found with this method is always above the inlet gas cut λ_0 computed using the gas and liquid flow rates. We attempted to develop a gas fraction sensor that would not require us to modify the impeller or diffuser physically. For this, we used a capacitance measurement based on the difference of relative permittivity between silicon oil ($\varepsilon_r(\text{oil}) = 1.8$) and nitrogen ($\varepsilon_r(\text{N}_2) = 1$). The first tests were done in a static

set-up, where two electrodes made of copper tape were positioned on each side a pump stage, as shown on Figure 2.7a. One electrode was subjected to an alternating voltage, while the other was grounded. Both were surrounded by an insulating layer and a grounded guard.

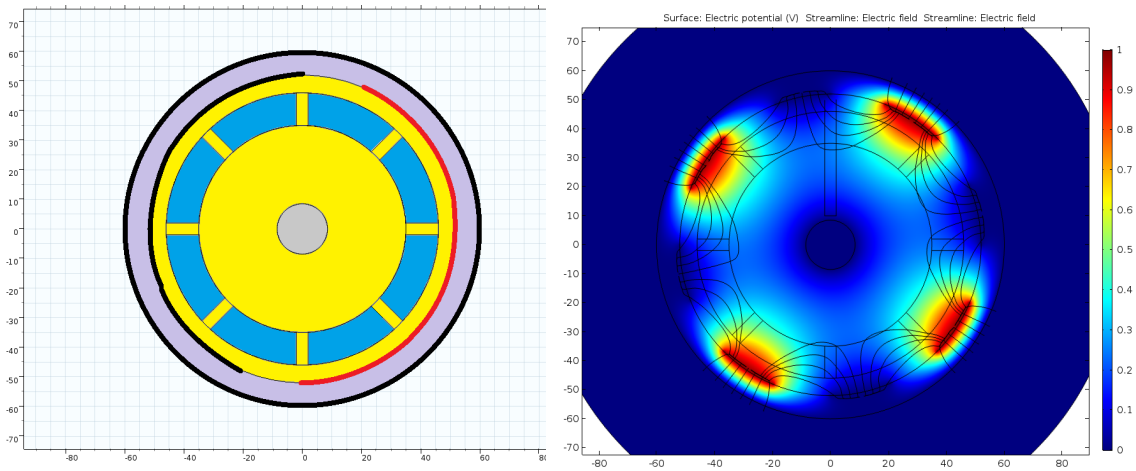

(a) Two-electrode capacitance sensor: the ground electrode and guard are represented in black, while the pump body is yellow, the fluids blue and the insulating layer purple.

(b) Electric potential field for a 8 electrode configuration, simulated in 2D with Comsol. Most of the field lines go through the fluid area, giving a higher sensitivity to the fluid.

Figure 2.7 Set-up and result of a 2D numerical simulation of the capacitance, using Comsol.

Using the commercial software Comsol, we computed the capacitance created by this two-electrode configuration with a two-dimensional model shown in Figure 2.7a. We found that by increasing the number of electrodes, this value could be substantially increased (from 50 to 300 pF). The computed electrical potential field for this configuration is shown in Figure 2.7b. We eventually used two 8-electrode configurations, shifted by $2\pi/8$ so that a grounded and a live electrode are facing each other. The final electrode arrangement (before adding the guard) is shown on Figure 2.8.

Figure 2.8 Picture of the copper electrodes and wires attached to the pump casing.

Custom made electronics was used to measure the resulting capacitance. Grounding of the shaft was found necessary in order to get a reliable signal, but the difference between single phase oil and single phase nitrogen (about 0.2 V in the raw signal) was finally judged too small to make this method useful to reliably measure the local gas fraction.

This is likely due to the small difference between the oil and air permittivity, but also the fact that only a small part (the flow passage) of the region surrounded by the electrodes is actually subject to a change in electrical properties. The liquid-filled non-flowing cavities, and the pump material make the bulk of the region crossed by the electrical field. Grounding the shaft made little difference to the measurement.

While this attempt at measuring the in-situ gas fraction using a clamp-on capacitance sensor did not work out, an in-situ gas fraction measurement remains an essential measurement in order to understand gas-liquid flows in centrifugal pumps. Using a different physical principle (conductivity, X-ray or gamma ray tomography) seem to be the best way forward in order to get an non invasive measurement, although all these techniques require an significant investment. An invasive conductivity or optical probe, at a carefully chose location could be an interesting alternative for future work.

Conclusions

This experimental study revolves around the flow-visualisation and velocity measurements in a multi-stage mixed-flow pump, which to our knowledge has not been reported before. The measurement techniques used (pressure, flow rate and torque measurement, high-speed imaging and LDV) are fairly standard and have a very good accuracy: less than 5% relative error in most cases. The stage geometry presented non-conformities

of the order of 2% which was considered negligible after comparing the velocity field measured in two different impellers (see Appendix E.2), Although the velocity at the impeller inlet has never been measured and small geometrical variations could make a difference there.

The installation itself (flow loop, pump stages, motor, shaft, bearings,...) is however not as robust. We identified the lack of repeatability for the torque measurement, due to the change in mechanical friction in the system. In multiphase flow, the flow loop operation could be difficult in some cases, because of the slugging and instabilities. This means that the boundary conditions at the pump inlet and outlet were not perfectly controlled. In the future, a more flexible control system would improve the measurement and allow a more accurate two-phase characterisation. The nature of the flow in the pump (phase slip) and the absence of local gas fraction measurement made the interpretation of the high speed videos difficult for medium gas fraction (10 - 20%).

In the next chapters, we study the single phase flow field using LDV and high speed videos, while sensitivity analysis are presented in Appendix E.3. In multiphase, we investigated in more details the uncertainty arising from the gas fraction variations within the pump, through high speed videos and pressure measurements.

Chapter 3

Experimental single phase flow characterisation

In single phase liquid flows, a common unwanted feature of mixed-flow ESP stage is the so-called "saddle point" (see for example Takács (2009)): at low flow rates, approximately 50% of the design flow rate, mixed-flow pumps often exhibit a slightly positive gradient of pressure rise versus flow rate ($d\Delta P/dQ$). As we have seen in Section 1.3.3, this is detrimental to the system stability.

In this chapter, we first examine the pressure produced by a three-stage mixed-flow pump at several liquid flow rates and compare these results with the catalogue curves. We then analyse the flow in the diffuser using a high speed camera and small seeding gas bubbles. We finally describe the velocity field measured by Laser Doppler Velocimetry at the impeller outlet and diffuser inlet for several stages.

3.1 Performance in single phase flows

We tested a three-stage pump in single phase flow (water or oil), and measured pressure rise ΔP and torque T for a range of liquid flow rates Q_w at a relatively low rotation speed $f = 20$ Hz, compared to what is typically used in real operating conditions (50 to 80 Hz). We compute the head coefficient per stage Ψ and the pump efficiency η which are independent of the rotation speed according to the affinity laws (see Section 1.1.2).

$$\Psi = \frac{\Delta P/3}{(\omega R_2)^2} \quad \text{and} \quad \eta = \frac{\Delta P Q_w}{T\omega},$$

where R_2 is the impeller outer diameter. The pressure rise ΔP and the torque T are divided by 3 which is the number of stages.

The catalogue curve are provided by the pump manufacturer as a polynomial equation. The American Petroleum Institute (API) standard API G11S22 from 1997 specifies the certification conditions for a commercial ESP. The acceptance criteria

for the head is to be within 2 % of the nominal value, and for the efficiency to be at least 90 % of the nominal value at the best efficiency point. The tested pump usually consists of 20 to 60 metal stages and are run in water at 60 Hz.

As shown in Figure 3.1, the measured head is about 5% below the catalogue curve, and the efficiency is substantially underestimated. This is due to the pressure losses occurring in the shaft supports, and the mechanical friction losses through the seal, couplings and bearings. We note that the measured efficiency is the combination of the hydraulic efficiency (only taking hydrodynamic losses into account) and the mechanical efficiency (taking the mechanical friction in the seal and bearings into account). For a large number of stages, the hydraulic efficiency makes most of the total efficiency, while the mechanical losses can become dominant in a short pump. Furthermore, the first stage is known to have lower performance than the others (Takács (2009)), as the flow entering the first impeller is not conditioned. This again leads to underestimating the stage performance when averaging it over a three-stage pump.

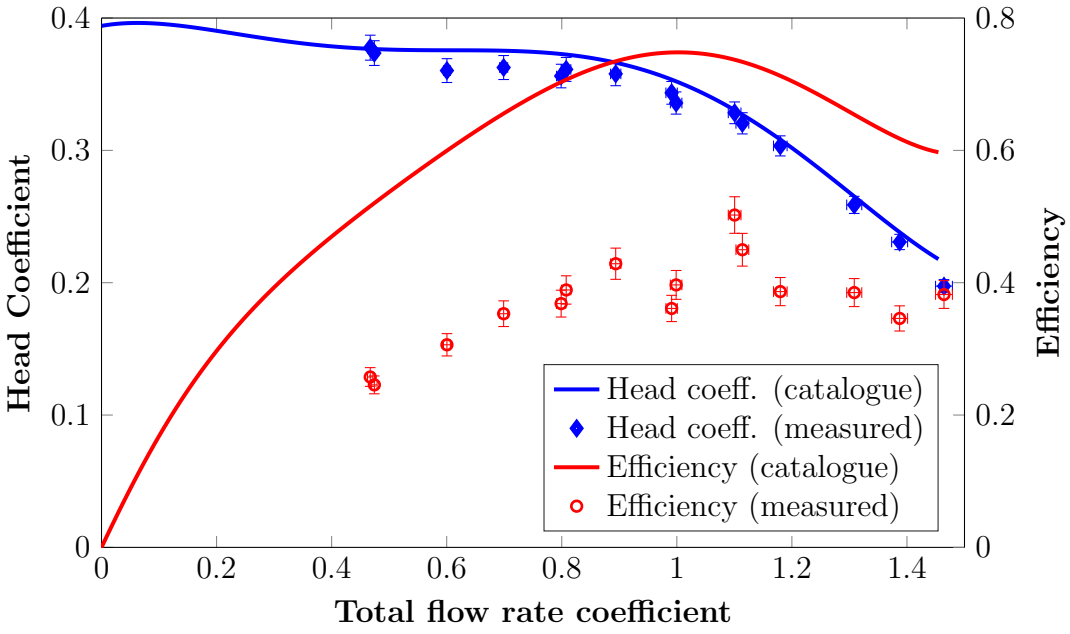

Figure 3.1 Catalogue (solid line) and measured (marks) head coefficient (blue) and efficiency (red). Experimental data correspond to the pump running horizontally in water at 20 Hz.

3.2 High speed video analysis

High speed videos of the second stage have been captured for various flow rates (Φ^* varying from 0.2 to 1.2) at 10,000 frames per second, while injecting fine gas bubbles. Using an image analysis software (Davis v.8), it was possible to represent the trace of the bubbles trajectories, and to visualize the streaklines. This visualisation was

possible only in one diffuser passage (space between two blades) as the distortion due to the PMMA interfaces makes the other passages difficult to see, and in the impeller, the blades interfere with the image processing. The three dimensional nature of the flow only allows a qualitative description. As shown on Figure 3.2, the diffuser passage has straight streaklines at design point and above ($\Phi^* \geq 1$), but recirculation cells appear for $\Phi^* \leq 0.8$. The unprocessed movies also showed bubbles travelling backwards at low flow rates.

We observed the recirculation cells to fluctuate in the diffuser passage depending on the flow rate as follow:

a. For $0.2 < \Phi^* < 0.3$, there are two recirculation cells: one at the diffuser inlet and a smaller one at the outlet, oscillating between the pressure and suction side.

b. At $\Phi^* \approx 0.4$, the size of the outlet recirculation cell is reduced, and it position stabilizes closer to the suction side.

c. For $0.5 < \Phi^* < 0.6$, the inlet recirculation cell is weaker (lower velocity) but remains large, while the outlet cell get smaller and disappears.

d. For $0.6 < \Phi^* < 0.9$, the inlet recirculation cell becomes smaller, leaving more and more space to the straight on the pressure side.

e. For $0.9 < \Phi^* < 1.2$, the streaklines are also well defined, use the whole passage and follow the blades. No recirculation is visible.

The transition from two to one recirculation cells roughly coincides with the flat portion of the head curve observed in Figure 3.1, at $\Phi^* \approx 0.5$. A specific study of the pressure recovery in the diffuser would be needed to confirm if the change in the recirculation pattern is indeed the cause of this phenomenon. Another suggested cause was the presence of a rotating stall at low flow rate (see Braun (2009)). The quantitative measurement of the flow velocity in the impeller and diffuser is used in Section 3.3 to explore this possibility.

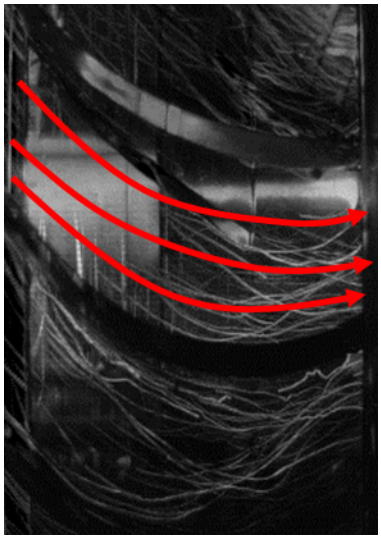

(a) Streaklines for $\Phi^* = 1$

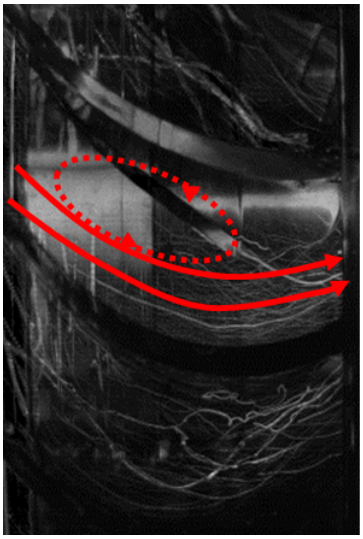

(b) Streaklines for $\Phi^* = 0.8$

(c) Streaklines for $\Phi^* = 0.5$

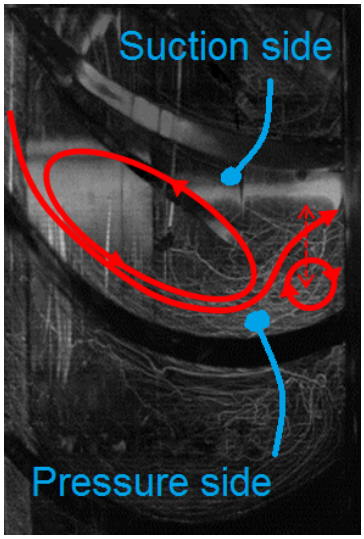

(d) Streaklines for $\Phi^* = 0.3$

Figure 3.2 Single phase flow visualisation for various flow rates in the second diffuser of a three stage mixed-flow pump: side view. The fine white lines are the streaklines highlighted by the injected bubbles, and the red lines outlines the recirculation pattern as observed on the raw videos. (a) and (b) show straigher streaklines than at the part load Figures (c) and (d), where they are disorganised and can form loops.

3.3 Velocity field in the impeller and diffuser

We used Laser Doppler Velocimetry (LDV) to measure the relative velocity field $\vec{w}$ at the impeller outlet: for $0.74 \leq z^* \leq 0.90$ (z^* as defined in Section 2.1.3), and at the diffuser inlet ($1 \leq z^* \leq 1.1$).

3.3.1 Flow field at design point in the impeller

In this Section, we only show the results at a single axial location ($z^* = 0.74$), but velocity maps in other planes ($0.77 \leq z^* \leq 0.90$) are presented in Appendix E.3 and are qualitatively similar. The standard deviation is of order 1 m/s for both axial and tangential velocities. Figure 3.3 shows the velocity map in the impeller frame of reference, using a cylindrical coordinate system (r^*, θ, z^*). Because the blades are leaning backwards (against the impeller rotation), we represent the opposite of the relative tangential velocity: $-w_\theta = \omega r - W_\theta$, where W_θ is the tangential velocity component in the laboratory frame of reference (absolute tangential velocity). The axial and tangential relative velocity components are also normalised using the impeller tip velocity: $w^* = w/\omega R_2$.

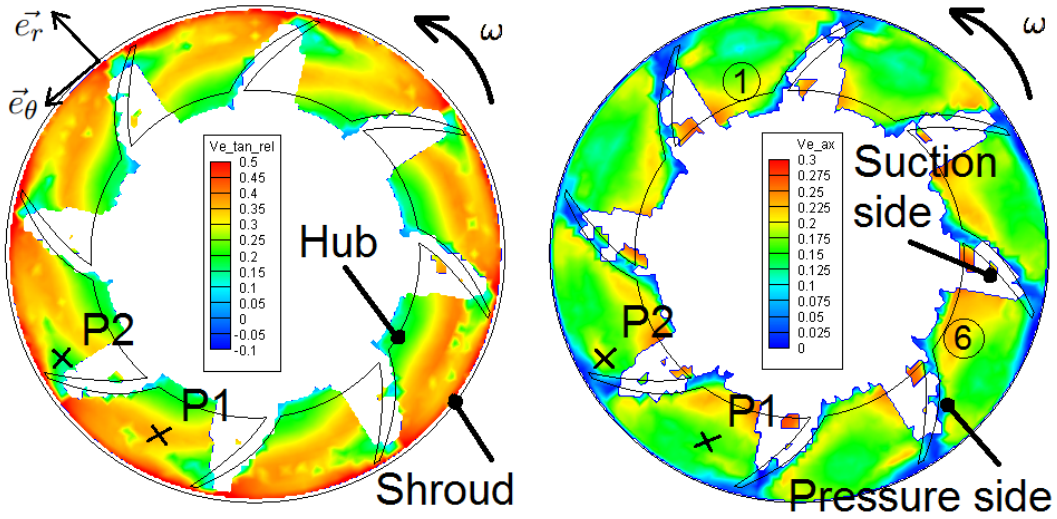

(a) $-w_\theta^*$ for $\Phi^* = 0.95$ (b) w_z^* for $\Phi^* = 0.95$

Figure 3.3 Case 21 (Table 2.1) : Relative velocity field in the impeller frame of reference, for $z^* = 0.74$. The white areas behind the blades are blind spots, where the set of samples was too small to be statistically representative (below 50). $-w_\theta^*$ is low in two regions: immediately after the blades tip (wake), and along the hub. On the contrary, w_z^* is high along the hub, and has a minimum in the middle of the passage. This minimum varies from 0.1 (passage numbered ①) to 0.2 (passage numbered ⑥). The points $P1$ and $P2$ are studied in more details in Figure 3.5.

Figure 3.3 shows that there is a wake area behind the blades characterised by a low tangential relative velocity, and that the axial velocity is not uniform across the different passages. In this particular section of the impeller, the blades are not shrouded and the tangential velocity close to the outer wall therefore tends to $-w_\theta = 1$ rather than zero: the wall is moving backwards in the impeller frame of reference. No recirculation (negative velocity component) is visible at this stage.

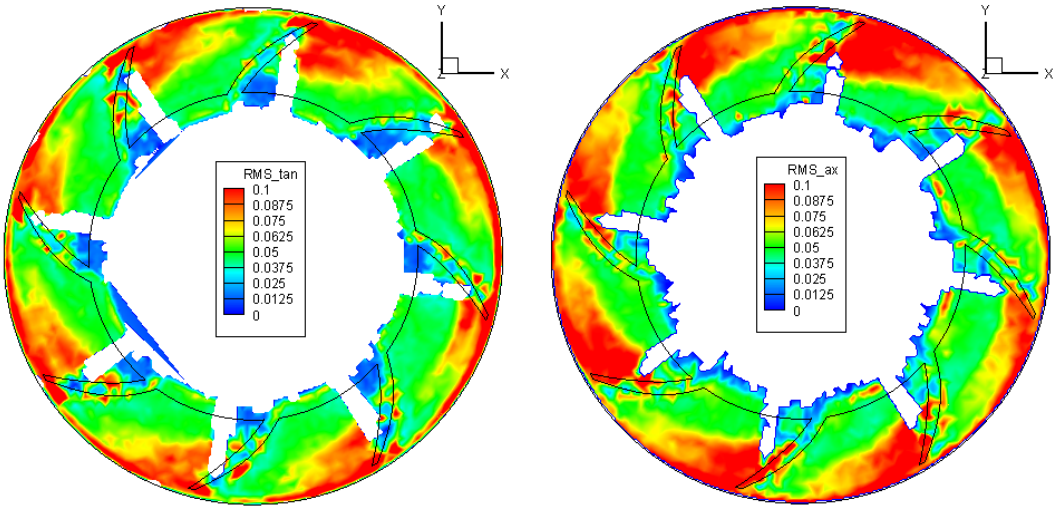

(a) Standard deviation of $-w_\theta^*$ (b) Standard deviation of w_z^*

Figure 3.4 Case 21 (Table 2.1): Standard deviation of the measured velocity in the impeller for $\Phi^* = 0.95$ and $z^* = 0.74$. The wake region (high standard deviation, in red) stands out and is wider for the axial velocity.

The blade wakes also stand out through the high standard deviation of both velocity components, as shown in Figure 3.4. Figure 3.5 shows the detail of two phase-averaged points: P_1 in the bulk of the passage flow, and P_2 in the wake of the blade. These locations are shown in Figure 3.3. Even though the mean velocity is always positive, a negative value is sometimes measured, suggesting that intermittent recirculation can exist in the wake of the impeller blades, at all flow rates in the same proportions.

It is not possible to compute precisely the turbulent kinetic energy with this data, as the radial component is missing, and the axial and tangential components were not measured at the same locations. However, we can give a two-dimensional estimation, by interpolating the standard deviation computed to produce Figure 3.4, and using the following definition also used by Pedersen et al. (2003) :

$$k_{2D}^* = \left(\sigma^2\langle W_\theta^*\rangle + \sigma^2\langle W_z^*\rangle\right),$$

where $\sigma\langle\rangle$ is the standard deviation of a quantity. The maps of turbulence kinetic energy looks very similar to the standard deviation maps in Figure 3.4, they are given in Appendix E.4. The two-dimensional turbulent intensity is defined as:

$$I_{2D} = \frac{k_{2D}^*}{\left|\vec{W}_{2D}\right|} \ .$$

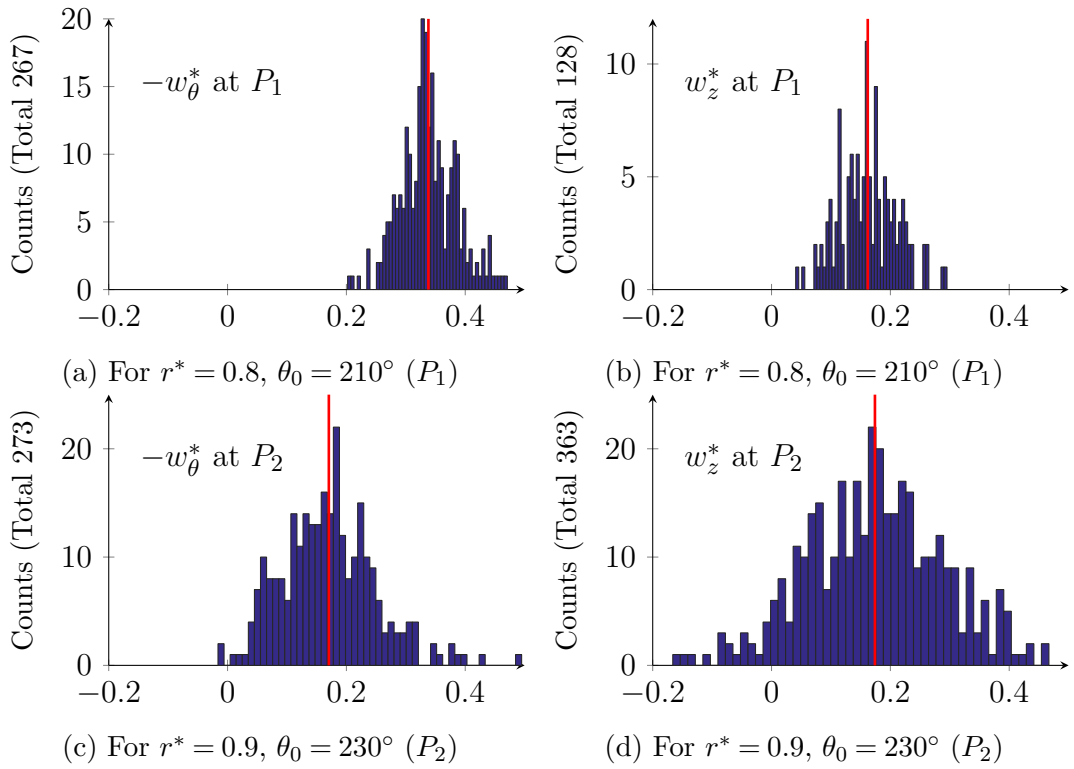

(a) For $r^* = 0.8$, $\theta_0 = 210°$ (P_1)

(b) For $r^* = 0.8$, $\theta_0 = 210°$ (P_1)

(c) For $r^* = 0.9$, $\theta_0 = 230°$ (P_2)

(d) For $r^* = 0.9$, $\theta_0 = 230°$ (P_2)

Figure 3.5 Case 21 (Table 2.1): Velocity measured in the angular bin $[\theta_0 - 1° < \theta < \theta_0 + 1°]$ in the plane $z^* = 0.74$, in the middle of the impeller passage (top, point P_1 on Figure 3.3) and in the blade wake (bottom, point P_2 on Figure 3.3). The red line represents the mean velocity plotted in Figure 3.3. The mean axial velocity (right plots) does not change between P_1 and P_2, but the standard deviation is greatly increased. The relative tangential velocity (left plots) decreases in the wake compared to the bulk of the flow, and its standard deviation slightly increases.

The turbulence intensity levels found correspond to what is expected in a turbomachinery flow, around 25 % in the blade wakes and 5 % in the bulk of the flow. A map of the turbulent intensity is also provided in Appendix E.4.

3.3.2 Flow field at design point in the diffuser

The tangential velocity decreases when going further into the diffuser (increasing z^*), while the axial velocity increases. As shown on Figure 2.4, the plane $z^* = 1$ comprises the leading edge of the diffuser blades, as well as the extremity of the impeller hub, resulting in a high tangential velocity at the hub on Figure 3.6a.

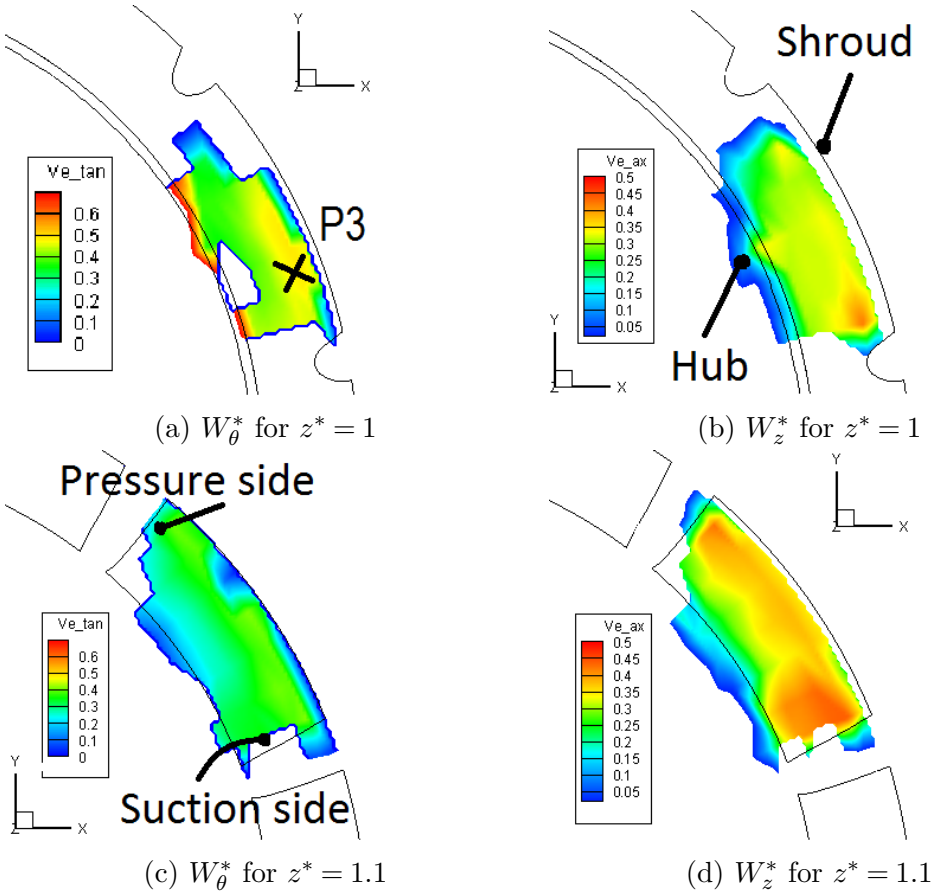

(a) W_θ^* for $z^* = 1$ (b) W_z^* for $z^* = 1$

(c) W_θ^* for $z^* = 1.1$ (d) W_z^* for $z^* = 1.1$

Figure 3.6 Case 3 (Table 2.1): Absolute velocity field at the diffuser inlet for $\Phi^* = 0.95$, at $z^* = 1$ (top) and $z^* = 1.1$ (bottom). The velocity field appears much more homogeneous in the diffuser than in the impeller (see Figure 3.3). The highest velocity is on the blade suction side. From Figures (a) and (c), we see that the tangential velocity decreases significantly over a short distance ($\Delta z^* = 0.1$), while the axial velocity increases (smaller flowing area, as the flow progresses in the diffuser).

With a data rate approaching 2 kHz, it is also possible to look at the time dependency of the measured velocity at a single location. In Figure 3.7, the phase average of the axial and tangential velocities measured at one location (P_3 in Figure 3.6) is presented as a function of the impeller angular position. The flow in the diffuser is found to be time-periodic, as it is affected by the passage of the impeller blades. The tangential velocity shows the largest variations, while the axial velocity becomes steadier further into the diffuser.

A Fourier transform was applied to the velocity time series to compute the energy spectrum in the diffuser and detect potential abnormal frequency peaks. As the acquired velocity samples are unevenly distributed in time, the signal had to be be interpolated on a finer grid (using four times the average sampling rate) and a classic Fast Fourier Transform has been applied to the interpolation. We also preconditioned the velocity signals by normalising it to zero-average series, and using a Hanning window. Depending on the data rate, the frequency resolution could be as low as 0.5 Hz. Figure 3.8 shows the energy density spectrum for the point P_3, placed at $z^* = 1.0$, $r^* = 0.9$ and $\theta = 35°$ (see Figure 3.6). The upper chart represents the whole frequency range and show a typical turbulent spectrum. The lower chart represents the same data plotted on a linear scale, to better identify the peaks. The only noticeable feature through this method was the impeller rotation (20 Hz) and blade passage (160 Hz) frequencies, and therefore no evidence of rotating stall was identified.

It is also possible to use a Lomb-Scarsdale periodogram to search for periodic behaviour in unevenly spaced data, as explained by Lomb (1976) and more recently by Van Dongen et al. (1999). This method resulted in the same peaks and yielded the same conclusions as the interpolation method described above.

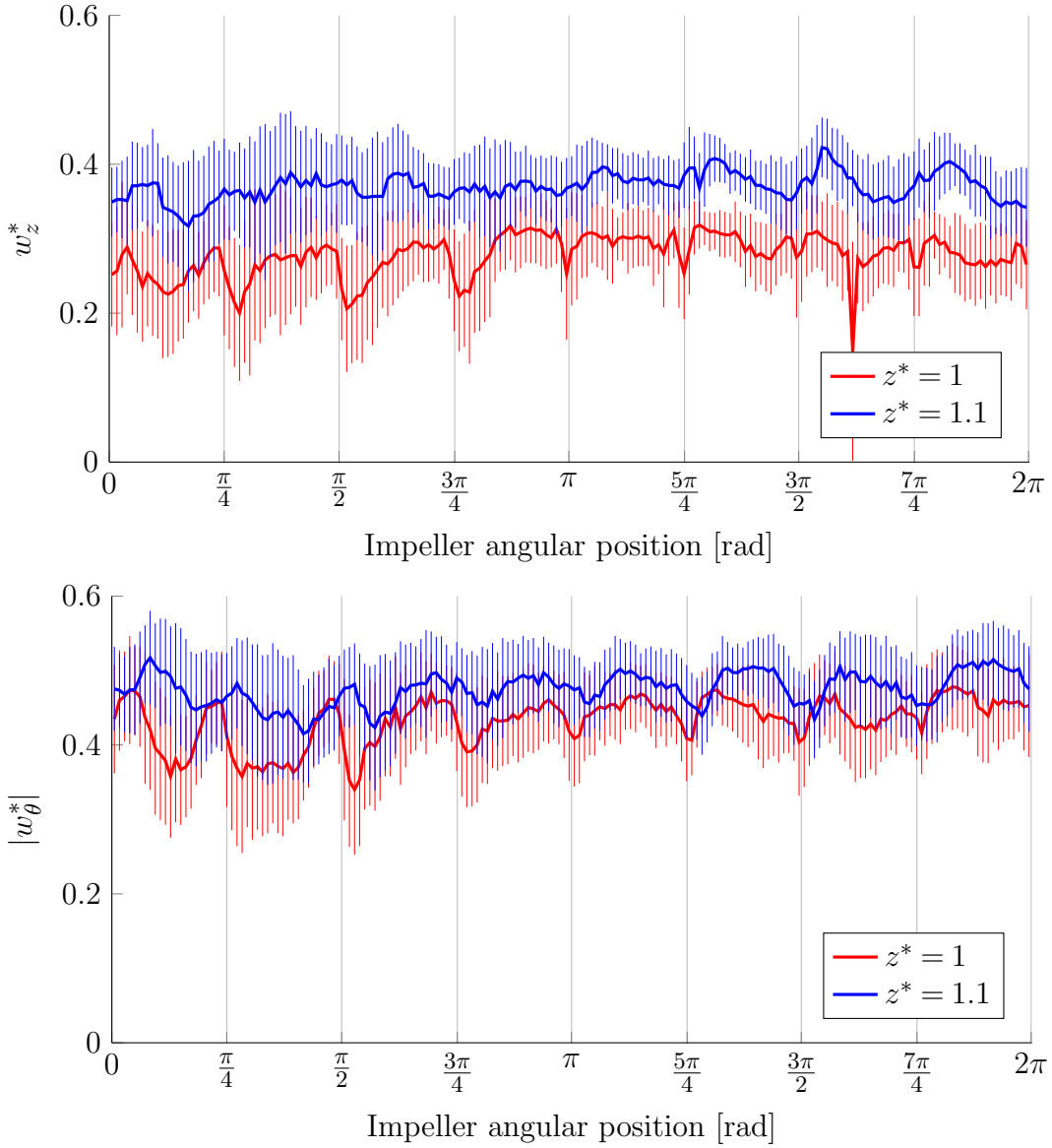

Figure 3.7 Case 3 (Table 2.1): Phase-averaged velocity in the diffuser, at the design point ($\Phi^* = 0.95$) for $r^* \approx 0.9$ and $\theta = 35$ degrees. The error bars represent the standard deviation. We observe a periodicity corresponding to the blade passage frequency (8 blades: $2\pi/8$)

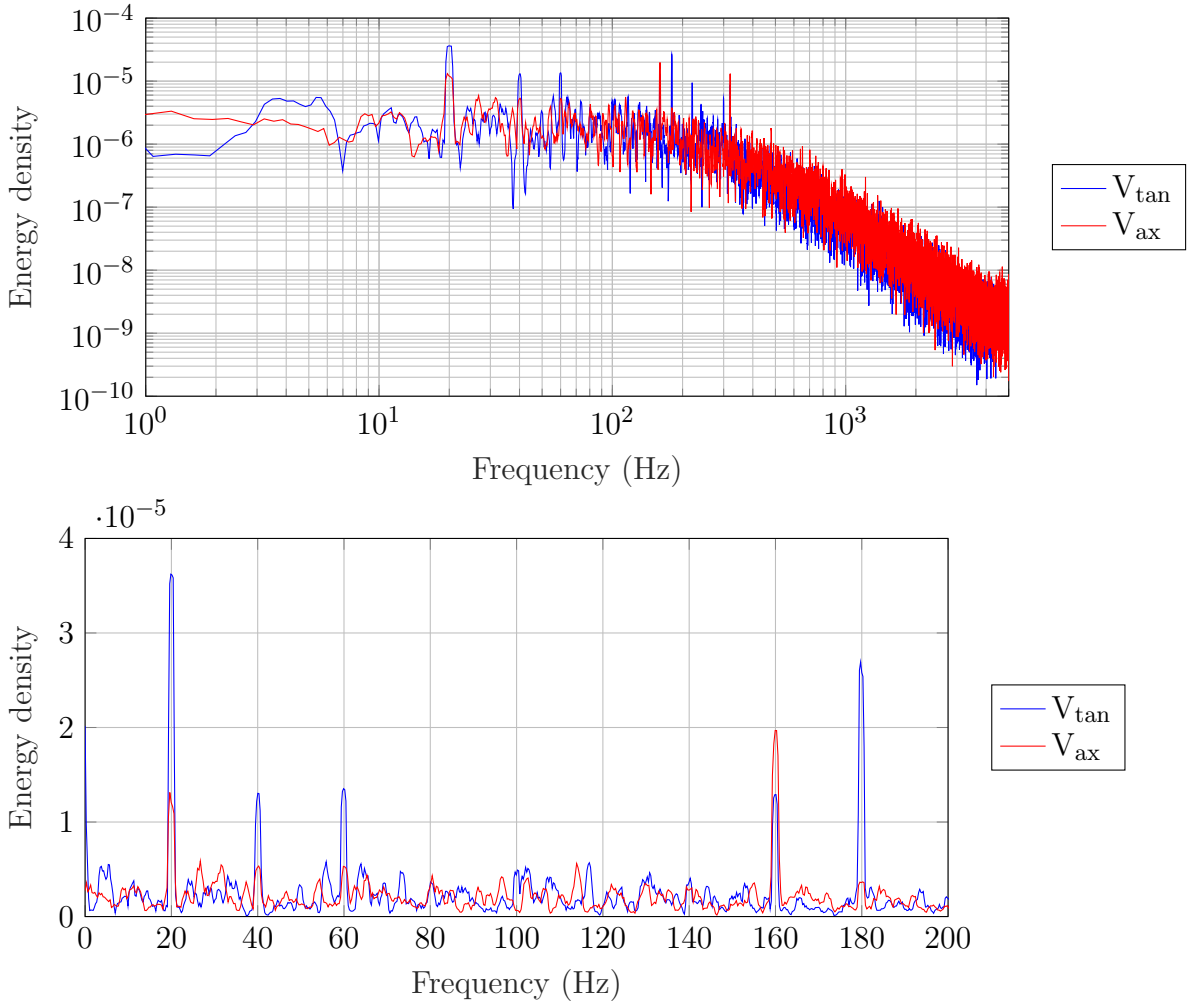

Figure 3.8 Case 3 (Table 2.1): Energy density spectrum for the normalised axial (red) and tangential (blue) velocities, at the location P_3 in the diffuser ($r^* = 0.94$, $\theta = 39$ deg, Case 3). Peaks can be observed at the rotation frequency (20 Hz) and its harmonic, and at the blade passage frequency (160 Hz).

3.3.3 Part-load behaviour

The pump was tested at several flow rates, in order to investigate the hypothesis of recirculation or rotating stall at $\Phi^* = 0.56$, where the head curve presents a saddle point (see Figure 3.1, and the introduction to this chapter).

In Figure 3.9, the relative tangential velocity (left column) presents two low-magnitude zones: close to the hub and in the blade wakes. These zones merge at low flow rate and the wake area diminishes when increasing the flow rate. At $\Phi^* = 0.56$, the axial velocity (bottom right) has a maximum on the pressure side of the blades, but at higher flow rate there is a minimum in the middle of the passage and the maximum seems to be on the suction side (hidden by the blades). The three cases show a strongly asymmetric flow, due to a defect in the impeller, as explained in Appendix E.2.

The circumferential average is computed using the phase average for each angular bin, rather than summing all collected velocity measurements to avoid a bias toward the areas where the seeding is more concentrated.

As shown in Figure 3.10, the axial and tangential velocity components decrease when the flow rate is reduced, but their radial profiles also change shape. At lower flow rates, there is a more pronounced dip in the axial velocity profile. The tangential velocity is also smoother when operating close to the design point ($\Phi^* = 0.95$). The tangential velocity profile is however not complete in some cases, as the data rate close to the hub was too low to get representative results.

Even though more variation in the velocity profiles suggest higher losses, these measurements do not give any indication on the origin of the saddle point. Measuring the meridional and tangential velocity components at the impeller inlet and outlet would give a better representation of the pump performance in single phase flow, as it is necessary to compute the change of angular momentum induced by the impeller, according to the Euler equation (1.7).

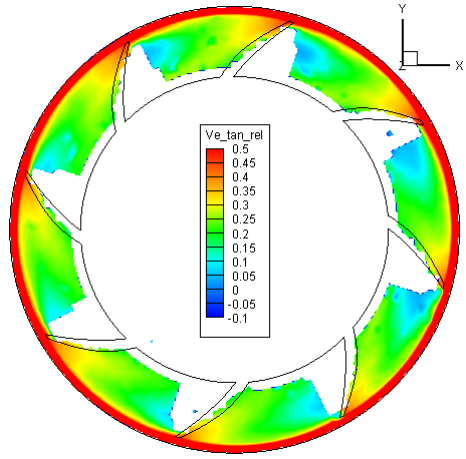

(a) $-w_\theta^*$ at $\Phi^* = 0.56$

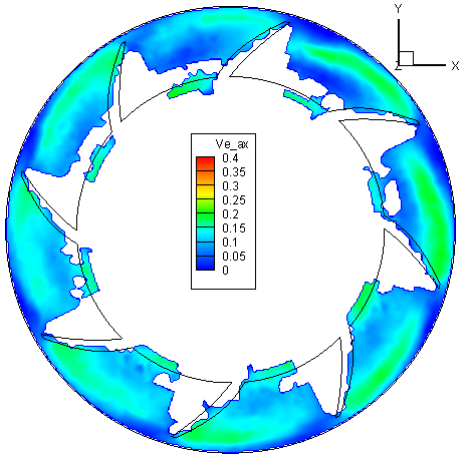

(b) w_z^* at $\Phi^* = 0.56$

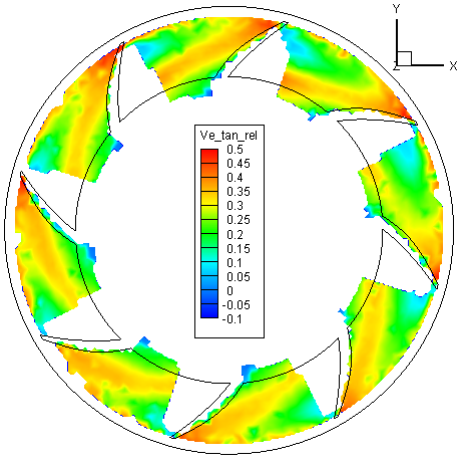

(c) $-w_\theta^*$ at $\Phi^* = 0.8$

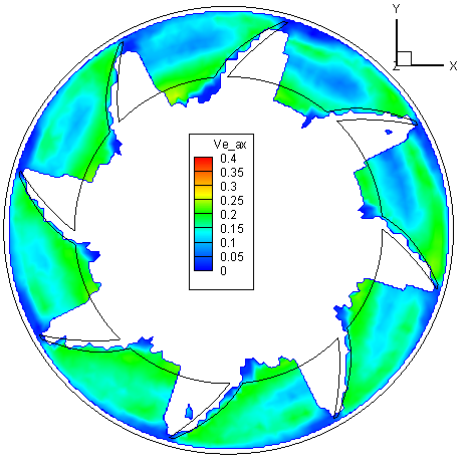

(d) w_z^* at $\Phi^* = 0.8$

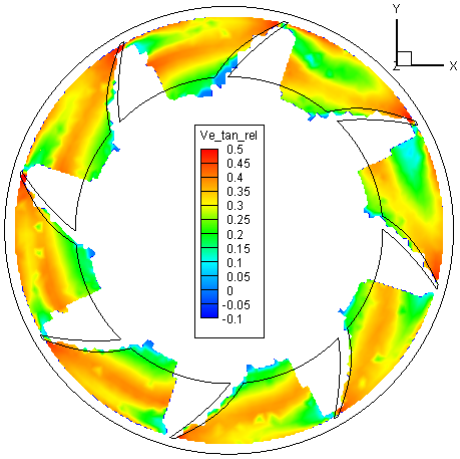

(e) $-w_\theta^*$ at $\Phi^* = 0.95$

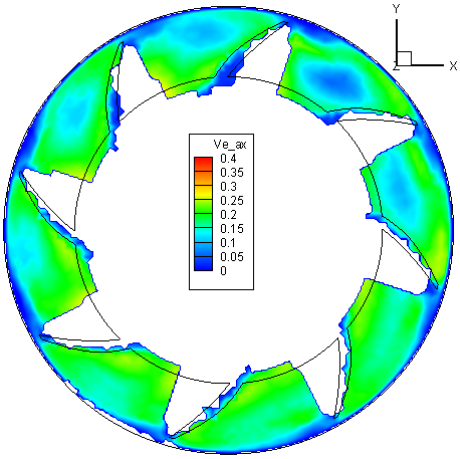

(f) w_z^* at $\Phi^* = 0.95$

Figure 3.9 Cases 13, 14 and 15 (Table 2.1): Axial and tangential velocities in the second impeller, at $z^* = 0.77$.

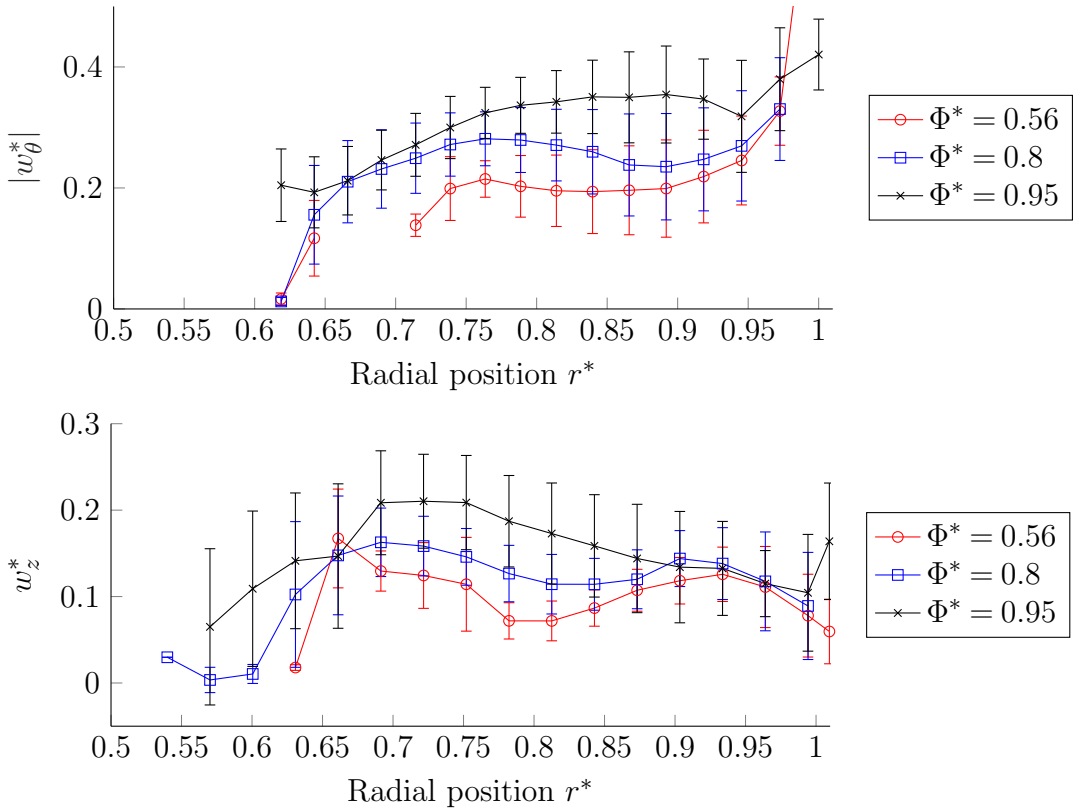

Figure 3.10 Cases 13, 14 and 15 (Table 2.1): Radial velocity profile (circumferential average) at $z^* = 0.77$ for three different flow rates: $\Phi^* = 0.56$, 0.8 and 0.95. The error bars represent the measurement standard deviation.

Conclusions

We have shown that recirculation cells are present in the diffuser at low flow rates (Figure 3.2), and the change in their pattern could be linked to the flat head curve observed ar low flow rates (Figure 3.1). No rotating stall has been found in the diffuser using either high speed imaging or LDV velocity measurements (Figure 3.8).

The velocity fields acquired showed a high turbulence level, especially in the blade wakes, but also some periodic unsteadiness at the impeller/diffuser interface (Figure 3.7). In the impeller and diffuser, it was observed that the flow field is not perfectly uniform, although it is hard to say whether this comes from geometrical imperfections or the nature of the flow, or both. Instantaneous negative velocities were observed on the suction side of the impeller blades, suggesting intermittent recirculation.

At part load, the change in the velocity profile partly explains the efficiency reduction (Figure 3.10), but a more comprehensive measurement (including the radial velocity component, and a finer axial resolution) would be needed to explain more precisely how the flow field relates to the pump performance (head and efficiency). In the future, these velocity measurements can be compared to numerical simulations and used as a benchmark for validation purposes.

Chapter 4

Experimental Gas-Liquid flow characterisation

In this chapter, we examine flow regimes in gas-liquid conditions for a four-stage mixed-flow pump, at the system scale and at the stage scale. The system behaviour is best described using time series of flow rate and pressure measurements, while the local distribution of each phase is identified using high speed video.

We first discuss the two-phase flow in terms of mixing: as the nature of the flow entering the pump seems to have an impact, we explore the different types of mixing and also the phenomena that make the flow unsteady, whether they are linked to the pump performance or not. We describe the flow regimes occurring in our experimental set-up, and define the concept of "gas lock" presented in Section 1.3.2 so that it can be studied in a test loop. Section 4.2 focuses on the flow pattern in the impeller and diffuser, and the gas bubble size distribution. Finally, we report the two-phase performance of the pump under test in Section 4.3, as well as the effect of different parameters that were varied in this experiment: gas fraction, flow rate, rotation speed, pump inclination and inlet pressure.

The high speed videos cited are attached to this thesis (included DVD), and described in more detail with high resolution stills in Appendix F.

4.1 Flow patterns in the pump

4.1.1 Mixing

It has been identified, for example by Kallas and Way (1995) or more recently by Knudsen (2013) that having a "well mixed" flow enhances the pump performance in gas-liquid flows. It is however important to distinguish between "time-wise" and "space-wise" mixing. "Space-wise" mixing refers to the local state of the flow: bubbly flows or emulsions are well mixed, while stratified flows are not. "Time-wise" mixing refers to a steady gas fraction at the pump inlet. Figure 4.1 shows that a spatially well

mixed flow can be unsteady (top), while a stratified flow can be perfectly uniform in time (bottom). Time-wise mixing can be achieved by the presence of a large volume upstream the device of interest, as proposed by Junior et al. (2015) while local mixers or specific pump designs as studied by Zhang et al. (2012) are ways to enhance space-wise mixing.

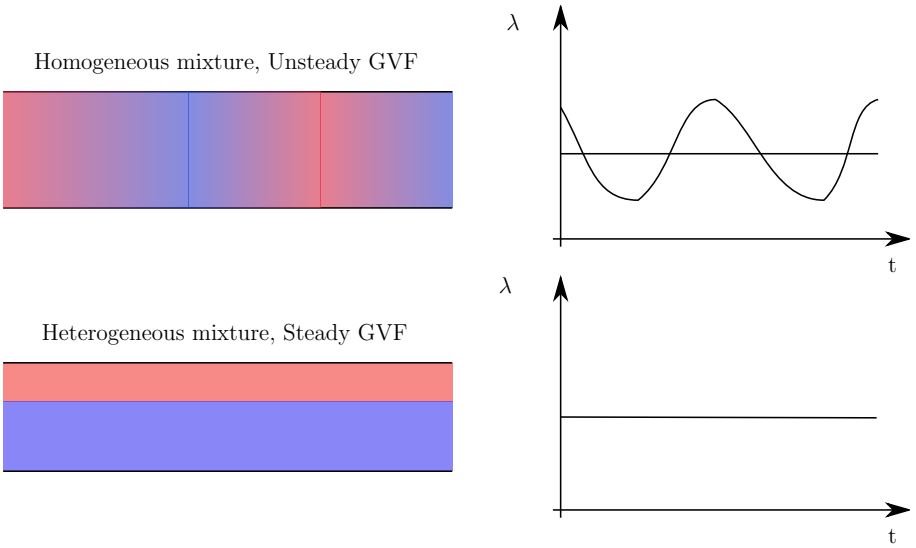

Figure 4.1 Schematic representation of a gas-liquid pipe flow (left) and the associated time series of the gas fraction averaged on a fixed cross-section (right). The upper figures represent a case where the flow is well mixed in each cross-section, but unsteady and the lower ones a case where the gas fraction is steady, but the phases are separated (stratified flow).

A combination of both mixing types is desirable in order to achieve good gas handling. Time-wise mixing avoids peaks of high gas fraction and the associated dramatic head degradation (or gas lock). Local mixing produces very small gas bubbles, which travel at about the same speed as the liquid phase and allows the pump to behave as if the flow was a homogeneous single phase mixture, showing little or no head degradation. This is explain in greater details in chapter 5.

4.1.2 Slugging and system instabilities

Working through the test matrix 2.2, we observed two types of unsteadiness: slugging and system instabilities. The system instability is denoted by the flow rate and outlet pressure variation, exhibiting large amplitude and low frequency variations, while slugging is characterised by higher frequency and lower amplitude variations, especially in the inlet pressure. They can be observed independently, but Figure 4.2 shows a case where they occur simultaneously. The pressure rise and torque measurements present variations that are affected by both instabilities. As we have seen in Section 1.3.3, the pump can have a stabilizing or destabilizing effect on the system, depending on the gradients $^{d\Delta P_P}/_{dQ}$ and $^{d\Delta P_T}/_{dQ}$.

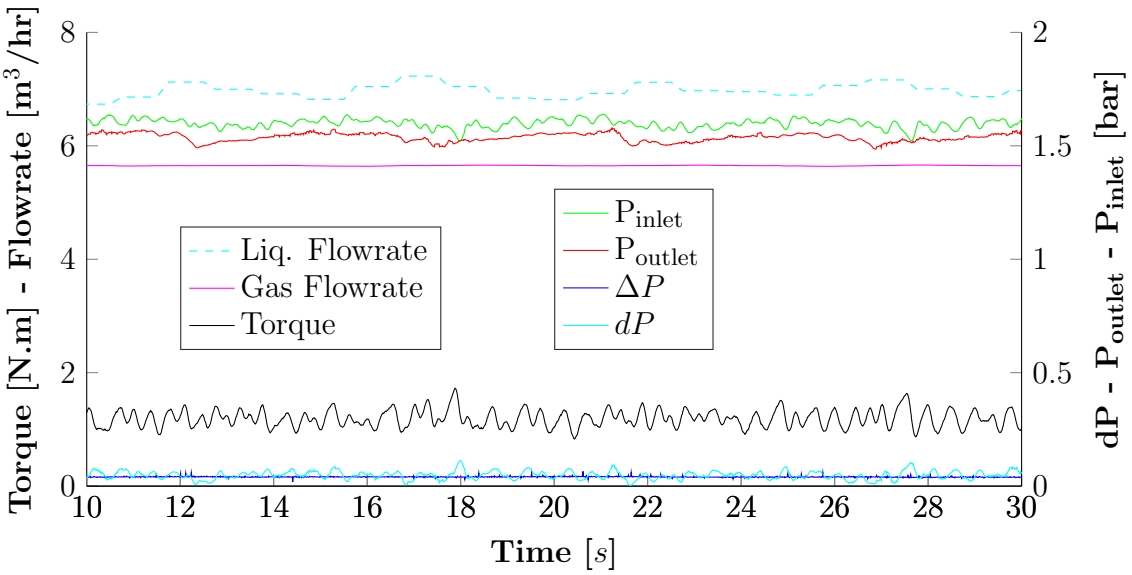

Figure 4.2 Measured torque, pressure and flow rates for 4-stage mixed-flow pump working at 20 Hz, $\Phi_T = 1.06$ ($Q_w = 7$ m^3/hr, $\lambda_0 = 33.5\%$) at an angle of 61 degrees from horizontal with the inlet pressure $P_{\text{inlet}} = 1.6$ bar. Slugging at the pump inlet has a frequency of approximately 2 Hz and mainly affects the inlet pressure, while a system instability is seen through the flow rate measurements with a lower frequency of about 0.2 Hz.

Even if the gas flow rate is measured very close to the injection point and the pump (less than 2 meters in a 12mm diameter pipe), the gas compressibility allows the flow rate to be steady at the flow meter while it is not at the pump inlet. Flow visualisation at the pump inlet shows gas slugs with a well defined interface when the pump is horizontal in Figure 4.3a. When the pump is set at an angle (61 degrees), the flow is bubbly at low gas fraction and slugs are observed at the top of the pipe from $\lambda_0 \approx 5\%$. The same behaviour exists for a vertical set-up for a gas fraction higher than 15% : Large cap bubbles (or Taylor bubbles) are observed in Figure 4.3b, propagating faster than the bulk flow (see Video A2). These variations are more pronounced at higher flow rates.

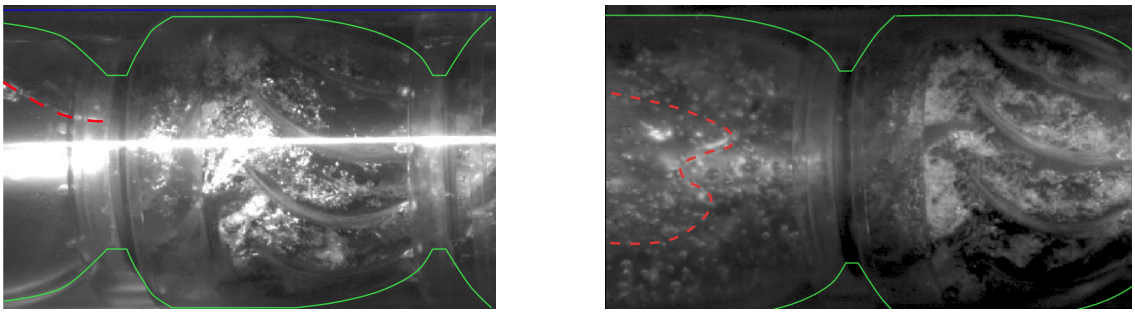

(a) Horizontal (b) Vertical

Figure 4.3 Stills from the videos A1 (left) and A2 (right). Pump inlet and first stage, rotating at 20 Hz, with $\Phi_T^* = 1.2$ and an inlet gas fraction of respectively 5 % (horizontal) and 17 % (vertical). The dashed red lines show the gas liquid interface. In (a), a gas slug is entering the pump inlet, while the first stage is radially stratified. In (b), the incoming flow is bubble, with a Taylor bubble on its way toward the inlet. In both cases the incoming flow is unsteady, for relatively low gas fractions.

Slugging can be related to the pipe layout topology (terrain slugging), as well as the gas and liquid flow rates and pipe diameter (hydrodynamic slugging). This terminology is often applied to pipe-line flows and refers to the causes of the phenomena, although terrain slugging is usually more severe and less predictable than hydrodynamic slugging, although they can occur concomitantly. Hanratty (2013) describes these phenomena, and the conditions in which they can occur. In our case, as the pipe between the gas injection point and the pump inlet is straight, the flow observed is likely to be hydrodynamic slugging. On the other hand, system instabilities are driven by the pump characteristics as well as the level of friction in the piping and the compressibility of the whole system. Table 4.1 summarizes the occurrence of each type of unsteadiness. The inlet pressure standard deviation in Figure 4.15 confirm the strong impact of the pump inclination on slugging and instabilities.

Table 4.1 Occurrence of system instability and slugging in the test loop. These results are based on the qualitative observation of the sensor data (pressure, flow rate) and high speed videos in the conditions scanned by the test matrix 2.2.

	Slugging	Instability
GVF <5 %	No	At very low flow, only when vertical
5% <GVF < 15%	When horizontal	At low flow only, any inclination
GVF > 15%	At any inclination	At medium and low flow, any inclination

4.1.3 Gas Lock

The phrase and concept of "gas lock" can have different meanings depending of the context in which it is used. In this section, we clarify this concept, proposing a definition that is appropriate for studying this phenomenon in a laboratory set-up, as opposed as what it refers to for pump operators (see Section 1.2). We then explain the mechanisms leading to this phenomena.

When testing a pump in laboratory or surface conditions, we wish to define "gas lock" conditions independently from the system in which a pump is used. We therefore consider the pump pressure curve, as a function of flow rate, and define gas lock as the point $Q_{\text{tot}} = 0$, $\Delta P = 0$ as can be seen in Figure 1.10. In the present experiments, the fluids (gas and liquid) flow through the pump regardless of the produced head, as we control the inlet pressure through the water booster pump (see Figure 2.1). In order to observe a gas lock in steady-state, one would have to set a high gas fraction in the pump stages in advance and rotate the pump in shut-in conditions ($Q_{\text{tot}} = 0$). Not only could this damage the stages due to the friction heat generated, but such a test would not give any information on the mechanisms leading to gas lock. However, as the gas fraction in our experiment was varying significantly (especially when the pump was horizontal), we have only observed "intermittent gas lock" over 10 to 50 milliseconds, at low flow rates.

For a moderate gas fraction ($\lambda_0 > 5\%$) and low flow rate ($0.4 < \Phi_T < 0.5$), the gas bubbles accumulate in the impeller and form a gas pocket that is associated with head degradation. The size of this pocket increases with increasing gas fraction, up to filling the blade to blade interval. At one point, the liquid flows in a thin layer along the shroud. The gas and liquid mix again when reaching the impeller/diffuser interface, and return back to an annular flow in the diffuser passages. Videos A1, C1 and D2 show examples of intermittent gas lock. The gas and liquid flow rates were only measured far from the pump, therefore their local variation could not be observed quantitatively.

4.2 Flow patterns in a stage

The flow patterns observed in the pump stages have been divided into four categories:

- **Bubbly flow**: The gas phase consists of spherical or ellipsiodal bubbles, smaller than the passage height flowing throughout the whole pump. (Video B1 and B2)
- **Gas pocket**: Gas accumulates, sometimes intermittently on the suction side of the impeller blades, close to the hub. Video B3 shows an intermittent gas pocket forming on the suction side, while Video C1 has permanent gas pockets in the impeller.
- **Stratified flow**: The impeller passages (and intermittently the diffuser passages) are filled with gas from suction to pressure side. Liquid is present as a thin film flowing along the shroud, it can also be described as a radially stratified flow. (Video A1)
- **Churn flow**: The bubbles become so large that they take up to the whole passage (Video D2). This pattern is sometimes visible in the diffuser only, while the impeller exhibits a separated flow.

Because of the unsteady nature of the flow, flow regimes are easy to identify only in extreme conditions (less than 5% gas fraction, or more than 30%). In mid-range, a single video lasting 0.5 second displays a large variety of patterns (see Video C1 - Appendix F.4). Figure 4.4 illustrates the four flow patterns described above, but most of the videos show a much more complex behaviour. All videos have been manually associated to a dominant flow regime (see Appendix G), and related to the pump performance in Section 4.3.2.

4.2.1 Effect of upstream stage

There were no qualitative differences observed between the second, third and fourth stages in terms of flow patterns. However, the first impeller was more likely to be gas locked than the others (Video D1 - Appendix F.5). This is due to the incoming flow carrying larger bubbles at the pump intake (horizontally stratified in horizontal set-up, very large bubbles in vertical set-up, see Videos A1 and A2 - Appendix F.1 and F.2), which have not been broken up by the impeller blades yet.

4.2.2 Bubble size

With the available video resolution, it was not possible to quantitatively analyse the bubble size, apart from a clear trend observed with the rotation speed: At the impeller outlet, the bubble size distribution seems to depend on the rotation speed as shown in Figure 4.5.

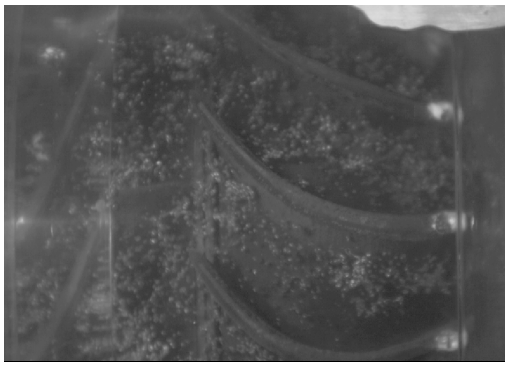

(a) Bubbly ($\lambda_0 = 2.5\%$)

(b) Gas pockets ($\lambda_0 = 10\%$)

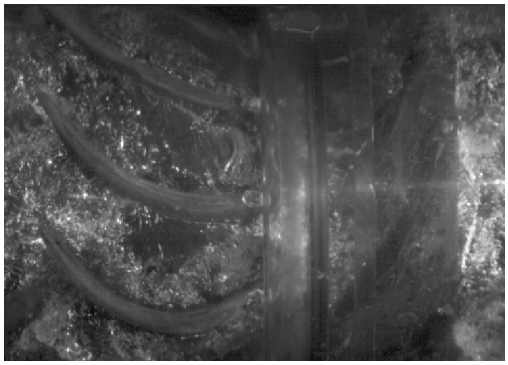

(c) Stratified ($\lambda_0 = 30\%$)

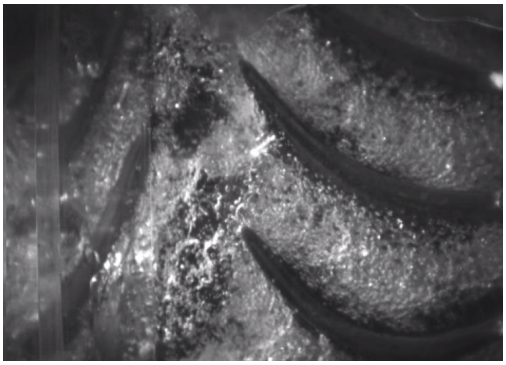

(d) Churn ($\lambda_0 = 15\%$)

Figure 4.4 Pictures representative of the different flow regimes, for the pump running horizontally at 20 Hz with $\Phi_T = 1.1$ (except for (d) where $\Phi_T = 0.58$.

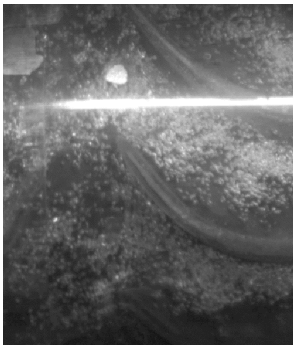

(a) 20 Hz - $d_{max} \approx 1$ mm

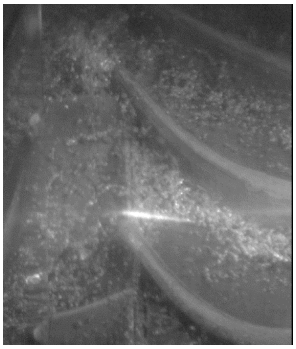

(b) 25 Hz - $d_{max} \approx 0.8$ mm

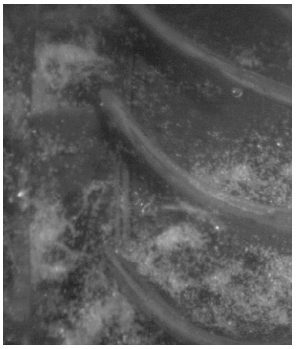

(c) 30 Hz - $d_{max} \approx 0.6$mm

Figure 4.5 Impeller outlet and diffuser inlet at BEP for 2.5 % GVF. Note that the GVF at the pump inlet is not steady over short time scales (100 to 200 ms), therefore the average GVF at the inlet is not necessarily equal to the instantaneous and local gas hold-up when the picture was taken. All pictures have the same length scale.

Following Hesketh et al. (1987) analysis based on a critical Weber number, we show that the maximal bubble diameter at the impeller tip should vary with the pump speed according to $d_{max} \propto \omega^{-5/6}$. The full derivation of this correlation is reported in Section 5.1.4.

Taking the bubble size in the impeller wake at 20 Hz (1 mm) as a reference, it is possible to calculate the theoretical bubble diameter at different pump speeds using the above relation. We obtain respectively 0.76 and 0.61 mm for 25 and 30 Hz rotation speeds. These values compare well with the bubble size observed in Figure 4.5.

When the bubbles get into the diffuser and if the gas fraction is high enough (above 5%) they tend to coalesce. At the diffuser outlet, the bubble mean diameter increases with gas volume fraction and decreases with the total flow rate. Video D1 (Figure 4.6) shows the change of bubble size distribution between the diffuser inlet and outlet. Unfortunately as explained in chapter 2, it was not possible to measure the actual bubble size distribution in the impeller or diffuser.

Figure 4.6 Bubbles at the diffuser outlet (right) are bigger than at the diffuser inlet (left), as they are recirculating when the total flow rate is low (from Video D1).

4.3 Performance in Gas-Liquid Flows

We measured the torque, flow rates as well as the differential, inlet and outlet pressure for a four-stage, mixed-flow pump in the set-up described in Section 2.1, for a range of inlet gas fractions λ_0 and total flow rates Q_{tot}. Above $\lambda_0 = 5\%$, the torque and pressure measurements present significant variations with time as shown in Figure 4.7. Pressure fluctuations were observed at the inlet for most gas-liquid cases, while the gas and liquid flow rates measured upstream of the test pump were generally steady.

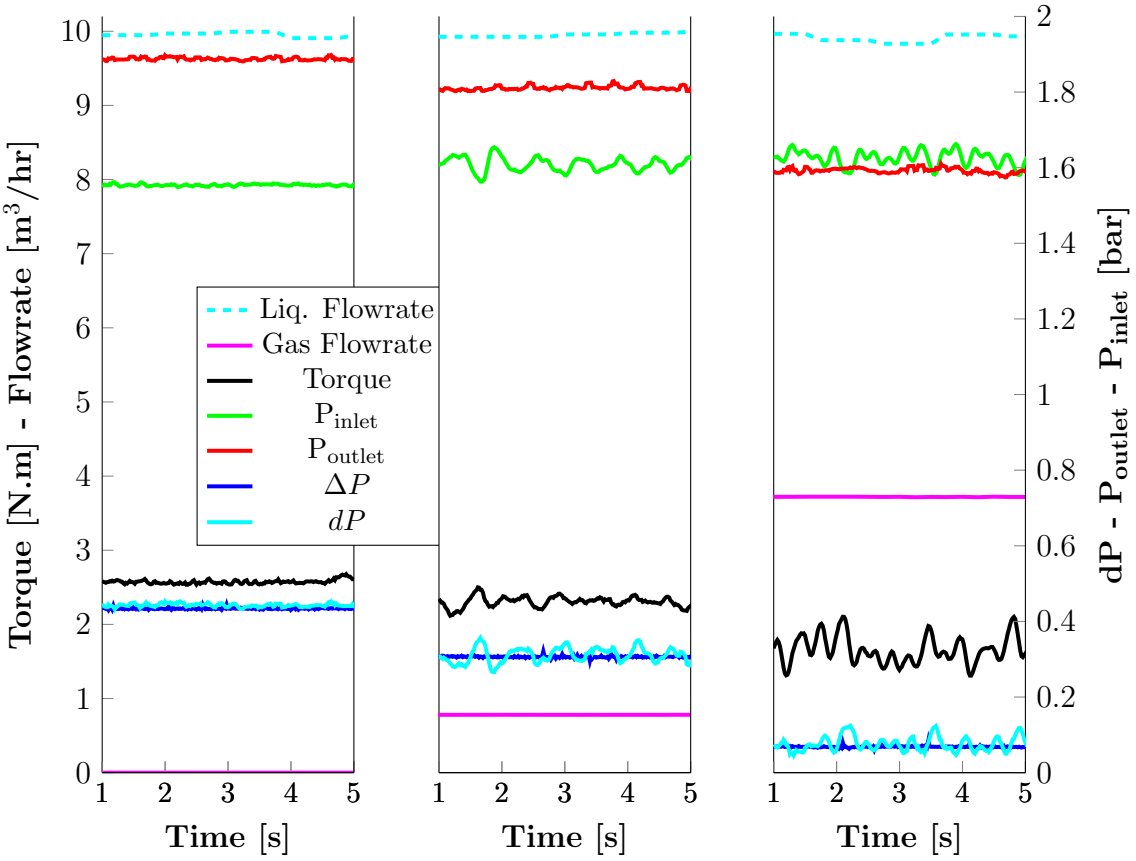

(a) $\lambda_0 = 0\%$ (b) $\lambda_0 = 4.7\%$ (c) $\lambda_0 = 18.8\%$

Figure 4.7 Measured torque, pressures and flow rates for the 4-stage mixed-flow pump working at its Best Efficiency Point (BEP) flow rate, at 20 Hz ($Q_{\text{BEP}} = 9.9$ m^3/hr), with an angle of 60 degrees from horizontal and an inlet pressure of 1.6 bar (Case A, see Table 2.2).

The pressure rise ΔP given by the differential sensor is strongly smoothed compared to the one calculated using the absolute pressure sensors:

$$dP = P_{\text{outlet}} - P_{\text{inlet}} + \rho_w g \Delta z,$$

where Δz is the height difference between the inlet and outlet pressure sensors. We checked that the time averages of both measurements match for all data points $\langle dP \rangle = \langle \Delta P \rangle$ within 2.5 %.

4.3.1 Gas fraction variations

The torque T and differential pressure dP obtained from absolute sensors are strongly correlated, as shown on Figure 4.8. The torque measurement is 0.08 seconds ahead compared to the pressure rise, as the discharge pressure accounts for most of the dP variations.

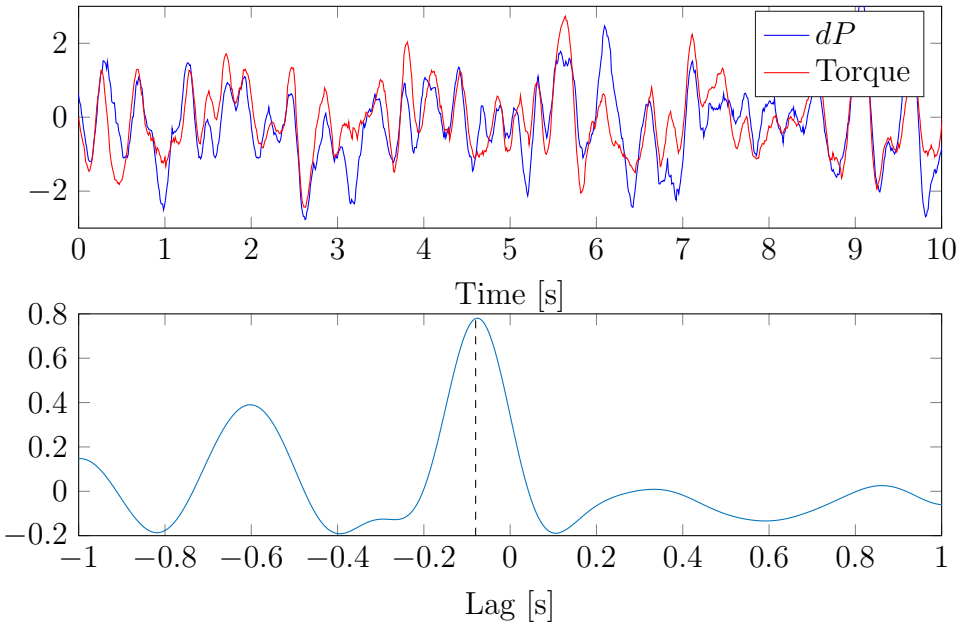

Figure 4.8 Torque and Pressure Rise for 4-stage mixed-flow running vertically at 20 Hz with an average inlet pressure $P_{\text{inlet}} = 1.6$ bar (case E), gas fraction $\lambda_0 = 17.5\%$ and for $Q_{tot} = 1.4\ Q_{\text{BEP}}$. The upper plot shows the two normalised signals and the lower plot their cross-correlation.

This correlation suggests that the observed oscillations arise from a gas fraction variation. We use the experimental data to estimate the average pressure rise delivered by the pump as

$$\Delta P_{2p} = \langle dP \rangle = f_{Q_l}\left(\langle \lambda_0 \rangle\right),$$

where $\langle\rangle$ denotes the time average over a minute with steady gas and liquid flow rates. f_{Q_l} is obtained using a local regression smoothing function, available in Matlab (`lowess`) to construct the response surface $\langle dP \rangle = f(\langle Q_l \rangle, \langle \lambda_0 \rangle)$ for each experiment (cases listed in Table 2.2).

Assuming that the liquid flow rate through the pump is constant and that the same relation holds for instantaneous quantities as for averages, we obtain:

$$dP = f_{Q_l}(\lambda_{1-4}), \tag{4.1}$$

where λ_{1-4} is the average gas fraction in the pump: $\lambda_{1-4} = \sum_{i=1}^{4} \lambda_i/4$.

We then approximate the gas fraction temporal variations by inverting (4.1) : $\lambda_{1-4} = f_{Q_l}^{-1}(dP) \equiv \lambda_{dP}$. This method is not very accurate as the function f_{Q_l} is not linear, but it gives an order of magnitude for the gas volume fraction variation. Figure 4.9 shows that the average of the local gas fraction, $\langle\lambda_{dP}\rangle$, is close to the reference inlet gas fraction λ_0. It is higher at low flow rates for $5\% < \lambda_0 < 30\%$, and lower for very high gas fractions. This indicates that the gas phase travels at a different speed than the liquid in the pump, a phenomenon also referred to as "phase slip". The same analysis based on the torque measurement shows similar results, but with a larger difference between λ_0 and $\langle\lambda_T\rangle$. In both cases, the standard deviation of the computed gas fraction increases with λ_0, is lower when the pump is inclined or vertical and decreases with the pump rotation speed.

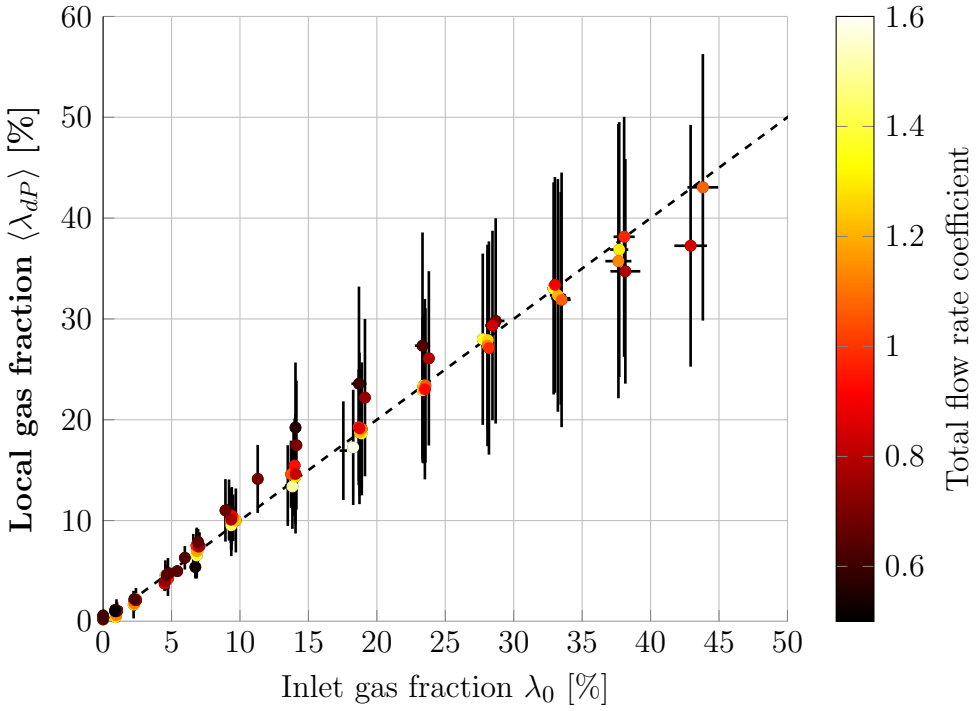

Figure 4.9 The computed gas fraction based on the pressure rise measurement $\langle\lambda_{dP}\rangle$ as a function of the inlet gas fraction obtained from gas and liquid flow rate measurement $\lambda_0 = Q_{g0}/(Q_{g0} + Q_l)$ and coloured by total flow rate coefficient Φ_T^*, for the Case C (see Table 2.2). The error bar represents the standard deviation ($\pm\sigma_{\lambda_{dP}}$).

We notice that the relative standard deviation $\sigma_{\lambda_{dP}}/\langle\lambda_{dP}\rangle$ varies depending on the operation conditions, and particularly the rotation speed and pump inclination. Figure 4.10 shows that increasing the rotation speed reduces the GVF relative variation, and

as we reported earlier a vertical pump results in a steadier flow than when it is placed horizontally (Table 1.2).

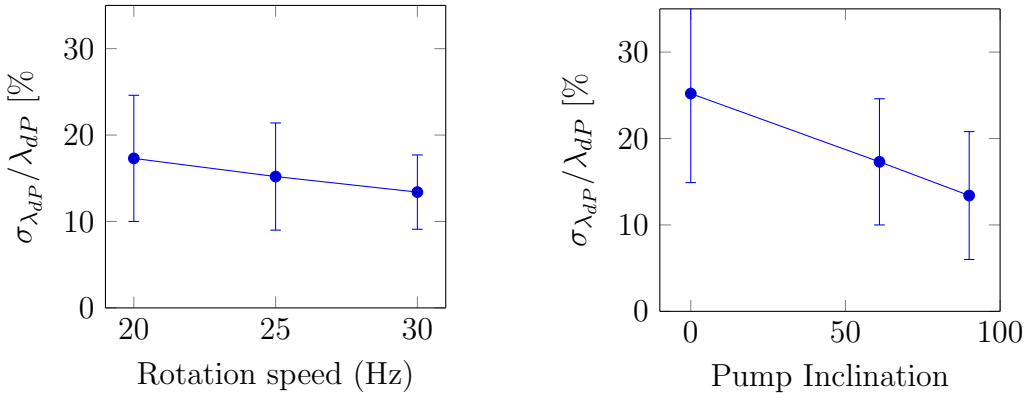

(a) Cases C, D, E (Tilted pump: 61°) (b) Cases A, C, F ($f = 20$ Hz)

Figure 4.10 Average standard deviation of the computed gas fraction λ_{dP} (for all Φ_T^*, λ_0). The error bars represent the standard deviation due to the variations of flow rate and gas fraction.

In the next Sections, we will use these values as the relative error for the GVF measurement, since they are related to the uncontrolled GVF fluctuations at the pump inlet.

4.3.2 Measured head degradation

We interpolated the collected data for each series of tests to create a surface representing the pump behaviour. Figure 4.11 shows the typical head curves obtained this way (a comparison of different cases will be made in the following Sections). When the gas fraction increases, the head curve becomes flatter in the low flow coefficient region, sometimes with a positive slope. This behaviour can lead to dynamic instabilities as explained in Section 1.3.3.

Following Ossia and Guénégo (2006) we use the head degradation factor as defined below in order to quantify the pump performance in a multiphase conditions.

$$\mathcal{M}_{2p}\left(\lambda_0, \Phi_T^*\right) = \frac{\text{Head in two phase}}{\text{Head in single phase}} = \frac{\rho_w \Delta P_{2p}\left(\lambda_0, \Phi_T^*\right)}{\rho_m\left(\lambda_0\right) \Delta P_w\left(\Phi_T^*\right)} \tag{4.2}$$

where $\rho_m = (1-\lambda_0)\,\rho_l + \lambda_0 \rho_g$ is the mixture density, ΔP_{2p} is the measured pressure rise in two-phases, and ΔP_w is the pressure rise for single phase water.

Figure 4.12 shows that the head degradation coefficient $\mathcal{M}_{2p}$ drops quickly with increasing gas fraction λ_0 between 2 and 10 %. From 10 to 15 %, the head degradation factor decreases at a much slow rate. At low flow rates, the degradation is more abrupt, leading to the flatter head curve observed in Figure 4.11.

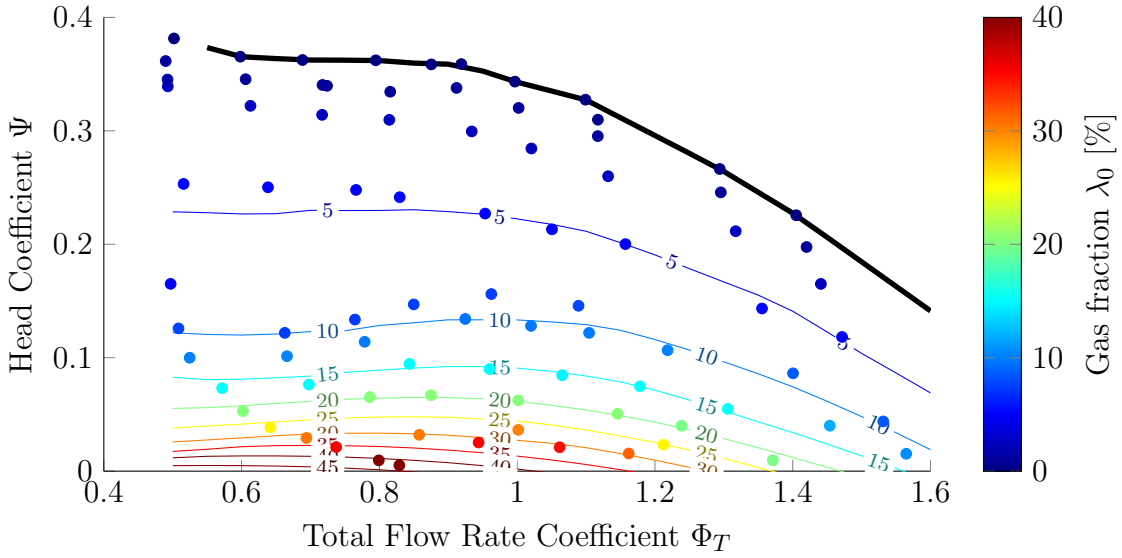

Figure 4.11 Head coefficient for the 4-stage pump rotating horizontally at 20 Hz with an inlet pressure of 2.5 bar (Case B), as a function of the normalised total flow coefficient Φ_T^*. The thick black line is the single phase data, and the thinner lines are the result of a smoothed local regression (`lowess`) of the experimental data represented by coloured dots.

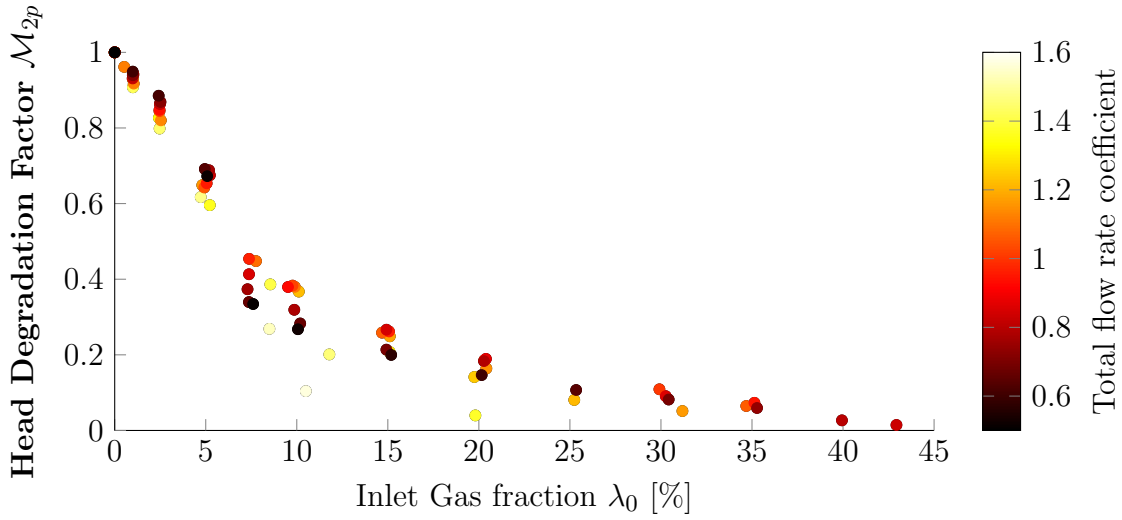

Figure 4.12 Head degradation factor of 4-stage mixed-flow pump, rotating horizontally at 20 Hz, with an inlet pressure of 2.5 bar (Case B). The error bars are hidden for better clarity, but are shown in the subsequent Figures.

These are a general qualitative results valid for all tested conditions, and we explore in the following subsections the impact of several parameters: the inlet pressure P_i, pump inclination and pump rotation speed ω.

Effect of inlet pressure

Changing the inlet pressure from 1.5 to 2.5 bar had very little effect on the pump performance (see Figure 4.13). The gas density increases proportionally with pressure, but this eventually only results in a 2% reduction in the phase density difference $\Delta\rho = \rho_l - \rho_g$.

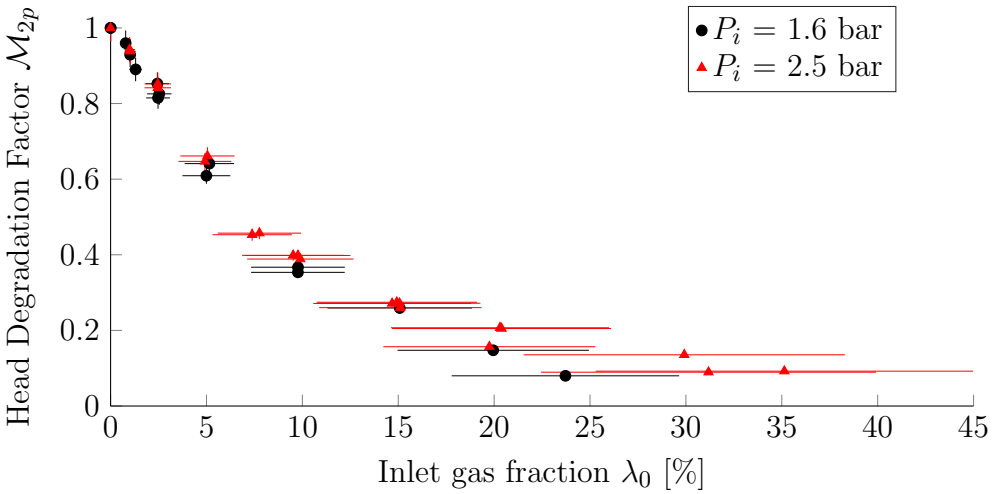

Figure 4.13 Head degradation for two different inlet pressures at design flow rate ($\Phi_T^* = 1$). Cases A and B as defined in Table 2.2. There is no noticeable effect of the inlet pressure in the studied range.

Effect of the pump inclination

As shown in Figure 4.14, the head degradation factor is consistently lower when the pump is horizontal than when it is vertical or tilted. This is probably due to the flow regime at the pump inlet, which changes depending on the pump inclination as shown in Figure 4.3 and Videos A1 and A2. The stratified flow at the inlet is detrimental to the performance of the first stage.

Moreover, slugging is more severe when flowing horizontally, as shown in Figure 4.15. The inlet pressure was much more stable when the pump was set at an angle. Such an effect was also observed on the torque and outlet pressure but not on the gas or liquid flow rates. The gas fraction temporal fluctuations (see Section 4.1 and Figure 4.1) lead to a lower average performance because of the shape of the degradation curve. Assuming that Figure 4.12 accurately represents the instantaneous response of the pump for a given gas fraction. For an average GVF of $\lambda_0 = 5\%$, the degradation factor should be around 0.65. However if the inlet gas fraction fluctuates between 0 and 10 %,

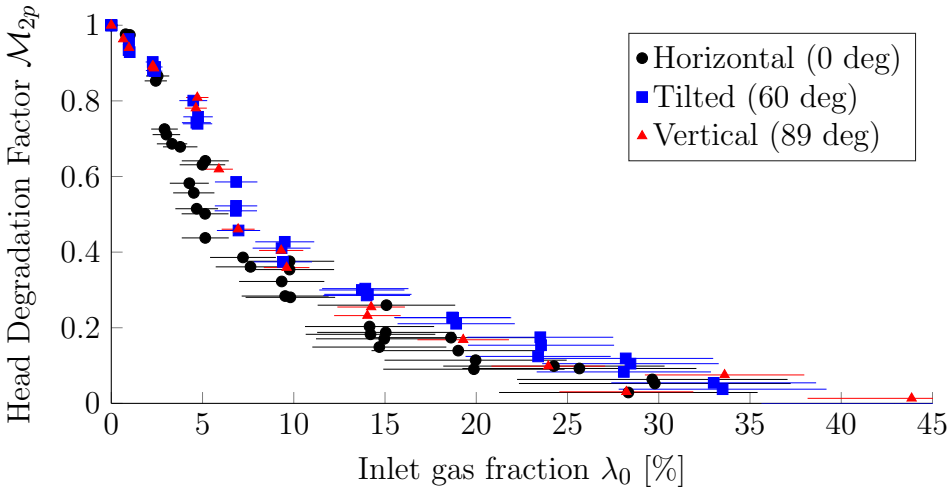

Figure 4.14 Head degradation for different pump deviations around the design flow rate ($0.8 < \Phi_T^* < 1.2$). Cases A, C and F (see Table 2.2). Horizontal operation shows more degradation, although this is likely due to the flow regime (larger slug amplitude) rather than to an intrinsic difference in the pump operation.

which is a realistic assumption given the observations made from high speed videos, the average head degradation factor will be of the order of 0.5, much lower than the steady state value. This is a threshold effect due to the non-linearity of the head degradation factor with GVF. In our case, the pump inclination has an impact on the inlet flow conditions: as shown on Figure 4.15 the inlet pressure fluctuations are larger when the pump is placed horizontally than vertically or inclined. This is a good indicator of slugging. Figure 4.10 (b) also shows that the gas fraction is more stable in a vertical setup. The threshold effect has more impact when the gradient variation of the curve $\mathcal{M}_{2\varphi} = f(\lambda_0)$ is larger, that is for $0 < \lambda_0 < 10\%$. This is confirmed by the fact that the difference between the three data sets in Figure 4.14 is smaller at higher gas fraction, away from the region where the head degradation factor decreases dramatically.

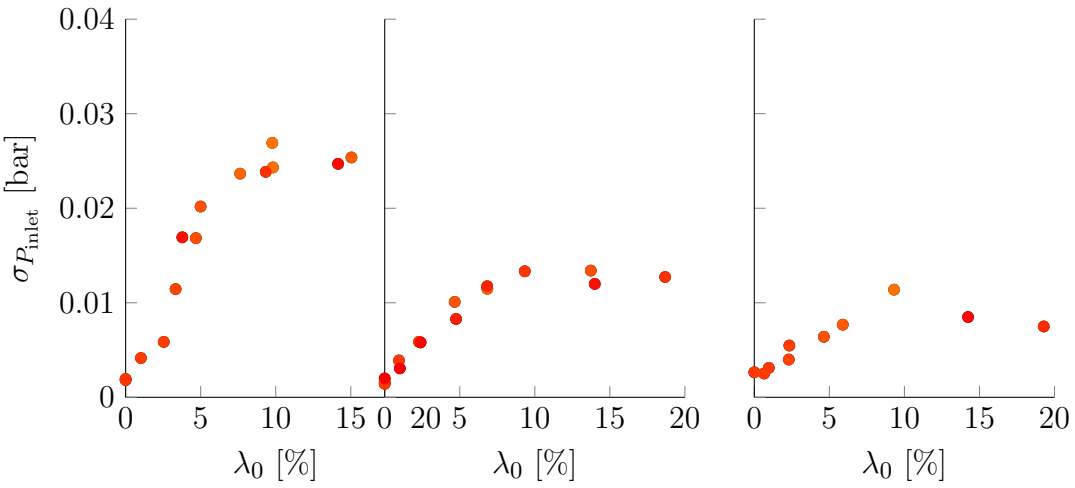

(a) Horizontal (0 deg.) (b) Tilted (61 deg.) (c) Quasi-Vertical (89 deg.)

Figure 4.15 Standard deviation of the inlet pressure for various flow coefficients as a function of the inlet gas fraction λ_0, with the pump rotating at 20 Hz and $\langle P_{\text{inlet}} \rangle = 1.5$ bar inlet pressure.

Effect of rotation speed

We have seen in Section 4.2.2, that increasing the rotation speed decreases the bubble size, which should improve the pump multiphase performance. This is backed-up by the experimental results obtained by Ossia and Guénégo (2006), and latter in this thesis by the mechanistic modelling (Section 5.4.3). We also see on Figure 4.10, that the gas fraction fluctuations decrease with the rotation speed. This should also lead to a better gas handling performance for higher rotation speed, through the same mechanism as described above for the pump inclination.

However, we observe in Figure 4.16 that the performance is slightly better when the impeller rotates at 20 Hz compared with 25 and 30 Hz. This contradicts all predictions and expectations. We note that the difference is very small between the data obtained at 20 Hz and at 25 and 30 Hz. However it is still significant, and it is the largest difference observed between any two cases from Table 2.2. In this experiment, the maximal rotation speed was limited by the maximal pressure generated in the PMMA housing. ESPs normally run at much higher speeds, between 50 and 80 Hz, where the Reynolds number is much larger: based on the passage height h and tip velocity ωR, we have $Re_{f=20Hz} = 50,000$ and $Re_{f=30Hz} = 75,000$. We have shown in Appendix E.1 that such a change in Reynolds number does not have a significant impact on the single phase flow. It could however have an impact on the bubble dynamics. This could be due to differences in the liquid flow field, and particularly the boundary layer, as the Reynolds number in the pump. This highlights the need for a wider range of rotation speed, as the typical values for ESPs are between 50 and 80 Hz.

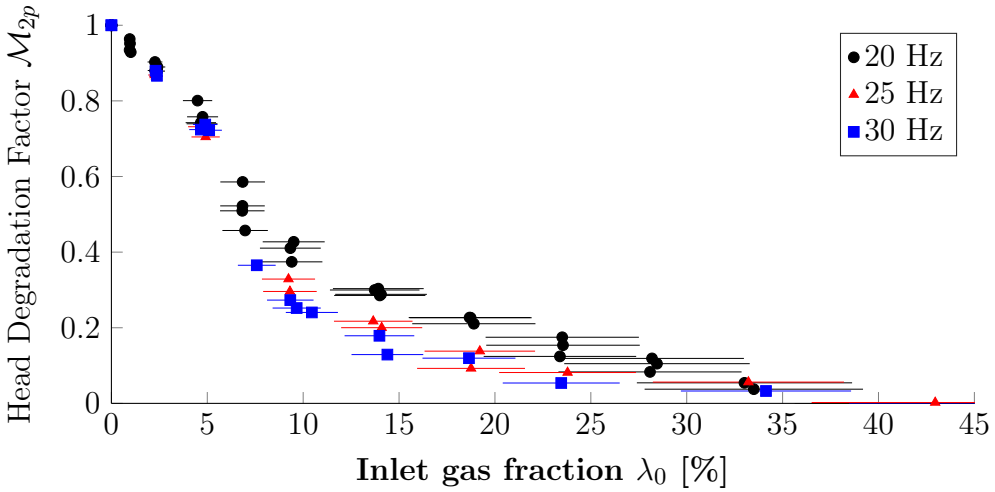

Figure 4.16 Head degradation for different pump speed. Cases C, D, E (see Table 2.2).

Effect of flow pattern on degradation

Finally, each high speed video is associated with one the flow regimes mentioned in Section 4.2: Bubbly, Gas Pockets or Stratified. As several flow regimes were often observed at different times through a single video, the most severe was always registered. The full list of videos and flow patterns as well as comments can be found in Appendix G. As shown in Figure 4.17, the head degradation factor is between 1 and 0.8 for bubbly flows, around 0.5 when a gas pocket appears and close to 0 for radially stratified flows (gas lock).

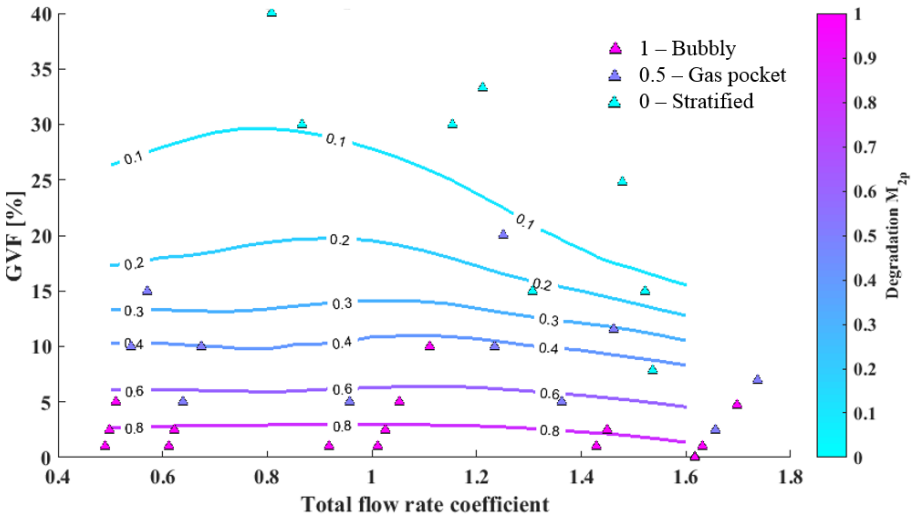

Figure 4.17 Contour map of the head degradation factor for the pump running horizontally at 20 Hz, with a 2.5 bar inlet pressure (Case B as per Table 2.2). The flow patterns defined by the high speed visualisation are superimposed. From Table G.1.

Conclusions

We have measured the head degradation factor $\mathcal{M}_{2\varphi}$ for a four stage mixed-flow pump (see Figure 4.12) and showed that it was only slightly affected by the flow rate coefficient, rotation speed (Figure 4.16), pump orientation (Figure 4.14) or inlet pressure (Figure 4.13). Because of practical limitations, the rotation speed and inlet pressure were not varied significantly enough to draw any conclusion. The small reduction in $\mathcal{M}_{2\varphi}$ for a horizontal pump compared to a vertical pump is explained by a change of regime at the pump inlet, rather than a change in the flow thought the pump. This is supported by the large inlet pressure variation recorded when the pump is horizontal (Figure 4.15). We underline that ESPs are normally run at 50 Hz, and there might be a quantitative and qualitative difference between the measurements and observation made in this work (20 to 30 Hz), and a typical application.

Using high speed imaging, we have demonstrated that the first stage acts as a mixer (Video D1, or Appendix F.5) and breaks up bubbles to a maximal size which can be related to the impeller rotation speed (Figure 4.5). The subsequent stages have a similar bubble size distribution, that varies through the flow passage, especially at low flow rates, where bubble coalescence is promoted by the recirculation cells in the diffuser (Figure 4.6).

For inlet gas fractions λ_0 higher than 5%, the flow regime, and particularly the gas fraction in the pump are unsteady. This is confirmed by the pressure and torque measurements which are closely correlated, and we can use them to estimate the gas fraction variation (Figure 4.9). The flow patterns correspond well to the measured head degradation, with bubbly flow corresponding to little head degradation, bubble accumulation to the onset of severe head degradation and radial separation to intermittent gas lock (Figure 4.17). The unsteadiness was mainly due to slugging at the pump inlet, which was worse when the pump was placed horizontally, but also existed in a vertical set-up. On some occasions the whole system (pump under test and booster pump) was unstable, as shown in Figure 4.12. This was more likely to happen at low flow rates in a vertical set-up, consistent with the approach derived in Section 1.3.3.

Chapter 5

Modelling gas head degradation for a mixed-flow impeller

We consider a pump impeller operating in gas-liquid conditions, and attempt to model the pressure reduction associated with the two-phase nature of the flow. The inlet gas fraction λ_0 is defined as the ratio of gas flow rate to the total volumetric flow rate at the impeller inlet, as opposed to the gas void fraction α which is a local quantity.

In Chapter 4, we noticed that the brutal performance degradation was occurring for $5\% < \lambda_0 < 7\%$, and that this coincided with the change in flow regime from a bubbly flow, where individual bubbles are easily identified, to bubbles accumulation in the impeller. This observation was similar to these reported in the literature (e.g. Barrios and Prado, 2011a), even though the critical gas fraction was lower ($\lambda_0 < 1\%$). We therefore focus our study on low gas fractions, and bubbly flows, where the gas bubbles do not interfere with each others. As the inlet gas fraction λ_0 increases, our model predicts a brutal increase in local gas fraction α, and a severe head degradation. At this point, the model assumptions are violated: the local gas fraction is too high to ensure a dispersed bubbly flow. We however have obtained an estimation of the critical gas fraction. This approach was also inspired by the observations made by Minemura and Uchiyama (1994): performing three-dimensional simulations of the two-phase flow in a mixed-flow impeller for increasing gas fractions, they showed that once a gas pocket is created in the impeller, the pump performance does not change significantly.

We derive two methods to compute the trajectory of a single bubble through a mixed-flow impeller: the Bubble Motion method (BM, Section 5.1.2) and the Equilibrium Velocity method (EV, Section 5.1.3). Both methods are based on a force balance, where the gas bubble has no impact on the liquid flow. A dimensional argument is used to estimate the maximal bubble size as a function of the fluids and flow properties (gas and liquid density, interfacial tension, impeller rotation speed and intake gas fraction). The liquid velocity field is determined in advance through three possible models: a parametric simplified three-dimensional flow field (S3D - Section 5.1.2), a parametric simplified one-dimensional flow field for a thin passage

(S2D - Section 5.2.1), and a more realistic one-dimensional flow field based on real geometrical features (R2D - Section 5.2.1). Any of these liquid flow fields can be combined with the methods cited above (BM, EV) to calculate the bubble trajectory, as presented in Table 5.2. Finally, we present in Section 5.2.4 a one-dimensional, two-fluid model (TF) that takes into account the coupling between the gas and liquid phases.

We first describe in Section 5.1 the motion of a single bubble, the forces exerted on it and estimate the maximal bubble size depending on the flow conditions. In Section 5.2, we detail the equations used to compute the pressure rise produced by the impeller in a two-phase flow. We implement the different methods in Section 5.3, for several geometries and operating parameters. Finally, the results given by the respective approaches are analysed in order to observe trends and validate the approximations that have been made in the previous sections.

5.1 Trajectory of a single spherical bubble

We investigate the trajectory of a spherical gas bubble of diameter d and mass M_b in a rotating liquid flow of constant density ρ_l and viscosity μ_l. The reference frame $\mathcal{R}_1$ is rotating at constant speed ω around its axis $\vec{e}_z$ in the laboratory frame of reference $\mathcal{R}_0$. We first derive the equation of motion of the bubble in any liquid rotating flow, and then we apply this equation to the flow in a pump impeller.

5.1.1 Gas bubble in a rotating liquid flow

We use an Eulerian description and cylindrical coordinates to describe the liquid flow field: $\vec{U}(r,\theta,z)$ in $\mathcal{R}_0$ and $\vec{u}(r,\varphi,z)$ in $\mathcal{R}_1$, where $\theta = \varphi + \omega t$. Its associated pressure field is $P_U(r,\theta,z)$. All the quantities used below are dimensional unless mentioned otherwise.

$$\vec{U}(r,\theta,z) = \vec{u}(r,\varphi,z) + \omega r \vec{e}_\theta \ .$$

Assuming no body forces on the liquid, the Euler equation in the inertial frame of reference $\mathcal{R}_0$ is

$$\rho_l \frac{D\vec{U}}{Dt} = -\vec{\nabla} P_U \ .$$

The bubble motion is described in a Lagrangian way by its position $\vec{y}(t)$, velocity $\vec{v}(t)$ and acceleration $\vec{a}(t)$ in the rotating frame $\mathcal{R}_1$,

$$\begin{cases} \vec{y}(t) = r\vec{e}_r + z\vec{e}_z \\ \vec{v}(t) = \dfrac{d\vec{y}(t)}{dt} = \dot{r}\vec{e_r} + r\dot{\varphi}\vec{e_\varphi} + \dot{z}\vec{e_z} \\ \vec{a}(t) = \dfrac{d\vec{v}}{dt}(t) = \left(\ddot{r} - r\dot{\varphi}^2\right)\vec{e}_r + \left(2\dot{r}\dot{\varphi} + r\ddot{\varphi}\right)\vec{e}_\varphi + \ddot{z}\vec{e}_z \ . \end{cases} \tag{5.1}$$

They correspond to the absolute position $\vec{Y}(t)$, velocity $\vec{V}(t)$ and acceleration $\vec{A}(t)$ in $\mathcal{R}_0$:

$$\begin{cases} \vec{V}(t) = \dfrac{d\vec{Y}(t)}{dt} = \vec{v}(t) + \vec{\omega} \times \vec{y}(t) \\ \vec{A}(t) = \dfrac{d\vec{V}(t)}{dt} = \dfrac{d\vec{v}(t)}{dt} + \vec{\omega} \times (\vec{\omega} \times \vec{y}(t)) + 2\vec{\omega} \times \vec{v} \ . \end{cases} \tag{5.2}$$

The forces acting on the bubble are gravity, and the stress resulting from the interaction with the liquid on its surface. The momentum equation in the inertial frame of reference $\mathcal{R}_0$ is:

$$M_b \frac{d\vec{V}}{dt}(t) = M_b \ \vec{g} + \iint_S \left(P_U \vec{n} + \mu_l \left(\vec{\nabla}\vec{U} + \left(\vec{\nabla}\vec{U}\right)^T \right) \cdot \ \vec{n} \right) dS \ .$$

In order to express the integral on the right hand side, it is assumed that the history effects (Basset force) are negligible compared to the viscous drag: $\left| d(\vec{V}-\vec{U})/dt \right| \ll |\vec{V}-\vec{U}|^2/d$.

The undisturbed liquid flow field at the bubble centre $\vec{W}(r,\theta,z)$ is used to express the force balance on the bubble, as described by Auton et al. (1988). All the forces are expressed so that they can be considered to act on the bubble centre.

$$\begin{aligned} (M_b + M_l C_v) \frac{d\vec{V}}{dt}(t) = \ & M_l (1 + C_v) \left. \frac{D\vec{W}}{Dt} \right|_{Y(t)} + \ C_d \frac{\rho_l S}{2} \left(\vec{W} - \vec{V} \right) \left| \vec{W} - \vec{V} \right| \\ & + C_l M_l \left(\vec{W} - \vec{V} \right) \times \left(\vec{\nabla} \times \vec{W} \right) + (M_b - M_l) \, \vec{g} \end{aligned} \tag{5.3}$$

where $M_l = \rho_l \pi d^3/6$ is the mass of liquid displaced by the bubble, M_b is the bubble mass $M_b = \rho_g \pi d^3/6$, and S its cross-sectional area $S = \pi d^2/4$.

The coefficients C_d, C_l and C_v are respectively called the drag, lift and added mass coefficients and depend on the bubble shape and size, but also on the interfacial tension between the gas and the liquid and the local properties of the undisturbed flow. A review of the forces acting on a gas bubble at finite bubble Reynolds number has been written by Magnaudet and Eames (2000) and is summarised in Appendix B.

We assume that the bubble stays spherical, and its diameter is only affected by the change of pressure through an isothermal transformation. If the initial bubble diameter is d_0 for the initial pressure P_0, then the bubble diameter under the local static pressure p^s is $d = d_0 \left(P_0/p^s\right)^{1/3}$.

Finally we use the relations (5.2) to write (5.3) in the rotating frame of reference $\mathcal{R}_1$,

$$
\begin{aligned}
(\rho_g + \rho_l C_v)\left(\frac{d\vec{v}}{dt}(t) + 2\ \vec{\omega}\times\vec{v}\right) &= (\rho_g - \rho_l)\left(\vec{g} - \vec{\omega}\times(\vec{\omega}\times\vec{r})\right) \\
&+ \rho_l\,(1+C_v)\left(\left.\frac{D\vec{w}}{Dt}\right|_{\vec{y}(t)} + 2\ \vec{\omega}\times\vec{w}\right) \\
&+ C_d\frac{3\rho_l}{4d}\,(\vec{w}-\vec{v})\,|\vec{w}-\vec{v}| \\
&+ \rho_l C_l\,(\vec{w}-\vec{v})\times\left(\vec{\nabla}\times\vec{w} + 2\omega\vec{e}_z\right)\ .
\end{aligned}
$$

The following non-dimensional parameters are defined:

$$
\begin{aligned}
\varepsilon &= {}^{d}/_{R_2} \qquad & Eu &= \frac{P_0}{\rho_l\omega^2 R_2^2} \\
\xi &= {}^{\rho_g}/_{\rho_l} \qquad & Ri &= {}^{g}/_{\omega R_2^2}\ .
\end{aligned}
$$

Ri and Eu are Euler and Richardson numbers, adapted to rotating flows. All other variables are normalised using R_2, ω and ρ_l, and are noted with a star superscript, for example: $r^* = r/R_2$.

The normalised bubble diameter ε and density ratio ξ at the pump inlet are noted ε_0 and ξ_0 and we have:

$$
\xi = \xi_0\ \frac{p^s}{Eu} \qquad \text{and} \qquad \varepsilon = \varepsilon_0\left(\frac{Eu}{p^s}\right)^{1/3}\ .
$$

The general non-dimensional equation of motion in the rotating frame of reference $\mathcal{R}_1$ is

$$
\begin{aligned}
(\xi + C_v)\left(\frac{d\vec{v}^*}{dt^*}(t^*) + 2\ \vec{e}_z\times\vec{v}^*\right) &= (\xi-1)\left(-Ri\ \vec{e}_z - \vec{e}_z\times(\vec{e}_z\times\vec{r}^*)\right) \\
&+ (1+C_v)\left(\left.\frac{D\vec{w}^*}{Dt^*}\right|_{\vec{y}^*(t^*)} + 2\ \vec{e}_z\times\vec{w}^*\right) \\
&+ \frac{3C_d}{4\varepsilon}\,(\vec{w}^*-\vec{v}^*)\,|\vec{w}^*-\vec{v}^*| \\
&+ C_l\,(\vec{w}^*-\vec{v}^*)\times\left(\vec{\nabla}^*\times\vec{w}^* + 2\vec{e}_z\right)\ .
\end{aligned}
\tag{5.4}
$$

We note (r^*, φ, z^*) the bubble coordinates in the rotating frame of reference, and its velocity and acceleration as per (5.1). If the flow field $\vec{w}^*$ is axisymmetric and steady, and neglecting the effect of gravity as $Ri << 1$, we obtain

$$
\begin{aligned}
(\xi + C_v)\left(\frac{d\vec{v}^*}{dt^*}(t^*) + 2\ \vec{e}_z \times \vec{v}^*\right) &= (\xi - 1)\, r^* \vec{e}_r \\
&+ (1 + C_v)\left(\left(\vec{w}^* \cdot \vec{\nabla}^*\right)\vec{w}^* + 2\ \vec{e}_z \times \vec{w}^*\right) \\
&+ \frac{3C_d}{4\varepsilon}\,(\vec{w}^* - \vec{v}^*)\,|\vec{w}^* - \vec{v}^*| \\
&+ C_l\,(\vec{w}^* - \vec{v}^*) \times \left(\vec{\nabla}^* \times \vec{w}^* + 2\vec{e}_z\right)\ .
\end{aligned}
\tag{5.5}
$$

5.1.2 Motion of a gas bubble through an impeller (BM)

We only consider the bladed portion of the impeller which is responsible for the largest part of the pressure rise, and can be approximated by a rotating annulus of increasing diameter, whose inner and outer boundaries are truncated cones, as represented in Figure 5.1.

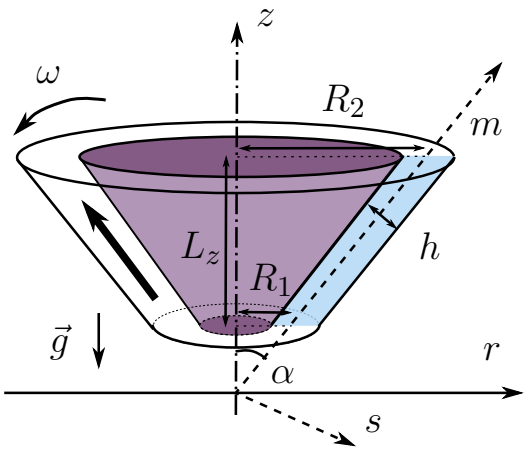

Figure 5.1 Sketch of the flow geometry: an annulus whose diameter increases in the flow direction.

The annulus has a constant width h and an increasing mean radius $R(Z) = Z \tan\alpha$, where R and Z are the coordinates of the impeller meanline $\mathcal{M}$ (see Appendix A for more details). The special cases $\alpha = \pi/2$ or $\alpha = 0$ are considered separately and correspond to purely radial or purely axial geometries. We use the term "relative velocity" to designate the undisturbed liquid velocity field $\vec{w}$ in the rotating frame of reference $\mathcal{R}_1$, as opposed to the term "absolute velocity" for the flow field $\vec{W}$ expressed in the laboratory frame of reference $\mathcal{R}_0$.

The relative velocity can be expressed using a cylindrical coordinate system (r, θ, z). As shown in Figure 5.1, rotating the base $(\vec{e_z}, \vec{e_r})$ by an angle α around $\vec{e_\varphi}$ gives the new base $(\vec{e_m}, \vec{e_s})$ with the associated coordinates (m, s). m is called the meridional coordinate and s the span-wise coordinate, defined by

$$\begin{cases} \vec{e_m} = \sin\alpha\ \vec{e_r} + \cos\alpha\ \vec{e_z} \\ \vec{e_s} = \cos\alpha\ \vec{e_r} - \sin\alpha\ \vec{e_z} \end{cases}$$

The total volumetric flow rate through the annulus is Q. We assume that the absolute velocity field $\vec{W}$ is axisymmetric, and that the meridional velocity is uniform across s, and the relative tangential velocity follows constant angle streamlines, represented by a free vortex of circulation $\Gamma_0 = -Q\cos\beta/h$. The proof is given in Appendix A.2.

$$\vec{W}(r,z) = \frac{Q}{2\pi h m \sin\alpha}\ \vec{e}_m + \left(\frac{\Gamma_0}{2\pi m \sin\alpha} + \omega r\right)\vec{e}_\theta, \tag{5.6}$$

where $m = r\sin\alpha + z\cos\alpha$. We will see below that β corresponds to the flow angle defined in Chapter 1, between the relative velocity and the opposite of the local tangential vector.

We define the non-dimensional parameters based on the impeller outer radius R_2, rotation speed ω and liquid density ρ_l. The Reynolds number is based on the pump radius and rotation speed, density ρ_l and viscosity μ_l. Φ is the flow coefficient, defined by (1.4).

$$\begin{aligned} \Phi &= Q/\omega R_2^3 \\ Re &= \rho_l \omega R_2^2/\mu_l\ . \end{aligned} \tag{5.7}$$

The other parameters and variables are also normalised using the length scale R_2, the time scale $1/\omega$ and the mass ρ_l/R_2^3. For the rest of this section, all quantities are assumed non-dimensional without any change in notation. In particular, we write $\vec{w}$ instead of $\vec{w}^*$ and r instead of r^*, except for the inlet radius noted $r_1 = R_1/R_2$ which is sometimes called the tip to hub ratio. The non-dimensional outlet radius is $r_2 = 1$.

The non-dimensional liquid velocity in the rotating frame of reference is

$$\vec{w}(r,z) = \frac{\Phi}{2\pi h m \sin\alpha}\left(\vec{e}_m - \cot\beta\ \vec{e}_\varphi\right)\ . \tag{5.8}$$

Assuming that the passage height is small compared to the pump diameter ($h\cos\alpha << 1$), we can make the approximation $r \approx m\sin\alpha$. The velocity field therefore describes an axisymmetric flow on a conical surface $R = Z\tan\alpha$ with streamlines forming logarithmic spirals of constant angle β relative to the tangential direction $\vec{e}_\varphi$, as shown on Figure 5.2. We verify that this approximation is valid in Section 5.5.1.

We define "forces" to group and analyse the terms on the right hand side of (5.11), even though not all of them correspond to a physical phenomenon. Some terms depend on the position of the bubble only, others on both its position and velocity.

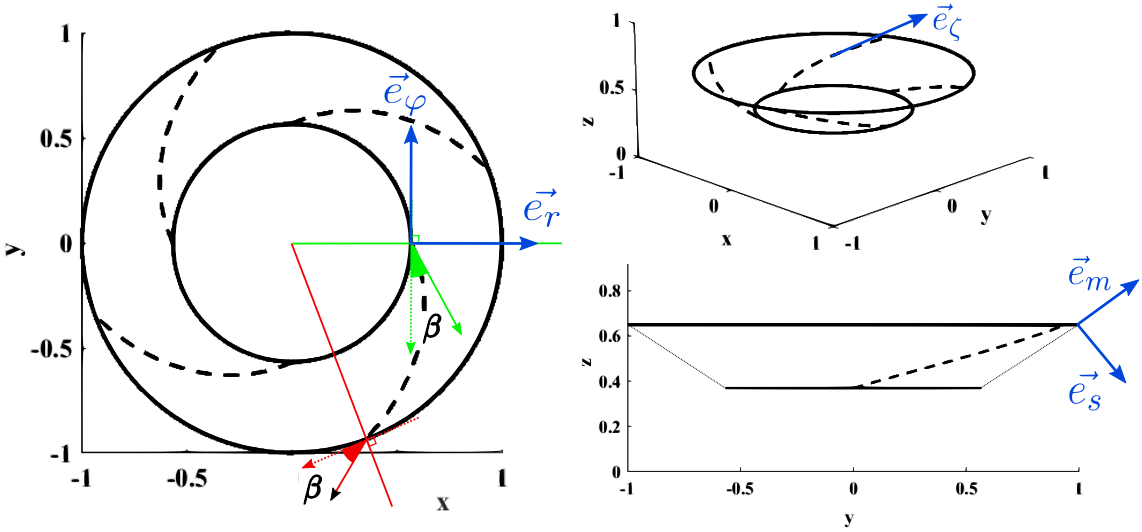

Figure 5.2 Top, side and perspective view of the streamlines (dashed lines) on a conical surface. The flow angle β is constant along logarithmic streamlines, (x, y, z) is the Cartesian coordinate system associated with (r, φ, z) in the rotating frame of reference.

$$\begin{aligned}
\vec{F}_{cent} &= (\xi - 1)\, r\vec{e}_r & \vec{F}_{cori} &= 2\,(1 + C_v)\ \vec{e}_z \times \vec{w} \\
\vec{F}_{lift} &= C_l\,(\vec{w} - \vec{v}) \times \left(\vec{\nabla} \times \vec{w} + 2\vec{e}_z\right) & \vec{F}_{flow} &= (1 + C_v)\left(\vec{w} \cdot \vec{\nabla}\right)\vec{w} \\
\vec{F}_{drag} &= \frac{3C_d}{4\varepsilon}\,(\vec{w} - \vec{v})\,|\vec{w} - \vec{v}|
\end{aligned} \tag{5.9}$$

We write the bubble acceleration as the sum $\vec{a} = \vec{a}_0 + \vec{a}_1$, where

$$\begin{aligned}
\vec{a}_0 &= \ddot{r}\vec{e}_r + \ddot{z}\vec{e}_z + r\ddot{\varphi}\vec{e}_\varphi \\
\vec{a}_1 &= 2\dot{r}\,(\dot{\varphi} + 1)\,\vec{e}_\varphi - r\dot{\varphi}\,(\dot{\varphi} + 2)\,\vec{e}_r\ .
\end{aligned}$$

$\vec{a}_0$ is called the inertial acceleration, and $\vec{a}_1$ the Coriolis acceleration. We will show that we can neglect $\vec{a}_0$ but not $\vec{a}_1$ (see Section 5.1.3 and Figure 5.13).

Centrifugal force

The Centrifugal term refers to the centrifugal acceleration defined in the rotating frame of reference. For $\xi < 1$, it pushes the bubble toward the rotation axis. It only depends on the bubble radial position and the density ratio between the gas and the liquid.

$$\vec{F}_{\text{cent}} = (1 - \xi)\, r\ \vec{e}_r$$

Coriolis force

The Coriolis term also refers to the Coriolis force associated with the liquid acceleration in the rotating frame of reference. It pushes the bubble toward the left of the liquid

streamlines.

$$\vec{F}_{\text{cori}} = (1+C_v)\,\frac{\Phi}{\pi h r}\,[\cot\beta\ \vec{e}_r + \sin\alpha\ \vec{e}_\varphi]$$

For backward leaning blades ($\cot\beta > 0$) its radial component brings the gas outwards, counteracting the centrifugal force and is independent of the meridional angle α, while its tangential component pushes the gas in the direction of rotation and vanishes for an axial design ($\alpha = 0°$). The Coriolis acceleration on the bubble itself is included in $\vec{a}_1$

Flow force

The Flow term corresponds to the pressure gradient induced by the expansion of the cross-flow area along the flow passage.

$$\vec{F}_{\text{flow}} = -\,(1+C_v)\left(\frac{\Phi}{2\pi h r}\right)^2\left[\frac{\sin\alpha}{r}\vec{e}_m + \frac{\cot^2\beta}{r}\vec{e}_r\right]$$

Its meridional component opposes the progression of the bubble through the passage and vanishes if the flowing area is constant, for example for an axial design with constant passage height. The radial component is associated to the flow angle and pushes the gas bubble toward the pump axis. For straight streamlines (radial blades, $\cot\beta = 0$), this term disappears. From (5.8) and with the approximation $r \approx m\sin\alpha$, we have $w_m = \Phi/2\pi h r$ so that the flow force proportional to $w_m dw_m/dr$.

Drag force

The drag term opposes the velocity difference between the gas bubble and the surrounding liquid.

$$\vec{F}_{\text{drag}} = \frac{3C_d}{4\varepsilon}\,|\vec{v_s}|\,\vec{v_s}$$

where

$$\vec{v}_s = \vec{w} - \vec{v} = \left(\frac{\Phi}{2\pi h\ r} - \dot{m}\right)\vec{e}_m - \left(\frac{\Phi\cot\beta}{2\pi h r} + r\dot{\varphi}\right)\vec{e}_\varphi + \dot{s}\vec{e}_s$$

It depends on the drag coefficient C_d which depends itself on the bubble Reynolds number $Re_b = Re\ \varepsilon\,|\vec{w} - \vec{v}|$.

The correlation $C_d\,(Re_b)$ derived by Clift et al. (1978), is used to define $\vec{F}_{\text{drag}}$:

$$\vec{F}_{\text{drag}} = \begin{cases} \dfrac{18}{Re\ \varepsilon^2}\ \vec{v}_s & \text{if } |\vec{v}_s| \leq \dfrac{6}{Re\ \varepsilon} \\ \dfrac{18}{Re\ \varepsilon^2}\left(1+0.15\,(Re\ \varepsilon\,|\vec{v}_s|)^{0.687}\right)\vec{v}_s & \text{if } |\vec{v}_s| \leq \dfrac{1000}{Re\ \varepsilon} \\ \dfrac{0.33}{\varepsilon}\,|\vec{v}_s|\,\vec{v}_s & \text{if } |\vec{v}_s| > \dfrac{1000}{Re\ \varepsilon} \end{cases} \tag{5.10}$$

This expression is illustrated in Figure 5.3, with typical values for Re and ε. As long as $\vec{w}\cdot\vec{v} > 0$, we have $|\vec{v}_s| < |\vec{w}| = \frac{\Phi}{2\pi hr\sin\beta}$ and therefore

$$\left|\vec{F}_{drag}\right| < \frac{0.33}{\varepsilon}\left(\frac{\Phi}{2\pi hr\sin\beta}\right)^2 .$$

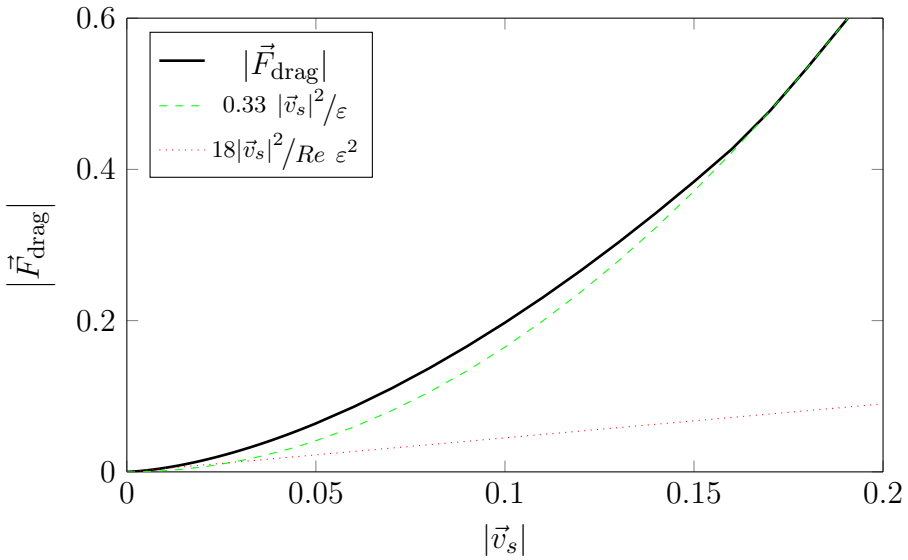

Figure 5.3 Drag magnitude for $Re = 1\cdot 10^5$ and $\varepsilon = 0.02$, compared with the approximations $C_d = 0.44$ (dashed line) and $C_d = 24/Re_b$ (dotted line).

As shown on Figure 5.3, there is a large difference between the Stokes law (red dotted line, $18|\vec{v_s}|/Re\varepsilon^2$) and the drag force given by (5.10) shown by a black solid line. The effect of using a constant drag coefficient (green dashed line) is important when the velocity difference between the gas bubble and the unperturbed liquid flow is small. We will investigate in Section 5.5.1 the impact of approximating C_d by a constant ($C_d = 0.44$) or, on the contrary, using Stokes law ($C_d = 24/Re_b$), for all Re_b.

Lift force

The lift force is usually neglected for uniform flows but should be taken into account in rotational flows. It corresponds to the force normal to the flow relative to the bubble,

due to the liquid flow local vorticity. More details about the lift and drag forces are given in Appendix B. We consider the lift force:

$$\vec{F}_{lift} = -2C_l \left[\left(\frac{\Phi \cot\beta}{2\pi hr} + r\dot{\varphi} \right) \sin\alpha \ \vec{e}_m + \left(\frac{\Phi}{2\pi hr} - \dot{r} \right) \vec{e}_\varphi \right] + C_l \cos\alpha \left(\frac{\Phi \cot\beta}{2\pi hr} + r\dot{\varphi} \right) \left(\frac{\Phi \cot\beta}{2\pi hr^2} - 2 \right) \vec{e}_s.$$

The meridional component is proportional to $\sin\alpha$ while the spanwise component is proportional to $\cos\alpha$. Both are proportional to $w_\varphi - v_\varphi$. We will also check in Section 5.5.1 the effect of neglecting this force.

5.1.3 Equilibrium Gas Velocity (EV)

We can calculate an "Equilibrium Gas Velocity" by setting $\vec{a}_0 = \ddot{r}\vec{e}_r + \ddot{z}\vec{e}_z + r\ddot{\varphi}\vec{e}_\varphi = \vec{0}$ in (5.5). This corresponds to the theoretical velocity achieved by a bubble that would indefinitely stay at a fixed position. Even though this is not achievable in practice, it provides a useful insight. This leads to a non-differential system of equations on $(\dot{r}, \dot{\varphi}, \dot{z})$, at each location (r, φ, z). In particular, it does not require an initial condition, such as that required for the trajectory equation developed in Section 5.1.

$$\begin{aligned} (\xi + C_v) \left[2\dot{r} \left(\dot{\varphi} + 1 \right) \vec{e}_\varphi \ - r\dot{\varphi} \left(\dot{\varphi} + 2 \right) \vec{e}_r \right] = (\xi - 1) \, r\vec{e}_r \\ + (1 + C_v) \left(\left(\vec{w} \cdot \vec{\nabla} \right) \vec{w} + 2 \ \vec{e}_z \times \vec{w} \right) \\ + \frac{3C_d}{4\varepsilon} \left(\vec{w} - \vec{v} \right) |\vec{w} - \vec{v}| \\ + C_l \left(\vec{w} - \vec{v} \right) \times \left(\vec{\nabla} \times \vec{w} + 2\vec{e}_z \right) \end{aligned} \tag{5.11}$$

5.1.4 Bubble size

This Section uses both dimensional and non-dimensional quantities. The nature of the quantities used will be indicated where necessary.

In our analysis, the bubble diameter is assumed to be known at the impeller inlet, and then to only vary with the local pressure. As we have seen in Chapter 2, the bubble size distribution varies with operational parameters, and also with the location in the pump: the bubbles tend to coalesce in the diffuser (especially at low flow rates, when recirculation cells are present) and to break up at the impeller tip, depending on the rotation speed. In order to compare two impeller designs, we need to know how good they are not only at handling bubbles of a specific size, but also at breaking bubbles into a more homogeneous mixture.

In this Section, we use a dimensional argument to predict the maximal bubble size, based on the break-up at the impeller tip (perfect mixer) or in the flow passage

(channel flow). When the local gas fraction is so low that bubble coalescence is negligible ($\alpha < \alpha_c$), the bubble size distribution is likely to be very narrow. However, the bubble distribution becomes wider as the local gas fraction increases. As the largest gas bubbles are the more likely to becomes trapped in the impeller, the maximal bubble size is the most relevant to gas handling. We therefore focus on the maximal bubble size rather than on a distribution.

To estimate the bubble size for large gas fraction, we use a simple quadratic rule filling the gap between the critical gas fraction α_c, and $\alpha = 1$. This is however a very rough estimation and would require an experimental verification.

Maximal bubble size

Following the analysis from Hesketh et al. (1991) and Levich (1962), the maximal bubble size can be determined using a Weber number defined as the ratio of the internal pressure due to the turbulent fluctuations and the capillary pressure of the deformed bubble.

$$We = \frac{\tau\ d}{\sigma}\left(\frac{\rho_g}{\rho_l}\right)^{1/3} \tag{5.12}$$

where τ is the dynamic pressure force on the bubble, σ the interfacial surface tension between the two phases and ρ_g and ρ_l the gas and liquid densities.

For a turbulent flow the dynamic pressure force τ on a bubble of diameter d depends on the turbulent energy dissipation ϵ and is given by Hinze (1955) and Levich (1962) as:

$$\tau = 2\rho_l\left(\epsilon\ d\right)^{2/5}$$

We estimate the average energy dissipation for two extreme cases: (a) the pump working as a perfect mixer and all its energy being used to break-up bubbles, or (b) the pump is passive regarding the bubbles are they are only broken up by the turbulent energy of the flow considered as a channel flow through the impeller passages.

(a) - In a pump rotating with no flow (working as a perfect mixer), the average energy dissipation can be expressed as:

$$\overline{\epsilon} = \frac{\text{Impeller Power}}{\text{Fluid mass}} \approx \frac{\Pi\ \rho_l\ \omega^3\ R_2^5}{\rho_l\ \pi\ R_2^3\ h^*\left(1-r_1^{*2}\right)} = \frac{\Pi\ \omega^3\ R_2^2}{\pi\ h^*\left(1-r_1^{*2}\right)}.$$

where Π is the non-dimensional power produced by the impeller rotation, h^* the non-dimensional passage height, R_2 the dimensional impeller outer radius and r_1^* the non-dimensional inlet radius. In absence of losses, all the power brought by the shaft is converted into pressure and flow rate ($\eta = 1$ in (1.4)). We have therefore $\Pi = \Phi\left(1-r_1^{*2}\right)$, and finally $\overline{\epsilon} \approx \Phi\omega^3 R_2^2/\pi h^*$

As per Hesketh et al. (1991), the maximal bubble diameter is achieved for the critical value $We_{crit} = 1.1$, so we have:

$$d_{mixer} = \omega^{-6/5} \left[\frac{We_{crit}^3 \ \sigma^3 \ h^{*2} \ \pi^2}{8 \ \Phi^2 \ \xi_0 \ \rho_l^3 \ R_2^4} \right]^{1/5}$$

(b) - In the impeller and diffuser passages, the flow can be considered as a simple pipe flow. According to Blasius (1913) the energy dissipation through turbulence in a smooth pipe is:

$$\bar{\epsilon} = \frac{2fw^3}{D_h} = \frac{0.158 \ Re_h^{-0.25} \ w^3}{D_h}$$

where $f = 0.079 \ Re_h^{-0.25}$ is a friction factor, Re_h the passage Reynolds number, w the dimensional relative velocity and D_h the dimensional passage diameter. We have $w = \Phi\omega R_2 / 2\pi h^*$, $D_h = R_2 h^*$, and $Re_h = \rho_l D_h w / \mu_l$ where h^* is the non-dimensional passage height.

This leads to a maximal bubble diameter:

$$d_{pipe} = 1.38 \ \omega^{-1.1} \left(\frac{2\pi}{\Phi} \right)^{1.1} \frac{1}{\mu_l^{0.1} \ \rho_l^{0.5}} \left[\frac{We_{crit}^3 \ \sigma^3 h^3}{R_2^3 \ \xi_0} \right]^{1/5}$$

The two proposed maximal diameters have a similar functionality in ω, We_{crit} and σ, but are different in magnitude.

We introduce the non-dimensional parameter B, ratio of the centrifugal acceleration to the surface tension effects, in order to write the maximal bubble size $\varepsilon = d/R_2$ in non-dimensional terms.

$$B = \frac{\rho_l \ \omega^2 \ R_2^3}{\sigma} \tag{5.13}$$

Finally,

$$\begin{cases} \varepsilon_{mixer} = \left(\dfrac{We_{crit}^3 \pi^2 h^{*2}}{8B^3 \ \Phi^2 \xi_0} \right)^{1/5} \\ \\ \varepsilon_{pipe} = 1.38 \ Re^{0.1} \left(\dfrac{2\pi}{\Phi} \right)^{1.1} \left(\dfrac{We_{crit}^3 \ \ h^{*3}}{B^3 \ \xi_0} \right)^{1/5} \end{cases} \tag{5.14}$$

where Re is the pump Reynolds number as defined in (5.7).

For the impeller design and conditions studied in Chapter 2, we obtain the maximal diameters $d_{mixer} = 0.3$ mm and $d_{pipe} = 5.8$ mm. The magnitude order is consistent with the bubble sizes observed at the impeller tip in the experiment, for low gas fraction (less than 5%) which was less than 1 mm at the impeller tip, and from 0.5 to 5 mm

in the impeller and diffuser channels. The predicted value ($d_{max} = 0.3$ mm at low gas fraction) does not correspond to the observation (1 mm). However, if we take the bubble size at 20 Hz as a reference, Table 5.1 shows that the functionality in ω given by our analysis is verified.

Table 5.1 Comparison between the observed bubble size and the predicted functionality in $\omega = 2\pi f$. The experimental values are from Figure 4.5. The bubble size is given in mm.

f	Experiment	$d_{max} \propto \omega^{-1.1}$	$d_{max} \propto \omega^{-1.2}$
20 Hz	1	1	1
25 Hz	0.8	0.78	0.77
30 Hz	0.6	0.64	0.61

A more accurate measurement of the bubble size would be needed to confirm this trend over different flow conditions, rotation speeds and fluids properties.

Large gas fraction

As the gas fraction increases, gas bubbles can coalesce. For two bubbles to coalesce, they first need to collide, therefore the rate of coalescence is linked to the average distance between bubbles. We draw a simple model of this phenomenon by assuming a mono-disperse bubble size distribution, where coalescence can happen if the bubbles are on average less than λ_d diameters away from each other. This value the only adjustable parameter in our analysis.

We define l as the dimensional distance between two bubbles of diameter d. For a local gas fraction α, we have:

$$l = d\left(2\left(\frac{4\pi}{3\alpha}\right)^{1/3} - 1\right)$$

Therefore, the gas fraction α_c above which the bubbles start to coalesce ($l = 5d$) is $\alpha_c \approx 0.15$. For $\alpha > \alpha_c$, we assume that the bubble size increases quadratically from ε_{mixer} up to ε_{pipe}, ensuring a smooth transition to the constant region $\alpha < \alpha_c$ to 1, where $\varepsilon = \varepsilon_{pipe}$. In this work, we chose $\lambda_d = 5$ but this value could be fine-tuned in order to fit experimental results better. Similarly, a different profile could be further developed, based on calibration experiment, as long as the same profile is used to compare different pump geometries.

$$\varepsilon = \frac{\varepsilon_{pipe} - \varepsilon_{mixer}}{(\alpha_c - 1)^2}(\alpha - \alpha_c)^2 + \varepsilon_{mixer} \tag{5.15}$$

Figure 5.4 shows the evolution of bubble size in:

a. Flow visualisation conditions: $f = 20$ Hz, $\rho_{g0}/\rho_l = 0.001$, $\sigma = 72$ mN/m.

b. Standard test conditions: $f = 60$ Hz, $\rho_{g0}/\rho_l = 0.004$, $\sigma = 72$ mN/m

c. Production conditions: $f = 60$ Hz, $\rho_{g0}/\rho_l = 0.075$, $\sigma = 15$ mN/m

The higher the pump angular rotation speed $\omega = 2\pi f$, and the closer the gas and liquid density, the smaller the bubbles. The interfacial surface tension σ also has a large impact on the bubble size, and it can be greatly affected by the presence of surfactants or small solid particles in the flow (see Appendix B.1.4).

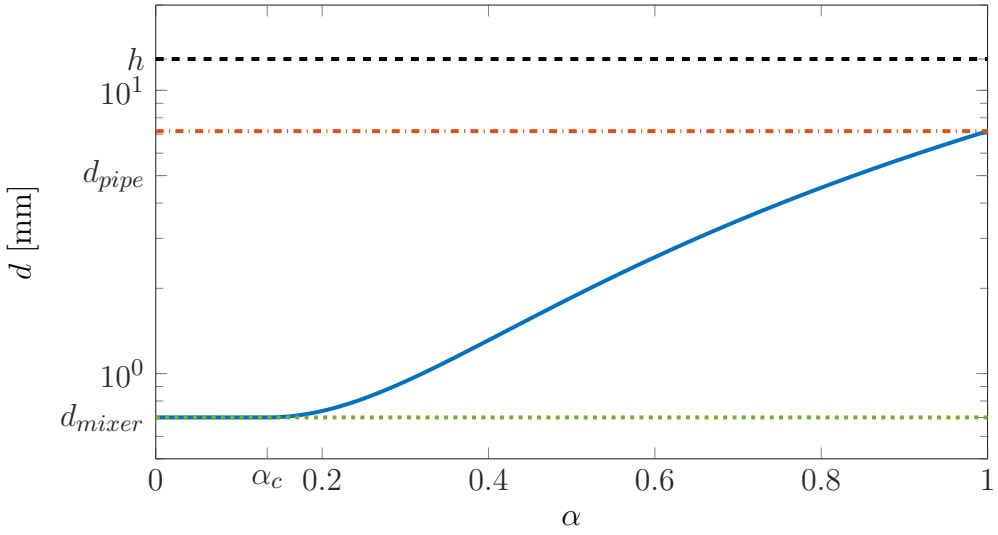

Figure 5.4 Maximal bubble size as a function of local gas fraction (blue, solid line). $d_{mixer} = 0.7$ mm is represented in green dotted line, $d_{pipe} = 5$ mm in red semi-dashed line, and h, the passage height in dashed black line.

5.2 Pressure rise for a two-phase flow

Only non-dimensional quantities are used in this section.

The pressure generation in a centrifugal impeller for a single phase flow is covered in Section 1.1.4. When bubbles of finite size travel with a lower meridional velocity than the liquid phase, the local gas volume fraction α is higher than the intake gas fraction λ_0. Both of these quantities are defined in (1.9).
In this Section, we describe the homogeneous flow in an impeller as a function of a single variable m: the streamline coordinate, defined as the length along the meanline $\mathcal{M}$ (see Figure A.4). This leads to a simple way of computing the pressure produced by the impeller, depending on the fluid density ρ. We then use the equation of motion (5.5) to define an "Equilibrium Bubble Velocity" throughout the impeller and we compute the resulting local gas fraction α. Finally, based on the undisturbed homogeneous flow field $\vec{w}$, and the local mixture density ρ_r, we compute the pressure rise in the impeller for a two-phase flow. This method will be used in Section 5.4 to estimate the gas handling performance of different impeller designs for a range of operating conditions. Figure 5.5 gives a schematic view of the steps involved.

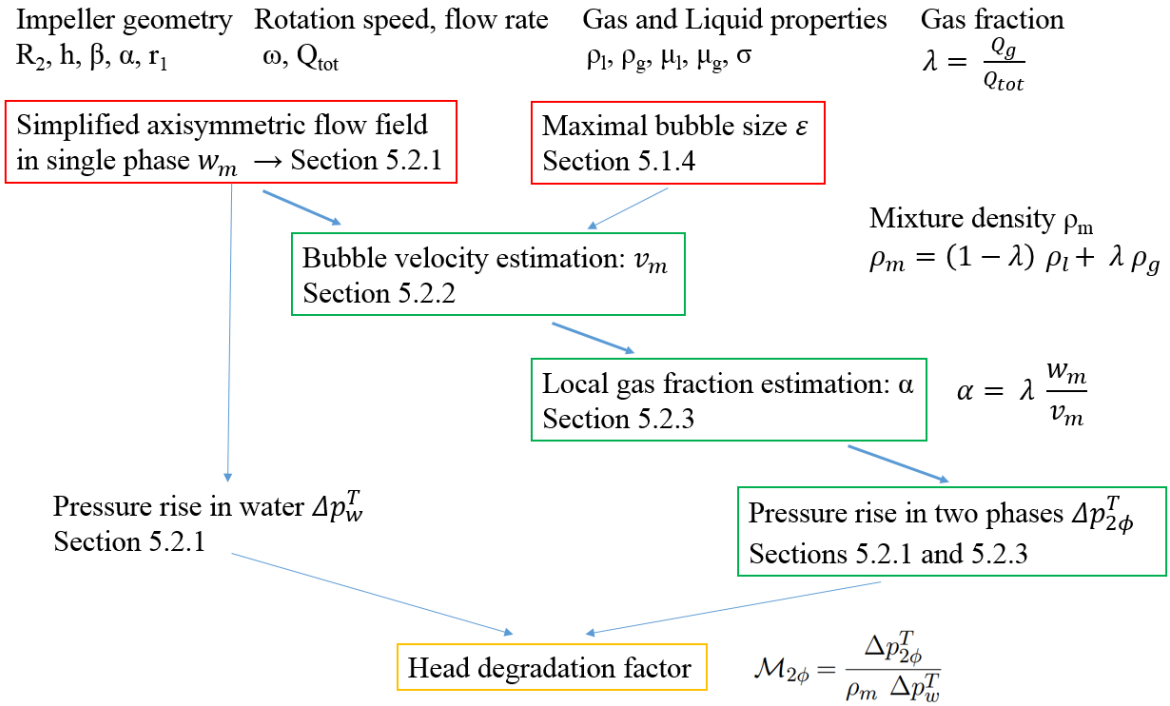

Figure 5.5 Flowchart summary of the equilibrium velocity method, used with a simplified parametric flow field (EV-S2D). The top row represents the required inputs. The red boxes (simplified flow field and maximal bubble size), are the preliminary computations which can be run independently, while the green boxes are the heart of the method described in this Section.

We also describe a two-fluid model as developed by Minemura et al. (1998) and Sherwood (2005), that takes into account the acceleration of the liquid phase when the local gas fraction increases. We will compare these two methods in Section 5.5.

5.2.1 Homogeneous flow through an impeller

We first present two ways of describing the homogeneous flow in an impeller using a one-dimensional model, using a very simplified geometry and then a more refined model. More details are given in Appendix A. We rescale the streamwise coordinate to have $m^* = 0$ at the inlet of the bladed passage inlet and $m^* = 1$ at the outlet.

Parametric flow field for a simplified geometry (S2D)

With the simplified flow described in Section 5.1.2 and using the approximation $r \approx m \sin\alpha$, we only need five parameters to describe the flow: the meridional angle α, blade angle β, the inlet radius r_1, corrected passage height $\widetilde{h}$ and flow coefficient Φ (as defined in (1.4)). The corrected passage height takes into account the blockage due to the blade thickness and is defined as $\widetilde{h} = h - N t_N$, where N is the number of blades and t_N the normalised blade thickness. The normalised streamwise coordinate is related to the meridional coordinate m through:

$$m^* = \frac{m - m_1}{m_2 - m_1}$$

where $m_1 = r_1 / \sin\alpha$ and $m_2 = 1/\sin\alpha$.

The meridional and blade angles are constant along the meanline $\mathcal{M}$ and we have $\tan\alpha = dR/dZ = w_r/w_z$ and $\tan\beta = w_m/w_\phi$.

Finally the relative velocity field is:

$$\begin{cases} w_m = \dfrac{\Phi}{2\pi h\ R} \\ w_\varphi = -\dfrac{\Phi \cot\beta}{2\pi h\ R} \end{cases} \tag{5.16}$$

The static pressure is computed from the differential equation:

$$\boxed{\frac{dp}{dr} = \rho \left[\frac{1}{r} \left(\frac{\Phi}{2\pi R h \sin\beta} \right)^2 + r \right]} \tag{5.17}$$

Ideal flow based on a real geometry (R2D)

We use a description of the impeller based on a real geometry to characterise the flow field. The information is provided by the pump manufacturer and we use the values

of the passage area $A_p(m^*)$, blade angle $\beta(m^*)$ and meanline radius $R(m^*)$ and axial coordinate $Z(m^*)$ at mid-span, in addition with the design flow coefficient Φ.

$$\begin{cases} w_m = \dfrac{\Phi \sin\beta}{A_p} \\ w_\varphi = -\dfrac{\Phi \cos\beta}{A_p} \end{cases} \tag{5.18}$$

The passage area A_p takes into account the flow angle and the blockage due to the blades. It relates to the total magnitude of the relative velocity: $A_p = A\sin\beta = \Phi/w$, where $w = \sqrt{w_m^2 + w_\phi^2}$.

The static pressure is computed from the differential equation:

$$\boxed{\frac{dp}{dr} = \rho\left(\frac{\Phi^2}{A_p^3}\frac{dA_p}{dr} + r\right)} \tag{5.19}$$

We show in Figure 5.6, the comparison between the simplified parametric flow field and the real values for the pump impeller used in Chapter 2, or Design E according to Table 5.3.

The main flow characteristics present some discrepancies, especially the meridional velocity, but the main features (order of magnitude and global trend) are preserved. A finer description of the velocity field in single phase can be obtained using commercial numerical packages.

5.2.2 Equilibrium Gas Velocity

Projecting (5.11) on $\vec{e}_m$ and $\vec{e}_\varphi$ reduces the system to two equations with two unknowns $\dot{r}$ and $\dot{\varphi}$ along a single variable r.

$$\begin{cases} -r\dot{\varphi}\,(\xi + C_v)\,(\dot{\varphi}+2)\sin\alpha = (1+C_v)\,\dfrac{\Phi\sin\alpha}{2\pi hr}\left[2\cot\beta - \dfrac{\Phi\left(1+\cot^2\beta\right)}{2\pi hr^2}\right] \\ \qquad\qquad + \dfrac{3C_d}{4\varepsilon}\left(\dfrac{\Phi}{2\pi hr} - \dfrac{\dot{r}}{\sin\alpha}\right)|\vec{w}-\vec{v}| - 2C_l\sin\alpha\left(\dfrac{\Phi\cot\beta}{2\pi hr} + r\dot{\varphi}\right) \\ \qquad\qquad + (1-\xi)\,r\sin\alpha \\ 2\dot{r}\,(\xi+C_v)\,(\dot{\varphi}+1) = -(1+C_v)\,\dfrac{\Phi\sin\alpha}{\pi hr} \\ \qquad\qquad - \dfrac{3C_d}{4\varepsilon}\left(\dfrac{\Phi\cot\beta}{2\pi hr} + r\dot{\varphi}\right)|\vec{w}-\vec{v}| - 2C_l\left(\dfrac{\Phi\sin\alpha}{2\pi hr} - \dot{r}\right) \end{cases} \tag{5.20}$$

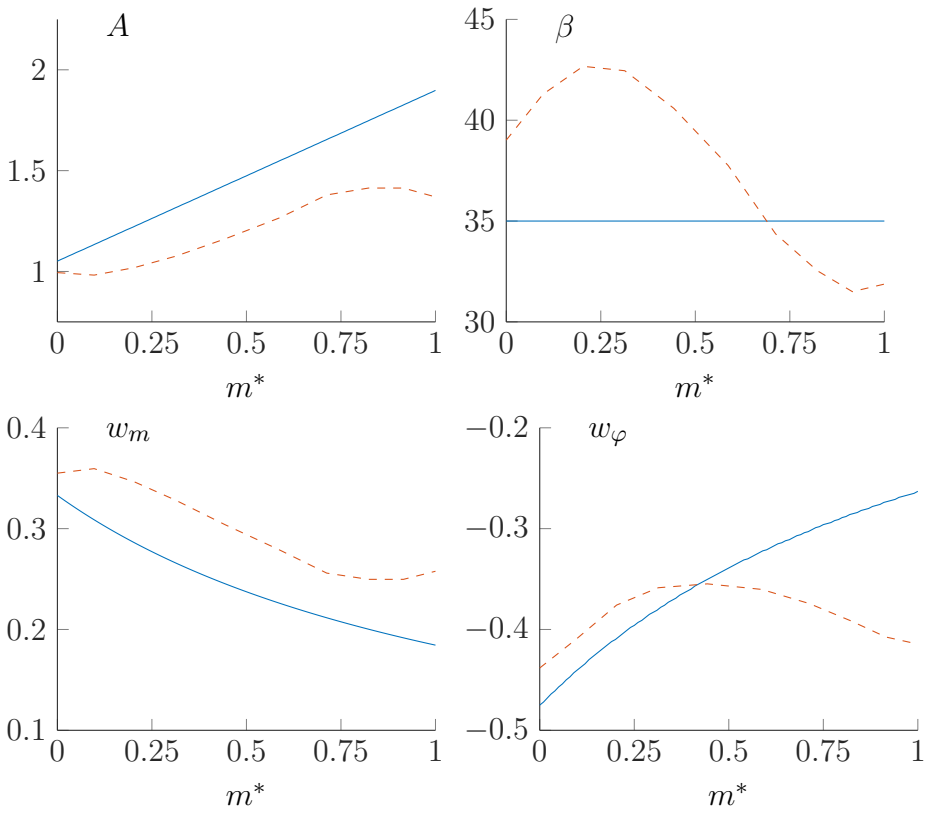

Figure 5.6 One-dimensional, normalised flow characteristics for a mixed-flow impeller. The blue plain curves show the simplified parametric flow field, while the red dashed curves represent the ideal flow field obtained for variable blade angle and passage height. We observe that none of characteristics is monotonic, which is common for real mixed-flow pumps.

The terms in the right hand side of the equations are the forces described in 5.1.2. For the flow field based on the real geometry, we directly use (5.11) and replace the velocity field components and their derivatives by the corresponding numerical data.

5.2.3 Dispersed gas model

For a dispersed gas phase, the local gas fraction α is defined as the ratio of the surface cross-flow area occupied by the gas, and the total available cross-flow area:

$$\alpha = \frac{A_g}{A_g + A_l} = \frac{\lambda\Phi/v_m}{\Phi/w_m} = \lambda\frac{w_m}{v_m} \tag{5.21}$$

where v_m and w_m are respectively the gas and liquid meridional velocities and $\lambda\Phi$ is the non-dimensional volumetric gas flow rate, where Φ is defined as in (5.7). This expression is only valid as long as α stays small. When v_m tends toward zero, the gas accumulates in the impeller and (5.21) is not valid anymore, as α tends toward 1.

We then define the local, non-dimensional mixture density ρ_r, based on the local gas fraction α:

$$\rho_r = (1-\alpha) + \alpha\xi$$

To compute the static pressure in the impeller, we use the one-dimensional equation (5.17) or (5.19), with the modified density ρ_r. Finally, the total pressure is

$$p_{2\phi}^T = p_{2\phi} + \frac{1}{2}\rho_r W^2. \tag{5.22}$$

5.2.4 Two-fluids model (TF)

The two-fluid approach has been used in many multiphase models for pumps, for example by Minemura et al. (1998) and Sherwood (2005). It takes the interaction between both fluids into account and therefore predicts the change in the liquid flow field due to the variation of the local gas fraction within the impeller.

We consider two distinct velocity fields in the stationary frame of reference $\mathcal{R}_0$: $\vec{V}$ for the gas and $\vec{W}$ for the liquid, and the local gas volume fraction α. Using the same normalisation as the previous sections, the total flow rate coefficient is Φ, while the volumetric gas cut is λ.

The momentum equations in the stationary frame of reference are:

$$\begin{cases} \alpha\xi\dfrac{D\vec{V}}{Dt} = -\alpha\vec{\nabla}p - \alpha\xi Ri\ \vec{e}_z + \vec{F}_d + \vec{F}_l + \vec{F}_v \\ (1-\alpha)\dfrac{D\vec{W}}{Dt} = -(1-\alpha)\vec{\nabla}p - (1-\alpha)\,Ri\ \vec{e}_z - \vec{F}_d - \vec{F}_l - \vec{F}_v, \end{cases} \tag{5.23}$$

where $\vec{F}_d$, $\vec{F}_l$ and $\vec{F}_v$ are the forces due to the interaction between the two phases, respectively the drag, lift and added mass.

Based on a gaseous phase consisting of bubbles of diameter ε not interacting with each other and sharing the same pressure as the liquid phase, we express the added mass after the analysis of Minemura et al. (1998), and the drag and lift forces after Auton et al. (1988).

$$\begin{aligned}
\vec{F}_d &= \alpha \frac{3C_d}{4\varepsilon} \left|\vec{W} - \vec{V}\right| \left(\vec{W} - \vec{V}\right) \\
\vec{F}_l &= \alpha C_l \left(\vec{W} - \vec{V}\right) \times \left(\nabla \times \vec{W}\right) \\
\vec{F}_v &= \alpha C_v \left(\frac{D\vec{W}}{Dt} - \frac{D\vec{V}}{Dt}\right)
\end{aligned}$$

Introducing the relative velocities in (5.23), and neglecting the effect of gravity ($Ri << 1$) we obtain for a steady flow:

$$\begin{cases}
\begin{aligned}
\alpha(\xi + C_v)\left[\left(\vec{v}\cdot\vec{\nabla}\right)\vec{v} + 2\vec{e}_z \times \vec{v}\right] &= -\alpha\vec{\nabla}p + \alpha\xi r\vec{e}_r \\
&+ \alpha\frac{3C_d}{4\varepsilon}|\vec{w} - \vec{v}|(\vec{w} - \vec{v}) + \alpha C_v\left(\vec{w}\cdot\vec{\nabla}\right)\vec{w} \\
&+ \alpha C_l(\vec{w} - \vec{v}) \times (\nabla \times \vec{w} + 2\vec{e}_z)
\end{aligned} \\
\begin{aligned}
(1 - \alpha + \alpha C_v)\left[\left(\vec{w}\cdot\vec{\nabla}\right)\vec{w} + 2\vec{e}_z \times \vec{w}\right] &= -(1-\alpha)\vec{\nabla}p + (1-\alpha)r\vec{e}_r \\
&- \alpha\frac{3C_d}{4\varepsilon}|\vec{w} - \vec{v}|(\vec{w} - \vec{v}) + \alpha C_v\left(\vec{v}\cdot\vec{\nabla}\right)\vec{v} \\
&- \alpha C_l(\vec{w} - \vec{v}) \times (\nabla \times \vec{w} + 2\vec{e}_z)
\end{aligned}
\end{cases}$$

The liquid and gas are assumed to flow in the same direction, so that the gas and liquid relative velocities are respectively $v\vec{e}_\zeta$ and $w\vec{e}_\zeta$, where $\vec{e}_\zeta$ is tangent to a streamline (see Figure 5.2).

$$\vec{e}_\zeta = \sin\beta\ \vec{e}_m - \cos\beta\ \vec{e}_\varphi$$

The conservation of mass for the two phases is:

$$\begin{cases}
(1-\alpha)\, wA_p = (1-\lambda)\Phi \\
\alpha v\xi A_p = \lambda\Phi\xi_0
\end{cases} \tag{5.24}$$

The derivation of the one-dimensional equations for the momentum is in Appendix A. We note q' the derivative of q along the streamline, in respect to r.

$$\begin{cases} \alpha\left(\xi+C_v\right)v\ v' = -\alpha p' + \alpha\xi r + \alpha\dfrac{3C_d}{4\varepsilon}\dfrac{|w-v|\,(w-v)}{\sin\alpha\sin\beta} + \alpha C_v w\ w' \\ \left(1-\alpha+\alpha C_v\right)w\ w' = -\left(1-\alpha\right)p' + \left(1-\alpha\right)r \\ \qquad\qquad\qquad\qquad - \alpha\dfrac{3C_d}{4\varepsilon}\dfrac{|w-v|\,(w-v)}{\sin\alpha\sin\beta} + \alpha C_v v\ v' \end{cases} \tag{5.25}$$

With the assumption that $\vec{w}$ and $\vec{v}$ are collinear, the lift and Coriolis terms do not appear in the final equation.

From the mass conservation (5.24):

$$w = \frac{\left(1-\lambda\right)\Phi}{\left(1-\alpha\right)A_p} \qquad \text{and} \qquad v = \frac{\lambda\Phi\xi_0}{\alpha A_p \xi}$$

For an isothermal flow, the gas density and bubble diameter are related to the local pressure as:

$$\xi = \xi_0\left(\frac{p}{Eu}\right) \qquad \text{and} \qquad \varepsilon = \varepsilon_0\left(\frac{Eu}{p}\right)^{1/3}$$

As a result, we have :

$$ww' = w^2\left(\frac{\alpha'}{1-\alpha} - \frac{A_p'}{A_p}\right) \qquad \text{and} \qquad vv' = -v^2\left(\frac{\alpha'}{\alpha} + \frac{A_p'}{A_p} + \gamma\frac{p'}{p}\right).$$

Finally we obtain a system of ordinary differential equations for p and α:

$$\begin{cases} \left[-\alpha + \dfrac{\alpha\left(\xi+C_v\right)v^2}{p}\right]p' + \left[\left(\xi+C_v\right)v^2 + \dfrac{\alpha C_v v^2}{1-\alpha}\right]\alpha' \\ \quad + \left[\alpha\left(\left(\xi+C_v\right)v^2 - C_v w^2\right)\dfrac{A_p'}{A_p} + \alpha\xi r + \alpha\dfrac{3C_d}{4\varepsilon}\dfrac{|w-v|\,(w-v)}{\sin\alpha\ \sin\beta}\right] = 0 \\ -\left[\left(1-\alpha\right) + \dfrac{\alpha C_v v^2}{p}\right]p' - \left[\dfrac{\left(1-\alpha+\alpha C_v\right)w^2}{1-\alpha} + C_v v^2\right]\alpha' \\ \quad + \left[\left(\left(1-\alpha\right) + \alpha C_v\left(w^2-v^2\right)\right)\dfrac{A_p'}{A_p} + \left(1-\alpha\right)r - \alpha\dfrac{3C_d}{4\varepsilon}\dfrac{|w-v|\,(w-v)}{\sin\alpha\ \sin\beta}\right] = 0 \end{cases} \tag{5.26}$$

The total pressure is computed as:

$$p_{2\phi}^T = p + \frac{1}{2}\left(\alpha\xi V^2 + \left(1-\alpha\right)W^2\right)$$

where $W = \sqrt{(w\sin\beta)^2 + (-w\cos\beta + r)^2}$ and $V = \sqrt{(v\sin\beta)^2 + (-v\cos\beta + r)^2}$.

5.2.5 Conclusions

We have described two methods (dispersed gas and two-fluid models) to calculate the total pressure rise produced by a mixed-flow impeller in gas-liquid conditions, based on geometrical input. This input can be given as five geometrical parameters: R_2, r_1, $\widetilde{h}$, α and β (simplified parametric flow field) or as a table of values $R(m^*)$, $Z(m^*)$, $A_p(m^*)$ and $\beta(m^*)$, where m^* is the normalised streamwise coordinate in the bladed section of the impeller.

The dispersed gas method is applicable to low gas fractions only, as the liquid velocity field is not updated to take into account the variation of the local gas fraction. It allows a different trajectory for the gas and the liquid, based on the equation of motion for a single gas bubble in the single phase liquid flow. Even though the liquid flow field is considered axi-symmetric and therefore represented by a one- or two-dimensional model, the gas bubble trajectory differs from the liquid streamline, and we therefore refer to these models as two- or three-dimensional representations.

The two-fluid method on the contrary assumes that both phases follow the same path, but take into account the acceleration of the liquid when the gas fraction locally increases.

In the next Section, we will implement theses methods for a set of commercial impellers and compare the results, using the head degradation factor already presented in the previous chapters and repeated here

$$\mathcal{M}_{2\phi} = \frac{\Delta p^T_{2\phi}}{\rho_{m0}\Delta p^T_w}, \tag{5.27}$$

where $\Delta p^T_{2\phi}$ is the pressure rise calculated by one of the methods described above, and ρ_{m0} is the non-dimensional mixture density assuming a perfectly homogeneous flow where the gas and liquid travel at the same speed and is given by

$$\rho_{m0} = (1 - \lambda_0) + \lambda_0\xi_0.$$

5.3 Numerical implementation

In this Section, we detail the numerical methods used to compute the bubble trajectory, gas velocity, local gas fraction and head degradation factor using the equations established above.

5.3.1 Methods to compute the gas velocity

We use the methods and equations developed in the previous sections to compute the gas-liquid flow through an impeller: bubble trajectory, forces exerted on the gas bubble, gas and liquid velocities, total pressure through the impeller and head degradation factor. Not all these quantities can be obtained with each method. Table 5.2 summarises what quantities are computed depending on the method used. The definition and numerical treatment of each method is detailed below. Although we will describe all the methods and their implementation, the Equilibrium Velocity with simplified parametric flow (EV-S2D) is the one that has been be used for the bulk of the work, and especially to compute the results described in Section 5.4.

Table 5.2 Explored methods and approximations, and their outcomes.

	Bubble motion		Equilibrium velocity			Two-fluids
Liquid flow field	S3D	S2D	S3D	S2D	R2D	S1D
Gas Trajectory	✓	✓	✓	✓	✓	
Forces	✓	✓	✓	✓	✓	
Gas Velocity	✓	✓	✓	✓	✓	✓
Head Degradation				✓	✓	✓

Bubble motion (BM)

The method "BM-S3D" uses the equation of motion of a bubble (5.5), which is an ordinary differential system of three equations for the bubble centre cylindrical coordinates (r, φ, z) and their derivatives with respect to time $(\dot{r}, \dot{\varphi}, \dot{z})$. The undisturbed liquid velocity field $\vec{w}$ is defined as per (5.8). The system is solved using a Runge-Kutta method with Matlab (function `ode15s`). We assume that the bubble is initially present at the inlet of the impeller ($r = r_1, \varphi = 0, z = r_1 \cot\alpha$) with the same velocity as the liquid. We obtain the three-dimensional trajectory of the gas bubble of given size. It is possible to compute the forces applied on the bubble at any point of its trajectory and the bubble velocity. The method "BM-S2D" is a simplification where we solve an ordinary differential system of two equations ((5.5) projected on $\vec{e}_\varphi$ and $\vec{e}_m$), for the two variables $r = m/\sin\alpha$ and φ, as we assume $s\cos\alpha << 1$. This results in a bubble trajectory on the conical surface defined by $r = z\tan\alpha$, and the associated forces and gas bubble velocity.

Equilibrium velocity (EV)

The gas equilibrium velocity is computed for a fixed bubble size by solving the system (5.11), using a trust-region dogleg method with Matlab (function `fsolve`).

The method "EV-S3D" uses the simplified three-dimensional liquid flow $\vec{w}$ defined in (5.8). We mesh the impeller passage with a Cartesian grid along m and s, and solve the non-linear system of three equations for $(\dot{r},\dot{\varphi},\dot{z})$ at each location (m,s). The gas equilibrium velocity field is reconstructed assuming an axisymmetric flow. Finally, the bubble trajectory is computed from the impeller inlet using a Matlab function calculating the streamline of a velocity field (function `stream3`) from the initial location $(r = r_1, \varphi = 0, z = r_1 \cot\alpha)$.

Again, assuming that $s\cos\alpha << 1$ and projecting the system (5.11) on $\vec{e}_\varphi$ and $\vec{e}_m$. The method "EV-S2D" consists in solving the equation (5.20), where we replace the liquid field $\vec{w}$ by its parametric definition (5.16). The method "EV-R2D" uses the liquid flow field $\vec{w}$ given by (5.18). For both methods, a bubble trajectory is determined from the gas flow field (v_m, v_φ), using the Matlab function `stream2`.

We use the dispersed gas model described in Section 5.2.3 with the Equilibrium Gas Velocity to compute the head degradation factor as a function of the intake gas fraction.

We first compute the total pressure through the impeller, assuming a homogeneous mixture (no phase slip). The (non-dimensional) mixture density $\rho_m = \lambda_0\xi_0 + (1-\lambda_0)$ is approximated to a constant, and we use it to calculate the total pressure in the impeller, using (5.17) or (5.19) depending on the method selected (respectively EV-S2D and EV-R2D). Because in both cases, the fluid density only appears as a scalar multiplier of the pressure gradient, we have

$$p^T_{hom} = \rho_m p^T_{water} \ .$$

Thus we compute the maximal bubble size using (5.15). Instead of using the local gas fraction α which is yet to be calculated, we use the intake gas fraction λ_0. This is an approximation, as α would be more appropriate, but would require an iterative process to find the maximal bubble size at any point in the impeller for a specific intake gas fraction.

$$\varepsilon = \begin{cases} \varepsilon_{mixer} & \text{if } \lambda_0 \leq \alpha_c \\ \dfrac{\varepsilon_{pipe} - \varepsilon_{mixer}}{(\alpha_c - 1)^2}\left(\lambda_0 - \alpha_c\right)^2 + \varepsilon_{mixer} & \text{if } \lambda_0 > \alpha_c. \end{cases} \tag{5.28}$$

The methods EV-S2D or EV-R2D presented above are used to compute the meridional gas equilibrium velocity throughout the impeller, for a given bubble size. The local gas fraction α is obtained using (5.21) to give:

$$\alpha = \begin{cases} \lambda \dfrac{w_m}{v_m} & \text{if } v_m > \lambda w_m \\ 1 & \text{if } v_m \leq \lambda w_m. \end{cases} \tag{5.29}$$

The total pressure is obtained from (5.22) using the local mixture density $\rho_r = \alpha\xi + (1-\alpha)$. Finally, we compute the head degradation factor from (5.27).

Two-Fluid (TF)

As described in Section 5.2.4, the two-fluid method accounts for the change of local gas fraction and its consequences on the liquid flow field. We obtain the gas and liquid velocities by solving the system of ordinary differential equations (5.25) for the static pressure p and local gas fraction α, using a Runge-Kutta method with Matlab (function `ode15s`). The streamline is fixed prior to solving the equation with the following geometrical parameters: the flow angle β, meridional angle α and passage area A_p. This streamline is determined using the parametric liquid flow field presented in Section 5.2.1. This is a one-dimensional model, contrary to the others where the gas streamline was not imposed prior to the computation, and we refer to this method as "TF-S1D".

We use this method to compute the total pressure rise Δp^T_{hom} in a single phase fluid of density ρ_m (only one equation), as well as for a two-phase mixture: $\Delta p^T_{2\varphi}$. The head degradation factor is calculated as:

$$\mathcal{M}_{2\varphi} = \frac{\Delta p^T_{2\varphi}}{\Delta p^T_{hom}}.$$

5.3.2 Geometrical and operational parameters

In order to explore the effects of different geometrical parameters, we look at a range of anonymised impeller designs, which are or have been commercialised, summarised in Table 5.3 and represented in Figure 5.7. The flow coefficient is defined for the design point (or Best Efficiency Point, BEP) of each impeller, according to the tested performances of the corresponding pump. The non-dimensional specific speed ω_s, defined in Section 1.1.2, is computed using the expression:

$$\omega_s = \frac{\Phi^{1/2}_{\text{BEP}}}{\Psi^{3/4}_{\text{BEP}}} = \frac{\Phi^{1/2}_{\text{BEP}}}{\left(1 - r_1^2\right)^{3/4}}$$

Figure 5.7 gives a schematic representation of the impeller designs summarised in Table 5.3, where we can observe the combination of low meridional angles, leading to relatively long impellers, while high meridional angles lead to flat impellers.

Table 5.3 Geometrical parameters for a range of impeller designs

Design	α	β	h^*	r_1^*	Φ_{BEP}	$h^* \cos\alpha$	ω_s	Φ_{BEP}/h^*
A	90	31	0.103	0.372	0.040	0	0.22	0.388
B	90	39	0.136	0.448	0.093	0	0.36	0.684
C	57	29	0.220	0.567	0.212	0.12	0.62	0.923
D	64	40	0.311	0.542	0.329	0.136	0.74	1.06
E	42	35	0.385	0.657	0.603	0.286	1.19	1.57
F	35	55	0.353	0.569	0.595	0.202	1.03	1.69
G	62	38	0.188	0.427	0.134	0.088	0.43	0.713
H	60	35	0.297	0.565	0.350	0.148	0.79	1.18

The rotation frequency, liquid density and viscosity, gas density and the inlet pressure vary in the ranges presented in Table 1.1. Very viscous oils ($\mu_l > 10$ cP) are excluded from this analysis, as are very low rotation speeds ($f < 20$ Hz).

We define three sets of operating conditions, representing respectively the flow visualisation conditions using water and nitrogen at low pressure (1 - Flow Vis.), the high pressure testing conditions correspond to the work done by Ossia and Guénégo (2006) (2 - Test) and the real production conditions with oil and gas (3 - Prod.). Tables 5.4 and 5.5 respectively give the dimensional and non-dimensional parameters associated to these three test cases.

Table 5.4 Dimensional operational parameters

	Conditions	f [Hz]	P_0 [bar]	ρ_{g0}	ρ_l [kg/m^3]	μ_l [cP]	σ [mN/m]
1	(Flow Vis.)	25	1.5	1.5	1000	1	72
2	(Test)	60	4	39	4	1	72
3	(Prod.)	60	30	60	800	5	15

Table 5.5 Non-dimensional operational parameters

	Conditions	Re	Eu	ξ_0	Bo
1	(Flow Vis.)	$2.5 \cdot 10^5$	3.8	$1.5 \cdot 10^{-3}$	34
2	(Test)	$6 \cdot 10^5$	1.7	$4 \cdot 10^{-3}$	520
3	(Prod.)	$9.6 \cdot 10^4$	16.5	$75 \cdot 10^{-3}$	36000

We also introduce a normalised non-dimensional flow rate, related to the design flow-rate:

$$\Phi^* = \frac{\Phi}{\Phi_{BEP}}$$

For all test cases, we vary the flow rate Φ^* from 0.6 to 1.2 and the intake gas fraction λ_0 from 0 to 0.5.

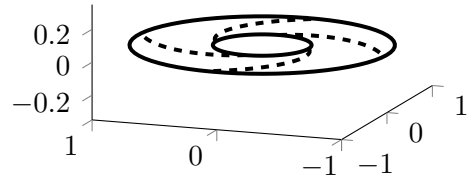

A - Radial, low capacity
$r_1 = 0.37$, $\omega_s = 0.22$
$\Phi_{BEP}/h = 0.39$, $\alpha = 90°$, $\beta = 31°$

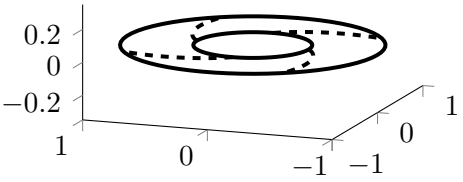

B - Radial medium capacity
$r_1 = 0.45$, $\omega_s = 0.36$
$\Phi_{BEP}/h = 0.68$, $\alpha = 90°$, $\beta = 39°$

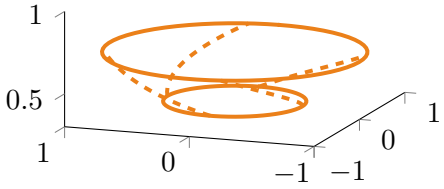

C - Short mixed-flow, low turn
$r_1 = 0.57$, $\omega_s = 0.62$
$\Phi_{BEP}/h = 0.92$, $\alpha = 57°$, $\beta = 29°$

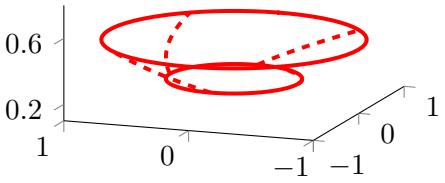

D - Short mixed-flow, medium turn
$r_1 = 0.54$, $\omega_s = 0.74$
$\Phi_{BEP}/h = 1.1$, $\alpha = 64°$, $\beta = 40°$

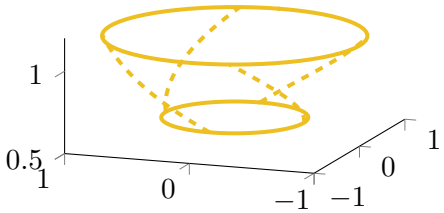

E - Long mixed-flow, medium turn
$r_1 = 0.66$, $\omega_s = 1.2$
$\Phi_{BEP}/h = 1.6$, $\alpha = 42°$, $\beta = 35°$

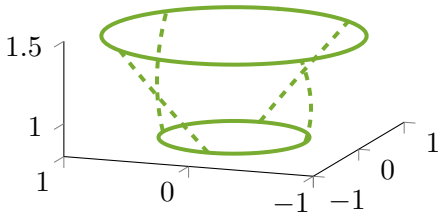

F - Very long mixed flow, high turn
$r_1 = 0.57$, $\omega_s = 1.0$
$\Phi_{BEP}/h = 1.7$, $\alpha = 35°$, $\beta = 55°$

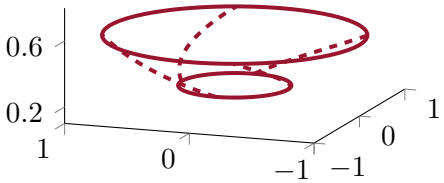

G - Large mixed-flow, medium capacity
$r_1 = 0.43$, $\omega_s = 0.43$
$\Phi_{BEP}/h = 0.7$, $\alpha = 62°$, $\beta = 38°$

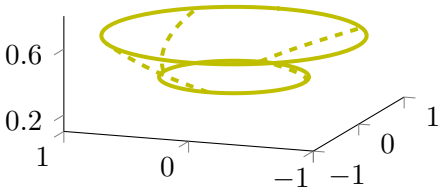

H - Large mixed-flow, high capacity
$r_1 = 0.57$, $\omega_s = 0.79$
$\Phi_{BEP}/h = 1.2$, $\alpha = 60°$, $\beta = 35°$

Figure 5.7 Normalised, three-dimensional representation of the impeller designs from Table 5.3. The dashed lines represent four liquid streamlines (following the blade angle). Only the meridional surface (mid-span) is represented.

5.4 Results

In this Section, we analyse the results obtained with the implementation presented in Section 5.3. We first compare the Bubble Motion and Equilibrium methods, taking two or three dimensions into account (methods BM-S3D, BM-S2D, EV-S3D and EV-S2D). We also observe the relative order of magnitude of the forces acting on a bubble, and how they vary with the impeller geometry or the bubble size.

We then use the method EV-S2D and the bubble size estimation from Section 5.1.4, in order to compute the local gas fraction, two-phase pressure rise and head degradation factor, for the impeller designs and operation conditions described above. We look at the impact on each design, of a small change in one geometrical feature at a time (blade angle, passage height, meridional angle,...), or changes in the operating conditions (rotation speed, flow rate coefficient,...).

Finally, a comparison is drawn with the experimental data from Chapter 4 and external references.

5.4.1 Methods comparison

We compare the trajectories, gas velocity and forces exerted on a bubble predicted by four of the five methods presented in 5.3.1: Bubble Motion (BM) and Equilibrium Velocity (EV), using either two (2D) or three-dimension geometries (3D), with a simplified parametric flow field. We observe the consequences of the approximations made for each method on the results, for different geometries and bubble sizes. As the Bubble Motion method in three-dimensions (BM-S3D) is the least approximate of the four methods, it will be used as a benchmark. We also examine the validity of the approximation $s\cos\alpha << 1$ (the bubble remains on a conical surface within the impeller passage) which is underlying in all methods, as explained in Section 5.1.2.

Bubbles trajectories

Bubbles deviate from the liquid streamline, either to the left (toward the suction side of a hypothetical blade), or to the right (toward the pressure side). For all designs presented on Figure 5.8, only the smallest bubble gets out of the impeller (green trajectory). The medium-sized bubble (blue) stops progressing radially about half-way through, and the largest one (red) travels back toward the impeller inlet after a short time. For Design B (radial impeller) only, the largest bubble is deviated toward the left of the liquid streamline, while all the other bubble sizes and all the other designs lead to a deviation to the right. The relative position of the bubble compared to the liquid streamline starting from the same point at the impeller inlet depends on the relative intensity of the centrifugal and Coriolis forces. The Coriolis force tends to push the bubble to the left of the liquid streamline, while the centrifugal force tends to push it to the right. As the centrifugal force increases with the radial coordinate, are more

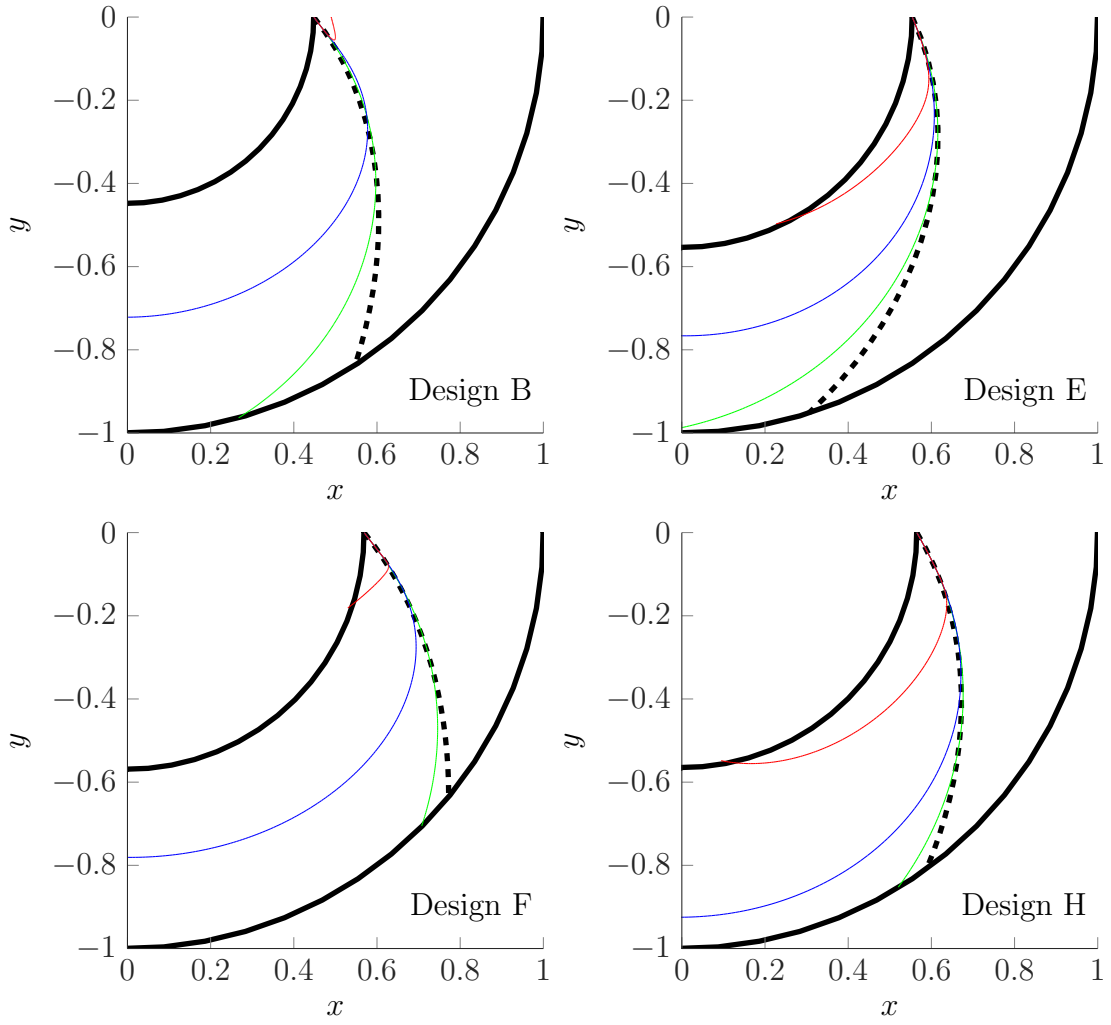

Figure 5.8 Projection in the plane perpendicular to the axis of rotation, or top view of the impeller, in the rotating frame of reference. The inlet and outlet radii are represented by two thick black lines. The bubble trajectories (coloured lines) are calculated with the method BM-S3D for $\varepsilon_0 = 0.005$ (green) $\varepsilon_0 = 0.02$ (blue) and $\varepsilon_0 = 0.1$ (red) for bubbles released at the pump inlet, with the liquid velocity. The corresponding liquid streamline is represented with a dashed line. The operational parameters are typical tests conditions (2 - Test) as presented on Tables 5.4 and 5.5.

likely to accumulate on the pressure side at the inlet and on the suction side at the outlet. This agrees with the observations by Barrios and Prado (2011a) and Caridad et al. (2008) in radial stages. The Coriolis force also increases when the meridional angle α or the flow angle β increase. This means that the mixed-flow impellers, and those with a low flow angle are more likely to deflect bubbles to the pressure side.

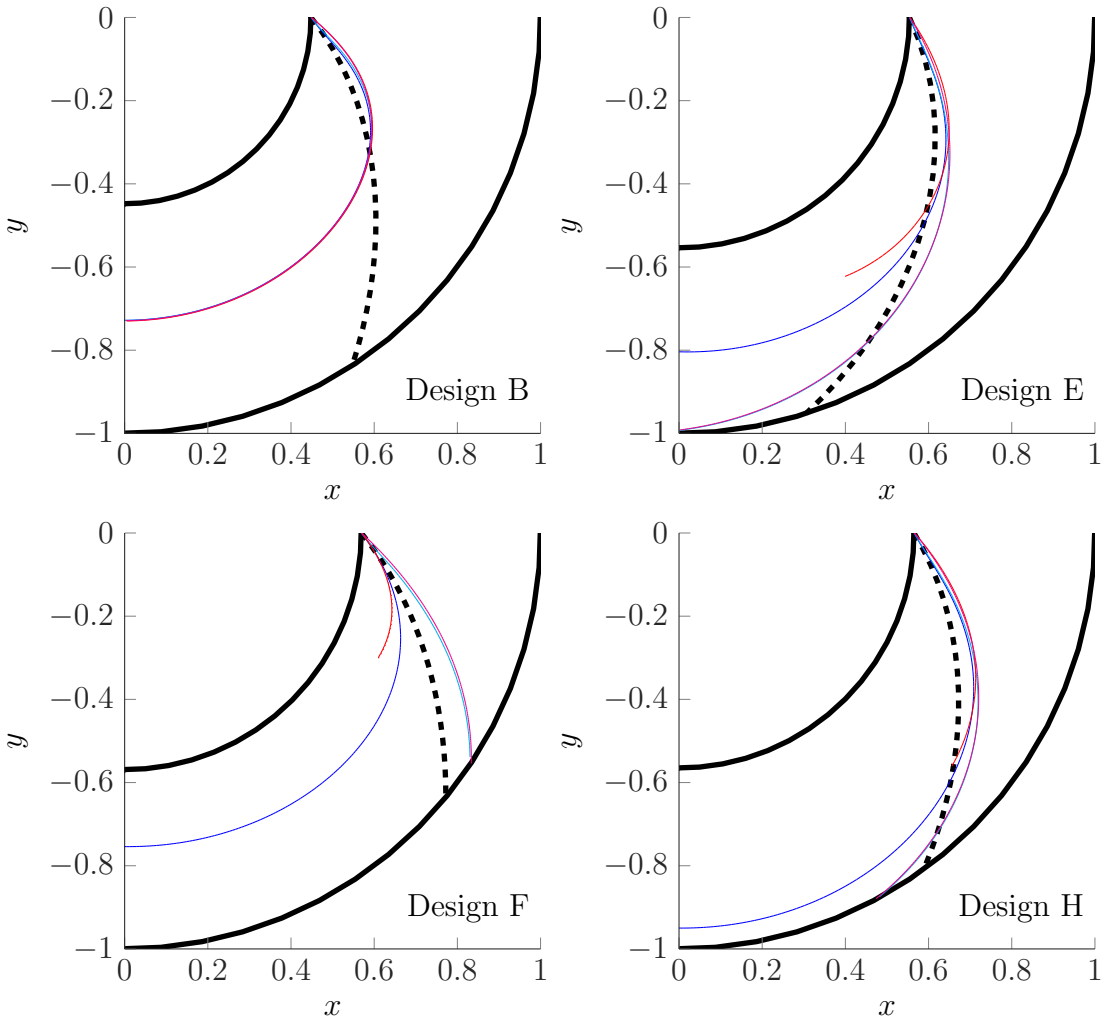

Figure 5.9 Projection in the (x, y) plane of the bubble trajectory for $\varepsilon = 0.02$ for different methods: Blue: BM-S3D, Cyan: BM-S2D, Red: EV-S3D, Magenta: EV-S2D. The equilibrium velocity in method EV-S3D is only computed within the flow passage, so the trajectory stops when $|s| > h/2$, explaining why the red lines abruptly stops for Designs E and F.

Figure 5.9 compares the trajectories computed with four different methods, with an initial bubble size of $\varepsilon_0 = 0.02$. As Design B is fully radial ($\alpha = 90°$), there is no difference between the 3D and 2D results ($s \cos\alpha = 0$). Design E and F are mixed-flow impellers and present the highest values for $h \cos\alpha$ (respectively 0.286 and 0.202), explaining the large difference between the 3D (blue and red) and 2D (magenta and cyan)

trajectories. The two-dimensional methods (BM-S2D, cyan and EV-S2D, magenta) consistently lead to trajectories that are closer to the liquid streamline, and deviate toward the left. This is due to the spanwise component of the centrifugal force, which is ignored in the 2D case, but is not negligible here. In Figure 5.14, the upper left plot shows the sum of all forces exerted on the bubble, and the spanwise force component (yellow solid and dashed lines) is of same order of magnitude as the other components. It is not compensated by the inertia terms, as only the components along $\vec{e}_\varphi$ and $\vec{e}_m$ are solved in the equation of motion. This is not a problem for the radial stages, as the total spanwise force is zero (Figure 5.13).

The Bubble Motion (BM: blue and cyan) and Equilibrium Velocity (EV: red and magenta) methods show qualitatively similar trajectories in Figure 5.9, with the main difference occurring close to the inlet. This comes from the arbitrary inlet velocity chosen for the bubble in the Bubble Motion method. Figure 5.12 shows the bubble velocity computed with the Bubble Motion method, as well as the equilibrium velocity.

As explained in Section 5.1.2, all calculations are based on the assumption of a uniform velocity field across the spanwise coordinate of the blade passage which is considered thin ($h\cos\alpha << 1$). The 2D equation considers that the bubbles only flow on the mid-span surface. We can test this approximation by looking at the s-coordinate of a bubble released with $s = 0$, as computed with the method BM-S3D. If the bubble position satisfies $|s\cos\alpha| << 1$, then the approximation taking only two components (meridional and tangential) into account is valid.

Figure 5.10 shows that, for a large initial bubble diameter ε_0, the spanwise component can exceed the width of the flow passage, which results in a non-physical trajectory. On the other hand, small bubbles stay within the impeller passage height.

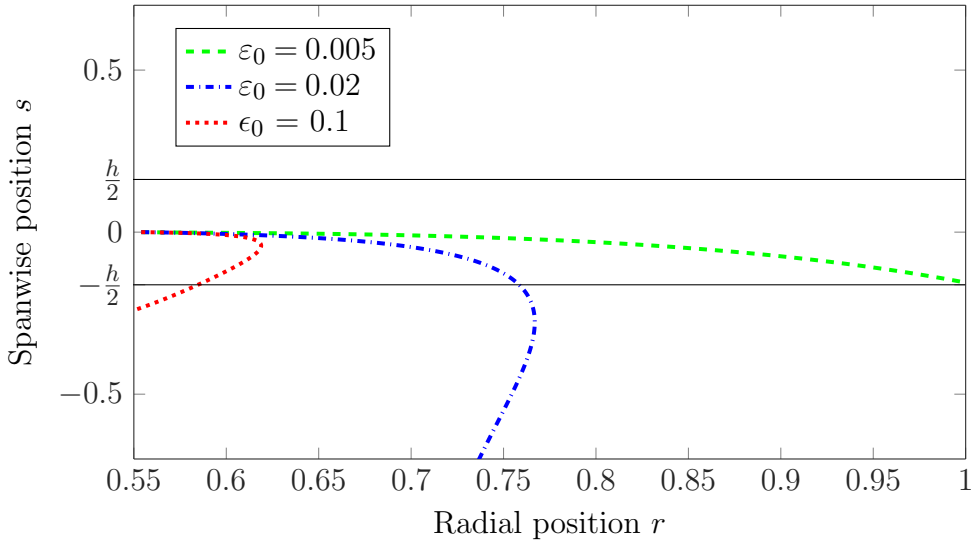

Figure 5.10 Spanwise coordinate s, along their radial position r for bubbles of different size in the impeller Design E (mixed-flow, medium turn). The trajectories are computed with the method BM-S2D. The solid black lines represent the passage boundaries (hub, $s = -h/2$ and shroud, $s = h/2$). A very small bubble ($\varepsilon_0 = 0.005$) stays in the passage, while bigger bubbles ($\varepsilon_0 = 0.02$ or 0.1) overstep the lower spanwise boundary (hub) as they progress through the impeller.

Gas and Liquid velocities

The main mechanism leading to head degradation is the reduction of the gas velocity in the impeller, due to the centrifugal force and adverse pressure gradient (or flow force). In Figure 5.11, we compare the gas and liquid velocities for the three and two-dimensional Bubble Motion methods, BM-S3D and BM-S2D. For the medium and large bubbles, the meridional velocity is overestimated in the two-dimensional case compared to the three-dimensional method, leading to underestimating the detrimental effect of the gas on the pressure rise delivered by the impeller.

Figure 5.12, shows the difference between the the Bubble Motion method (BM) which takes the bubble inertia into account, and the Equilibrium Velocity method (EV) which does not. This time we neglect the spanwise component in both cases and focus on the two-dimensional methods. The BM method requires the initial bubble velocity as an input, and we arbitrarily chose the same velocity as the liquid. The resulting velocity quickly converges to the equilibrium velocity as the bubble travels through the impeller. We conclude that the Equilibrium velocity method is a good approximation to the Bubble Motion method, with the advantage of not requiring an inlet condition, and only involving a system of two standard equations, rather than differential equations. Similar conclusions can be drawn for the three-dimensional case.

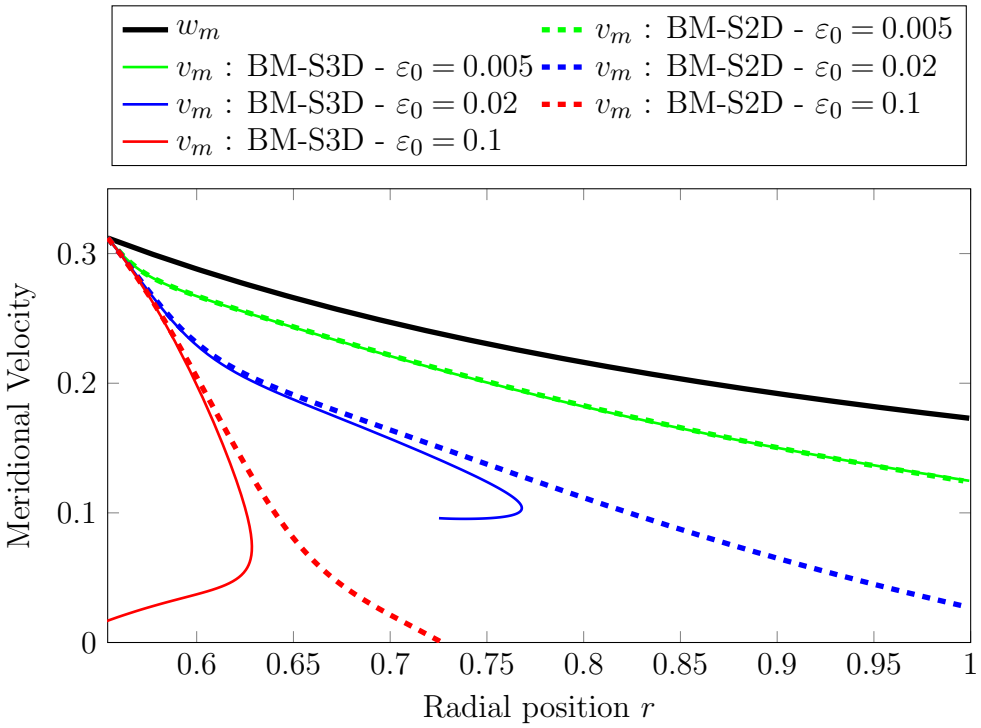

Figure 5.11 Meridional velocity for three bubble sizes ($\varepsilon_0 = 0.005$, 0.02 and 0.1) in Design E, computed with the methods BM-S2D (dashed lines) and BM-S3D (plain lines), plotted along the bubble radial coordinate in the impeller. The velocities are the same for the smallest bubbles, while they depart as the bubbles start to travel backwards for the medium and large bubbles.

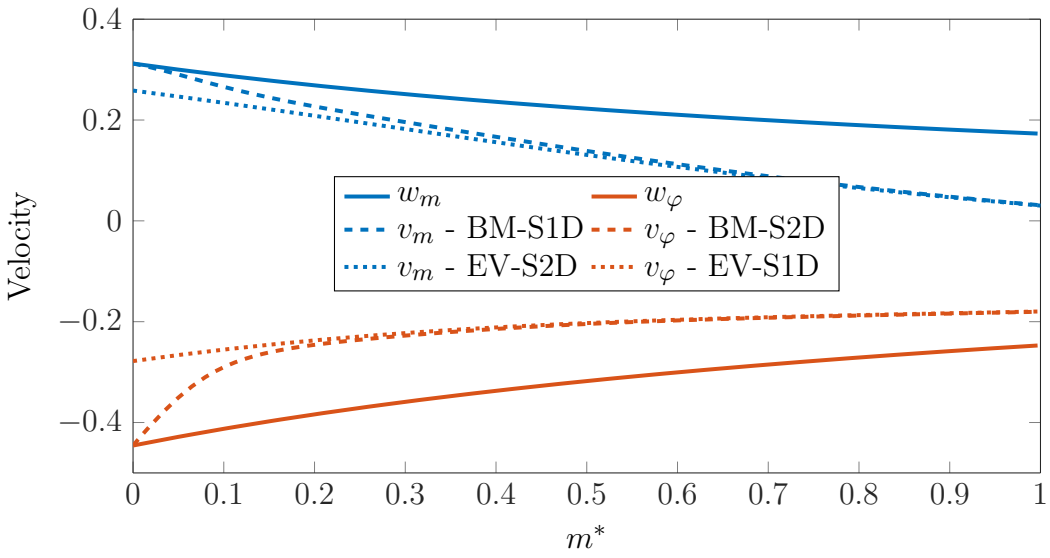

Figure 5.12 Tangential and meridional velocity of a bubble ($\varepsilon_0 = 0.02$) in Design E, computed with and without taking the inertia into account. In the inertial case, the initial velocity is taken equal to the liquid velocity. The final velocities are the same for both calculations.

Forces exerted on the bubble

Using the definitions from (5.9), we examine the relative magnitude of the non-dimensional forces exerted on a bubble in an impeller, as predicted by the Bubble Motion, and Equilibrium Velocity methods.

The total force applied on the bubble $\vec{F}_{tot}$ is:

$$\vec{F}_{tot} = \vec{F}_{cent} + \vec{F}_{flow} + \vec{F}_{cori} + \vec{F}_{drag} + \vec{F}_{lift}$$

This sum is equal to the total inertia: $\vec{F}_{tot} = (\xi + C_v)\,[\vec{a}_0 + \vec{a}_1]$ as per the Bubble Motion Equation (5.5) or to the Coriolis inertia $\vec{F}_{tot} = (\xi + C_v)\,\vec{a}_1$ as per the Equilibrium Velocity Equation (5.11).

Figure 5.13 shows that the largest forces having an effect on the bubble in a radial impeller (Design B) are the centrifugal, Coriolis, flow and drag force. The lift force and Coriolis inertia are much smaller. The approximation consisting in neglecting the inertial acceleration $\vec{a}_0$ (EV method) is confirmed here, as this term quickly drops to zero as shown in the bottom middle plot of Figure 5.13. With the method BM-S3D, the forces are not computed beyond the point where the meridional velocity reaches zero, as the bubble does not progress past this. The Coriolis inertia (bottom right plot) however should not be neglected as it does not cancel out . Apart from the inlet section, the two methods present very similar results. If the bubble initial velocity were chosen equal to the gas equilibrium velocity at the inlet, instead of the liquid velocity,

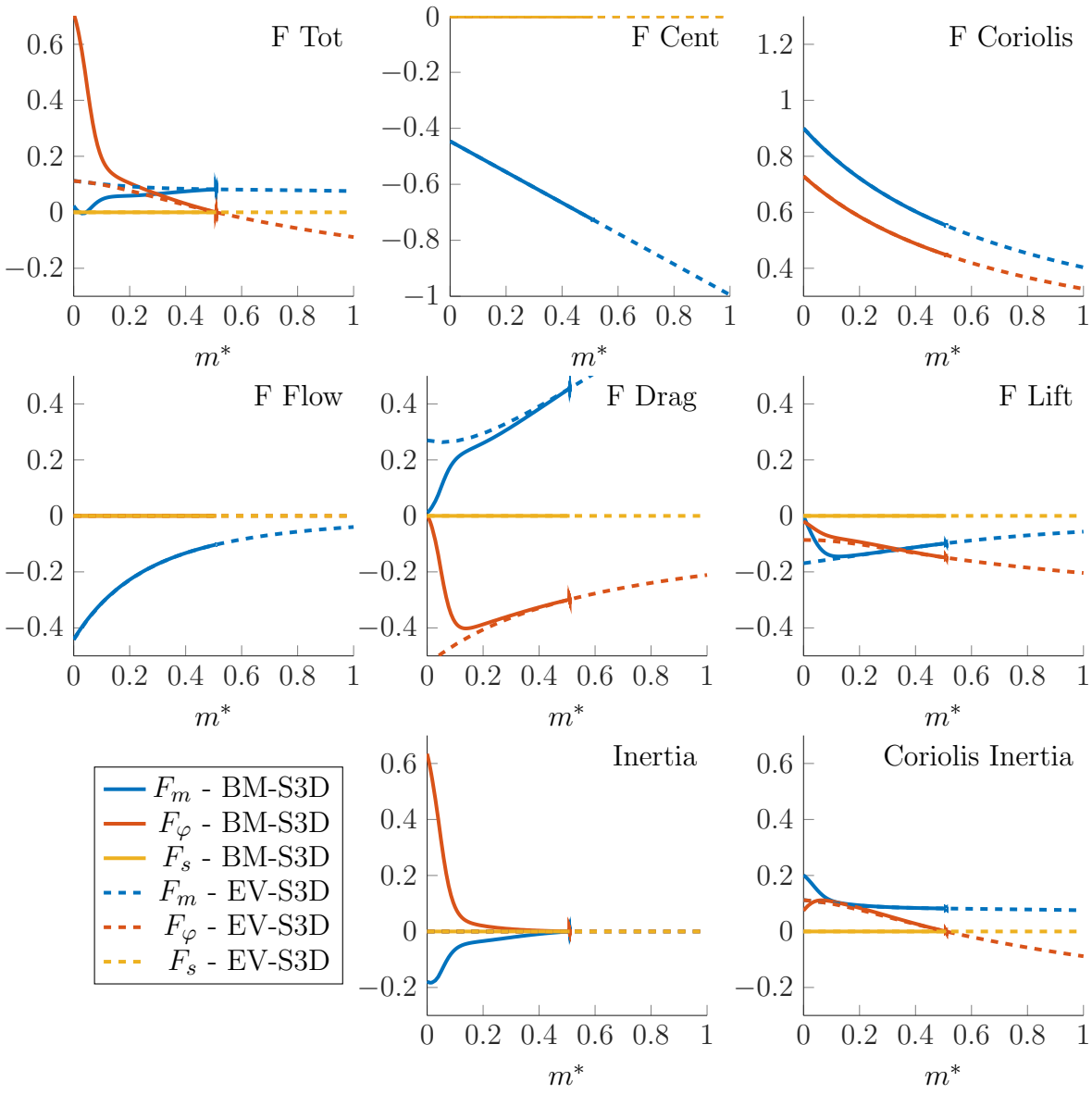

Figure 5.13 Forces exerted on a bubble ($\varepsilon_0 = 0.02$) in the impeller Design B (radial), and operating conditions (2 - Test), calculated with the methods BM-S3D (solid line) and EV-S3D (dashed line). The scaling of the vertical axis is the same for all plots.

the inertial acceleration would be uniformly zero for the whole trajectory (but not the Coriolis acceleration).

Figure 5.14 shows the effect of the bubble size on the non-dimensional forces in a mixed-flow impeller (Design E). The centrifugal, Coriolis and flow forces are not affected by the bubble size, but the drag and lift forces are. For the largest bubble ($\varepsilon_0 = 0.1$), the lift force is not negligible but is still small compared to the drag force. For all cases considered, the Coriolis force is of similar magnitude as the centrifugal force. This is important because the Coriolis force counteracts the effect of the centrifugal force in the meridional direction. The spanwise components (along $\vec{e}_s$) of $\vec{F}_{tot}$ and $(\xi + C_v)\,\vec{a}_1$ along $\vec{e}_s$ do not match (top left and bottom right plots). This is expected as the method EV-S1D only solves the Equilibrium Velocity Equation along $\vec{e}_m$ and $\vec{e}_\varphi$. The difference in these terms is an indicator of the quality of the approximation.

Conclusion on methods comparison

We have seen that the differences between the two methods Bubble Motion or Equilibrium Velocity are small, especially if we only consider the gas meridional velocity, which is the result required to compute the pressure produced in the impeller for a gas-liquid flow (this is presented in the next Section). For mixed-flow stages, there are some quantitative differences between the trajectories calculated with only two components of the systems of equations compared to a 3D model, as shown in Figures 5.9 and 5.11. These differences are amplified when the thin passage approximation is weak (when $s\cos\alpha > 0$) and for large bubble sizes. They lead to overestimating the gas meridional velocity and therefore underestimating the head degradation. It would therefore be more accurate to use a three-dimensional approach. The order of magnitude is however respected as long as the bubble stays close to the mid-span surface, and we will only use two-dimensional methods to compute the head degradation factor in the rest of this work.

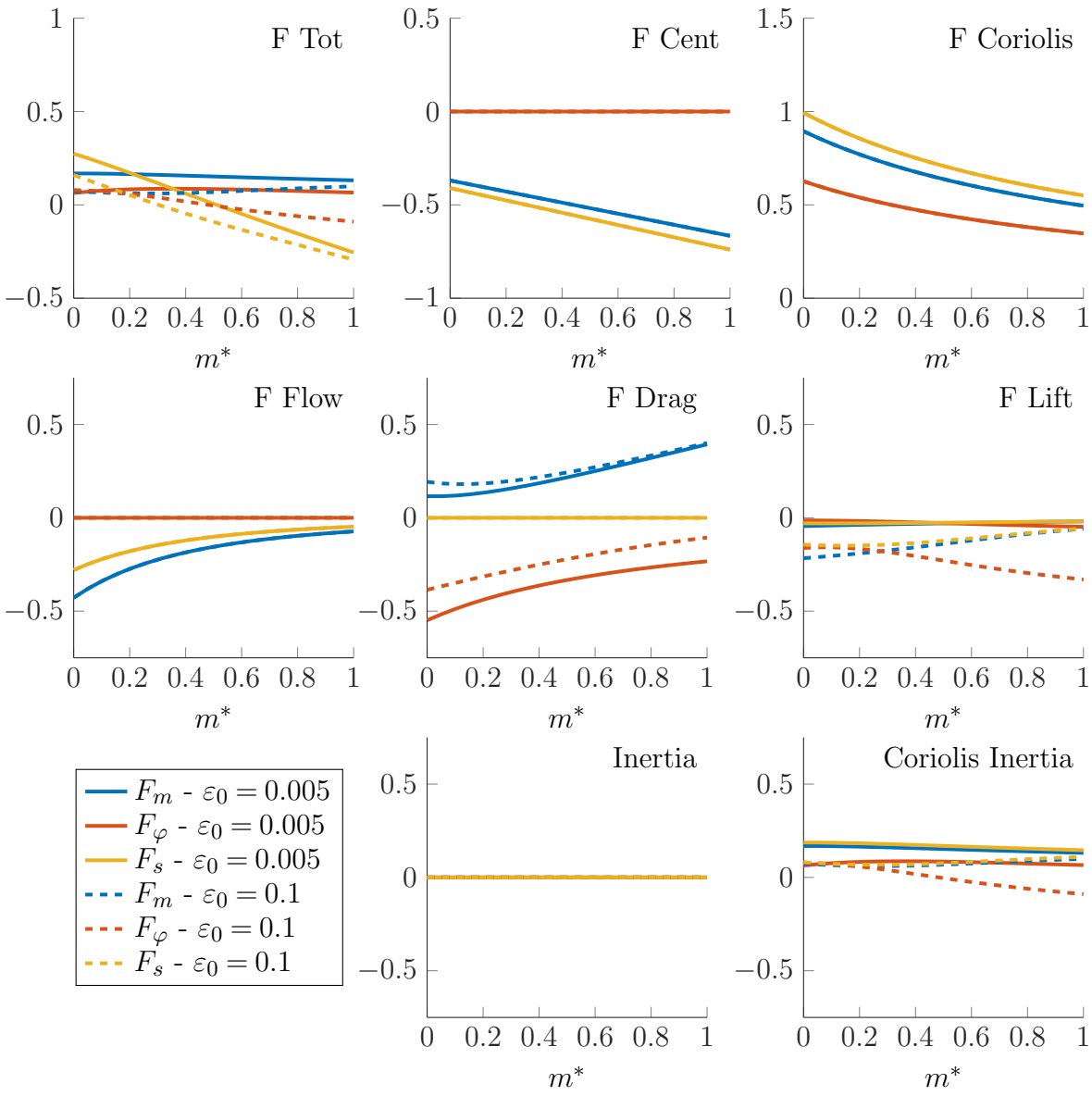

Figure 5.14 Forces exerted on a bubble in the impeller Design E and operating conditions (Test - 2), calculated with the method EV-S1D, for $\varepsilon_0 = 0.005$ (solid line) and $\varepsilon_0 = 0.1$ (dashed line). The scaling of the vertical axis is the same for all plots.

5.4.2 Pressure rise through an impeller

When the bubble diameter increases, the gas meridional velocity decreases, and as shown on Figure 5.15, it can reach negative values for large bubbles ($\varepsilon_0 = 0.1$). It has a negative meridional velocity from about half-way through the impeller. This means that there is little chance for this bubble to pass through the impeller. Instead, these bubbles will accumulate in the impeller, increasing the local gas fraction and average fluid density.

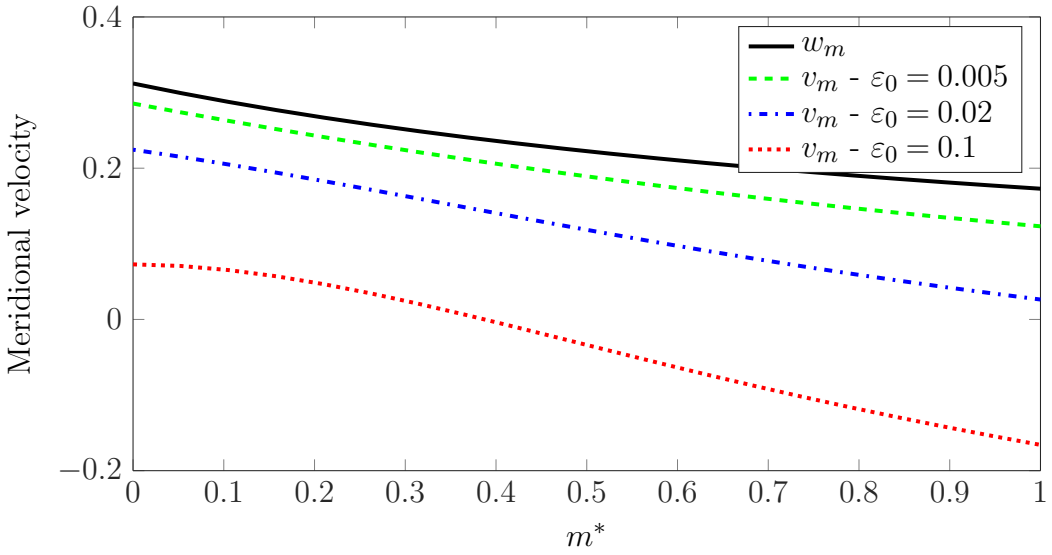

Figure 5.15 Meridional gas and liquid velocities, for $\varepsilon_0 = 0.005$ (green), $\varepsilon_0 = 0.02$ (blue), $\varepsilon_0 = 0.1$ (red), in Design E.

We compute the local gas fraction α using (5.21), and setting $\alpha = 1$ when the calculated local gas fraction is above 1 (or for negative gas meridional velocity).

Figure 5.16 shows that for an intake gas fraction $\lambda_0 = 5\%$, the local gas fraction α reaches 10 % at the impeller outlet for a bubble size $\varepsilon_0 = 0.02$. For a large bubble, the local gas fraction increases up to $\alpha = 1$ half-way through the impeller.

We compute the head degradation factor according to (5.27) for each impeller design in Table 5.3, for a range of initial bubble sizes. As shown on Figure 5.17, the head degradation factor decreases abruptly with the bubble size, revealing the existence of a threshold value, when the bubbles are too big to progress through the impeller. Several designs present a very similar head degradation factor profile with bubble size (B and G, C and D, E and H). This can be explained by the fact that they share similar geometrical design parameters (α, β, Φ/h, see Table 5.3). Design A (radial, low capacity) is characterised by a head degradation factor of zero, for the smallest bubble size considered in our calculations, and therefore does not appear on the plots.

We now vary the gas intake gas fraction, while keeping the bubble size constant ($\varepsilon_0 = 0.005$ for all designs). Figure 5.18 shows that the head degradation factor also

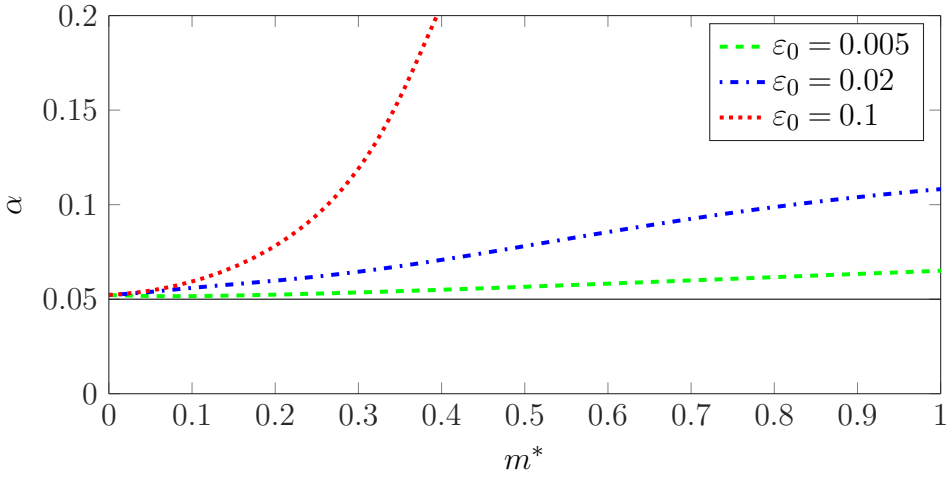

Figure 5.16 Computed local gas fraction α along the normalised meridional coordinate in the impeller (Design E), for the test condition (2 - Test), and three different initial bubble sizes.

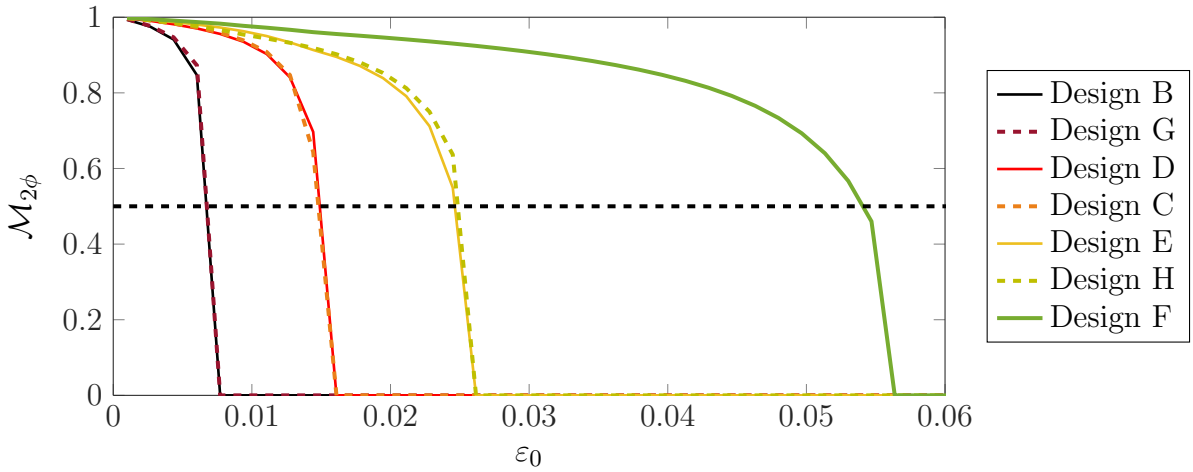

Figure 5.17 Head degradation factor computed for condition (2 - Test) with EV-S2D for $\lambda_0 = 0.05$. The head degradation factor drops abruptly for a threshold bubble size. The pairs (B, G), (C, D) and (E, H) have very similar curves.

decreases with λ_0, and drops to 0 from a threshold value of λ_0, different for each design. The slope is more gentle, as the gas meridional velocity does not change (fixed bubble size), but local gas fraction progressively increases, before reaching $\alpha = 1$ leading to the head degradation factor $\mathcal{M}_{2\varphi} = 0$.

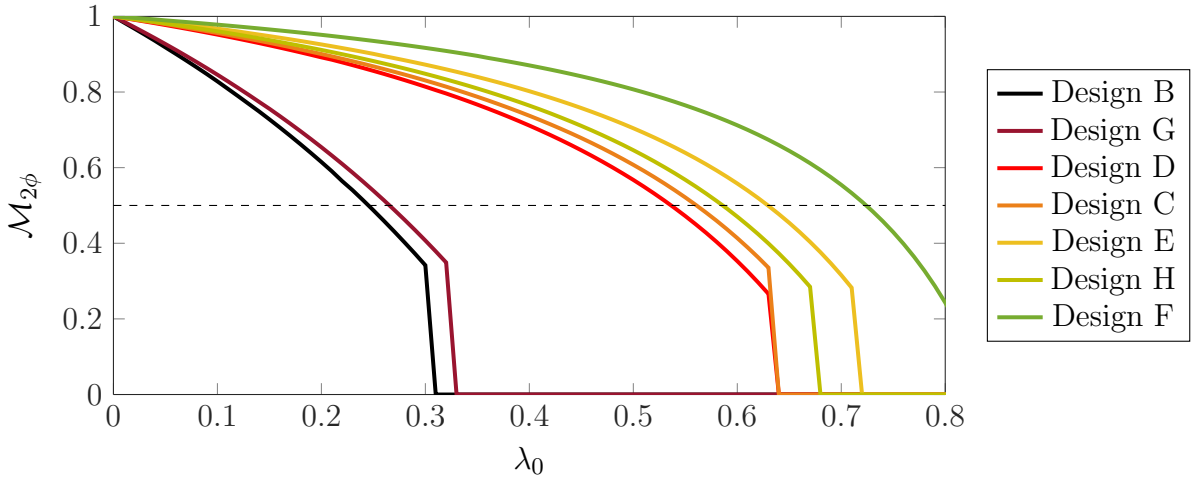

Figure 5.18 Head degradation factor computed with EV-S2D in conditions (2 - Test) for $\varepsilon_0 = 0.005$.

In Figure 5.18, we already observe a large discrepancy between the impeller designs, based on their design flow coefficients, and specific speed. The Designs A, B and G present the lowest values and also have the lowest head degradation factor, even though their outer radius is different. The impeller outer radius only appears in the pump Reynolds number (1.4) when computing the gas meridional velocity for a fixed size bubble and has a negligible effect: two geometrically similar impellers would have the same head degradation when scaled.

Using (5.28) to compute the bubble size as a function of the intake gas fraction, we obtain the results shown in Figure 5.19. This time, the impeller outer radius has a non-negligible impact on the bubble size, through the parameter B defined in (5.13). This means that larger pumps will handle gas better as they are able to break the bubbles into smaller ones.

We define the cut-off gas fraction λ_c, as the intake gas fraction for which $\mathcal{M}_{2\phi} = 0.5$. This quantity will be used in Sections 5.4.4 and 5.4.3 in order to compare different geometries or operational parameters. As stated in Section 5.2, this analysis is only valid for dispersed bubbly flow, that is for very low gas fraction, so we should only consider the results obtained for $\lambda_0 < \alpha_c$. Figure 5.20 shows that the relative design ranking is the same when focusing on the low gas fraction area.

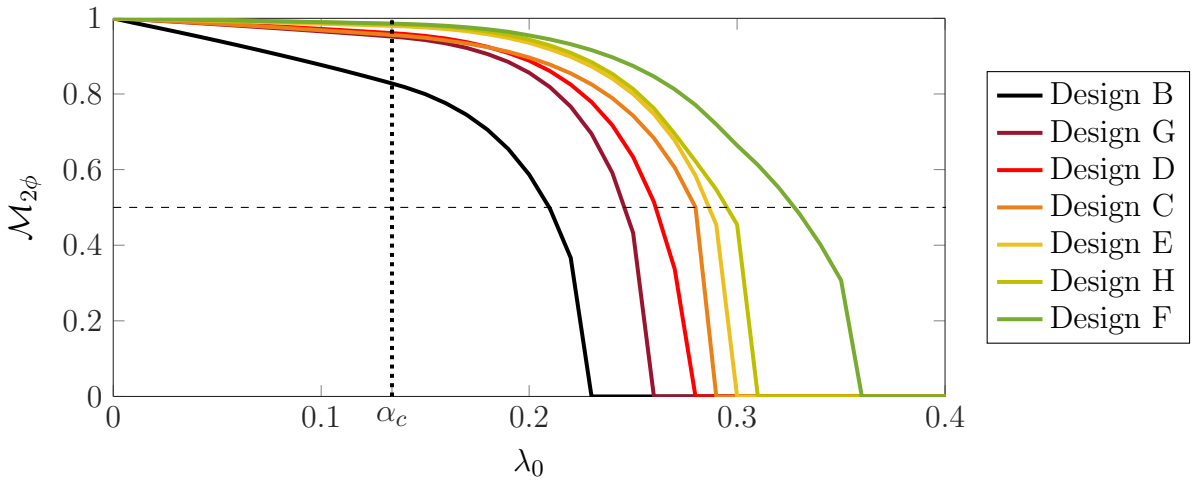

Figure 5.19 Head degradation factor computed with EV-S2D in conditions (2 - Test) and initial bubble size fixed as per (5.15).

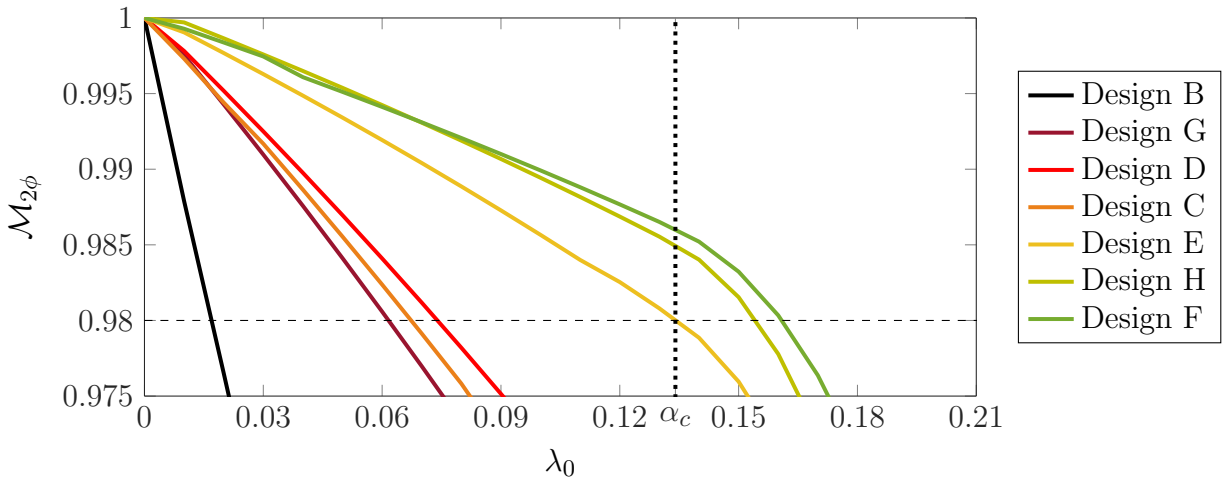

Figure 5.20 Same as Figure 5.19, focussing on $\lambda_0 < 21\%$

Liquid flow field based on a real geometry

We obtained the exact geometrical description of three impeller designs from their manufacturer, to compute a more realistic velocity profile than the simplified flow field used above. The liquid flow field and method to compute the resulting pressure rise were detailed in Section 5.2.1, and the two flow fields and their features are compared in Figure 5.6. Figure 5.21 shows that the liquid meridional velocity w_m obtained from the geometrical description (R2D) is higher than the one computed with the parametric method (S2D), as the blade blockage was not taken into account. The meridional velocity gradient dw_m/dr is also lower in the R2D case than in the S2D case, and w_m even present a maximum at $m^* = 0.1$ and a minimum at $m^* = 0.85$. The liquid deceleration implies a positive pressure gradient, helping the bubbles out of the impeller ($\vec{F}_{flow}$). As a results the difference between the gas and liquid meridional velocity is reduced in these regions ($m^* < 0.1$ and $m^* > 0.85$).

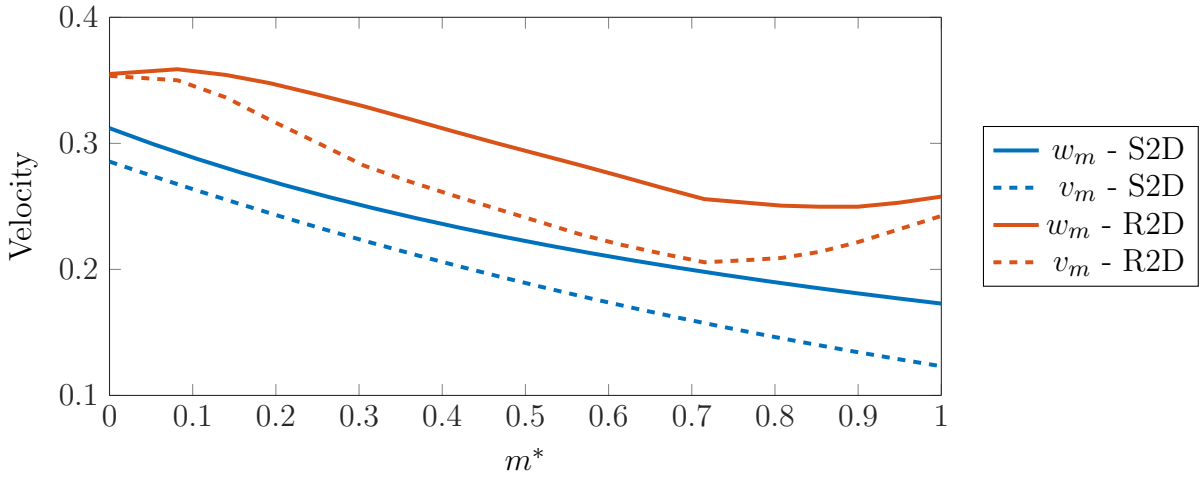

Figure 5.21 Gas (v_m) and liquid (w_m) meridional velocities for the conditions (2 - Test.) in the Design E with $\varepsilon_0 = 0.005$, for the methods EV-S2D and EV-R2D. Where the liquid velocity has a shallow slope, the gas velocity increases. On the contrary, the parametric model exhibit monotonic velocity fields.

The computed gas equilibrium meridional velocity is driven by the same phenomena, and is lower than the one predicted with the parametric flow field, as shown in Figure 5.22.

We compare in Figure 5.23 the head degradation factor obtained for the three impellers designs B, C and G, using the two methods, and see that even if the more realistic flow field gives consistently higher head degradation factor, the designs ranking in terms of cut-off gas fraction is the same for both methods.

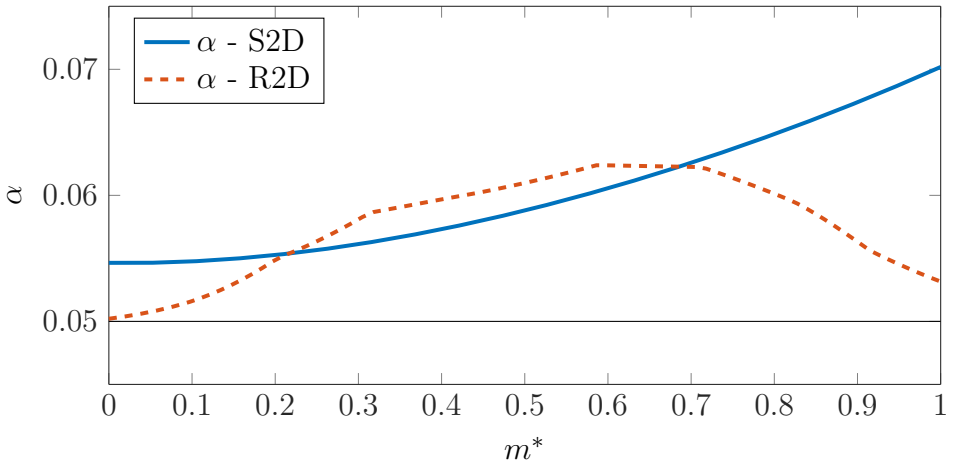

Figure 5.22 Local gas fraction computed for the conditions (2 - Test.) in the Design E with $\varepsilon_0 = 0.005$, for the methods EV-S2D and EV-R2D. The local gas fraction α is close to the inlet gas fraction λ_0 at the impeller inlet and outlet, as the computed gas velocity is close to the undisturbed liquid meridional velocity w_m in these areas.

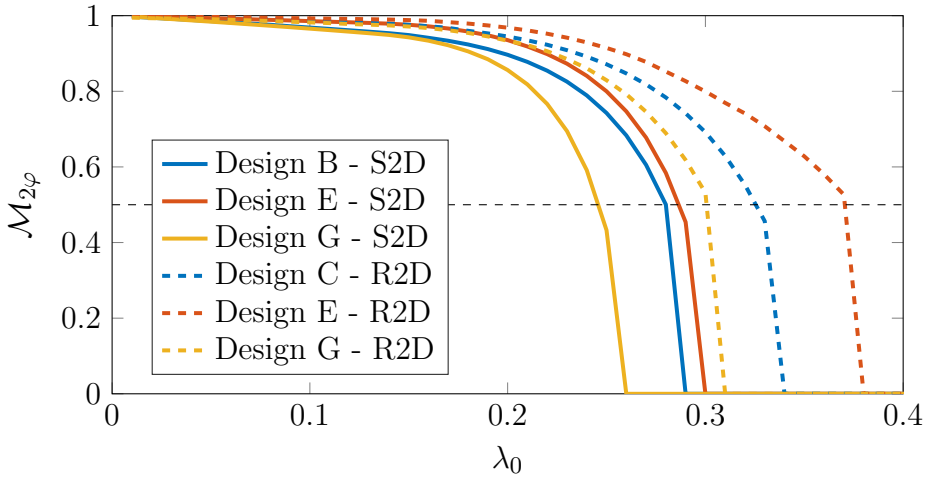

Figure 5.23 Head Degradation Factor for the Design E in conditions (2 - Test), using the methods EV-S2D and EV-R2D. The geometrical liquid flow field (R2D) leads to a higher the head degradation factor than the parametric flow field (S2D). This however does not affect the relative performance of the three designs.

5.4.3 Effect of geometrical and operational parameters

In this section we slightly vary the geometrical and operational parameters for the designs and conditions presented in Tables 5.3 to 5.5. We computed the cut-off intake gas fraction for four impeller designs and a range of operating conditions (varying ω and Φ^*), and investigated the effect of small variation on the geometrical parameters (h, r_1, α and β) for seven designs.

Operational parameters

Increasing the impeller rotation speed ω increases the pump Reynolds number Re and the non-dimensional B number defined by (5.7) and (5.13). Both of these numbers have an effect on the non-dimensional drag force $\vec{F}_{drag}$ only, as shown in (5.10). In the turbulent regime, we have $\left|\vec{F}_{drag}\right| \sim \omega^{1.2}$, so the non-dimensional drag increases with the rotation speed. In transition or laminar regime, the dependency on ω is even stronger: $\left|\vec{F}_{drag}\right| \sim \omega^{3.5}$. Figure 5.24 shows that the head degradation factor increases for higher values of $f = \omega/2\pi$.

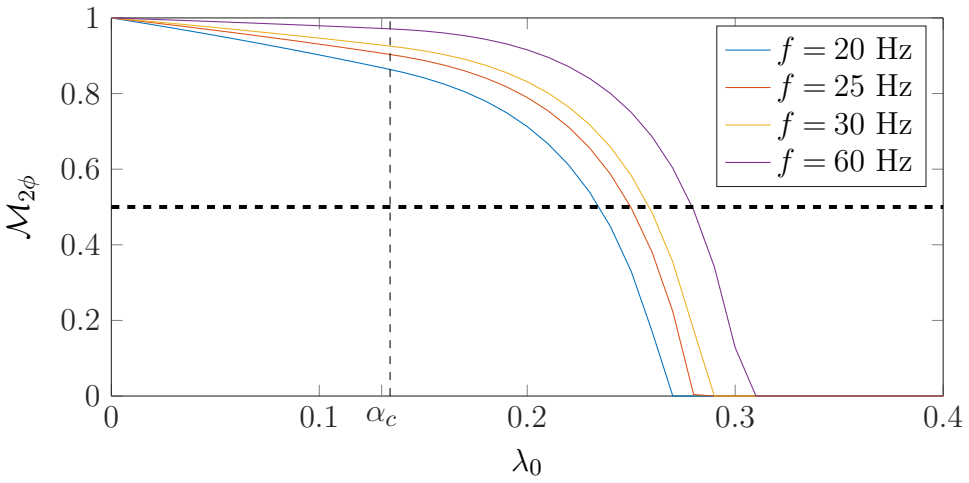

Figure 5.24 Head Degradation Factor for the impeller Design E with varying rotation speed, computed with method EV-S2D and a variable bubble size as per Equation (5.28).

It is also possible to look at the evolution with the rotation speed of the cut-off gas fraction λ_c as defined in Section 5.4.2 in order to compare different designs. According to Figure 5.25, for all the four designs the cut-off gas fraction increases with rotation speed. However, this increase is more pronounced at lower rotation speed, and does not affect all designs equally. The radial design B is more severely affected than the others. While this positive effect of rotation speed has been documented by Ossia and Guénégo (2006) and Pirouzpanah et al. (2016), the non-linear relationship and the different response for different pump models has to our knowledge never been reported or quantified.

In our model it comes from the fact that the only non-dimensional force affected by a change in ω is the drag force, which varies in a highly non-linear way. These findings will require experimental verification in the future, as the estimation of bubble size and drag force is one of the most approximated element in this model.

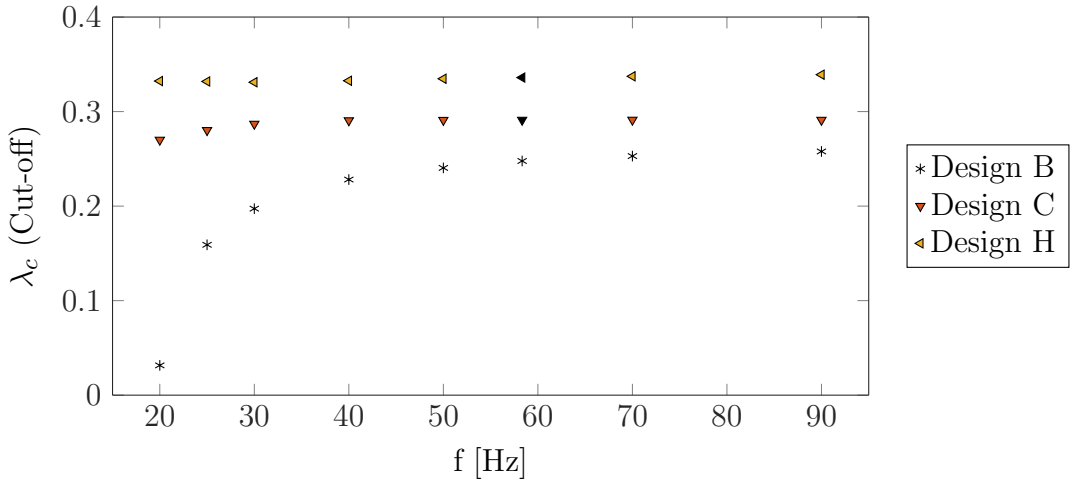

Figure 5.25 Cut-off gas fraction for a range of impeller rotation speed. Computed with EV-S2D and a bubble size as per Equation (5.28).

Increasing the flow rate affects all the non-dimensional forces acting on the bubble, apart from the centrifugal force. The normalised flow coefficient is defined as $\Phi^* = \Phi/\Phi_{BEP}$ in order to compare designs aimed at different flow conditions.

Figure 5.26 shows that the Coriolis force increases and the Flow force decreases when the flow rate coefficient Φ^* is increased from 1 to 1.1. It seems that both variations cancel each other. The two forces however, depend on the flow rate and bubble radial position in a different way, as explained in Section 5.1.2: $F_{\text{cori}} \propto \Phi/r$ while $F_{\text{cori}} \propto \Phi^2/r^3$. This leads to a larger variation of the Coriolis force at the impeller outlet ($m^* = 1$), compared to the flow force. In other words, for a fixed bubble size increasing Φ^* from 1 to 1.1 has a small impact on the bubble meridional velocity, and is slightly in favour of gas handling. The Drag and Lift force only change slightly.

The flow rate coefficient is nevertheless an important parameter when determining the bubble size, as shown in (5.14). We have $\varepsilon \propto 1/\Phi^x$, where x varies between 0.8 and 1.1. Similarly to the rotation speed, the flow coefficient impacts the pressure rise mainly through the bubble size, and therefore through drag force.

Overall as shown in Figure 5.27, increasing the flow rate tends to improve the gas handling performance. This is consistent with the observations reported in several publications, *e.g.* Lea and Bearden (1982), Barrios and Prado (2011a) or Ossia and Guénégo (2006), but not with the observation made in this work: we did not observe a

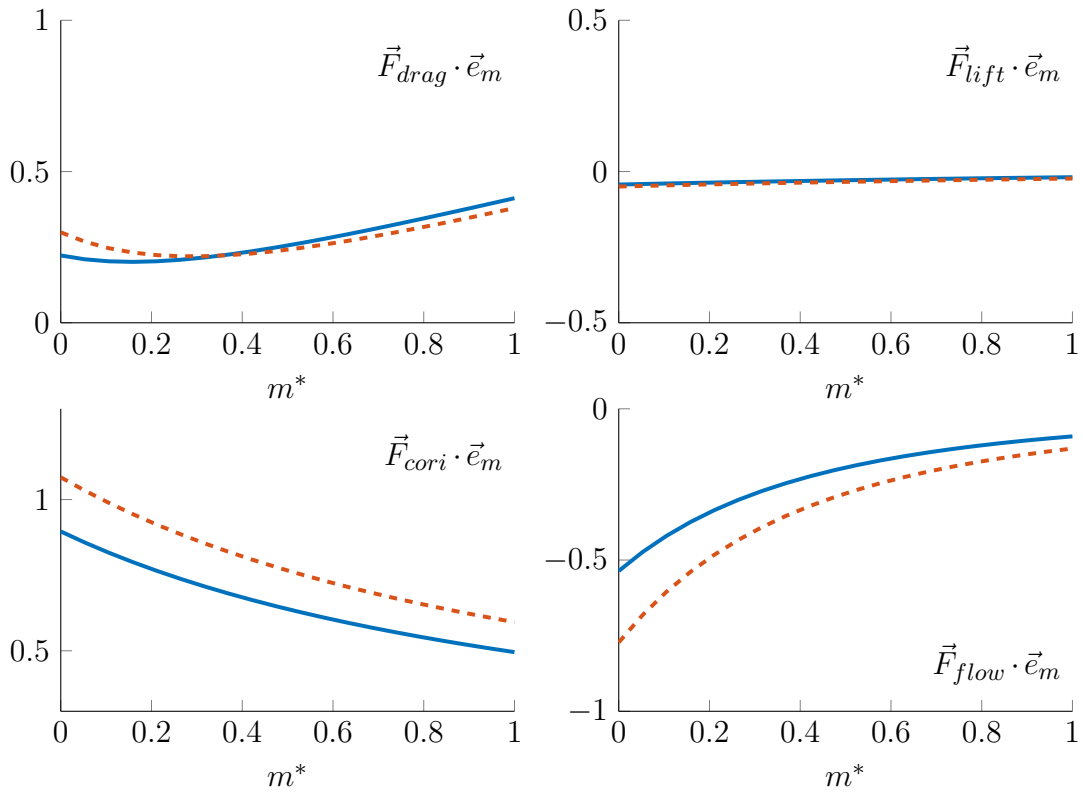

Figure 5.26 Meridional components of the Coriolis, Flow, Drag and Lift forces acting on a bubble of initial size $\varepsilon_0 = 0.005$ through the impeller Design E (mixed-flow, medium flow angle). The forces are computed with the method EV-S2D for $\Phi^* = 1$ (solid blue line) and $\Phi^* = 1.2$ (dashed red line).

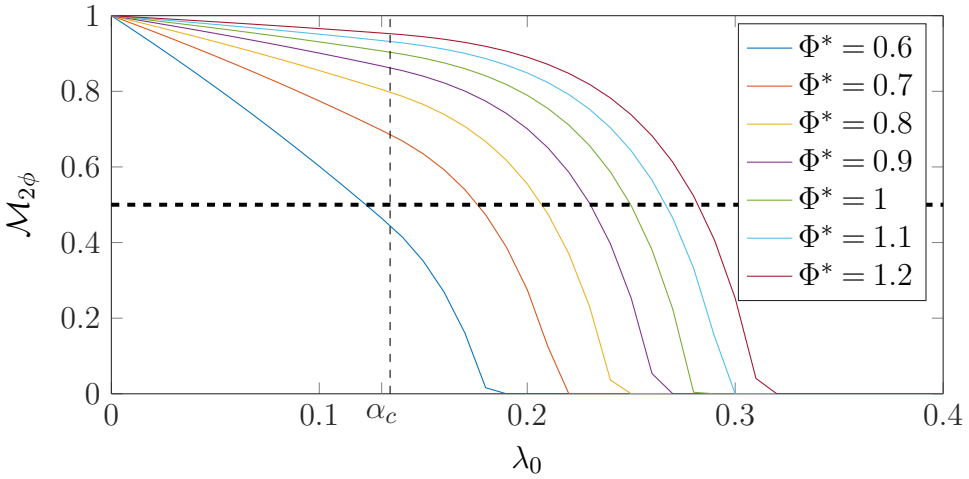

Figure 5.27 Head Degradation Factor for the impeller Design E with varying flow coefficient, computed with method EV-S2D.

variation the head degradation factor variation was not significant (see Figure 4.12). We did however observed larger bubbles at low flow rate seemingly promoted by the recirculation in the diffuser rather than the low average flow velocity (see Section 4.2.2 and Figures 4.6). This shows the limitation of this model: the recirculation at low flow rate is not taken into account, while (5.28) forces the bubble size to decrease with flow rate.

Geometrical parameters

The geometrical parameters can be slightly varied for each design, in order to observe their influence on the cut-off gas fraction. All figures have been generated with the (2 - Test) operating conditions and the bubble size as defined in (5.15).

Figure 5.28 shows the evolution of λ_c as a function of the meridional angle α and the flow angle β. Lower meridional angles and lower flow angles improve the gas handling performance of a fixed design. Reducing the meridional angle changes the relative direction of the flow path and the centrifugal force, making the component $\left|\vec{F}_{cent} \cdot \vec{e}_m\right|$ smaller, while reducing the flow angle changes the direction of the Coriolis force, increasing the value of $\left|\vec{F}_{cori} \cdot \vec{e}_m\right|$. As the centrifugal force retains the gas in the impeller, and the Coriolis force pushes it out, this leads to increasing the meridional velocity of the bubble in the impeller, and therefore limiting the head degradation.

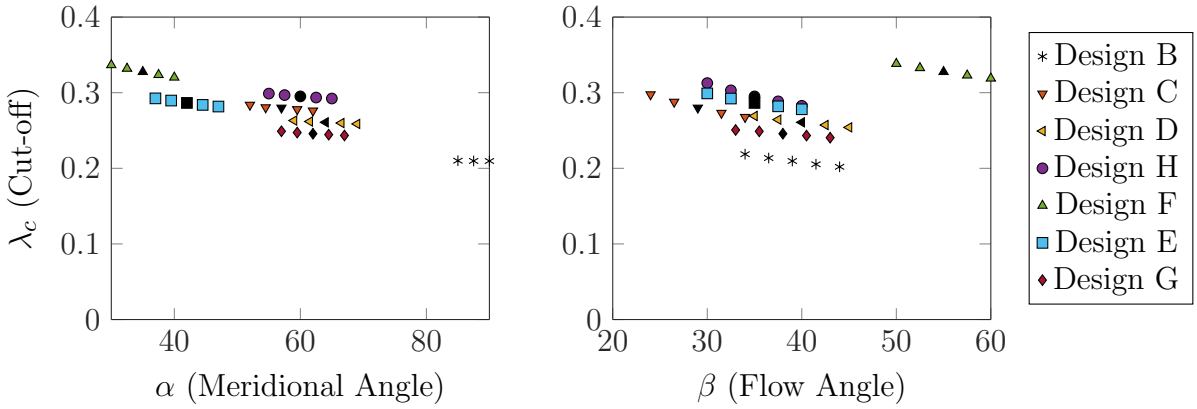

Figure 5.28 Cut-off gas fraction as a function of meridional angle α and flow angle β for different impeller designs.

Figure 5.29 shows that the passage height has a large impact on the gas handling performance of the impeller. A narrower passage is associated with a higher flow velocity, the effect is similar to increasing the total flow rate coefficient. In all the equations presented for the simplified flow, Φ and h only appear as the ratio Φ/h. For a more realistic flow, a narrower passage might induce more friction losses and therefore be less efficient overall. The inlet to outlet radius ratio has a mild impact on the cut-off gas fraction in the range considered. A smaller radius is beneficial to

gas handling, as the flow is not affected, but the flow path added at the inlet (from $r_1 - \Delta r_1$ to r_1) is less affected by the centrifugal force because of its smaller radius.

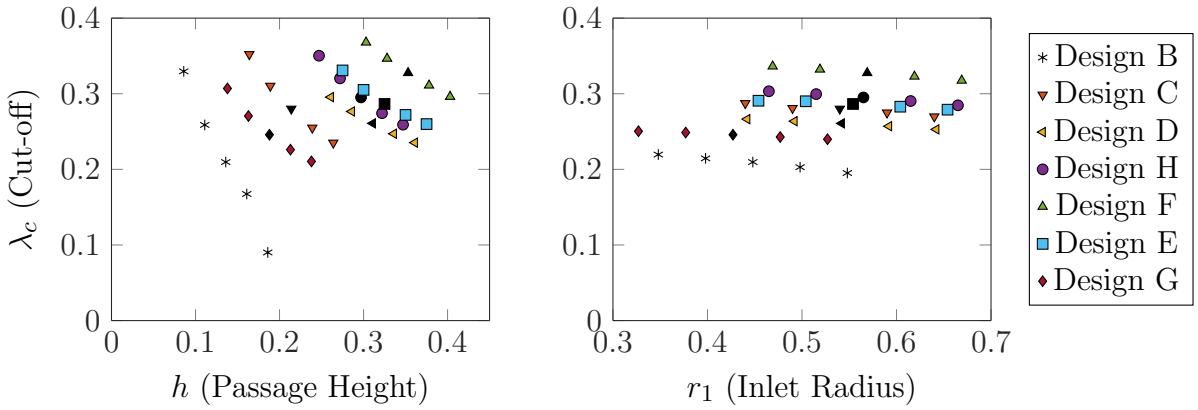

Figure 5.29 Cut-off gas fraction as a function of the non-dimensional passage height h and inlet radius r_1 for different impeller designs.

Specific speed

The specific speed defined in (1.6), can be expressed based on our simplified model as $\omega_s = \Phi^{1/2}/(1-r_1)^{3/4}$. It has been widely used as an indicator of the potential performance of a pump with gas. As shown on Figure 5.30, this trend is confirmed by by our model as the computed cut-off gas fraction increases with the specific speed.

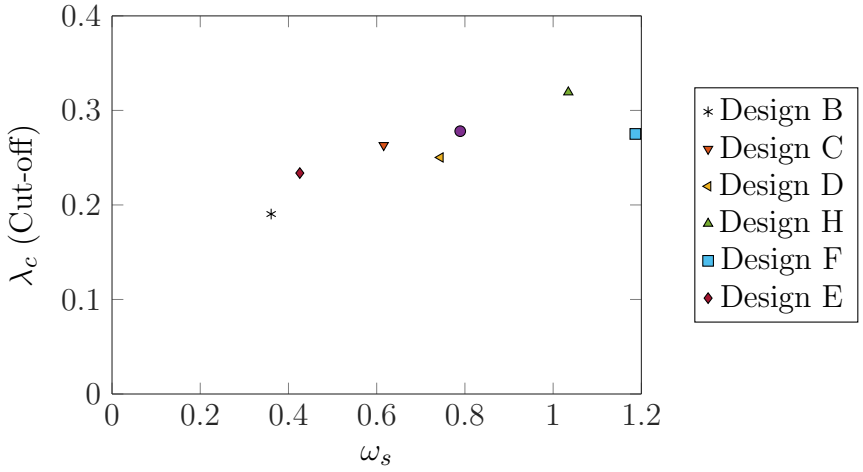

Figure 5.30 Cut-off gas fraction plotted against the pump specific speed.

Production fluids and operating conditions

The conditions of pressure and temperature, as well as the nature of the produced fluids are very different in a well and in a testing facility. Tables 1.1, 5.4 and 5.5 give

the expected or typical properties of the fluids and operation conditions. Changing the density ratio and interfacial surface tension has an impact on the bubble size. Figure 5.31 shows the dimensional bubble diameter obtained for different conditions using (5.15). The smaller maximal bubble size obtained with this model for the conditions (3 - Prod.) is 25 µm. The gas fraction α_c from which the bubbles start to coalesce however depends on the chemistry of the fluids involved and this has not been taken into account here.

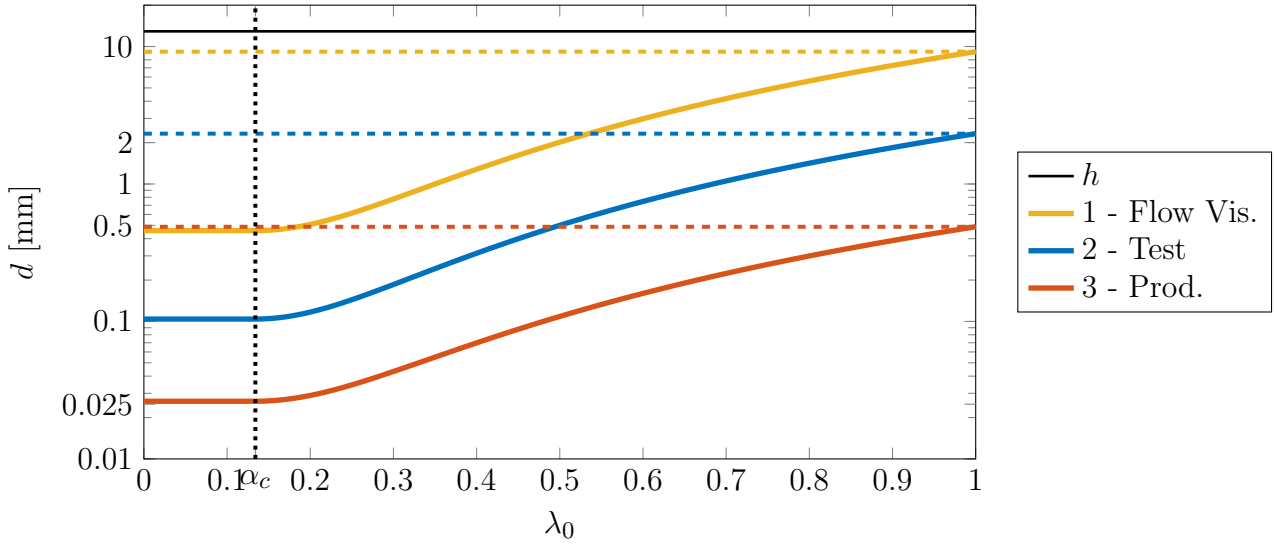

Figure 5.31 Bubble diameter d (logarithmic scale) as a function of the intake gas fraction λ_0 for the impeller Design E in different conditions, according to Equation (5.15). The solid black line is the passage height, while the coloured dashed lines represent the respective values for d_{pipe}.

We compute the head degradation for different designs in these conditions and show the results on Figure 5.32. Because of the much smaller bubble diameter, the gas handling performance is much better, and we had to push the calculation up to $\lambda_0 = 0.8$ to observe a substantial head degradation, as shown on Figure 5.19. The relative performance from one design to another is comparable to what is obtained for the (2 - Test) conditions, legitimising the tests done in air and water for the purpose of improving the performance of a design.

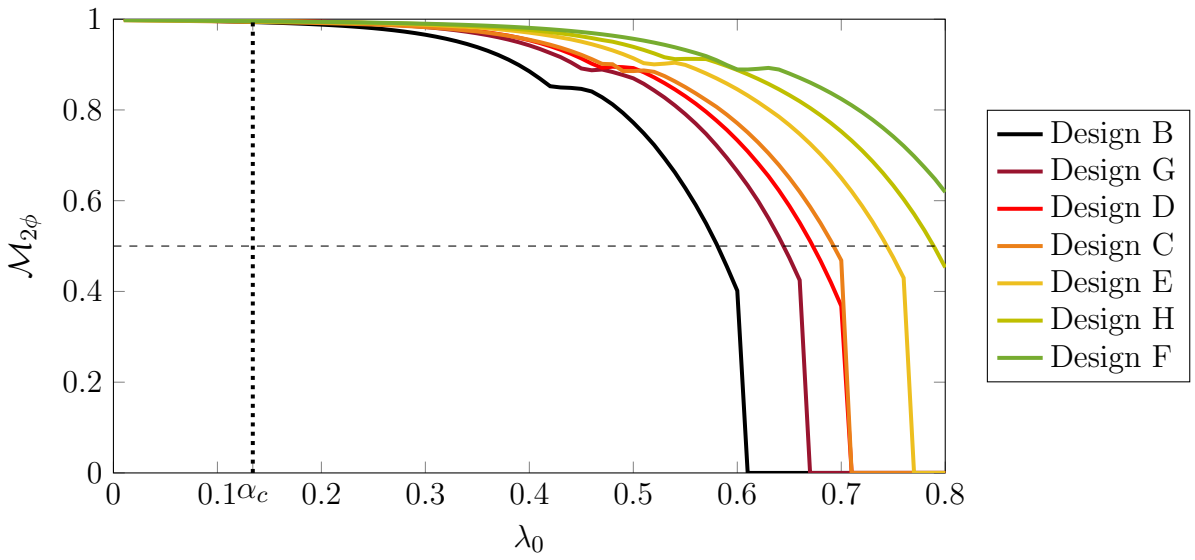

Figure 5.32 Head degradation factor computed with EV-S2D in conditions (3 - Prod.) and initial bubble size fixed as per Equation (5.15). The change of slope about $\lambda_0 = 0.5$, is due to the discontinuity of the drag force (5.10), at $Re_b = 6$. This could be corrected by modifying the expression of the drag coefficient, but was not seen as necessary for this study.

5.4.4 Comparison with experimental data

We compare the results of the method EV-S2D with the correlations given by Ossia and Guénégo (2006) from the experiments presented in Section 1.2.3 for 5 different impeller designs. It is essential to this work to compare the results for a wide range of design and operating conditions, in order to test the limits of our model.

As shown on Figure 5.33, the EV-S2D overestimates the head degradation factor $\mathcal{M}_{2\phi}$ at low and medium gas fraction, and underestimates it at high gas fraction. A common feature of the theoretical and experimental curves is the abrupt drop of $\mathcal{M}_{2\varphi}$ from a certain threshold, and the relatively low gradients at very low and high gas fraction.

The poor match at high gas fraction can be linked to the observations made in Section 4.1, where we noted that in these conditions, the flow in the pump is unsteady, with an actual gas fraction at the pump intake varying between 1 and a value lower than the average. The flow rate in the pump also seems to be unsteady, although it could not be measured. This leads to a higher average total pressure rise than if the flow had been constant.

Design D differs significantly from the theoretical calculation. A possible explanation for this is the relatively low hydraulic efficiency of that design (which has since been made obsolete by the manufacturer), compared to the other designs. This low efficiency could be associated with recirculation in the impeller, making our computa-

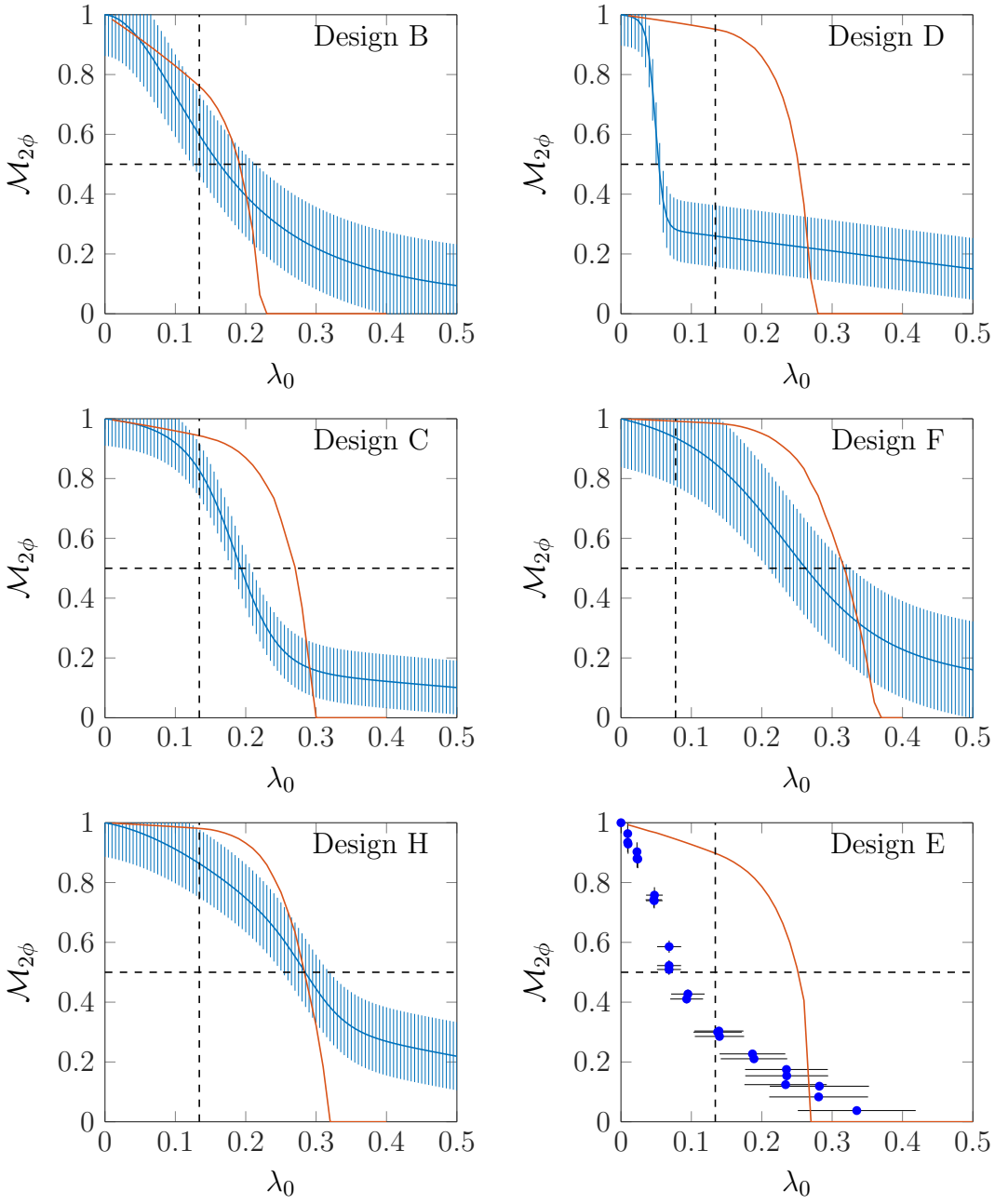

Figure 5.33 Experimental (blue - from Ossia and Guénégo (2006) except Design E) and theoretical (red - this chapter) head degradation factors, for $\Phi^* = 1$, $\xi_0 = 0.004$, and $f = 60$ Hz. The error bars on the experimental curves correspond to the root mean square error of the correlation function for the whole data set. For Design E only, $\xi_0 = 0.0015$ and $f = 20$ Hz, and the experimental results are from Figure 4.12.

tion inapplicable.

Design E is the stage used in Chapter 4, Figure 5.33 shows that the theoretical results are not consistent with the experiment. It has to be noted that the experiment conditions in this work were very different to the ones used by Ossia and Guénégo (2006), with a lower rotation speed, stage number, and intake pressure. However, our model is expected to take these into account.

In Figure 5.34, we compare the experimental and theoretical cut-off gas fraction λ_c for several designs.

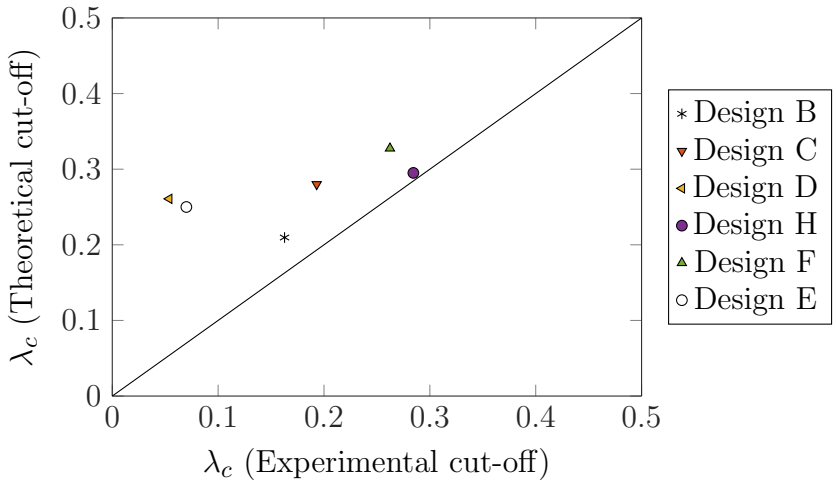

Figure 5.34 Cut-off gas fraction for different designs: experimental data (from Ossia and Guénégo (2006) and Chapter 4) on horizontal axis and present calculations (method EV-S2D, from the curves presented in Figure 5.33) on the vertical axis.

We observe that apart from Designs D and E, the values obtained theoretically are close to the experimental ones, and the trend is overall respected. Design H is the only large impeller tested experimentally.

We have seen in Section 5.3.2 that our model respects the trends found experimentally in terms of rotation speed and flow rate, although the physical phenomenon leading to lower performance at lower flow rate is not well captured by the model. This Section showed that the agreement with experimental results for several designs is only partial, but the trend in terms of cut-off gas fraction is respected (for Designs B, C, H and F).

In our model, only the role of the impeller has been taken into account, and the liquid velocity profiles are tremendously simplified. The bubble size is modelled by (5.15) in a simplified but consistent way for all designs. This demonstrates the potential of this method in predicting the gas handling performance of a design before it is possible to test it, but also shows that more work is required to fill the gaps concerning the bubble size, role of the diffuser and effect of the recirculation at part-load.

5.5 Other methods

In this Section, we look at approximations on the Equilibrium method which have not been used in the bulk of this work but were raised as possible ways to simplify the balance equation. We observe the impact of these approximations on the final result (the head degradation factor, defined in (5.27), for two different designs (radial and mixed-flow) and two different bubble sizes. We also present the results obtained with the Two-Fluids, one-dimensional model, and explain why this method was not pursued.

5.5.1 Approximations

In this section, we investigate what approximations can be made without any serious consequences in the present analysis. We give a short account of this, using the method EV-S2D developed in Section 5.2 as a benchmark, for two different impeller geometries and bubble sizes.

We have already shown in Section 5.4.1 that the simplified flow (combination of free and forced vortex) can be approximated with a one-dimensional version, considering an axisymmetric problem in a thin flow passage. This is only valid if the bubble stays close to centre of the passage ($s \approx 0$), which is verified for small bubbles.

We have also shown that the bubble inertia $(\xi + C_v)\,\vec{a}_0$ could be neglected, using the bubble equilibrium velocity to compute trajectories or estimate the local gas fraction α.

Zhu and Zhang (2016) assume that the added mass, characterised by the coefficient C_v is negligible. We investigate the consequences of setting $C_v = 0$ in our model. Minemura et al. (1998) suggests different expressions for this coefficient leading up to $C_v = 0.55$, depending on the density ratio ξ and the local gas fraction α. We also investigate the effect of such a change.

The lift force has very often been neglected in modelling the transport of gas bubbles in a rotating impeller, for example by Minemura et al. (1998). While it has been first described by Auton et al. (1988), Zhu and Zhang (2016) are the first to explicitly mention the lift force in the context of pumping gas-liquid mixtures, but only used it in the CFD calculations and not in their mechanistic model. We look at the impact of taking or not the lift force into account in our analysis.

Finally, the drag force is given as the composite Equation (5.10). We investigate whether it could be approximated with a quadratic law, with $C_d = 0.44$, or on the contrary with a Stokes law as suggested by Sherwood (2005).

	Design E				Design B			
	$\varepsilon_0 = 0.005$		$\varepsilon_0 = 0.02$		$\varepsilon_0 = 0.005$		$\varepsilon_0 = 0.02$	
	$\mathcal{M}_{2\phi}$	Error	$\mathcal{M}_{2\phi}$	Error	$\mathcal{M}_{2\phi}$	Error	$\mathcal{M}_{2\phi}$	Error
EV-S1D	0.985		0.826		0.918		0.157	
No lift	0.986	+0.2 %	0.925	+12 %	0.927	+1 %	0.245	+56 %
Incompressible	0.984	-0.1 %	0.779	-6 %	0.906	-1 %	0.154	-2 %
$C_v = 0$	0.984	-0.1 %	0.924	+12 %	0.791	-14 %	0.197	+25 %
$C_v = 0.55$	0.984	-0.1 %	0.807	-2 %	0.915	-0.3 %	0.154	-2 %
Stokes Drag	0.191	-81 %	0.005	-99 %	0.005	-99 %	0.005	-97 %
$C_d = 0.44$	0.974	-1 %	0.826	0 %	0.552	-40 %	0.157	0 %

Table 5.6 Head degradation factor and error compared to the EV-S1D method for different approximations described above.

We consider the impact of an approximation as negligible if it produces less than 10 % error compared to the reference head degradation factor. Table 5.6 shows the head degradation factor computed with these approximations for two different designs: B and E, and two bubble sizes: $\varepsilon_0 = 0.005$ and 0.02. Only the incompressible fluid assumption and added mass coefficient variation have a negligible impact on the head degradation factor. Using Stokes law to compute the drag force on the bubble leads to an error of almost 100 %, invalidating this approximation. Assuming that the bubble is always in a turbulent regime ($C_d = 0.44$) works in some cases but not all. For small bubble in low flow designs, the approximation leads to 40 % error which is not acceptable. The case of the lift force is more complex, as its impact is mild for small bubbles. For larger bubbles, neglecting the lift force leads to overestimating the head degradation factor.

5.5.2 Two-Fluid model

The Two-Fluid approach takes the effect of the change in local gas fraction into account to give an updated liquid velocity. It is fundamentally different from the methods used above, as it is a purely one-dimensional calculation. The Coriolis force acting perpendicularly to the streamline, does not appear in the equations, but its effect is assumed to be fully represented by the trajectory curvature.

This leads to an overestimated gas meridional velocity, especially for geometries with a low blade angle, compared to the one computed with the Equilibrium Velocity method. Figure 5.9 shows that the trajectory of the gas bubble is straighter with the EV method than with the TF method (no change in the streamline, we only consider the back dashed line). Overall, the Two-Fluids model predicts a milder head degradation than the Equilibrium Velocity method. Figure 5.35 shows that the head degradation is higher than one at low gas fraction, and then decreases mildly until it reaches a point when the impeller is full of gas ($\alpha = 1$) and stops producing any pressure.

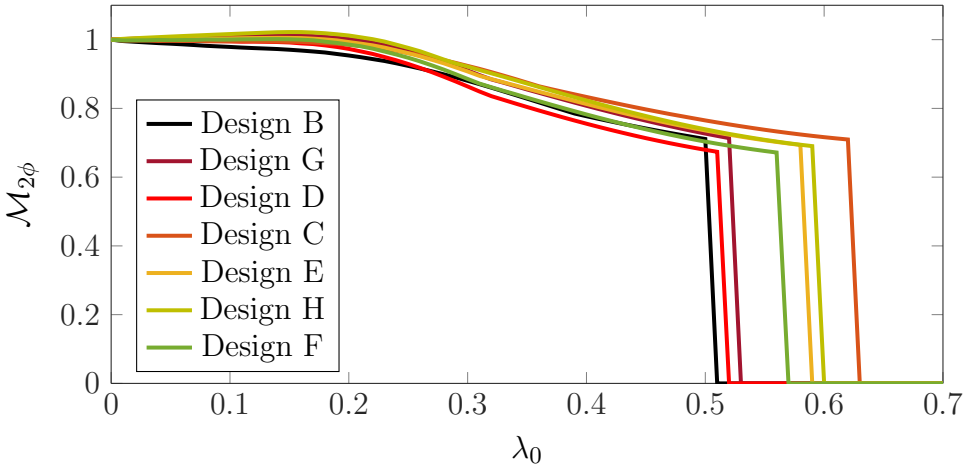

Figure 5.35 Head degradation factor computed with TF-S1D in conditions (2 - Test) and initial bubble size fixed as per Equation (5.15).

The counter-intuitive value of the head degradation factor at low gas fraction is due to a higher meridional velocity for the gas than for the liquid, as shown in Figure 5.36.

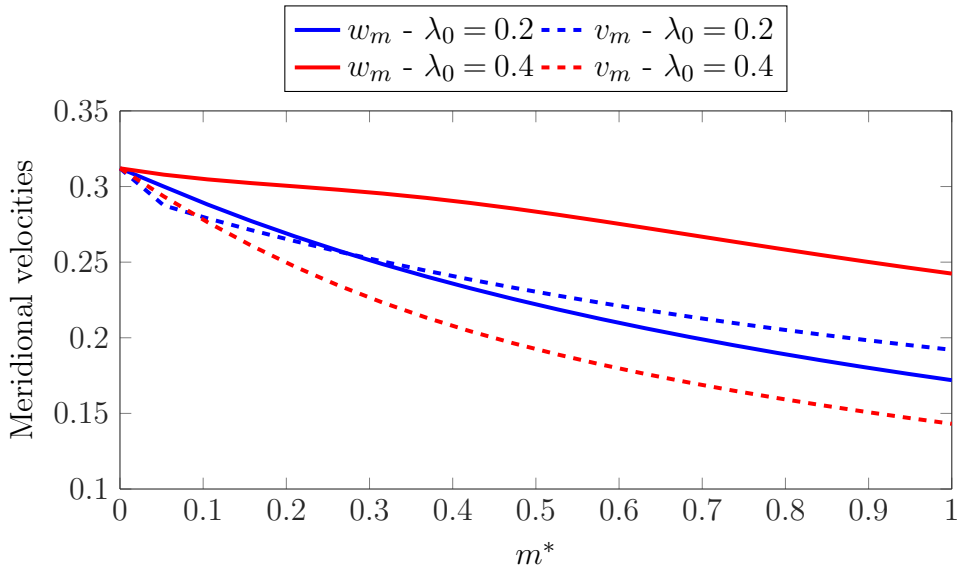

Figure 5.36 Meridional gas and liquid velocities, for $\lambda_0 = 0.2$ (blue) and $\lambda_0 = 0.4$ (red) in Design E, with the bubble size predicted by equation (5.15).

In order to obtain more realistic results, and observe the variations of the cut-off gas fraction with the geometrical parameters, we have used a larger bubble size than the one predicted by the equation (5.15) (five times larger), leading to the head degradation profiles shown on Figure 5.37. The relative performances of different designs are different that is observed in Figure 5.19: the impeller with a lower flow angle (*e.g.*

Design C) produces a higher head degradation factor, while the meridional angle does not seem to have an important role.

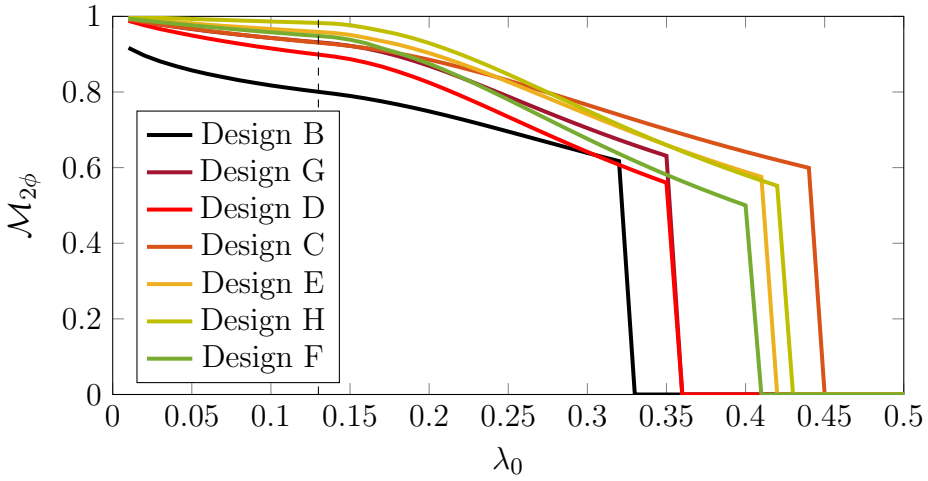

Figure 5.37 Head degradation factor computed with TF-S1D in conditions (2 - Test) and initial bubble size five times bigger than what is predicted by (5.15). The legend (and colours) are in the ranking order found with the Equilibrium Velocity method. This order is changed with the Two-Fluids method.

The results given with this methods TF-S1D are largely overestimated compared to the EV-S2D model, and to the experiments presented in Chapter 4 or given by Ossia and Guénégo (2006), as we can see in Figure 5.38. This is likely due to an over estimation of the Coriolis force, which is forced by having the gas phase following the same streamline as the liquid.

The method TF-S1D predicts that higher meridional or blade angles decrease the performance of a design in gas liquid flows. However, the effect of the meridional angle is reduced in the case of the TF-S1D model compared to the EV-S2D model, and to the experimental observations by Ossia and Guénégo (2006). On the contrary, the blade angle has a disproportionate effect on the cut-off gas fraction. The geometrical parameters (meridional and flow angles) have the same effect showing the same variation with the method TF-S1D as with the method EV-S1D. Only the flow angle β has a much larger effect on the cut-off gas fraction.

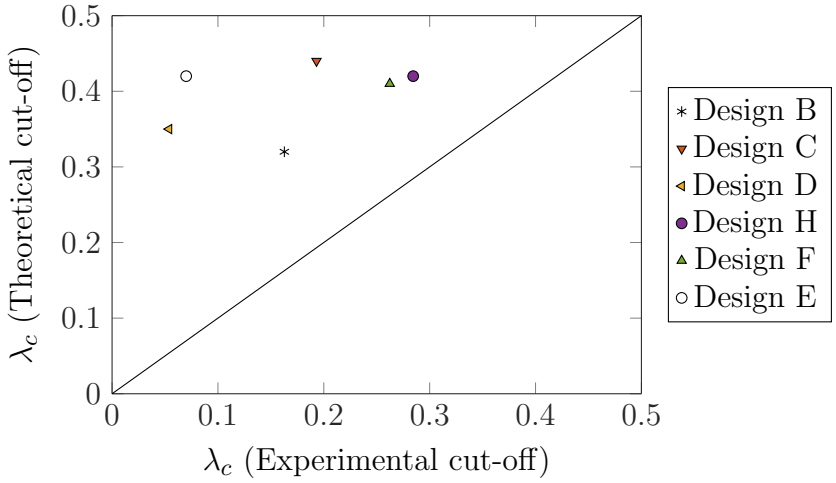

Figure 5.38 Cut-off gas fraction for different designs: experimental data (from Ossia and Guénégo (2006) and Chapter 4) on horizontal axis and present calculations (method TF-S1D, from the curves presented in Figure 5.37) on the vertical axis.

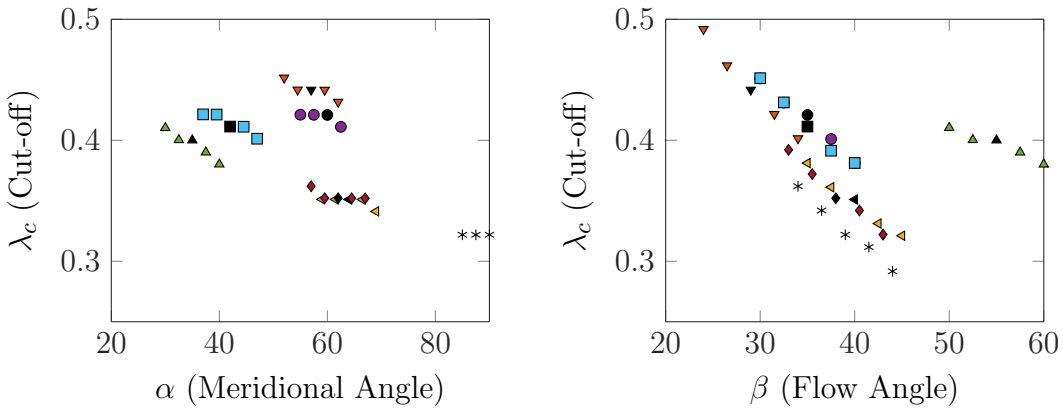

Figure 5.39 Cut-off gas fraction as a function of meridional angle α and flow angle β for different impeller designs as computed with the method TF-S1D.

Conclusions

We modelled the head degradation in radial and mixed-flow impellers, based on a dispersed flow of fixed size gas bubbles. The forces acting on a single bubble have been expressed as a direct function of the parameters representing a simplified flow in an impeller (Section 5.1.2). We found that the main contributing terms were the centrifugal force, the adverse pressure gradient due to the flow deceleration, the Coriolis force and the drag force (Figure 5.14). The lift force has a much smaller effect and is negligible for small bubbles.

Our results are based on the Equilibrium Gas Velocity two-dimensional equations (5.20) used with a dispersed gas model (Section 5.2.3), in order to predict the head degradation factor. This is an approximation of the bubble motion equations in three dimensions (5.5). We have shown that neglecting the inertial term was acceptable (Figure 5.12), while reducing the problem to a thin passage could slightly modify the results for large bubbles, if the condition $h \cos\alpha << 1$ is not respected, which can be the case for mixed flow impellers with a large passage area (5.15). Two-dimensional equilibrium gas velocity equations give the meridional gas velocity which is used to calculate the local gas fraction in the impeller and consequently the pressure rise for the two phase flow.

This model successfully predicted the trend observed in the literature, regarding the detrimental effect of high meridional angle (radial design) or high blade angle (radial blades), as shown in Figure 5.28. We also looked at two operational parameters: the flow rate and rotation speed, and found that our model predicted that increasing any of them is beneficial to gas handling, in agreement with the literature. They both contribute to decreasing the bubble size. We however observed in Chapter 4 that the increase of bubble size due to low flow rate was associated with the recirculation in the diffuser (Figure 4.6), which are not taken into account in our model. We should therefore consider this result with caution. The change of bubble size due to increasing the rotation speed was observed experimentally (Figure 4.5).

We compared the results obtained for typical test conditions in air and water, with that expected in an oil well, *i.e.* higher gas density and interfacial surface tension. The results show better predicted performances in the production case (Figure 5.32), but the relative performance of the different designs was respected. We examined which approximation could be made without consequences on the head degradation factor (Table 5.6). Considering the gas as incompressible through a single impeller is acceptable, while using a simplified drag coefficient correlation like $C_d = 0.44$ or the Stokes law is not.

Finally, we compared our method with the widely used Two-Fluid approach, and found qualitatively and quantitatively different results (Figure 5.35). The difference might come from the treatment of the Coriolis force in an intrinsically one-dimensional model, while the Equilibrium Velocity method is partly two-dimensional. The trends given for the variation of the geometrical parameters underestimate the effect of the

meridional angle and overestimate the effect of the blade angle (Figure 5.39).

We have shown that despite the many approximations made to develop this model (EV-S2D), it gives a good insight into the physical phenomena at play in head degradation due to gas, which a more complex model might not have given. This model can be used as a benchmark for further improvement. Refining the bubble size calculation, using a three-dimensional, more realistic liquid flow field, and taking the volume occupied by the gas into account would be the next steps to make this model more accurate.

Chapter 6

Conclusions

We have built an experimental facility to test gas-liquid performance and perform flow visualisations and velocity measurements for a mixed-flow ESP at a reduced speed (20 to 30 Hz), and developed a model to predict the pressure produced by mixed-flow impellers in gas-liquid conditions. Previous experimental and modelling studies were based on single radial stages (Barrios and Prado (2011a), Schäfer et al. (2015), Sterrett (1994), Zhu and Zhang (2016), Minemura and Murakami (1980)), used numerical simulations (Ossia and Godeluck (2006), Zhu et al. (2014), Minemura and Uchiyama (1994)) or focused on mapping the performance of a particular pump (Ossia and Guénégo (2006), Gamboa and Prado (2012)). Although they all brought interesting insights to the physics leading to head degradation in gas-liquid conditions, we investigated a more realistic geometry which typically allows higher gas fractions (most radial designs gas lock for $\lambda_0 < 3\%$, while mixed-flow stages can still be effective up to $\lambda_0 \approx 15\%$ (Takács, 2009).

In this chapter, we summarise our main findings and the answers to the questions stated in the first chapter, and provide avenues for improving the present work. Finally, we identify the themes requiring a particular effort to fill the knowledge gap in order to improve the capabilities of pumping systems in gas-liquid flows for the oil and gas industry.

6.1 Achievements

The model developed in this work (Equilibrium Velocity, EV) is an approximation applicable to low gas fractions, which we used to look for the onset of gas accumulation in the impeller. We expressed the forces applied on a single bubble of fixed size, and showed that the role of the Coriolis force was not negligible. In a mixed-flow stage, its meridional component opposes the centrifugal force, and therefore promotes good gas handling (Figure 5.13). The equilibrium gas velocity is computed at a several locations within the impeller, and used to calculate the local gas fraction. The pressure produced by the impeller for the two-phase mixture is then calculated based on the single phase velocity field and the corrected local mixture density. We wrote a parametric description

of the single phase flow for a mixed flow impeller, based on the tip to hub ratio r_1, the average passage height h, the average blade angle β and average meridional angle α, and also the flow coefficient Φ and density ratio ξ. Using the EV model, which is computationally inexpensive, we showed in particular that the lower the angles β and α, the better the gas handling performance (Figure 5.28). These results were expected but had not been demonstrated through modelling before.

According to Takács (2009), the specific numbers, based on the pump head and flow rate at design point and given by (1.5), is a good indicator of the gas-handling performance, with low values associated to poor has handling. Our model reproduces this trend (Figure 5.30), but also shows that it is possible for two designs to have the same specific speed and different gas handling capabilities. This is important because the flow rate, rotation speed and head at design point are often non-negotiable requirements when designing a pump, while parameters such as the blade angle, passage height or meridional angle can be adjusted to improve the performance.

We successfully used the Equilibrium Velocity model to advise Schlumberger (sponsor company) in designing the impeller of a new pump stage, by calibrating the bubble size function on available test data for a similar pump. Several impeller designs were evaluated and the gas handling capability predicted by our model was used as one of the selection criteria along others like produced head, hydraulic efficiency or manufacturability. The results are not shared here because of confidentiality.

The experiment carried out in gas-liquid conditions showed that the process leading to gas lock is the same for mixed-flow stages as for radial stages: as the inlet gas fraction increases, the gas bubbles become larger, then a gas pocket forms in the impeller until it extends through the whole passage. It was not possible to point out the exact position of the gas pocket, because the impeller view is impaired by the shroud and blades. However, we found through modelling that bubbles could be deviated toward the suction or pressure side depending on the force balance between the Coriolis and centrifugal forces (see Figure 5.8), explaining contradictory results found in the literature. We also observed experimentally that the flow in the diffuser could be radially stratified during gas lock events (see Figure 4.4), which was assumed in the model developed by Barrios and Prado, but to our knowledge never observed.

We qualitatively observed the flow pattern and when applicable the bubble size distribution, and found that apart from the first impeller which acted as a mixer, all the subsequent stages showed the same characteristics. However, the bubble size distribution within a single stage was not uniform: especially at low flow rates, the bubbles in the diffuser recirculation were larger than at the impeller outlet (Video D1, Figure 4.6). These observations were used to make the bubble size estimation presented in Section 5.1.4.

The rapid variation of the local gas fraction and associated flow patterns within the pump was recorded through both high speed videos and pressure and torque measurements. We showed that the pump performance was only slightly affected by the pump inclination, despite the low rotation speed. The measured difference (Figure

4.14) was likely to be due to the inlet conditions, rather than to the flow in the pump itself: a horizontal pump resulted in more intense slugging and therefore worse gas handling performance than a vertical set-up (see Videos A1 and A2, and Figure 4.15).

The velocity measurements and flow visualisation carried out in single phase liquid flow exposed a possible cause to the flat head curve in this particular mixed-flow design: no rotating stall was observed, in the impeller or diffuser, but the change in the recirculation pattern at low flow rate could be a reason for a change in the head curve gradient. Moreover, the large standard deviation of the measured velocity, especially in the impeller blade wakes, showed that the instantaneous flow field can be substantially different from the average flow field.

6.2 Possible improvements

One of the original ideas of this work was to use the single phase liquid velocity data obtained with the LDV system as a basis for predicting the bubbles trajectory at low gas fraction. This ambitious objective was not achieved, as the quality and extent of the velocity measurement was not suitable to be used in modelling, and also because the resolution of the high speed videos was too low and the image processing technique used could not produce a reliable bubble trajectory. An automated traverse system, and the use of alternative materials or fluids to reduce the beam distortion induced by the pump curvature are key elements that would improve the quality and extent of the velocity measurement.

From the flow visualisation perspective, using a macro lens, an additional camera and the image processing technique proposed by Besagni and Inzoli (2016) could give quantitative results on the bubbles trajectories and size distribution.

We have also seen in chapter 4 that the inlet conditions in multiphase flow were unsteady (Figure 4.15). A tighter control on the inlet pressure should provide more accurate data, and perhaps a better understanding of the effect of flow rate and rotation speed on the head degradation factor. Using the same pump design in a flow loop facility that can handle the pressure required to run at full speed (at least 50 Hz) would enable a comparison with the low speed experiments, where flow visualisation is possible.

The model presented in chapter 5 only takes the impeller into account and neglects the flow in the diffuser. Since most of the pressure is produced in the impeller, it was assumed that most of the head degradation would also occur in the impeller. In mixed-flow pumps, the diffuser role is to straighten the flow and to bring it to the next impeller inlet, while minimising the pressure losses. It is likely that in the absence of recirculation, the flow in the diffuser has a negligible effect on the head degradation. However this would need to be proven, for example through further experimental measurements comparing two well-designed diffusers with the same impeller. Similarly, it would be useful to carry out more experiments with impeller designs that are close enough to each other in order to verify that the model sensitivity to each parameter is

consistent with reality. This validation work requires a close collaboration with pump designers.

Finally, the Equilibrium Velocity method developed in this thesis could be used with the results from three-dimensional, single-phase flow simulation, which are routinely carried out for pump design or research, in order to obtain more accurate gas-handling prediction, particularly regarding recirculation patterns which are not taken into account in the present work.

6.3 Further work

This work has exposed several important knowledge and technical gaps in the field of gas-liquid flows through ESPs. The bubble size distribution appears as a critical parameter, and even though we have proposed a model (Section 5.1.4) to determine the maximal bubble size depending on the fluids properties and pump operation conditions, there are still many unknowns, particularly in the role of density, viscosity, interfacial tension and the presence of surfactants. Small scale experiments with different fluids could be carried out to reach a better fundamental understanding of bubble size distributions in fluids typically seen in oil and gas production (hydrocarbons, brine, surfactants). For practical reasons, it is easier to validate a model predicting the pump performance with a nitrogen-water mixture at low pressure, but it is therefore necessary to find a way to extrapolate these results to the fluids actually produced. In particular, the effect of the alternative Bond number B, defined in (5.13) and density ratio ξ between the two phases are important to assess as their order of magnitude change between test and production conditions (see Table 5.5).

The problem of system stability has also been briefly discussed in Section 1.3.3 but needs further developments: knowing the head curve of a pump in the presence of gas is only the first step in designing an ESP string to produce a gassy well. Numerical models exist to assess the stability of a production system, especially for multiphase flows. However, the pump is usually modelled as a simple pressure increment, and the head degradation due to gas is rarely taken into account. These simulations also require a lot of computational resources. An analytical analysis could be very useful for selecting the equipment needed for a simple installations, where gas is a problem but such complex simulations are too costly.

Bibliography

anonymous (1997). Recommended practice for electric submersible pump testing. Standard API G11S22, American Petroleum Institute.

Auton, T. R. (1984). *Dynamics of bubbles, drops, and particles in motion in liquids.* PhD thesis, University of Cambridge.

Auton, T. R., Hunt, J. C. R., and Prud'Homme, M. (1988). The force exerted on a body in inviscid unsteady non-uniform rotational flow. *Journal of Fluid Mechanics*, 197:241–257.

Bagci, A. S., Kece, M., and Nava, J. (2010). Challenges of using electrical submersible pump (ESP) in high free gas applications. In *Proceedings of SPE International Oil and Gas Conference and Exhibition in China*, 131760. Society of Petroleum Engineers.

Barrios, L. and Prado, M. G. (2011a). Experimental visualization of two-phase flow inside an electrical submersible pump stage. *Journal of Energy Resources Technology*, 133(4):042901.

Barrios, L. and Prado, M. G. (2011b). Modeling two-phase flow inside an electrical submersible pump stage. *Journal of Energy Resources Technology*, 133(4):042902.

Basset, A. B. (1888). On the motion of a sphere in a viscous liquid. *Philosophical Transactions of the Royal Society of London. A*, 179:43–63.

Batchelor, G. K. (1987). The stability of a large gas bubble rising through liquid. *Journal of Fluid Mechanics*, 184:399–422.

Bedrin, V. G., Khasanov, M. M., Khabibullin, R. A., Krasnov, V. A., Pashali, A. A., Litvinenko, K. V., Elichev, V. A., and Prado, M. (2008). High GLR ESP technologies comparison, field test results. In *Proceedings of SPE Russian Oil & Gas Conference and Exhibition*, page 117414. Society of Petroleum Engineers.

Bel Fdhila, R. and Duineveld, P. C. (1996). The effect of surfactant on the rise of a spherical bubble at high Reynolds and Peclet numbers. *Physics of Fluids*, 8(2):310–321.

Benjamin, T. B. (1987). Hamiltonian theory for motions of bubbles in an infinite liquid. *Journal of Fluid Mechanics*, 181:349–379.

Besagni, G. and Inzoli, F. (2016). Bubble size distributions and shapes in annular gap bubble column. *Experimental Thermal and Fluid Science*, 74:27–48.

Blasius, H. (1913). *Das ähnlichkeitsgesetz bei reibungsvorgängen in flüssigkeiten*, pages 1–41. Springer.

Bluemink, J. J., Lohse, D., Prosperetti, A., and Van Wijngaarden, L. (2008). A sphere in a uniformly rotating or shearing flow. *Journal of Fluid Mechanics*, 600:201–233.

Boussinesq, J. (1885). *Applications des potentiels à l'étude de l'équilibre des corps solides élastiques*. Gauthier-Villars, Paris.

Bratu, C. (1995). Two-phase pump transient behaviour. In *SPE Annual Technical Conference and Exhibition*.

Braun, O. (2009). *Part Load Flow in Radial Centrifugal Pumps*. Phd thesis, Ecole Polytechnique de Lausanne.

Brennen, C. E. (2011). *Hydrodynamics of pumps*. Cambridge University Press.

Brunings, C. and Ramirez, M. (2013). Automated surface gas handling through expert systems for optimization of artificial lift systems. In *2013 SPE Artificial Lift Conference-Americas*, page 165009. Society of Petroleum Engineers.

Bush, J. and Eames, I. (1998). Fluid displacement by high Reynolds number bubble motion in a thin gap. *International Journal of Multiphase Flow*, 24(3):411–430.

Cadot, O., Douady, S., and Couder, Y. (1995). Characterization of the low pressure filaments in a three dimensional turbulent shear flow. *Physics of Fluids*, 7(3):630–646.

Camilleri, L., Segui, E., Valette, P., and Brunet, L. (2009). Poseidon gas handling technology: A case study of two ESP wells in congo. In *Proceedings of Gulf Coast Section Electric Submersible Pump Workshop*. Society of Petroleum Engineers.

Cardona, A., O'Quinn, R., and Fry, S. (2014). ESP gas handling technology increases oil production over 100Mature reservoir in the Gulf of Mexico: A case history. In *Proceedings of OTC 2014*, 25324, OTC. Offshore Technology Conference.

Caridad, J., Asuaje, M., Kenyery, F., Tremante, A., and Aguillòn, O. (2008). Characterization of a centrifugal pump impeller under two-phase flow conditions. *Journal of Petroleum Science and Engineering*, 63(1-4):18–22.

Chen, J. (1974). Growth of the boundary layer on a spherical gas bubble. *Journal of Applied Mechanics*, 41(4):873–878.

Cheung, S. C. P., Deju, L., Yeoh, G. H., and Tu, J. Y. (2013). Modeling of bubble size distribution in isothermal gas-liquid flows: Numerical assessment of population balance approaches. *Nuclear Engineering and Design*, 265(0):120–136.

Clift, R., Grace, J. R., and Weber, M. E. (1978). *Bubbles, drops, and particles*. Courier Corporation.

Cuenot, B., Magnaudet, J., and Spennato, B. (1997). The effects of slightly soluble surfactants on the flow around a spherical bubble. *Journal of Fluid Mechanics*, 339:25–53.

Darwin, C. (1953). Note on hydrodynamics. In *Mathematical Proceedings of the Cambridge Philosophical Society*, volume 49, pages 342–354. Cambridge University Press.

Duineveld, P. (1995). The rise velocity and shape of bubbles in pure water at high reynolds number. *Journal of Fluid Mechanics*, 292:325–332.

Euler, L. (1754). Théorie plus complète des machines qui sont mises en mouvement par la reaction de l'eau. *Histoire de L'Academie Royale des Sciences et Belle Lettres*, pages 227–295.

Furukawa, A., Shirasu, S., and Sato, S. (1996). Experiments on air-water two-phase flow pump impeller with rotating-stationary circular cascades and recirculating flow holes. *JSME International Journal*, 39(3).

Gamboa, J. (2008). *Prediction of the transition in two-phase performance of an electrical submersible pump*. Phd thesis, University of Tulsa.

Gamboa, J. and Prado, M. (2011). Review on ESP surging correlations and models. In *SPE Production and Operations Symposium*, 140937. Society of Petroleum Engineers.

Gamboa, J. and Prado, M. (2012). Experimental study of two-phase performance of an electric-submersible-pump stage. *SPE*.

Greitzer, E. M. (1981). The stability of pumping systems. *Journal of Fluids Engineering*, 203:103–242.

Gulich, J. F. (2007). *Centrifugal pumps*. Springer.

Han, L., Luo, H., and Liu, Y. (2011). A theoretical model for droplet breakup in turbulent dispersions. *Chemical Engineering Science*, 66(4):766–776.

Hanratty, T. J. (2013). *Physics of Gas-Liquid Flows*. Cambridge University Press.

Hassenpflug, W. C. (2010). The incompressible two-dimensional potential flow through blades of a rotating radial impeller. *Mathematical and Computer Modelling*, 52(9-10):1299–1389.

Hesketh, R. P., Etchells, A. W., and Russell, T. W. F. (1991). Bubble breakage in pipeline flow. *Chemical Engineering Science*, 46(1):1–9.

Hesketh, R. P., Fraser Russell, T. W., and Etchells, A. W. (1987). Bubble size in horizontal pipelines. *AIChE Journal*, 33(4):663–667.

Hinze, J. O. (1955). Fundamentals of the hydrodynamic mechanism of splitting in dispersion processes. *AIChE Journal*, 1(3):289–295.

Hua, G., Falcone, G., Teodoriu, C., and Morrison, G. L. (2012). Comparison of multiphase pumping technologies for subsea and downhole applications. *Oil and Gas Facilities*.

Junior, R., Domingos, P. V. S. R., and dos Reis, D. C. (2015). Experimental evaluation of behavior of intermittent flow in scenario of application of electrical submersible pump. In *SPE Artificial Lift - Latin America and Caribbean*, 173958, SPE. Society of Petroleum Engineers.

Kallas, P. and Way, K. (1995). An electrical submergible pumping system for high GOR wells. In *SPE Electrical Submergible Pump Workshop*.

Karn, A., Ellis, C., Arndt, R., and Hong, J. (2015). An integrative image measurement technique for dense bubbly flows with a wide size distribution. *Chemical Engineering Science*, 122:240–249.

Knudsen, H. R. (2013). *Multiphase performance validation*. Master thesis, Norwegian University of Science and Technology.

Kowe, R., Hunt, J., Hunt, A., Couet, B., and Bradbury, L. (1988). The effects of bubbles on the volume fluxes and the pressure gradients in unsteady and non-uniform flow of liquids. *International journal of multiphase flow*, 14(5):587–606.

Lakshminarayana, B. (1995). *Fluid dynamics and heat transfer of turbomachinery*. John Wiley & Sons.

Lamb, H. (1932). *Hydrodynamics*. Cambridge University Press.

Lea, J. F. and Bearden, J. L. (1982). Effect of gaseous fluids on submersible pump performance. *Journal of Petroleum Technology*.

Lee, W. Y. (1997). Downhole pumping system for recovering liquids and gas. Patent Patent 5628616, Camco International Inc.

Legendre, D. and Magnaudet, J. (1998). The lift force on a spherical bubble in a viscous linear shear flow. *Journal of Fluid Mechanics*, 368:81–126.

Levich, V. G. (1962). *Physicochemical hydrodynamics*. Prentice-Hall, Englewood Cliffs, N.J.

Liao, Y. and Lucas, D. (2010). A literature review on mechanisms and models for the coalescence process of fluid particles. *Chemical Engineering Science*, 65(10):2851–2864.

Lighthill, M. J. (1956). Drift. *Journal of Fluid Mechanics*, 1(01):31–53.

Lomb, N. R. (1976). Least-squares frequency analysis of unequally spaced data. *Astrophysics and space science*, 39(2):447–462.

Lunde, K. and Perkins, R. J. (1997). Shape oscillations of rising bubbles. *Applied Scientific Research*, 58(1):387–408.

MacNeil, D. and Dass, P. (2012). Replacing ESP and gas lift with ESTSP (electric submersible twin screw pumps). In *SPE Artificial Lift Conference and Exhibition*, 163115.

Magnaudet, J. and Eames, I. (2000). The motion of high-reynolds-number bubbles in inhomogeneous flows. *Annual Review of Fluid Mechanics*, 32(1):659–708.

Markets and Markets (2013). Artificial lift market, by types (rod lift, esp, pcp, gas lift) & geography - global trends & forecasts to 2018. *Markets and Markets*.

Martinez-Bazan, C., Rodriguez-Rodriguez, J., Deane, G. B., Montanes, J. L., and Lasheras, J. C. (2010). Considerations on bubble fragmentation models. *Journal of Fluid Mechanics*, 661:159–177.

Maxey, M. R. and Riley, J. J. (1983). Equation of motion for a small rigid sphere in a nonuniform flow. *Physics of Fluids*, 26(4):883–889.

Maxworthy, T., Gnann, C., uuml, rten, M., and Durst, F. (1996). Experiments on the rise of air bubbles in clean viscous liquids. *Journal of Fluid Mechanics*, 321:421–441.

Mei, R., Klausner, J. F., and Lawrence, C. J. (1994). A note on the history force on a spherical bubble at finite reynolds number. *Physics of fluids*, 6(1):418–420.

Meiron, D. (1989). On the stability of gas bubbles rising in an inviscid fluid. *Journal of Fluid Mechanics*, 198:101–114.

Merle, A., Legendre, D., and Magnaudet, J. (2005). Forces on a high Reynolds-number spherical bubble in a turbulent flow. *Journal of Fluid Mechanics*, 532:53–62.

Michaelides, E. E. (2003). Hydrodynamic force and heat/mass transfer from particles, bubbles, and drops - the Freeman scholar lecture. *Journal of Fluids Engineering*, 125(2):209–238.

Milne-Thompson, L. (1968). Theoretical hydrodynamics. *London: MacMillan, 1968, 5th ed.*

Minemura, K. and Murakami, M. (1980). A theoretical study on air bubble motion in a centrifugal pump impeller. *Transaction of the ASME*, 102(4).

Minemura, K. and Uchiyama, T. (1994). Three-dimensional calculation of air-water two-phase flow in a centrifugal pump based on a bubbly flow model with fixed cavity. *JSME International Journal*, 37(4).

Minemura, K., Uchiyama, T., Shoda, S., and Egashira, K. (1998). Prediction of air-water two-phase flow performance of a centrifugal pump based on one-dimensional two-fluid model. *Journal of Fluids Engineering*, 120:327–334.

Moore, D. (1965). The velocity of rise of distorted gas bubbles in a liquid of small viscosity. *Journal of Fluid Mechanics*, 23(4):749–766.

Moore, D. W. (1963). The boundary layer on a spherical gas bubble. *Journal of Fluid Mechanics*, 16(2):161–176.

Naciri, A. (1992). *Contribution à l'étude des forces exercées par un liquide sur une bulle de gaz: portance, masse ajoutée et interactions hydrodynamiques*. Thesis, Ecole Centrale de Lyon.

Odar, F. and Hamilton, W. S. (1964). Forces on a sphere accelerating in a viscous fluid. *Journal of Fluid Mechanics*, 18(2):302–314.

Oseen, C. W. (1913). *Uber den Goltigkeitsbereich der Stokesschen Widerstandsformel*. Friedländer.

Ossia, S. and Godeluck, J. (2006). Gas-liquid flow cfd study of SN8500. Internal Report GeMS 100318644, Schlumberger Ltd.

Ossia, S. and Guénégo, M. (2006). ESP performance in gas-liquid flows- experimental analysis of head degradation. Internal Report GeMS 100318163, Schlumberger Ltd.

Pedersen, N., Larsen, P. S., and Jacobsen, C. B. (2003). Flow in a centrifugal pump impeller at design and off-design conditions - part 1: Particle image velocimetry (PIV) and laser doppler velocimetry (LDV) measurements. *Journal of Fluids Engineering*, 125(1):61.

Peyramale, F. (2013). Study of the correlation between ESP run life and starts and stops. Internal Report GFE Project - AL - CDPH 103560, Schlumberger Ltd.

Pirouzpanah, S., Gudigopuram, S. R., and Morrison, G. L. (2016). Two-phase flow characterization in a split vane impeller electrical submersible pump. *Journal of Petroleum Science and Engineering*.

Prasser, H.-M., Krepper, E., and Lucas, D. (2002). Evolution of the two-phase flow in a vertical tube - decomposition of gas fraction profiles according to bubble size classes using wire-mesh sensors. *International Journal of Thermal Sciences*, 41(1):17–28.

Rahime, F., Sakr, K., Areekat, M., and Suryadi, R. (2013). Application of the gas handlers in KOC. In *SPE Middle East Oil and Gas Show and Conference*, 164309. Society of Petroleum Engineers.

Rastello, M., Marié, J.-L., and Lance, M. (2011). Drag and lift forces on clean spherical and ellipsoidal bubbles in a solid-body rotating flow. *Journal of Fluid Mechanics*, 682:434–459.

Ravelet, F., Colin, C., and Risso, F. (2011). On the dynamics and breakup of a bubble rising in a turbulent flow. *Physics of Fluids*, 23(10):103301.

Rivero, M., Magnaudet, J., and Fabre, J. (1991). Quelques résultats nouveaux concernant les forces exercées sur une inclusion sphérique par un écoulement accéléré. *Comptes rendus de l'Académie des sciences. Série 2: Mécanique, physique, chimie, sciences de l'univers, sciences de la terre*, 312:1499–1506.

Saffman, P. (1956). On the rise of small air bubbles in water. *Journal of Fluid Mechanics*, 1(3):249–275.

Schäfer, T., Bieberle, A., Neumann, M., and Hampel, U. (2015). Application of gamma-ray computed tomography for the analysis of gas holdup distributions in centrifugal pumps. *Flow Measurement and Instrumentation*, 46, Part B:262–267.

Schiff, J. (2013). *A Preliminary Design Tool For Radial Compressors*. Master thesis, Lund University.

Schobeiri, M. (2005). *Turbomachinery flow physics and dynamic performance*. Springer, Berlin.

Sherwood, J. (2005). One-dimensional modelling of two-phase flow: comparison of two pumps. Internal Report OFSR/DN/2005/008/FLM/C, Schlumberger Ltd.

Sterrett, J., Knight, R. W., and Reece, J. W. (1996). Analytical investigation into the kinematics of a single bubble passing through the impeller of a centrifugal pump. *ASME, New York*, 1(372).

Sterrett, J. D. (1994). *An experimental and analytical investigation into the performance of centrifugal pumps operating with air-water mixtures*. Phd thesis, Auburn University.

Stokes, G. G. (1851). *On the effect of the internal friction of fluids on the motion of pendulums*, volume 9. Transactions of the Cambridge Philosophical Society.

Takács, G. (2009). *Electrical submersible pumps manual: design, operations, and maintenance*. Gulf professional publishing.

Taylor, G. I. (1928). The forces on a body placed in a curved or converging stream of fluid. In *Proceedings of the Royal Society of London A: Mathematical, Physical and Engineering Sciences*, volume 120, pages 260–283. The Royal Society.

Taylor, T. and Acrivos, A. (1964). On the deformation and drag of a falling viscous drop at low Reynolds number. *Journal of Fluid Mechanics*, 18(3):466–476.

Thomas, N., Auton, T., Sene, K., and Hunt, J. (1983). Entrapment and transport of bubbles by transient large eddies in multiphase turbulent shear flows. In *International conference on the physical modelling of multi-phase flow*, pages 169–184.

Tillack, P. (1998). *Förderverhalten von Kreiselpumpen bei viskosen, gasbeladenen Flüssigkeiten*. Phd thesis, TU Kaiserslautern.

Tomiyama, A., Tamai, H., Zun, I., and Hosokawa, S. (2002). Transverse migration of single bubbles in simple shear flows. *Chemical Engineering Science*, 57(11):1849–1858.

Tryggvason, G. and Ervin, E. (1997). The rise of bubbles in a vertical shear flow. *Journal of Fluids Engineering*, 119:443–449.

Tryggvason, G., Scardovelli, R., and Zaleski, S. (2011). *Direct numerical simulations of gas–liquid multiphase flows*. Cambridge University Press.

Turpin, J. L., Lea, J. F., and Bearden, J. L. (1986). Gas-liquid flow through centrifugal pumps - correlation of data. In *Proceedings of the Third International Pump Symposium*, pages 13–20.

Van Dongen, H. P., Olofsen, E., VanHartevelt, J. H., and Kruyt, E. W. (1999). Searching for biological rhythms: peak detection in the periodogram of unequally spaced data. *Journal of Biological Rhythms*, 14(6):617–620.

Velasquez, G., Kain, J., Villamizar, M., Yong, Z., Dhar, J., Carvajal M, G. A., Goel, H. K., Nasr, H., Moricca, G., Cullick, A. S., Bermudez, F., Querales, M., Rodriguez, J. A., and Al-Jasmi, A. K. (2013). ESP "smart flow" integrates quality and control data for diagnostics and optimization in real time. In *Proceedings of SPE Conference 2013*, 163809. Society of Petroleum Engineers.

Visser, F. C. (1996). *On the Flow in Centifugal Impellers*. Phd thesis, University of Twente, NL.

Wiesner, F. (1967). A review of slip factors for centrifugal impellers. *Journal of Engineering for power*, 89(4):558–566.

Xue, J. (2004). *Bubble velocity, size and interfacial area measurements in bubble columns*. Phd thesis, Sever Institute of Washington University.

Yang, S. and Leal, L. (1991). A note on memory integral contributions to the force on an accelerating spherical drop at low Reynolds number. *Physics of Fluids A: Fluid Dynamics*, 3(7):1822–1824.

Ye, Z., Rutter, R., Martinez, I., and Marsis, E. (2016). Cfd and fea-based, 3d metal printing hybrid stage prototype on electric submersible pump esp system for high-gas wells. In *North American Artificial Lift Conference and Exhibition*, 181221. Society of Petroleum Engineers.

Zhang, J. Y., Zhu, H. W., Ding, K., and Qiang, R. (2012). Study on measures to improve gas-liquid phase mixing in a multiphase pump impeller under high gas void fraction. *IOP Conference Series: Earth and Environmental Science*, 15(6):062023.

Zhu, J. and Zhang, H.-Q. (2016). Mechanistic modeling and numerical simulation of in-situ gas void fraction inside ESP impeller. *Journal of Natural Gas Science and Engineering*, 36, Part A:144–154.

Zhu, J., Zhang, H.-q., et al. (2014). CFD simulation of ESP performance and bubble size estimation under gassy conditions. In *SPE Annual Technical Conference and Exhibition*, 170727. Society of Petroleum Engineers.

Appendix A

Simplified flow field in a mixed-flow impeller

A.1 Euler pump equation

In this Appendix, we first give a derivation of the Euler pump equation (1.7) and detail the underlying assumptions, based on the analysis by Schobeiri (2005).

A.1.1 General equations

The relative velocity $\vec{w}$ and absolute velocity $\vec{W}$ are expressed using cylindrical coordinates (r, θ, z). We define the control volume V_c as shown on Figure A.1, going from the inlet to the outlet of the bladed part of the impeller, with the inlet surface S_1 and outlet surface S_2. The mass flow rate is $\dot{m}$ and fluid density ρ.

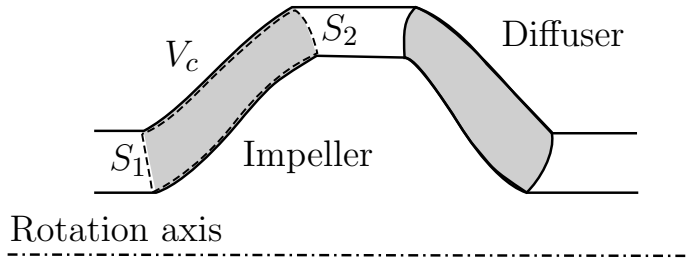

Figure A.1 Side cut (plane including the rotation axis) of a mixed-flow impeller and diffuser, with the volume control in the impeller blade passage area, where the Euler equations are applied.

Neglecting shear stresses at the inlet and outlet in the conservation of angular momentum for the control volume V_c, gives the moment of the force exerted by the flow on the blades $\vec{M}_0$:

$$\vec{M}_0 = -\frac{\partial}{\partial t}\left(\int_{V_c} \vec{X} \times \vec{W} dm\right) + \int_{S_1} \vec{X} \times \vec{W} d\dot{m} - \int_{S_2} \vec{X} \times \vec{W} d\dot{m},$$

where $\vec{X}$ is the position vector in V_c, $dm = \rho\ dV$ and $d\dot{m} = \rho\ \vec{n} \cdot \vec{W} dS$

The axial angular momentum is:

$$M_z = \vec{M}_0 \cdot \vec{e}_z = -\frac{\partial}{\partial t}\left(\int_{V_c} r\ W_\theta\ dm\right) + \int_{S_1} r\ W_\theta\ d\dot{m} - \int_{S_2} r\ W_\theta\ d\dot{m}. \tag{A.1}$$

We denote by $\mathcal{Q}$ the thermal energy, $\mathcal{W}$ the mechanical work added to the fluid in a fixed control volume V_c, e the specific total energy, and u the specific internal energy of the fluid, with $e = u + 1/2 W^2 + gz$. The conservation of energy for the control volume V_c gives

$$\dot{\mathcal{Q}} + \dot{\mathcal{W}} = \frac{\partial}{\partial t}\left(\int_{V_c} \rho e\ dV\right) + \int_{S_2} e d\dot{m} - \int_{S_1} e d\dot{m}.$$

The mechanical power $\dot{\mathcal{W}}$ comes from the shaft through the impeller blades, and from the pressure of fluid present upstream and downstream of the control volume.

$$\dot{\mathcal{W}} = \dot{\mathcal{W}}_{shaft} + \dot{\mathcal{W}}_{flow} = \dot{\mathcal{W}}_{shaft} + \int_{S_1} \frac{p}{\rho}\ d\dot{m} - \int_{S_2} \frac{p}{\rho}\ d\dot{m}$$

where p is the static pressure.

Finally, we have

$$\dot{\mathcal{Q}} + \dot{\mathcal{W}}_{shaft} = \frac{\partial}{\partial t}\int_{V_c} \rho e\ dV + \int_{S_2} h^T\ d\dot{m} - \int_{S_1} h^T\ d\dot{m} \tag{A.2}$$

where $h^T = p/\rho + u + 1/2 W^2 + gz$ is the total enthalpy.

A.1.2 Simplifying assumptions

Assuming an **adiabatic** flow ($\dot{\mathcal{Q}} = 0$) and **uniform density , pressure and velocity fields on** S_1 **and** S_2, the mechanical power transmitted to the fluid by the shaft is:

$$\dot{\mathcal{W}}_{shaft} = \frac{\partial E}{\partial t} + \left[\dot{m}\left(\frac{p}{\rho} + u + \frac{1}{2}W^2 + gz\right)\right]_1^2 = \frac{\partial E}{\partial t} + \left(\dot{m}_2 h_2^T - \dot{m}_1 h_1^T\right)$$

where $E = \int_{V_c} \rho e\ dV$.

If the system is **steady** and the **mass flow rate is constant** through the pump, we have $\partial E/\partial t = 0$ and $\dot{m}_1 = \dot{m}_2 = \dot{m}$. This results in $\dot{\mathcal{W}}_{shaft} = \dot{m}\ \Delta h^T$.

In the **absence of thermal, mechanical or hydraulic losses**, the power transmitted by the shaft to the fluid within the control volume V_c is:

$$-\omega M_z = \dot{m}\ \Delta h^T. \tag{A.3}$$

Since the velocity field is constant and uniform on S_1 and S_2, we use (A.1) to write the axial momentum exerted by the fluid on the blades

$$M_z = \int_{S_1} r\ W_\theta\ d\dot{m} - \int_{S_2} r\ W_\theta\ d\dot{m} = \dot{m}\left(\overline{R}_1 W_{\theta 1} - \overline{R}_2 W_{\theta 2}\right)$$

where $\overline{R} = \int r^2 dr / \int r dr$.

From (A.3), we obtain the total enthalpy variation through the impeller:

$$\Delta h^T = \omega\left(\overline{R}_2 W_{\theta 2} - \overline{R}_1 W_{\theta 1}\right)$$

Finally, if the working **fluid is inviscid and incompressible**, $h^T = p^T/\rho$ so we have the so-called Euler equation for pumps, as it was first derived by Euler (1754)):

$$\boxed{\Delta p^T = \rho\ \omega\left(\overline{R}_2 W_{\theta 2} - \overline{R}_1 W_{\theta 1}\right).}$$

In practice, $\vec{W}$ is never uniform on S_1 or S_2, so this formula is only an approximation.

Assuming that $\vec{W}$ is well represented by the superimposition of a solid body rotation and a free vortex, we can derive a similar expression:

$$\Delta p^T = \rho\ \omega\left(R_2 W_{u2} - R_1 W_{u1}\right),$$

where R_1 and R_2 is the geometrical average of the hub and shroud radii, respectively at the inlet (subscript 1) and outlet (subscript 2). $R = \sqrt{(R^2_{shroud} + R^2_{hub})/2}$, and $W_u = \vec{W}(R) \cdot \vec{e}_\theta$.

A.2 Parametric three dimensional flow

We consider a simplified impeller made of a rotating annulus of increasing diameter, whose inner and outer boundaries are truncated cones, as represented in Figure 5.1.

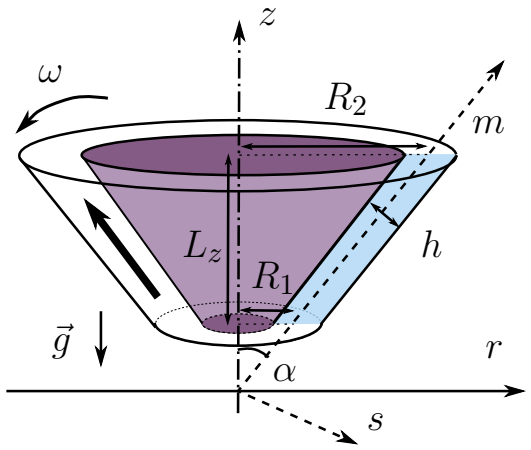

Figure A.2 Sketch of the flow geometry: an annulus whose diameter increases in the flow direction.

The annulus has a constant width h and an increasing mean radius $R(z) = z\tan\alpha$. The special cases $\alpha = \pi/2$ or $\alpha = 0$ are considered separately and correspond to purely radial or purely axial geometries.

Rotating the base $(\vec{e_z}, \vec{e_r})$ by an angle α around $\vec{e_\varphi}$ gives the new base $(\vec{e_m}, \vec{e_s})$ with the associated coordinates (m, s). m is called the meridional coordinate and s the span-wise coordinate, defined by

$$\begin{cases} \vec{e_m} = \sin\alpha\ \vec{e_r} + \cos\alpha\ \vec{e_z} \\ \vec{e_s} = \cos\alpha\ \vec{e_r} - \sin\alpha\ \vec{e_z} \end{cases}$$

The annular cross-flow area $A(z) = 2\pi h z \tan\alpha$ increases along the flow path and the meridional flow velocity consequently decreases.

A.2.1 Analytical liquid velocity profile

The absolute velocity field $\vec{W}$ is axisymmetric and the total volumetric flow rate through the annulus is Q. We assume that the relative tangential velocity follows a free vortex of circulation Γ_0, and the meridional velocity is uniform across s.

$$\vec{W}(r,z) = \frac{Q}{2\pi h m \sin\alpha}\ \vec{e_m} + \left(\frac{\Gamma_0}{2\pi m \sin\alpha} + \omega r\right)\vec{e_\theta} \tag{A.4}$$

where $m = r\sin\alpha + z\cos\alpha$.

We define the non-dimensional parameters based on the impeller outer radius R_2, rotation speed ω and water density ρ_w. The Reynolds number is based on the density ρ and viscosity μ of the working fluid. Φ is the flow coefficient, defined similarly to (1.4).

$$\begin{aligned} \Phi &= Q/\omega R_2^3 \\ \Phi \cot\beta &= -\Gamma_0/\omega h R_2^2 \\ Re &= \rho\omega R_2^2/\mu \end{aligned} \tag{A.5}$$

The other parameters and variables are also normalised using the length scale R_2, the time scale $1/\omega$ and the mass ρ_w/R_2^3. For the rest of this section, all quantities are assumed non-dimensional without any change in notation, except for the inlet radius noted $r_1 = R_1/R_2$ which is sometimes called the tip to hub ratio. The non-dimensional outlet radius is $r_2 = 1$.

The non-dimensional absolute velocity is therefore:

$$\vec{W}(r,z) = \frac{\Phi}{2\pi h m \sin\alpha}\ \vec{e}_m + \left(-\frac{\Phi\cot\beta}{2\pi h m\sin\alpha} + r\right)\vec{e}_\theta \tag{A.6}$$

The relative non-dimensional liquid velocity is

$$\vec{w}(r,z) = \frac{\Phi}{2\pi h m\sin\alpha}\left(\vec{e}_m + \cot\beta\ \vec{e}_\varphi\right)$$

A.2.2 Streamlines

The liquid streamlines in the rotating frame of reference are defined by the equation $d\vec{r}\times\vec{w} = \vec{0}$. For a streamline starting at $(r = r_0, \varphi = 0, z = r_0\cot\alpha)$,

$$r(\varphi) = r_0\ e^{\varphi\ \tan\beta\sin\alpha} \qquad \text{and} \qquad z(r) = r\ \cot\alpha$$

The divergence and vorticity of this flow field are

$$\begin{cases} \vec{\nabla}\cdot\vec{w} = \dfrac{\Phi}{2\pi h m\sin\alpha}\left(\dfrac{\sin\alpha}{r} - \dfrac{1}{m}\right) \\ \vec{\nabla}\times\vec{w} = -\dfrac{\Phi\cot\beta}{2\pi h m^2\sin\alpha}\left[\cos\alpha\ \vec{e}_r + \dfrac{m - r\ \sin\alpha}{r}\vec{e}_z\right] \end{cases}$$

Assuming that the passage height is small compared to the pump diameter ($h\cos\alpha << 1$), we can make the approximation $r \approx m\sin\alpha$. The velocity field therefore describes a two dimensional flow on a conical surface $r = z\tan\alpha$ with streamlines forming logarithmic spirals of constant angle β relative to the tangential direction $\vec{e}_\varphi$, as shown on Figure 5.2.

With this approximation, the flow divergence is $\vec{\nabla}\cdot\vec{w} = 0$ and its vorticity is:

$$\vec{\nabla} \times \vec{w} = \frac{\Phi \cot\beta \cos\alpha}{2\pi h r^2}\ \vec{e}_m$$

This correspond in dimensional notation to a vorticity of $\Gamma_0 \cos\alpha$. The material derivative is

$$\left(\vec{w}\cdot\vec{\nabla}\right)\vec{w} = -\left(\frac{\Phi}{2\pi h}\right)^2 \frac{\left(\sin^2\alpha + \cot^2\beta\right)\vec{e}_r + \cos\alpha\ \sin\alpha\ \vec{e}_z}{r^3}$$

A.2.3 Pressure field

The pressure p in the undisturbed, absolute liquid flow $\vec{W}$ follows:

$$-\frac{\vec{\nabla} p}{\rho} = \frac{D\vec{W}}{Dt} = \frac{\partial \vec{W}}{\partial t} + \left(\vec{W}\cdot\vec{\nabla}\right)\vec{W}$$

Using the expression of the absolute velocity (A.6), the pressure gradient is

$$\begin{aligned}\frac{\vec{\nabla} p(r,\theta,z)}{\rho} = &\left(\frac{\Phi}{2\pi h \sin\alpha}\right)^2 \frac{\vec{e}_m}{m^3} + \left[\left(\frac{\Phi\cot\beta}{2\pi h\sin\alpha}\right)^2 \frac{1}{m^2 r} + \frac{\Phi\cot\beta}{\pi h m \sin\alpha} + r\right]\vec{e}_r \\ &+ \left[\frac{\Phi^2\cot\beta}{4\pi^2 h^2 m^2}\left(\frac{\sin\alpha}{m} - \frac{1}{r}\right) - \frac{\Phi}{\pi h m}\right]\vec{e}_\theta\end{aligned}$$

With the approximation $r \approx m\sin\alpha$ and from a known pressure P_0 at the location $(r = r_0, \theta = 0, z = r_0\cot\alpha)$, it is possible to integrate the pressure gradient according to

$$\begin{aligned}\frac{\vec{\nabla} p(r,\theta,z)}{\rho} &= \frac{1}{\rho}\left[\frac{\partial p}{\partial r}\vec{e}_r + \frac{1}{r}\frac{\partial p}{\partial \theta}\vec{e}_\theta + \frac{\partial p}{\partial z}\vec{e}_z\right] \\ &= \left(\frac{\Phi}{2\pi h\sin\beta}\right)^2 \frac{\vec{e}_r}{r^3} + \left(\frac{\Phi\cot\beta}{\pi h r} + r\right)\vec{e}_r - \frac{\Phi\sin\alpha}{\pi h r}\ \vec{e}_\theta\end{aligned}$$

For a uniform fluid density, we obtain after integration:

$$\begin{aligned}p(r,\theta,z) - P_0 = &-\frac{\rho}{2}\left(\frac{\Phi}{2\pi h\sin\beta}\right)^2\left(\frac{1}{r^2} - \frac{1}{r_0^2}\right) + \frac{\rho}{2}\left(r^2 - r_0^2\right) \\ &+ \rho\frac{\Phi\cot\beta}{\pi h}\log\left(\frac{r}{r_0}\right) - \rho\frac{\Phi\sin\alpha}{\pi h}(\theta - \theta_0)\end{aligned}$$

Along a streamline, $\theta = \varphi - t = -\log\left(\frac{r}{r_0}\right)\cot\beta/\sin\alpha - t$. Assuming that at the inlet: $P(r_1,\theta,z_1) = P_0$, the pressure in the rotating frame of reference along the streamline starting at r_1, $\varphi = 0$ and z_1 is:

$$p(r) - P_0 = -\frac{\rho}{2}\left(\frac{\Phi}{2\pi h\sin\beta}\right)^2\left(\frac{1}{r^2} - \frac{1}{r_1^2}\right) + \frac{\rho}{2}\left(r^2 - r_1^2\right) \tag{A.7}$$

The total pressure p^T is the sum of the static pressure p and the kinetic energy $E_c = 1/2\rho W^2$. The variation of total pressure along a streamline between the inlet r_1 and outlet $r_2 = 1$ is

$$\begin{aligned}\Delta p^T &= p^T(r_2) - p^T(r_1) = p(r_2) - p(r_1) + \frac{1}{2}\rho\left(W(r_2)^2 - W(r_1)^2\right) \\ &= \rho\left(1 - r_1^2\right),\end{aligned}$$

which is consistent with the total pressure variation found in (1.8) when applying the Euler equation with a constant blade angle.

A.2.4 Residence time

A particle of liquid in the flow described above will stay in the impeller for a time t_{res} given by

$$t_{res} = \int_{m_1}^{m_2} \frac{dm}{w_m} = \frac{\pi h \Phi}{\sin\alpha}\left(1 - r_1^2\right) \tag{A.8}$$

A.3 One-dimensional representation

All quantities in this section are normalised with the pump outer diameter R_2, the rotation speed ω and the water density ρ_w as in the previous sections. We consider a three-dimensional flow through a pump impeller. We assume the flow to be steady and axi-symmetrical. If there is no recirculation in the impeller or diffuser channels, the flow can be described with a one-dimensional model, also called a streamline model.

The reduction of a three-dimensional flow field, for example obtained by numerical simulation, to a one-dimensional representation is frequently used in order to make the results easier to visualise and understand for turbo-machinery designers, as described by Schiff (2013). In our case, it is a way of using a simple but realistic flow field to estimate the head degradation in an impeller.

Lines called "quasi-orthogonals" are shown in Figure A.3 and defined as a parametric curves:

$$\begin{aligned}\Gamma : [0,1] &\longrightarrow \mathbb{R}^2 \\ s &\longmapsto r(s),\ z(s)\end{aligned}$$

Several methods exist to define these lines which are "almost" orthogonal to the flow passage. An example is derived by Schiff (2013). The surface of revolution S is obtained by rotating the quasi-orthogonal Γ around the axis $\vec{e}_z$. The surface area A and the mass flow rate $\dot{m}$ through S are:

$$A = \int_S dS = \int_{\theta=0}^{2\pi} \int_\Gamma r d\theta d\Gamma = 2\pi \int_0^1 r(s) \left|\Gamma'\right| ds$$

$$\dot{m} = \int_S \rho \vec{W} \cdot \vec{n} \; dS = 2\pi\rho \int_\Gamma r \; \vec{W} \cdot \vec{n} \; d\Gamma = 2\pi\rho \int_0^1 r(s) \; W_n(s) \left|\Gamma'\right| ds$$

where $\vec{n}$ is the unit vector normal to S, and $W_n = \vec{W} \cdot \vec{n}$.

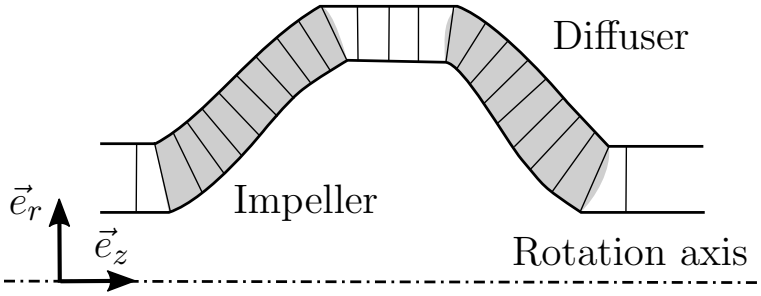

Figure A.3 The quasi-orthogonals join the hub to the shroud in the meridional plan. The blade extend is shown in grey.

For a straight quasi-orthogonal, $|\Gamma'|$ and $\vec{n}$ are constant. This is the case we consider in the following. We define the area average $\overline{q}$ and mass-flow average $\widetilde{q}$ of a quantity q as:

$$\overline{q} = \int_S q \; dS \Big/ A = \int_0^1 q(s) \; r(s) \; ds \; \Big/ \int_0^1 r(s) \; ds$$

$$\widetilde{q} = \int_S q \; d\dot{m} \; / \; \dot{m} = \int_0^1 q(s) \; W_n(s) \; r(s) \; ds \; \Big/ \int_0^1 W_n(s) \; r(s) \; ds$$

If W_n is constant along the quasi-orthogonal, then $\overline{q} = \widetilde{q}$.

We use the mean radii R and z-coordinates Z of each quasi-orthogonal to define the meridional streamline $\mathcal{M}$, or meanline shown in Figure A.4. The distance along the meridional profile is normalised so that the impeller extends from $m^* =$ to 1, and the diffuser from $m^* = 1$ to 2.

$$\begin{aligned} \mathcal{M} : [0,2] &\longrightarrow \mathbb{R}^2 \\ m^* &\longmapsto R(m^*), \; Z(m^*) \end{aligned}$$

The unit vector $\vec{e}_m$ tangent to the meridional streamline makes an angle α with $\vec{e}_z$. We make the simplifying assumption that the vectors $\vec{e}_m$ and $\vec{n}$ are collinear, and only refer to $\vec{e}_m$ in the rest of this analysis.

The streamline $\mathcal{L}$ is a three-dimensional curve drawn on the surface of revolution defined by the rotation of the meanline $\mathcal{M}$ around the rotation axis, associated to the relative velocity field $\vec{w}$.

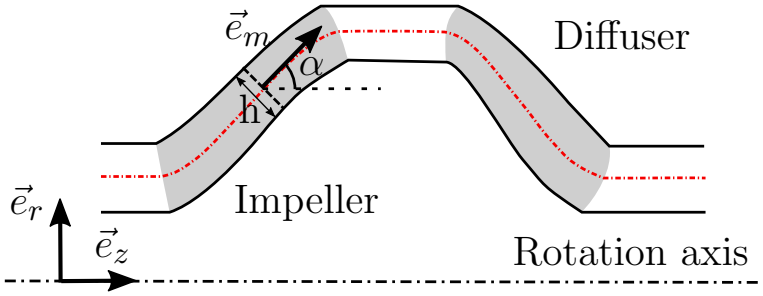

Figure A.4 Sketch of the impeller and diffuser passages in the (r, z) plane. The red dashed-dotted line is the mean streamline along which m is measured. The dashed perpendicular segment is a quasi-orthogonal. The meridional angle α is variable along the streamline as are the flow angle β and the passage height h.

$$\begin{aligned} \mathcal{L} : [0,2] &\longrightarrow \mathbb{R}^3 \\ m^* &\longmapsto R(m^*),\ \phi(m^*),\ Z(m^*) \end{aligned}$$

Ideally, the relative velocity is tangent to the streamline at all points. In practice, two cases are possible: If the streamline is determined geometrically and supports a one-dimensional computation of the velocity field, the relative velocity is tangential to the streamline by construction. If the velocity along the streamline is obtained by averaging a known three-dimensional velocity field, an iterative method can be used to ensure that the streamline respects this condition.

The definition of the streamline $\mathcal{L}$ implies the following relationship between the components R, ϕ, Z and the relative velocity field:

$$\begin{cases} \dfrac{d\phi}{dR} = \dfrac{w_\varphi}{r w_r} = \dfrac{\cot \beta_h}{r} = \dfrac{\cot \beta}{r \sin \alpha} \\ \dfrac{dZ}{dR} = \dfrac{w_z}{w_r} = \cot \alpha \end{cases} \tag{A.9}$$

Figures A.5 and A.6 define the angles α, β and β_h associated to the relative velocity as well as the streamline.

Considering an adiabatic and inviscid flow, the static pressure is obtained from the Euler equations in the rotating frame of reference:

$$-\vec{\nabla} p = \rho \left[\left(\vec{w} \cdot \vec{\nabla} \right) \vec{w} - r \vec{e}_r + 2 \vec{e}_z \times \vec{w} \right] \tag{A.10}$$

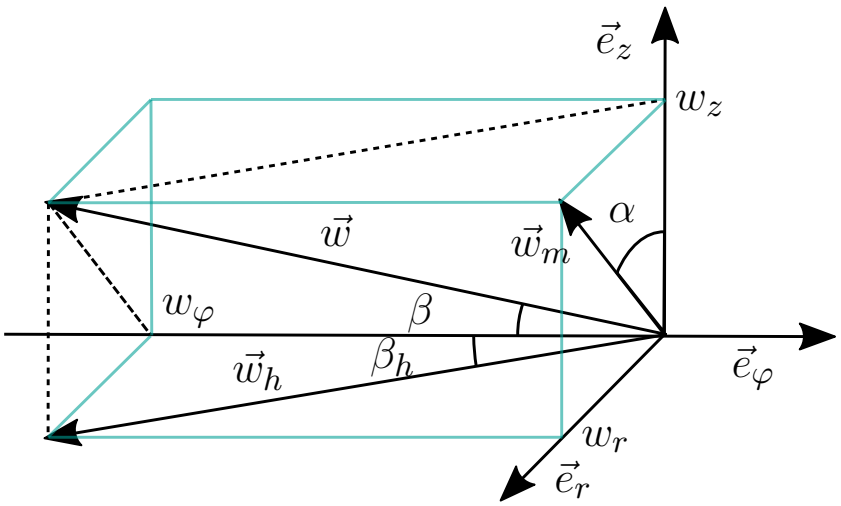

Figure A.5 Relative velocity in the cylindrical base, and associated angles.

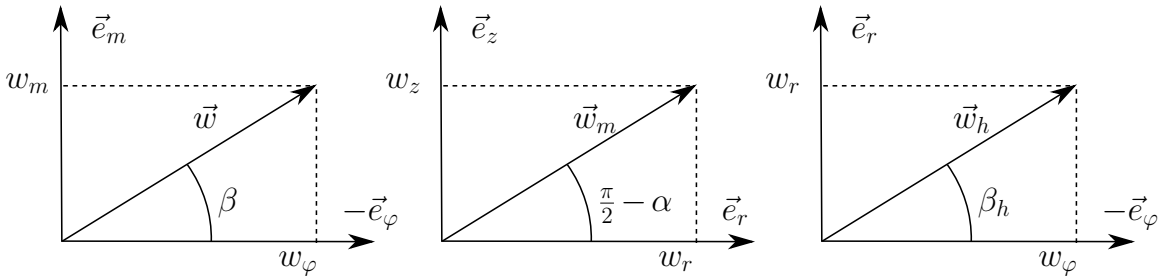

(a) Plane ($\vec{e}_\varphi$,$\vec{e}_m$). (b) Plane ($\vec{e}_r$,$\vec{e}_z$). (c) Plane ($\vec{e}_\varphi$,$\vec{e}_r$).

Figure A.6 Definition of the flow angles and relative velocity components.

This correspond to the following three equations in cylindrical coordinates:

$$-\frac{\partial p}{\partial r} = \rho\left[w_r\frac{\partial w_r}{\partial r} + w_z\frac{\partial w_r}{\partial z} - \frac{w_\varphi^2}{r} - r - 2w_\varphi\right] \tag{A.11a}$$

$$-\frac{1}{r}\frac{\partial p}{\partial \varphi} = \rho\left[w_r\frac{\partial w_\varphi}{\partial r} + w_z\frac{\partial w_\varphi}{\partial z} + \frac{w_\varphi w_r}{r} + 2w_r\right] \tag{A.11b}$$

$$-\frac{\partial p}{\partial z} = \rho\left[w_r\frac{\partial w_z}{\partial r} + w_z\frac{\partial w_z}{\partial z}\right] \tag{A.11c}$$

The total radial derivative of the pressure along the streamline is:

$$\frac{dp}{dr} = \frac{\partial p}{\partial r} + \frac{1}{r}\frac{\partial p}{\partial \varphi}\,\frac{d\phi}{dR} + \frac{\partial p}{\partial z}\,\frac{dZ}{dR}$$

Using the equations (A.9) and (A.11), we compute the radial pressure gradient along the streamline with the combination (A.11a) + (A.11b) $\times\, {}^{w_\varphi}/_{w_r}$ + (A.11c) $\times\, {}^{w_z}/_{w_r}$:

$$\begin{aligned}
-\left.\frac{dp}{dr}\right|_{\mathcal{L}} &= \rho\left[w_r\frac{\partial w_r}{\partial r} + w_z\frac{\partial w_r}{\partial z} + w_\varphi\frac{\partial w_\varphi}{\partial r} + \frac{w_z w_\varphi}{w_r}\frac{\partial w_\varphi}{\partial z} + w_z\frac{\partial w_z}{\partial r} + \frac{w_z^2}{w_r}\frac{\partial w_z}{\partial z} - r\right] \\
&= \rho\left[w_r\frac{\partial w_r}{\partial r} + w_\varphi\frac{\partial w_\varphi}{\partial r} + w_z\frac{\partial w_z}{\partial r} + \frac{w_z}{w_r}\left(w_r\frac{\partial w_r}{\partial z} + w_\varphi\frac{\partial w_\varphi}{\partial z} + w_z\frac{\partial w_z}{\partial z}\right) - r\right] \\
&= \rho\left[\frac{1}{2}\left(\frac{\partial w^2}{\partial r} + \frac{w_z}{w_r}\frac{\partial w^2}{\partial z}\right) - r\right]
\end{aligned}$$

On the other hand, the total radial derivative of the square relative velocity magnitude along the streamline is:

$$\left.\frac{dw^2}{dr}\right|_{\mathcal{L}} = \frac{\partial w^2}{\partial r} + \frac{1}{r}\frac{\partial w^2}{\partial z}\,\frac{d\phi}{dR} + \frac{\partial w^2}{\partial \varphi}\,\frac{dZ}{dR} = \frac{\partial w^2}{\partial r} + \frac{w_z}{w_r}\frac{\partial w^2}{\partial z}$$

Therefore,

$$\boxed{-\left.\frac{dp}{dr}\right|_{\mathcal{L}} = \rho\left(\frac{1}{2}\left.\frac{dw^2}{dr}\right|_{\mathcal{L}} - r\right).} \tag{A.12}$$

A.4 Two-Fluid one-dimensional equation

In this section, we demonstrate how to obtain the two-fluid one-dimensional equation (5.25), starting from the three-dimensional equation (5.23).

Expressing the forces applied on a bubble as defined by Auton et al. (1988), and neglecting gravity, we obtain the following non-dimensional equations in the stationary frame of reference $\mathcal{R}_0$:

$$\begin{cases} \alpha\xi\dfrac{D\vec{V}}{Dt} = -\alpha\vec{\nabla}p + \alpha\dfrac{3C_d}{4\varepsilon}\left|\vec{W}-\vec{V}\right|\left(\vec{W}-\vec{V}\right) + \alpha C_l\left(\vec{W}-\vec{V}\right)\times\left(\nabla\times\vec{W}\right) \\ \qquad\qquad + \alpha C_v\left(\dfrac{D\vec{W}}{Dt} - \dfrac{D\vec{V}}{Dt}\right) \\ (1-\alpha)\dfrac{D\vec{W}}{Dt} = -(1-\alpha)\vec{\nabla}p - \alpha\dfrac{3C_d}{4\varepsilon}\left|\vec{W}-\vec{V}\right|\left(\vec{W}-\vec{V}\right) - \alpha C_l\left(\vec{W}-\vec{V}\right)\times\left(\nabla\times\vec{W}\right) \\ \qquad\qquad - \alpha C_v\left(\dfrac{D\vec{W}}{Dt} - \dfrac{D\vec{V}}{Dt}\right). \end{cases}$$

To write these equation in the rotating frame of reference $\mathcal{R}_1$ (rotating around $\vec{e}_z$ at the angular speed ω), we use the following relationships between the absolute flow velocity fields for gas and liquid ($\vec{V}$ and $\vec{W}$), and the relative flow velocity fields $\vec{v}$ and $\vec{w}$.

$$\begin{aligned} \frac{D\vec{V}}{Dt} &= \frac{\partial\vec{v}}{\partial t} + \left(\vec{v}\cdot\vec{\nabla}\right)\vec{v} + \vec{e}_z\times(\vec{e}_z\times\vec{v}) + 2\vec{e}_z\times\vec{v} \\ \frac{D\vec{W}}{Dt} &= \frac{\partial\vec{w}}{\partial t} + \left(\vec{w}\cdot\vec{\nabla}\right)\vec{w} + \vec{e}_z\times(\vec{e}_z\times\vec{w}) + 2\vec{e}_z\times\vec{w} \\ \vec{\nabla}\times\vec{V} &= \vec{\nabla}\times\vec{v} + 2\vec{e}_z \\ \vec{\nabla}\times\vec{W} &= \vec{\nabla}\times\vec{w} + 2\vec{e}_z \end{aligned}$$

We get:

$$\begin{aligned} \alpha(\xi+C_v)\left[\left(\vec{v}\cdot\vec{\nabla}\right)\vec{v} + 2\vec{e}_z\times\vec{v}\right] &= -\alpha\vec{\nabla}p + \alpha\xi r\vec{e}_r \\ &\quad + \alpha\frac{3C_d}{4\varepsilon}|\vec{w}-\vec{v}|(\vec{w}-\vec{v}) + \alpha C_v\left(\vec{w}\cdot\vec{\nabla}\right)\vec{w} \\ &\quad + \alpha C_l(\vec{w}-\vec{v})\times(\nabla\times\vec{w}+2\vec{e}_z) \end{aligned} \tag{A.13a}$$

$$\begin{aligned} (1-\alpha+\alpha C_v)\left[\left(\vec{w}\cdot\vec{\nabla}\right)\vec{w} + 2\vec{e}_z\times\vec{w}\right] &= -(1-\alpha)\vec{\nabla}p + (1-\alpha)r\vec{e}_r \\ &\quad - \alpha\frac{3C_d}{4\varepsilon}|\vec{w}-\vec{v}|(\vec{w}-\vec{v}) + \alpha C_v\left(\vec{v}\cdot\vec{\nabla}\right)\vec{v} \\ &\quad - \alpha C_l(\vec{w}-\vec{v})\times(\nabla\times\vec{w}+2\vec{e}_z) \end{aligned} \tag{A.13b}$$

We assume that both the gas and liquid flow field are axisymmetrical and uniform on all quasi-orthogonals Γ (see Figure A.3. The liquid and gas are assumed to flow in

the same direction, so that the gas and liquid relative velocities are respectively $v\vec{e}_\zeta$ and $w\vec{e}_\zeta$. $\vec{e}_\zeta$ is tangent to a streamline (see Figure 5.2).

$$\vec{e}_\zeta = \sin\beta\ \vec{e}_m - \cos\beta\ \vec{e}_\varphi$$

This leads to defining a streamline $\mathcal{L} : m^* \longmapsto R(m^*),\ \phi(m^*),\ Z(m^*)$ and we have:

$$\begin{cases} \dfrac{d\phi}{dR} = \dfrac{w_\varphi}{rw_r} = \dfrac{v_\varphi}{rv_r} = \dfrac{\cot\beta}{r\sin\alpha} \\ \dfrac{dZ}{dR} = \dfrac{w_z}{w_r} = \dfrac{v_z}{v_r} = \cot\alpha \end{cases}$$

We use the same methods as in Section A.3 to reduce this system of equations (A.13) to a one-dimensional system:

$$\begin{cases} (\text{A.13a}) \cdot \vec{e}_r + (\text{A.13a}) \cdot \vec{e}_\varphi \times \dfrac{v_\varphi}{v_r} + (\text{A.13a}) \cdot \vec{e}_z \times \dfrac{v_z}{v_r} \\ (\text{A.13b}) \cdot \vec{e}_r + (\text{A.13b}) \cdot \vec{e}_\varphi \times \dfrac{w_\varphi}{w_r} + (\text{A.13b}) \cdot \vec{e}_z \times \dfrac{w_z}{w_r} \end{cases} \tag{A.14}$$

For simplicity, we use the notation $q' = dq/dr\,|_{\mathcal{L}}$ in the following identities:

$$\vec{e}_r + \frac{w_\varphi}{w_r}\vec{e}_\varphi + \frac{w_z}{w_r}\vec{e}_z = \frac{\vec{e}_\zeta}{\sin\alpha\sin\beta}$$

$$\vec{\nabla}p \cdot \vec{e}_r + \vec{\nabla}p \cdot \vec{e}_\varphi \frac{w_\varphi}{w_r} + \vec{\nabla}p \cdot \vec{e}_z \frac{w_z}{w_r} = \left.\frac{dp}{dr}\right|_{(L)} = p'$$

$$\begin{aligned} \left[\left(\vec{w}\cdot\vec{\nabla}\right)\vec{w}\right] \cdot \vec{e}_r + \left[\left(\vec{w}\cdot\vec{\nabla}\right)\vec{w}\right] \cdot \vec{e}_\varphi \frac{w_\varphi}{w_r} + \left[\left(\vec{w}\cdot\vec{\nabla}\right)\vec{w}\right] \cdot \vec{e}_z \frac{w_z}{w_r} &= \frac{1}{2}\frac{\partial w^2}{\partial r} + \frac{w_z}{2w_r}\frac{\partial w^2}{\partial z} \\ &= \left.\frac{dw^2}{dr}\right|_{\mathcal{L}} = w\left.\frac{dw}{dr}\right|_{\mathcal{L}} = ww' \end{aligned}$$

$$\begin{aligned} \left[\left(\vec{v}\cdot\vec{\nabla}\right)\vec{v}\right] \cdot \vec{e}_r + \left[\left(\vec{v}\cdot\vec{\nabla}\right)\vec{v}\right] \cdot \vec{e}_\varphi \frac{v_\varphi}{v_r} + \left[\left(\vec{v}\cdot\vec{\nabla}\right)\vec{v}\right] \cdot \vec{e}_z \frac{v_z}{v_r} &= \frac{1}{2}\frac{\partial v^2}{\partial r} + \frac{v_z}{2v_r}\frac{\partial v^2}{\partial z} \\ &= v\left.\frac{dv}{dr}\right|_{\mathcal{L}} = vv' \end{aligned}$$

$$[(\vec{w}-\vec{v}) \times (\nabla \times \vec{w} + 2\vec{e}_z)] \cdot \frac{\vec{e}_\zeta}{\sin\alpha\sin\beta} = \frac{(w-v)}{\sin\alpha\sin\beta}\left[\vec{e}_\zeta \times (\nabla \times \vec{w} + 2\vec{e}_z)\right] \cdot \vec{e}_\zeta = 0$$

Finally, (A.14) leads to:

$$\begin{cases} \alpha\left(\xi+C_v\right)v\ v' = -\alpha p' + \alpha\xi r + \alpha\dfrac{3C_d}{4\varepsilon}\dfrac{|w-v|\,(w-v)}{\sin\alpha\sin\beta} + \alpha C_v w\ w' \\ \left(1-\alpha+\alpha C_v\right)w\ w' = -\left(1-\alpha\right)p' + \left(1-\alpha\right)r \\ \qquad\qquad\qquad\qquad - \alpha\dfrac{3C_d}{4\varepsilon}\dfrac{|w-v|\,(w-v)}{\sin\alpha\sin\beta} + \alpha C_v v\ v' \end{cases} \tag{A.15}$$

Appendix B

Gas bubble in a non-homogeneous flow

This Appendix is a summary of the review by Magnaudet and Eames (2000) on the motion of gas bubbles at high Reynolds number. We define the bubble Reynolds number as

$$Re_b = \frac{2R|V_s|}{\nu},$$

where R is the bubble radius, $|V_s|$ is the difference between the velocity of the bubble centre and the velocity of the undisturbed liquid velocity U at the bubble location. In the bubble frame of reference, $U = V_s$.

B.1 Small bubble in slightly viscous fluid

B.1.1 Drag coefficient

For a clean bubble, when the Reynolds number is high enough, we can consider that there is no shear stress at the interface (the interface velocity is non-zero in the bubble frame of reference). We write the drag applied on the bubble in the form:

$$F_d = \frac{1}{2} C_d \pi \rho R^2 |V_s|,$$

where C_d is a drag coefficient, ρ the liquid density and R the bubble radius.

Levich (1962) uses the fact that there is no flow separation on a clean bubble at high Reynolds number to write:

$$C_d = \frac{48}{Re_b}$$

At low Reynolds number ($Re_b < 1$). Taylor and Acrivos (1964) find:

$$C_d = \frac{16}{Re_b} + 2 \tag{B.1}$$

For $Re_b > 50$, Moore (1963) showed that the thickness of the boundary layer is or order $\mathcal{O}(Re_b^{-1/2})$, while the extent of the near wake follows $\mathcal{O}(Re_b^{-1/4})$, except at the rear stagnation point, where the two region match. He concludes with an estimation of the drag coefficient for $Re_b > 50$:

$$C_d = \frac{48}{Re_b}\left(1 + \frac{2.21}{Re_b^{1/2}}\right) + \mathcal{O}\left(Re_b^{-1/6}\right) \tag{B.2}$$

At high Reynolds number, the drag comes for a third from the pressure variation around the bubble and two-third from the normal viscous stress.

Mei et al. (1994) give the following empirical drag coefficient for all Reynolds numbers:

$$C_d = \frac{16}{Re}\left(1 + \left[\frac{8}{Re} + \frac{1}{2}\left(1 + 3.315Re^{-1/2}\right)\right]^{-1}\right) \tag{B.3}$$

B.1.2 Elliptical bubble

For an elliptical bubble, we use the elliptical factor and Weber number defined as

$$\chi = \frac{\text{major axis}}{\text{minor axis}} \qquad \text{and} \qquad We = \frac{2\rho|V_s|^2 R}{\sigma}$$

Moore (1965) finds:

$$\chi = 1 + \frac{9}{64}We + \mathcal{O}(We^2), \tag{B.4}$$

and:

$$C_d = \frac{48G(\chi)}{Re_b}\left(1 - \frac{2.21H(\chi)}{Re_b^{1/2}}\right) + \mathcal{O}(Re_b^{-11/6}),$$

where G and H are two functions of the elliptical factor only. Duineveld (1995) shows that across the range, $100 < Re_b < 700$, $\max(We) \approx 3.27$ and $\max(\chi) \approx 0.72$.

At higher Reynolds number, the wake behind the bubble is separated. The vorticity production is independent of Re_b while the its advection increases with Re_b. Meiron (1989) observes a standing eddy behind an elliptic bubble in a specific (χ, Re_b) region. The potential flow theory cannot deal with separated wake or non-symmetrical bubbles which limits its use to study highly deformed bubbles at high Reynolds number $(100 \leq Re_b \leq 1000)$.

B.1.3 Path instability

Medium elliptical bubbles rising in a quiescent liquid can display a zig-zag or helical path. Saffman (1956) shows that the path can go from a zig-zag trajectory (in a plane)

to a helical trajectory (spiral) and instability only occurs for bubbles with an elliptical ratio $1.2 \leq \chi \leq 2.2$. Meiron (1989) indicates that the critical Reynolds number at which the instability starts to develop depends on the water purity:

For a clean bubble, the wake looses its axi-symmetry from $Re_b \approx 210$, and at this point the trajectory can become helical, with two vortex filaments. For a contaminated bubble, the next bifurcation is at $Re_b \approx 280$, where we see a zig-zag trajectory. Hairpin-like vortex are then shed from the bubble. Shape variation or interface slip are not necessary for path instability, but can play a role. Comparing the capillary time:

$$\left(\frac{8\rho R^3}{\sigma}\right)^{1/2}$$

with the gravity time

$$\left(\frac{2R}{g}\right)^{1/2}$$

f_2 deformation mode, can be locked to the shedding frequency (12 Hz), from $Re_b = 3000$, or $R \approx 4$ mm (in tap water)

B.1.4 Surfactants

Surfactants are molecules that change the surface tension of a fluid. They can be molecules with a hydrophilic and a hydrophobic end, that gather on the gas-liquid interface and restrain the transmission of momentum between the two phases.

Examples of surfactants are:

- Isotridecand
- Ethoxylated alcool
- Sodium Dodecyl Sulfate (SDS)
- Poly Ethoxy (Triton X_{100} or Brij 30)
- Decanoic acid

They affect the bubbles coalescence and break-up mechanism, their ability to dissolve, and also their drag coefficient when rising in a quiescent liquid. Maxworthy et al. (1996) found a 30 % difference in the terminal velocity for an elliptical bubble calculated with Moore's law, and what he observed in a water-glycerine solution, when the water was contaminated with surfactants. Bel Fdhila and Duineveld (1996) found that there is a critical surfactant concentration above which the bubble drag coefficient switches from the one of a spherical bubble to the one of a solid sphere. This threshold depends on the nature of the surfactant as well as on the bubble diameter.

Modelling the effect of the surfactants implies to examine the local effect of a certain concentration of surfactant on the surface tension, but also how the bulk fluid surfactant concentration is related to the interface surfactant concentration. The

adsorption and desorption of surfactant in and out of the interface are modelled using several non-dimensional numbers representing the main physico-chemical processes at play.

Peclet number:

$$Pe = \frac{\text{advection}}{\text{diffusion}} = \frac{2R|U|}{D},$$

Schmidt number:

$$Sc = \frac{\text{viscous diffusion}}{\text{molecular diffusion}} = \frac{\nu}{D},$$

Marangoni number:

$$\frac{\text{surface tension}}{\text{viscous forces}} = \frac{R_G T \Gamma_\infty}{\rho \nu U_\infty},$$

Langmuir number:

$$\frac{\text{adsorbtion}}{\text{desorbsion}} = \frac{C_\infty}{\beta},$$

Hatta number:

$$\frac{\text{mass flux}}{\text{advective flux}} = \frac{2Rk_a C_\infty}{U_\infty},$$

Adsorbtion length:

$$K = \frac{\Gamma_\infty}{2RC_\infty},$$

where R is the bubble radius, D the molecular diffusion coefficient, C_∞ the bulk surfactant concentration, $|U_\infty|$ the bubble terminal velocity, Γ_s the surfactant concentration on the interface, U_s the velocity at the bubble interface, ν the liquid viscosity, ρ the liquid density.

The Langmuir kinetic law states:

$$\vec{j}_N = -D\left(\vec{\nabla}C\right)_s \cdot \vec{N} = k_a\left[C_s\left(\Gamma_\infty - \Gamma\right) - \beta\Gamma\right]$$

Two closure laws are needed to complete this analysis: the surface concentration $\Gamma_\infty = f(C_\infty, U_\infty, R)$ and the interfacial surface tension $\sigma(\Gamma)$.

The surfactant concentration varies on the bubble surface: there is little to no surfactant at the stagnation point, and the polarised molecules gather at the back of the bubbles. Cuenot et al. (1997) define the critical angle θ_c (see Figure B.1) under which there is no surfactant at all and a shear-free condition is imposed, and above which the surfactant concentration is constant and the tangential velocity is zero. This leads to expressing the bubble drag coefficient as:

$$\frac{C_D(\theta_c) - C_D(\pi)}{C_D(0) - C_D(\pi)} = \frac{1}{2\pi}\left[2\left(\pi - \theta_c\right) + \sin\theta_c + \sin(2\theta_c) - \frac{1}{3}\sin(3\theta_c)\right]. \tag{B.5}$$

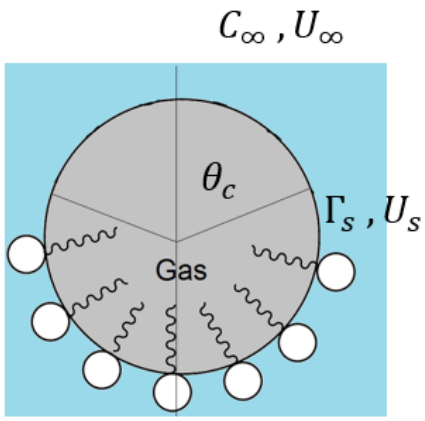

Figure B.1 The surfactant molecules are represented with a circle for the hydrophilic end, and a spiralling line for the hydrophobic end. For $\theta < \theta_c$, there is no surfactant at the bubble surface, while for $\theta > \theta_c$, the surfactant concentration is Γ_s.

B.2 Forces on a sphere in an inviscid flow

On a clean bubble, the boundary layer is very thin, which makes the inviscid flow approximation acceptable (Batchelor (1987)). We need to predict the pressure field around the bubble, in order to express the force on it in terms of momentum far from it. This leads to the D'Alembert paradox, stating that a bubble in a steady motion in a uniform, inviscid flow is not subjected to any force.

B.2.1 Unsteady motion (uniform flow)

For an unsteady motion in a uniform flow, the force applied on the bubble consists of an inertia and an added mass components:

$$F_{Iu} + F_{Au} = \rho_L V \frac{du}{dt} + \rho_L C_M V \frac{d(u-v)}{dt}, \tag{B.6}$$

where ρ_L is the liquid density, V is the bubble volume, and C_M is the added mass coefficient, which is 1/2 for a spherical bubble (Batchelor (1987)) and $C_M > 1/2$ for an ellipsoidal bubble. Using an added mass tensor $\mathbf{C_M}$ for non-spherical bubbles, leads to the following expression of the torque acting on a bubble (Lamb (1932), Milne-Thompson (1968))

$$T = \rho V \vec{U} \times \left(\mathbf{C_M} \cdot \vec{U} \right)$$

According to Benjamin (1987), this expression partly explains the zig-zag and helical paths mentioned in B.1.3, although it does not take into account the vorticity creation on the bubble surface.

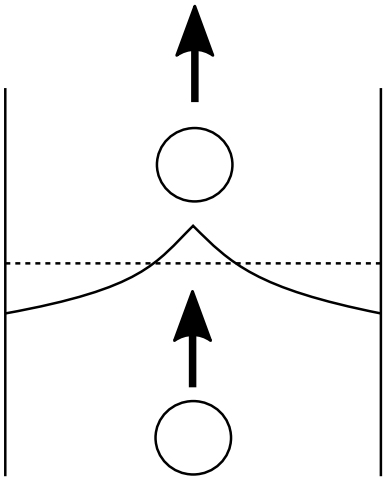

Figure B.2 Concept of drift flux, reproduced from Bush and Eames (1998). The bubble deforms the material surface shown in dotted line into the one in solid line. Some of the liquid is advected in the bubble wake, but there is a reflux of liquid at the container edges.

B.2.2 Drift model

Darwin (1953) suggested that bubbly flow can be studied by considering the drift volume $D_f = C_M V$ which is advected forward when a bubble passes through an interface (Figure B.2). This theory has also been derived by Lighthill (1956), with a geometrical argument.

The reflux depends on the container shape, and is uniformly spread across the channel area. The vorticity is advected and related to the downstream momentum deficit. Bush and Eames (1998) have carried out experiments to measure the drift volume in non-rotational flow, by suppressing the trailing vorticity using stratified flows.

B.2.3 Shear-induced lift forces

We consider a shear flow along the x-axis: $\vec{u} = (U + \alpha y)\,\vec{e}_x$. A three-dimensional body in a uniform shear will permanently affect the vorticity field. For a weak shear ($R|\alpha\ U| << 1$), the vortical elements are advected. A vortex line passing through the spherical bubble will become an attached horseshoe vortex. Lighthill (1956) used a Lagrangian drift coordinate system to calculate this vorticity. Auton (1984) calculated the lift force generated by the pressure variations on the bubble surface, for a unidirectional weak shear flow.

$$\vec{F_L} = \rho C_L\,(\vec{u} - \vec{v}) \times \vec{\omega}, \tag{B.7}$$

where $\vec{\omega} = \vec{\nabla} \times \vec{u}$ is the undisturbed liquid flow vorticity, $\vec{v}$ the bubble velocity, and C_L the lift coefficient. For a sphere, $C_L = 1/2$.

Taylor (1928) gives the force applied on a bubble in a steady, non-uniform flow:

$$F_{IS} + F_{AS} = \rho V \left([(\mathbf{I} + \mathbf{C_M}) \cdot \vec{u}] \cdot \vec{\nabla} \right) \vec{u} \tag{B.8}$$

For a weak rotational component and a small unsteadiness ($R\omega/U << 1$ and $|\partial u/\partial t| << 1$), Auton et al. (1988) writes:

$$\begin{aligned} \vec{F} &= \vec{F}_I + \vec{F}_A + \vec{F}_L \\ &= \rho V \left[\frac{\partial \vec{u}}{\partial t} + \left(\vec{u} \cdot \vec{\nabla} \right) \vec{u} \right] + \rho C_M V \left[\frac{\partial \vec{u}}{\partial t} + \left(\vec{u} \cdot \vec{\nabla} \right) \vec{u} - \frac{d\vec{v}}{dt} \right] + \rho C_L V \left(\vec{u} - \vec{v} \right) \times \vec{\omega} \end{aligned} \tag{B.9}$$

For a fixed sphere in a solid body rotation flow, $\left(\vec{u} \cdot \vec{\nabla} \right) \vec{u} = \frac{1}{2} \vec{u} \times \vec{\omega}$, therefore $C_{L\omega} = C_L - \frac{1}{2}(1 + C_M) = -\frac{1}{4}$ (Auton et al. (1988)).

B.3 Small, clean bubble in unsteady or inhomogeneous high Reynolds flow

For a bubble of fixed shape, the viscous history effect (Basset force) and the wake effect (shedding vorticity) are coupled at finite Reynolds number (Legendre and Magnaudet (1998)).

At low Reynolds number ($Re_b << 1$), it is possible to decompose the hydrodynamic force on the bubble as $F = \text{drag} + \text{history} + \text{added-mass}$. At high Reynolds number, this decomposition has no theoretical grounds, but we can define F_{Au} the added mass force due to the flow unsteadiness as:

$$F_{Au} \equiv F - F_s,$$

where F is the total hydrodynamic force in presence of a flow acceleration and F_s the remaining force when the acceleration is suddenly stopped.

Rivero et al. (1991) showed using this decomposition that C_M is not affected by the unsteadiness, is independent of Re_b and of the boundary conditions, and can be determined using the inviscid theory (for a sphere, $C_M = 1/2$).

B.3.1 Unsteady effects due to diffusion of vorticity around bubbles

We define the advective and acceleration time scales as follow:

$$t_{ad} = \frac{R}{||\vec{u} - \vec{v}||}$$

$$t_{acc} = \sqrt{\frac{R}{||d\vec{u}/dt||}}$$

According to Chen (1974), if $t << t_{ad}$,

$$C_D(t) = \frac{48}{Re}\left[1 - 4\left(\frac{\nu t}{\pi R^2}\right)^{1/2} + \mathcal{O}\left(\frac{\nu t}{R^2}\right)\right]. \tag{B.10}$$

At $t = 0$, the vorticity has not diffused yet, so the viscous and high Re flows have the same drag coefficient $C_D(0)$: the boundary layer is still very thin. This stays true as long as $\sqrt{\nu t}/R << 1$

The drag coefficient variation is larger for a solid sphere than for a bubble.

B.3.2 Generalisation of the Basset-Boussinesq-Oseen equation

Yang and Leal (1991) give:

$$F_\nu(t) = 4\pi\rho\nu R\left[u(t0 - v(t) + 2\int_{-\infty}^{t} e^{9\nu(t-\tau)/R^2}\mathrm{erfc}\left(\frac{9\nu(t-\tau)}{R^2}\right)\frac{du(\tau) - v(\tau)}{d\tau})d\tau\right].$$

The history term represents the unsteady diffusion of vorticity around the bubble. For a rigid sphere, Basset (1888) gives:

$$F_\nu = 6R^2\sqrt{\pi\rho\mu}\int_0^t \left(\frac{\frac{Du}{D\tau} - \frac{Dv}{D\tau}}{\sqrt{t-\tau}}\right)d\tau.$$

This expression diverges for short times. It characterise the long time behaviour as a function of the flow characteristics, only for rectilinear flows (Odar and Hamilton (1964)). It is valid for $Re << 1$, and leads to an overestimation from $Re_b > 5$. Mei et al. (1994) shows that the history force is negligible when $Re_b > 50$.

B.3.3 Forces dues to strain and vorticity of the outer flow

We note L the length scale of the flow inhomogeneity ($L << R$). For a unidirectional flow $\vec{u} = (U + \alpha y)\,\vec{e}_x$ in the bubble frame of reference, we define the strain parameter: $Sr = 2R\alpha/U$, based on the strain rate $\alpha = dU_x/dy$. The added-mass coefficient is not affected by the viscous effects at finite Reynolds number, and the viscous drag is not affected by the strain when $Re_b \longrightarrow \infty$.

For a finite Reynolds number, the viscous force due to the pressure distribution around the bubble decreases with the strain parameter, while the viscous force due to the viscous stress on the bubble surface increases with the strain parameter. As a result, for moderate strain number ($Sr < 0.2$), the viscous force is overall unaffected by changes in Sr.

Effect of viscosity on lift coefficient

Legendre and Magnaudet (1998) show that for $Re_b > 5$

$$C_L(Re_b) = \frac{1}{2}\left(\frac{1+16Re_b^{-1}}{1+29Re_b^{-1}}\right) \tag{B.11}$$

For $Re_b << 1$, we have $C_L = 0.5$, and the lift coefficient decreases sharply with increasing Reynolds number. At finite Reynolds number, it increases again to follow (B.11). There is therefore a minimum $C_L \approx 0.3$ around $Re_b = 5$. For large Reynolds numbers ($Re_b > 500$), $C_L \to 0.5$.

The value of C_L at high Reynolds number also weakly depends on the strain parameter. For $Sr = 0.02$, Legendre and Magnaudet (1998) find $C_L = 0.48$, while for $Sr = 1$, we have $C_L = 0.45$:

For a clean bubble, the boundary layer vorticity does not depend on the Reynolds number. The flow vorticity dominates the viscous drag. For a solid sphere, the boundary layer varies with $\mathcal{O}(Re_b^{1/2})$, and the sphere is also able to rotate, therefore the vorticity in the wake and in the boundary layer dominates the viscous effects.

Effect of shear on drag coefficient

For a moderate strain ($Sr < 0.2$), there is no effect on the drag coefficient, as the viscous stress effects and the pressure effect balance out. When $Sr \propto \mathcal{O}(1)$, we have:

$$C_D(Re, Sr) = C_D(Re, 0)\left[1 + 0.55Sr^2\right]. \tag{B.12}$$

The front stagnation point is shifted upwards by the shear, while the back-flow is not affected, creating a pressure unbalance ($Re > 50$). On the contrary, at low Reynolds number, the flow present a fore-aft symmetry because of viscous effects.

Drag and lift coefficient for simple strain flows

For a rotating flow, Legendre and Magnaudet (1998) showed that $C_L = C_{L\Omega} = -1/4$.

For a pure straining flow ($\vec{V} = (V_0 + \alpha x)\,\vec{e}_x + \alpha y \vec{e}_y$), they find $C_{LS} = 3/4$.

Flows can be superimposed as soon as the vorticity effects are secondary ($Re \geq 5$).

Contaminated bubbles have a significantly different lift force than clean bubble:

$$C_L(\text{solid}) >> C_L(\text{clean}) \qquad \text{and} \qquad C_L(\text{solid}) \propto Sr^{-3/4}$$

for $20 \leq Re_b \leq 80$ and $Sr < 0.2$.

Coupled effects of shear and deformation

Tryggvason and Ervin (1997) show that strongly deformed bubbles rising in a linear vertical shear flow migrate in opposite direction to spherical bubbles. For $20 \leq Re_b \leq 50$, the lateral migration reverse at $We = 4$. Tomiyama et al. (2002) measured that when the Reynolds number decreases, the critical deformation χ increases. The causes to this phenomenon are unclear, probably linked to the wake asymmetry or a non-zero recirculation.

B.4 Examples of bubble motion in inhomogeneous flows (low volume fraction)

For a clean, spherical bubble, Thomas et al. (1983) write:

$$\rho_b V \frac{dv}{dt} = F_I + F_A + F_L + F_D + F_B,$$

where F_I represent the inertia force, F_A the added mass, F_L the lift, F_D the drag and F_B the buoyancy.

Considering the undisturbed liquid flow field $\vec{u}$, Legendre and Magnaudet (1998) write:

$$\begin{aligned}(\gamma + C_M)\frac{d\vec{v}}{dt} = (1 + C_M)\left[\frac{\partial \vec{u}}{\partial t} + \left(\vec{u}\cdot\vec{\nabla}\right)\vec{u}\right] + C_L\,(\vec{u}-\vec{v})\times\vec{\omega} \\ + \frac{3C_D}{8R}\,|\vec{u}-\vec{v}|\,(\vec{u}-\vec{v}) + (\gamma - 1)\,\vec{g}\ ,\end{aligned} \tag{B.13}$$

where C_M is the added-mass coefficient, C_D the drag coefficient (B.3), and C_L the lift coefficient (B.11). γ is the phase density ratio:

$$\gamma = \rho_b / \rho_l.$$

This is valid for $Re_b \geq 5$, $Sr \leq 0.2$ and $AcRe_b \leq 1$. The last condition corresponds to the absence of history effects, with Ac defined as the non-dimensional acceleration.

$$Ac = \frac{2R\dfrac{\partial(v-u)}{\partial t}}{|v-u|^2}.$$

B.4.1 Bubble dynamics in vortical flows: Rankine vortex

A Rankine vortex velocity field is modelled as

$$v_\theta = \begin{cases} \Omega r, & \text{for } |r| < a \\ \Omega \frac{a^2}{r}, & \text{for } |r| \geq a. \end{cases}$$

Cadot et al. (1995) show that the bubble motion is governed by the strain parameter Sr and the relative vortex strength Π:

$$Sr = \frac{a\Omega}{\nu_T} \qquad \text{and} \qquad \Pi = \frac{\Omega a^2}{g}$$

Naciri (1992) shows that the effect of the coherent structures in a flow can also be apprehended using these number, with a more general expression:

$$Sr = \frac{\Delta U}{\nu_T} \qquad \text{and} \qquad \Pi = \frac{\Delta U^2}{g\delta m} \ ,$$

where ΔU is the velocity jump across the mixing layer, and δm the local momentum thickness.

B.4.2 Bubble in converging / diverging flows

Using (B.9), Auton et al. (1988) showed that a bubble in a converging flow accelerates faster than the fluid:

$$\left(v^2 - v_0^2\right) = \frac{1+C_M}{\gamma+C_M}\left(u^2 - u_0^2\right),$$

where v_0 is the initial gas bubble and u_0 is the undisturbed liquid axial velocities on the pipe centreline.

Kowe et al. (1988) used a drift model with the locally averaged liquid velocity field $\left\langle \vec{U} \right\rangle$, and the bubble volume fraction α, to find:

$$\left\langle \vec{U} \right\rangle (\vec{x},t) = (1-\alpha)\,\vec{u}_0\,(\vec{x},t) + C_M \alpha\,(\vec{v}-\vec{u})\,(\vec{x},t)$$

Appendix C

Patent review: Gas handling pumps

C.1 Helico-axial stage (Poseidon)

The Poseidon pump was licenced to and sold by Schlumberger until early 2017. Several patents have been granted to IFP related to this invention, some of them are described below.

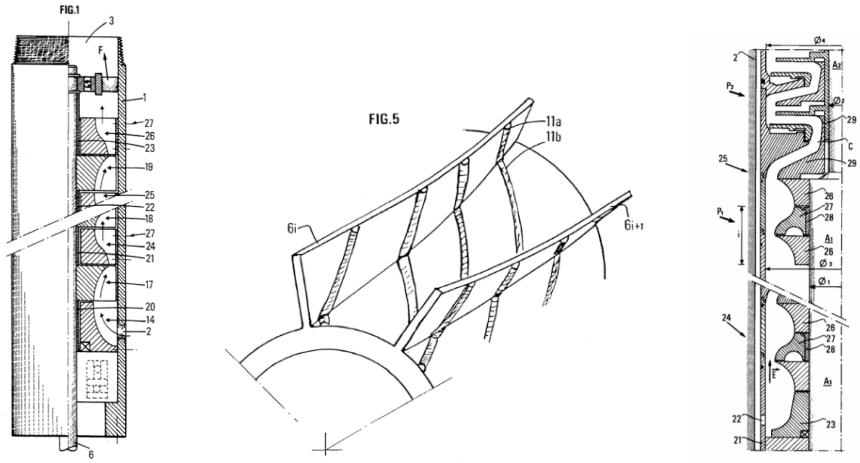

Figure C.1 Patented "Poseidon-like" devices. Left: Multiphase compression device (US 5,375,976 / 1993), Right: Axial and centrifugal pumping system (US 5,961,282 / 1997), Middle: Multiphase turbo machine for improved phase mixing and associated method (US 6,312,216 / 1999)

US 5,375,976 (IFP, 1993)

Pumping or multiphase compression device and its use.

- Device to compress a multiphase fluid such as petroleum effluent comprising a liquid phase and a gaseous phase
- At least one channel or passage is defined by two successive blades (29, 30) whose orthoradial section S(x) is of the form, within 5% and preferably within less than 3%: $S(x) = ax^2 + b(c - x^2)^{1/2} + d$

US 5,961,282 (IFP, 1997)

Axial-flow and centrifugal pumping system

- System having in combination at least one pair of pumping elements, comprising a first pumping means of the axial-flow type and a second pumping means of the centrifugal type provided downstream.

US 6,312,216 (IFP, 1999)

Multiphase turbo machine for improved phase mixing and associated method

- At least one flow channel containing at least one turbulence producing structure which generates a turbulent zone

C.2 Multi-Vane Pump

Patent US 6,676,366 (Baker Hughes, 2002)

Submersible pump impeller design for lifting gaseous fluid.

- Impeller blades split in two, with different angles and an offset
- Exit angle from 50 to 90 degrees
- Balance hole of diameter between 45% and 100% of the flow passage

Contrarily to the AGH which is considered as a primer, the MVP is used as the main and only pump for gassy applications. Three successful installations are reported by Rahime et al. (2013) with an average of 30% GVF and a highest GVF of 56%.

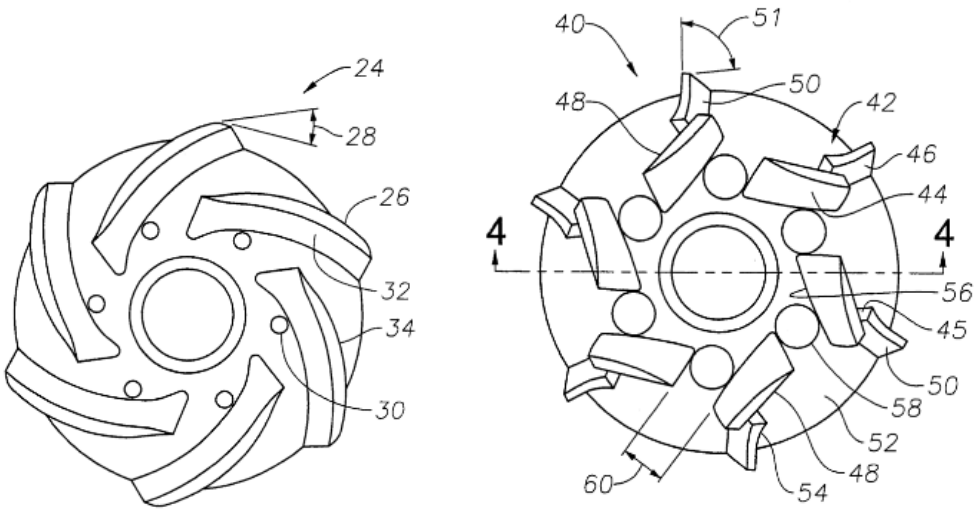

Figure C.2 Prior art (left) and new design (right) of the multi-vane pump, from the patent US 6,676,366

C.3 Hybrid encapsulated stage

Patent application: US 2015/0044027 (GE Oil & Gas, 2013)

System and apparatus for pumping a multiphase fluid

- The impeller comprises a helico-axial section (inducer) and a mixed-flow section.
- The two sets of vanes in the impeller overlap and have grooves
- The impeller outlet area is smaller than the inlet area
- The diffuser can have two sets of vanes, with overlap and grooves
- There are balance holes in the impeller hub

The diffuser is particularly long compared to the Poseidon design. GE claims that this system can handle up to 70% of gas. Figure C.3 shows an illustration from the patent and a proposed product from their online brochure.

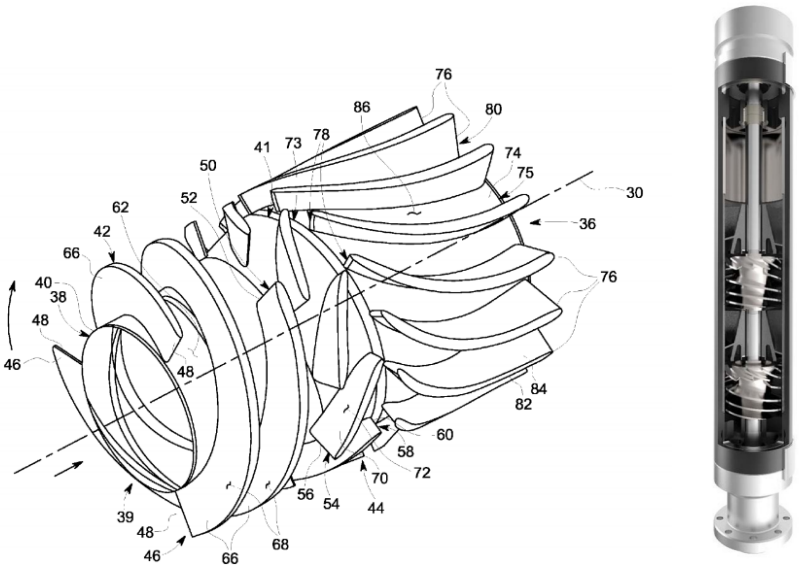

Figure C.3 Hybrid stage: The impeller blades have a helical section followed by a conventional section where the hub diameter increases substantially.

C.4 Hybrid alternated stages

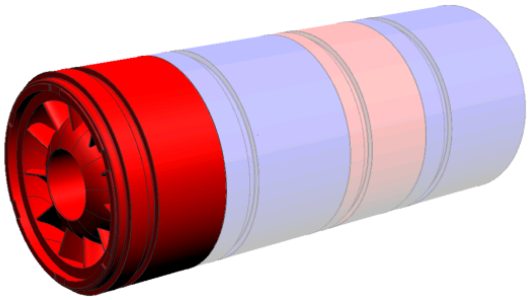

Figure C.4 Housing showing the stage type alternation (charger / primary), from Ye et al. (2016)

A new approach to multiphase pumping is presented by Ye et al. (2016) from Baker Hughes, where "charger" and "primary" stages are alternated to produce a well mixed flow and improve the gas handling capacity of the whole pump. No IP was found related to this device although Baker Hughes propose a new gas handling pump stage under the name of MVPER on their institutional website, corresponding to this description (last consulted in August 2017).

C.5 Compact mixed-flow stage

Patent: US8221067B2 (2007, IFP) Compact multiphase pump

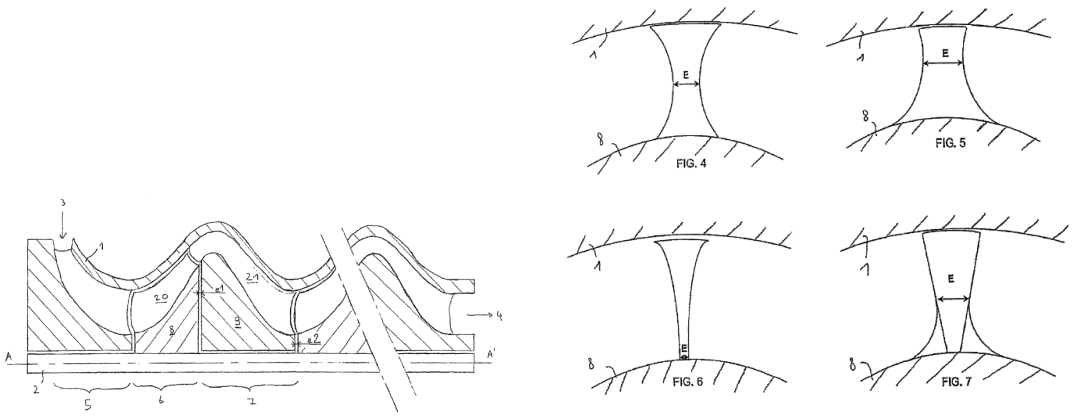

Figure C.5 Illustrations of the compact multiphase pump described by IPF in US8221067B2

Claims:

- Mixed-flow design with meridional angles (from rotation axis) ranges from $-20°$ and $+20°$ at the leading edge to $0.1°$ and $70°$ at the trailing edge
- The blade angle is larger than $60°$.
- Diffuser has at least twice as many channels as the impeller.
- The housing inside radius at the trailing edge of the impeller is larger than at the leading edge.
- The impeller blade thickness is minimum at a radius smaller than 0.9 times the largest radius.

Appendix D

Laser properties and optical corrections

Optical corrections are based on the Snell's law and ray tracing, leading to different corrections for the axial and tangential component as they reach the pump outer wall in two different planes (Z-plane for the tangential set of beams, X-plane for the axial set of beams).

The beams cross two interfaces: air-wall and then wall-liquid. As these material have different refractive index, the beams are refracted according to the wall thickness they go through. In our case, the wall is made of Perspex ($n_{\text{Perspex}} = 1.5$) and the fluid can be either water ($n_{\text{water}} = 1.33$) or kerosene ($n_{\text{oil}} = 1.45$) . The outer wall position is referred to as $R_1 = 50$ mm and the inner wall as R_2. R_2 varies with the axial position of the laser and is computed based on the meridional passage profile. r is the radial position of the measurement volume if there were no interfaces. For the axial component, the corrected position can be approximated assuming small angles:

$$r_{ax} = R_2 - \frac{n_{fluid}}{n_{wall}}(R_1 - R_2) - \frac{n_{fluid}}{n_{air}}(R_1 - r)$$

For the tangential component, the correction is not linear and is computed referring to the incidence angles at each interface: δ_1 and δ_2 at the air-wall interface and ϵ_1 and ϵ_2 at the wall-fluid interface. From the geometrical configuration:

$$R_1\, sin\delta_1 = r\, sin(\pi - \alpha)$$

Then from Snell's law: $n_{air}\, \sin\delta_1 = n_{wall}\, \sin\delta_1$ and $n_{wall}\, \sin\epsilon_1 = n_{fluid}\, \sin\epsilon_1$. The final correction is:

$$r_{tan} = \frac{R_2\, \sin\epsilon_2}{\sin(\alpha - \delta_1 - \epsilon_1 + \delta_2 + \epsilon_2)}$$

As the laser beams go through non-planar interfaces, the location of the measurement volume needs to be corrected, as shown in Figure D.1.

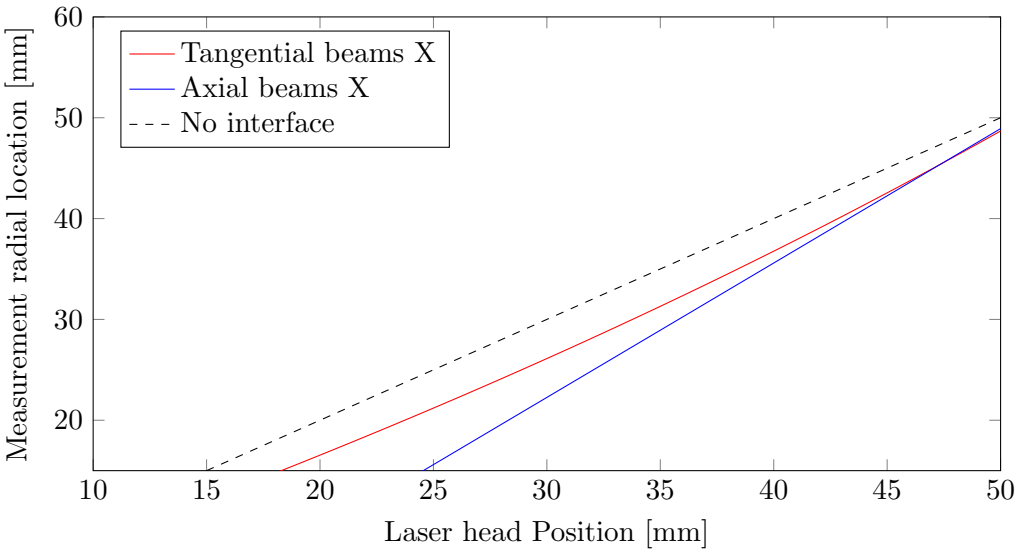

Figure D.1 Correction to the measurement location: Both measurements are made at the same location only close to the wall. When the measurement is in the inner part of the pump, the radial spacing can be up to 3 mm.

	Laser 1 (V_θ)	Laser 2 (V_z)
Wave length	660 nm	750 nm
Incidence angle	$\alpha = 5.71°$	$\alpha = 5.71°$
Volume (Δx,Δy,Δz)	$0.1 \times 0.1 \times 1.1$ mm	$0.1 \times 0.1 \times 1.1$ mm
Focal length	300 mm	300 mm

Table D.1 Laser properties

Appendix E

Sensitivity analysis for the measured velocity field

E.1 Effect of flowing fluid

A set of experiments have been carried on using transparent kerosene instead of water. The refractive index of oil is $n_{\text{oil}} = 1.45$, closer to the one from Perspex ($n_{\text{Perspex}} = 1.5$) than while water has $n_{\text{water}} = 1$. Should attenuates the effect of the interfaces on the laser beam path. However, kerosene has a density of 800 $kg.m^{-3}$ and viscosity 1.8 $cP = 1.8\ .10^{-3} Pa.s$. This brings the pump Reynolds number ($Re = 2\omega R_2^2/\nu$) from 50,000 to 22,000 while the case we are interested in (full scale, $f = 60Hz$) has $Re = 150,000$. We also had to change the seeding particles from gas bubbles (or oil droplets) to water droplets, which are heavier than the working fluid.

Thanks to the higher refractive index in the case of oil, more data have been collected, particularly behind the blades, as shown in Figure E.1. This confirms that higher velocities regions were "hidden" behind the blades. The two flow fields are qualitatively and quantitatively very close to each others, suggesting that the Reynolds number is high enough for its variation to be a negligible.

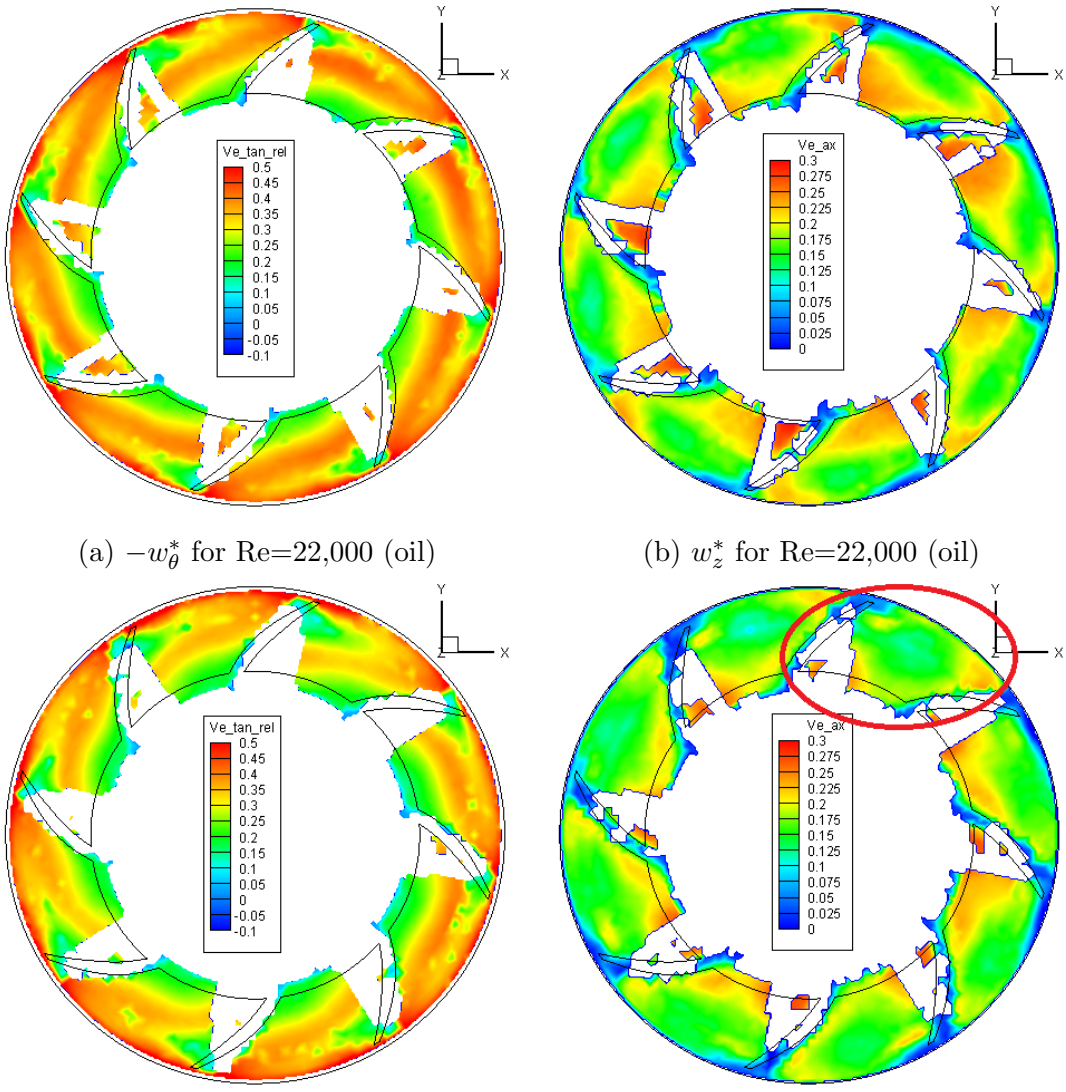

(a) $-w_\theta^*$ for Re=22,000 (oil)

(b) w_z^* for Re=22,000 (oil)

(c) $-w_\theta^*$ for Re=50,000 (water)

(d) w_z^* for Re=50,000 (water)

Figure E.1 Cases 23 and 21 (2.1) : Velocity field at $\Phi^* = 0.95$ for $z^* = 0.71$, flowing oil (top) and water (bottom).

E.2 Sensitivity to geometrical imperfection

When first starting this work, the impeller blades were made out of Perspex, leading to poor manufacturing tolerances, and occasionally gaps between the shroud and the blades, ranging from 0.1 to 1.5 mm. In particular, the impeller labelled B, placed in second position had two blades presenting a large gap (Cases 3-16, Impeller order: ABC). Another set of measurements was carried out after changing the impeller order (Cases 21-23, Impeller order: CAB), and finally the gaps along the impeller blades were filled with glue and the same measurements carried on in the modified impeller B* with the new order (Case 25: Impeller order CAB*).

We conclude from Figure E.2 that the strong asymmetry observed in the Case 12 is caused by the geometrical non-conformity of the impeller B. Correcting the geometry (filling the gaps with glue, Case 25) reduces the asymmetry and the flow field is then closer to the one observed for the impeller A. It can also be noticed that the position (second or third) of the impeller in the pump does not seem to affect the velocity field.

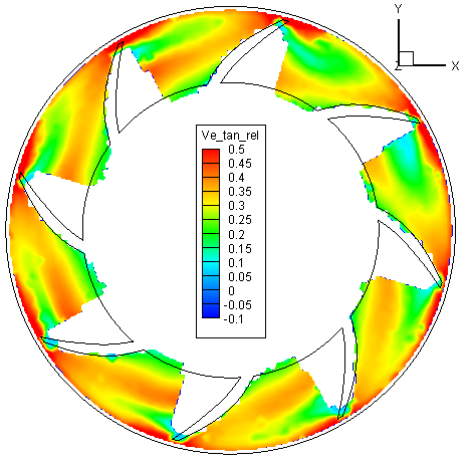

(a) $-w_\theta^*$ in Impeller B in 2nd position

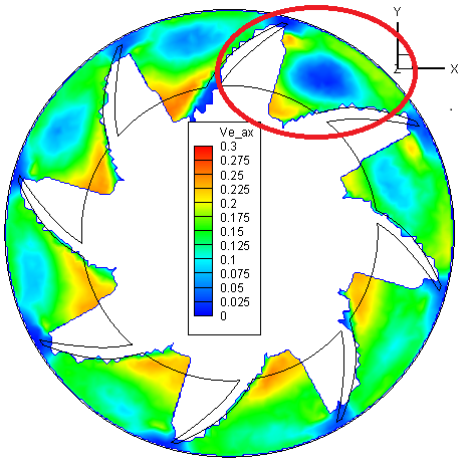

(b) w_z^* in Impeller B in 2nd position

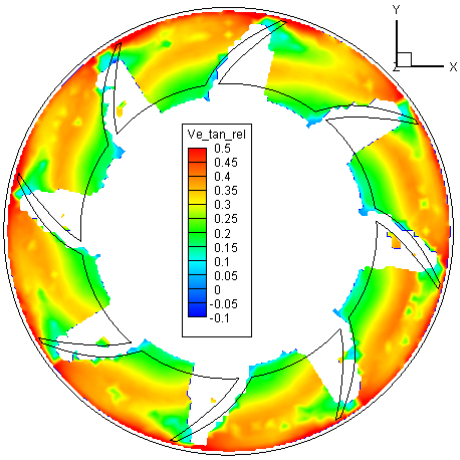

(c) $-w_\theta^*$ in Impeller A in 2nd position

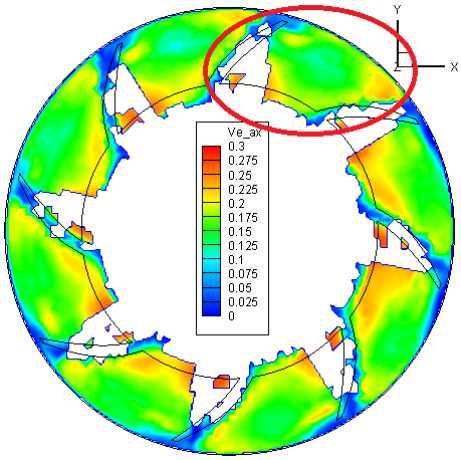

(d) w_z^* in Impeller A in 2nd position

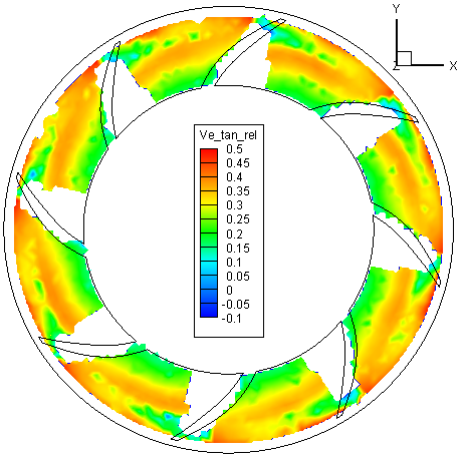

(e) $-w_\theta^*$ in Impeller B* in 3rd position

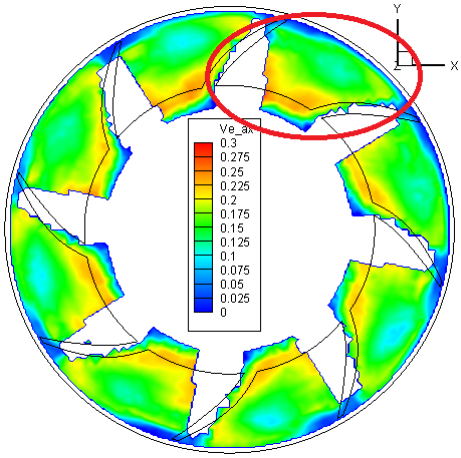

(f) w_z^* in Impeller B* in 3rd position

Figure E.2 Cases 12,21 and 25 (Table 2.1): Velocity field for different impellers. The red circles underline the passage where a deficit of axial velocity for the impeller B compared to impeller A. This was due to a geometrical defect of impeller B, which was fixed (impeller B*).

E.3 Velocity maps in different planes

Only the plane $z^* = 0.74$ is presented in the main text, although experiments have been carried on for different locations, from $z^* = 0.74$ to 0.89. The measured velocity fields are qualitatively similar in the impeller exit although the average axial velocity changes as the available cross-section varies. Moving closer to the diffuser, the flow is no longer steady in the impeller frame of reference.

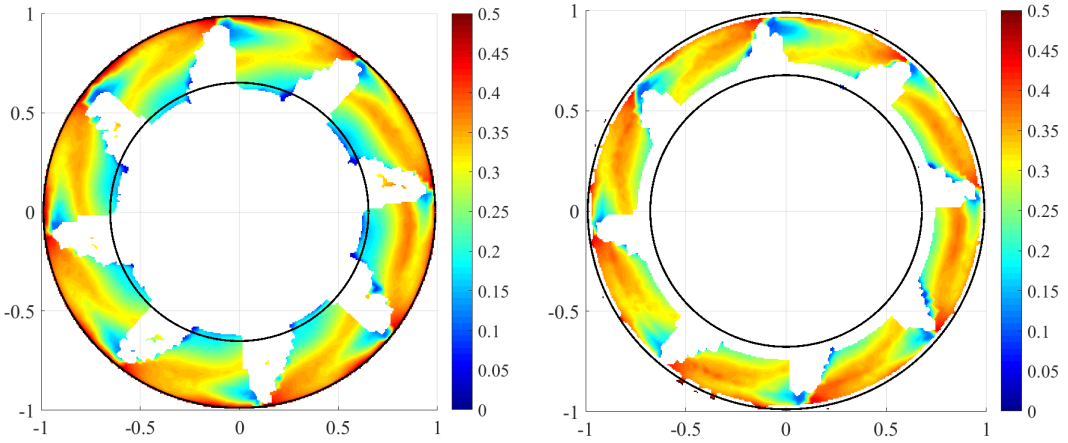

(a) $-w_\theta^*$ at $z^* = 0.74$.

(b) $-w_\theta^*$ at $z^* = 0.77$.

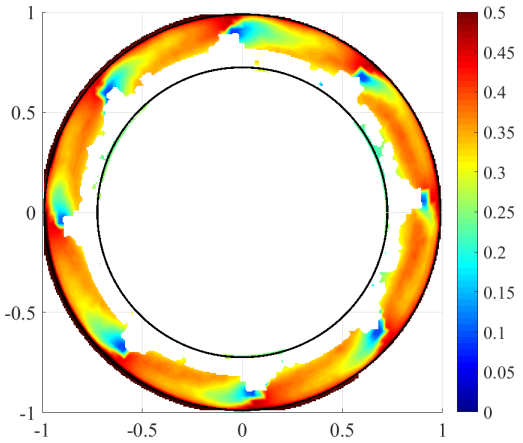

(c) $-w_\theta^*$ at $z^* = 0.83$.

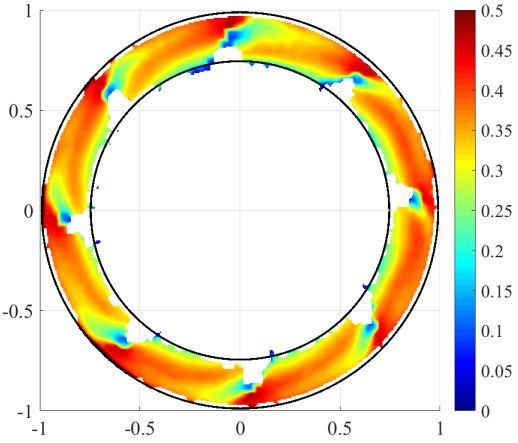

(d) $-w_\theta^*$ for at $z^* = 0.89$.

Figure E.3 Case 21: Relative tangential relative velocity field in several planes.

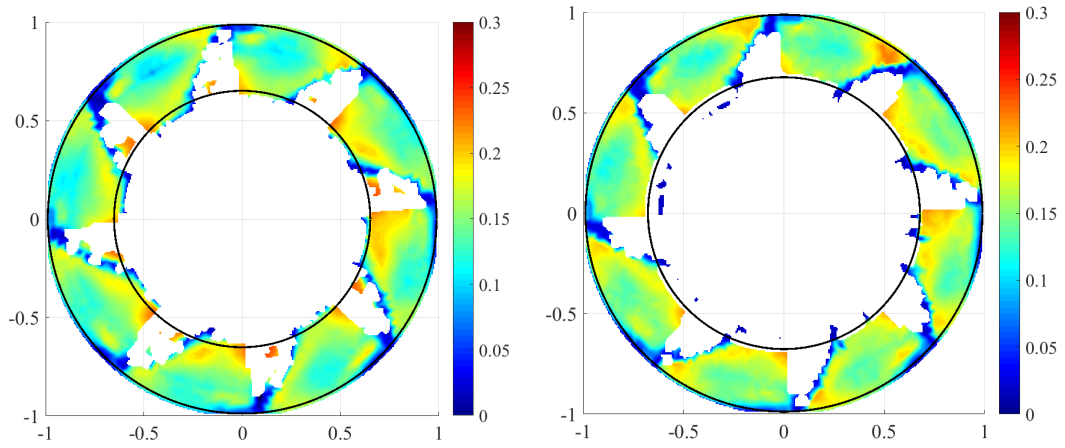

(a) w_z^* at $z^* = 0.74$.

(b) w_z^* at $z^* = 0.77$.

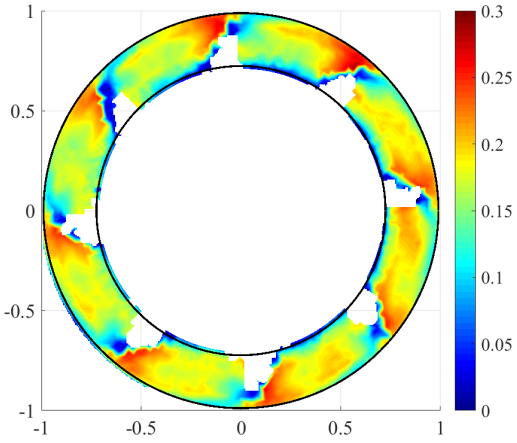

(c) w_z^* at $z^* = 0.83$.

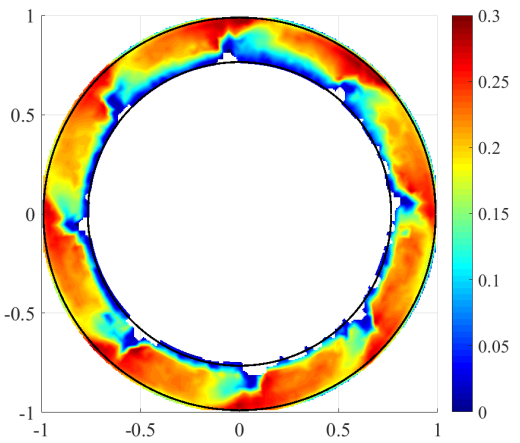

(d) w_z^* at $z^* = 0.89$.

Figure E.4 Case 21: Axial velocity field in several planes for $\Phi^* = 0.95$.

E.4 Turbulence intensity

We show in Figure E.5 the two-dimensional turbulence intensity defined in Section 3.3:

$$I_{2D} = \frac{k^*_{2D}}{\left|\vec{W}_{2D}\right|} \ .$$

The turbulence intensity levels found correspond to what is expected in a turbomachinery flow, around 25 % in the blade wakes and 5 % in the bulk of the flow.

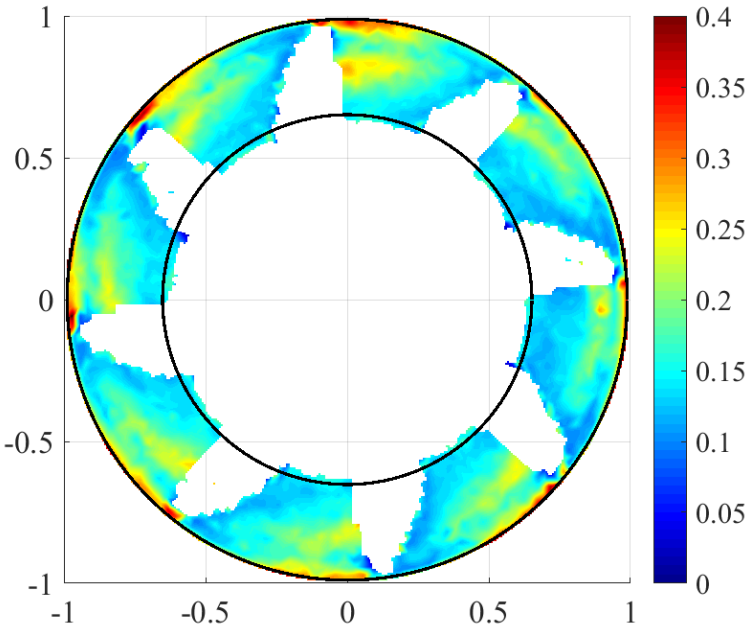

Figure E.5 Case 21: Turbulence intensity for $\Phi^* = 0.95$, $z^* = 0.74$

E.5 Sensitivity to particle seeding

We used two different seeding methods (see Section 2.2): gas bubbles and oil droplets. In both cases, the size distribution is estimated to peak below 100 µm. Most of the experiments have been done using gas bubbles which are much lighter than the running fluid (water). Oil droplet on the contrary have a density close to that of water (800 kg/m^3). We compare the flow field given by both method in Figure E.6, and show that there are no significant difference between the two. This means that the gas bubble do not deviate considerably more than the oil droplets from the water streamlines. The relative velocity difference between the two fields is of the order of 5 %.

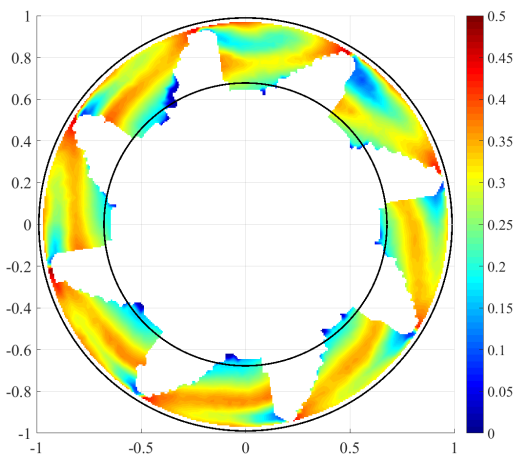

(a) $-w_\theta^*$ with gas bubbles seeding

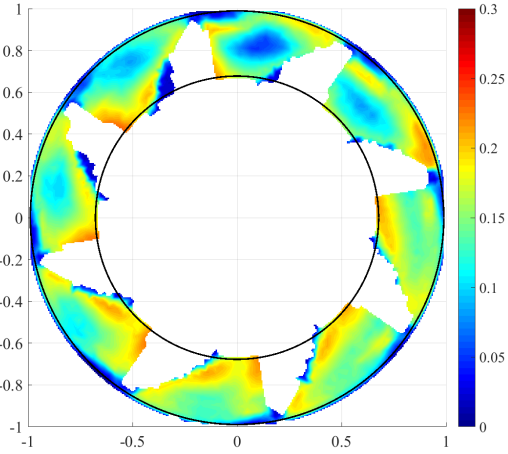

(b) w_z^* with gas bubbles seeding

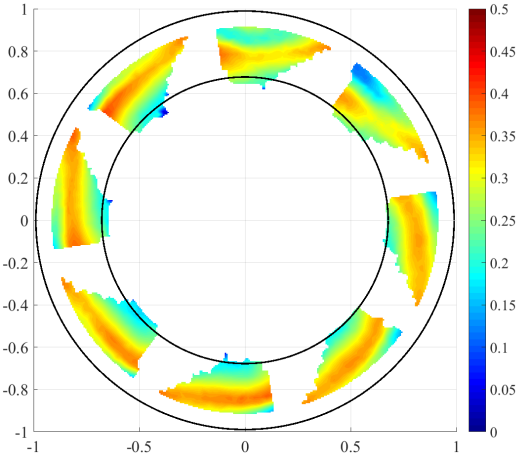

(c) $-w_\theta^*$ with oil droplets seeding

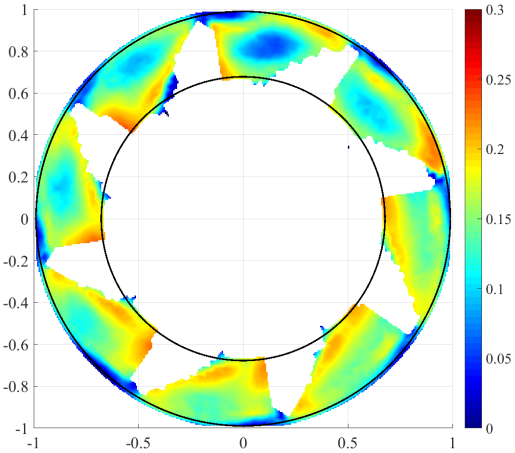

(d) w_z^* with oil droplets seeding

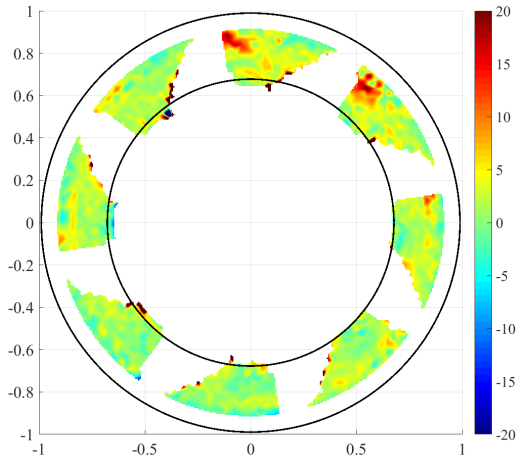

(e) Relative difference (in percent) between gas and oil seeding for $-w_\theta^*$

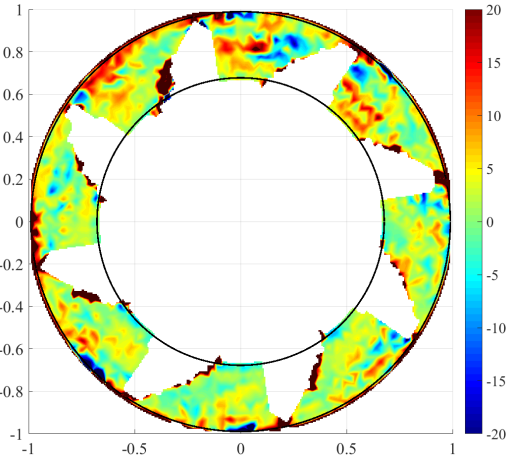

(f) Relative difference (in percent) between gas and oil seeding for w_z^*

Figure E.6 Cases 12 and 13: Axial and relative tangential velocity fields for gas and oil seeding, with $\Phi^* = 0.95$, at $z^* = 0.77$. (e) and (f) represent the relative difference between the two fields.

Appendix F

Selected High Speed Videos

In this Appendix, we describe the videos attached to this thesis, and used in Chapter 4. The table 2.3 is copied below for convenience.

Table F.1 List of the attached movies with their main features and characteristics. The column "Case" refers to Table 2.2.

File Name	Case	Φ_T	λ_0	f	**Angle**	**Rate**	**View**
Units	-	-	%	Hz	deg	fps	-
A1	A	1.2	33	20	0	500	0 I1 - I2
Inlet Horizontal	Horizontal slugging and fully separated flow (gas lock)						
A2	C	1	43	20	89	1000	0 - I1 - I2
Inlet Vertical	Taylor bubble, separated flow						
B1	A	1	1	20	0	7200	I3 - I4
BEP Bubbly	Bubbly flow						
B2	A	1	2.5	20	0	7200	I3 - I4
BEP Accumulation	Bubbly flow with accumulation in impeller suction side						
B3	A	1	5	20	0	7200	I3 - I4
BEP GasPocket	Bubbly flow with intermittent gas pockets in impeller						
C1	D	1.54	9.5	25	0	7200	I1 - I2
HighFlow Slug	Flow features, short slugs with separation in diffuser						
D1	A	0.62	2.5	20	0	6000	0 - I1 - I2
LowFlow LowGVF	Bubbly flow with recirculation in diffusers.						
D2	A	0.57	15	20	0	5400	I3 - I4
LowFlow HighGVF	Very large bubbles in diffuser, gas pocket in impeller.						

F.1 Horizontal slugging (Video A1)

At the inlet, we see that the incoming flow is stratified (gas on top and liquid on bottom). A gas slug comes in and propagates into the pump. The first impeller mixes

the phases into a bubbly flow which rapidly turns into a radially separated flow in the diffuser, when the gas fraction is high enough. The radial phase segregation is indicated by the small ripples visible at the outlet of the diffuser, corresponding to surface waves at the gas-liquid interface. The second stage is less affected by the gas than the first one: the flow is more often bubbly than separated. The first stage therefore acts as a mixer, but also as a buffer, stabilising the gas fraction for the rest of the pump.

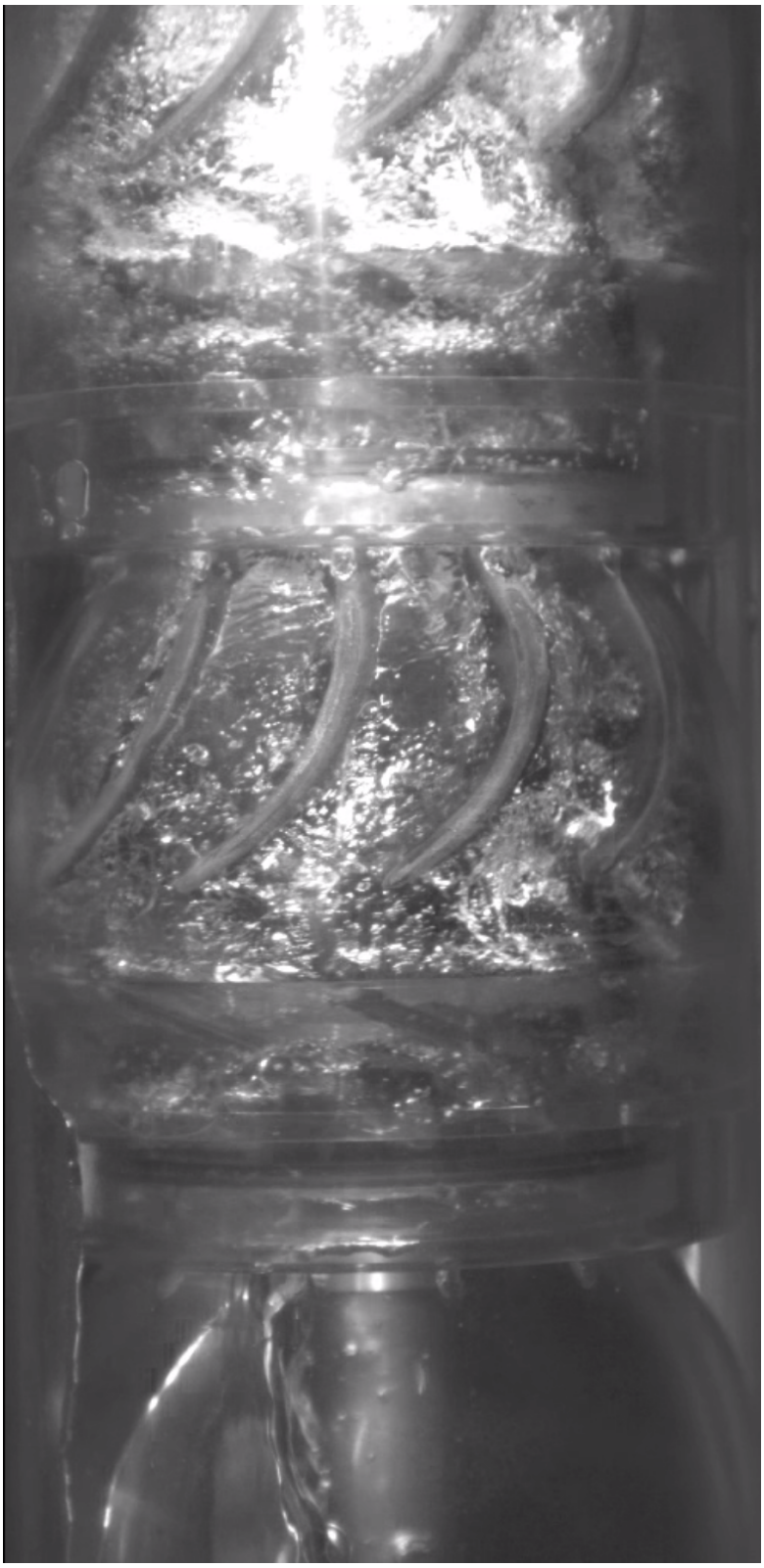

Figure F.1 Horizontal slugging and fully separated flow. $\Phi^* = 1.2$, $\lambda_0 = 33$ %, Inlet and Impellers 1-2, 500 fps.

F.2 Vertical slugging (Video A2)

At high gas fraction ($\lambda_0 = 44$ %), slug flows develop in the vertical inlet section. The incoming flow to the pump is mostly bubbly, but large bubbles are travelling at the centre of the pipe. Figure F.2 shows the first and second impellers a few milliseconds apart. The flow is radially separated in the first impeller then in the second one, as the slug progresses through the pump.

(a) t = 550 ms (b) t = 650 ms

Figure F.2 Vertical slugging and fully separated flow. $\Phi^* = 1$, $\lambda_0 = 43$ %, Inlet, Impellers 1-2, 1000 fps at two different times. We can see the slug progressing through the pump.

F.3 Bubbly Flow to Gas Pocket (Videos B1-3)

At design flow rate ($\Phi^* = 1$) and very low gas fraction ($\lambda_0 = 1$ %, Figure F.3), bubbles can be individually identified, and the rate of break-up and coalescence is very low. The bubbles roughly follow the liquid streamlines, which are aligned with the blades. The flow appears quite homogeneous. When the gas fraction slightly increases ($\lambda_0 = 2.5$ %, Figure F.4) it is already possible to observe an accumulation of bubbles in certain areas: the suction side of the diffuser blades (blue ellipse), and the inlet of the impeller (red ellipses). Still at design flow rate, another increase in the gas fraction ($\lambda_0 = 5$ %) sees intermittent gas pockets appearing in some impeller passages. They are characterised by a shiny light (red ellipse) and bubbles detach from them to be carried downstream. In the video B3, almost every other impeller passage presents a small gas pocket. The gas pocket appears at the impeller inlet, on the suction side, although it is difficult to precisely locate because of the viewing angle and the rotation of the blades. The flow at the outlet of the impeller is always a bubbly flow, whether or not the feeding passage presented a gas pocket.

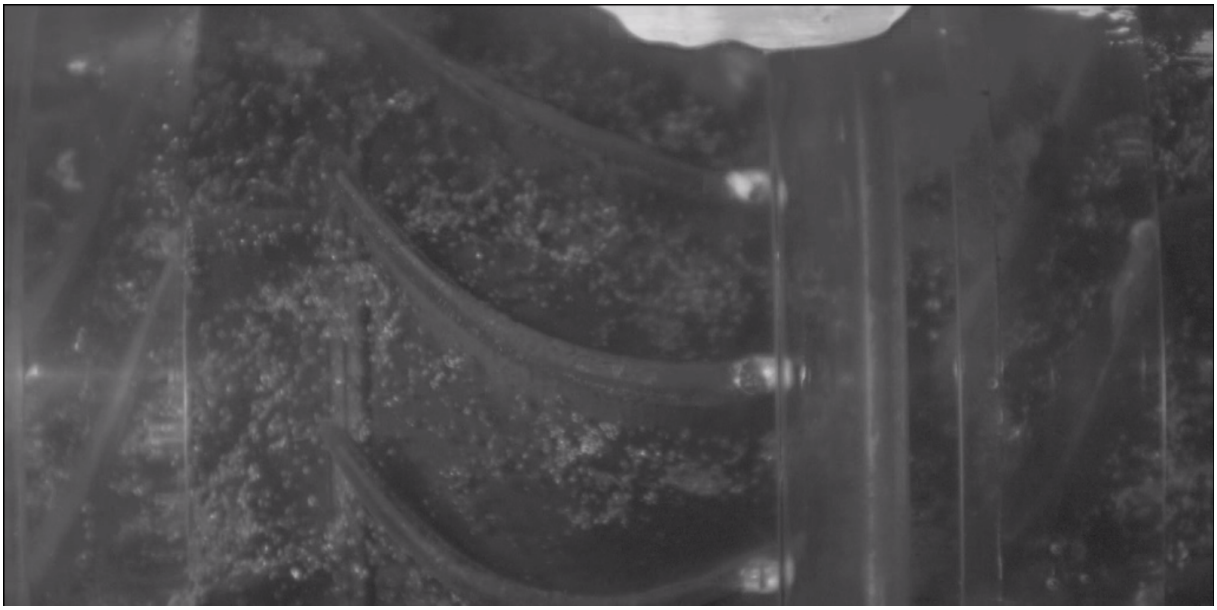

Figure F.3 Bubbly flow - Non coalescing bubbles. $\Phi^* = 1$, $\lambda_0 = 1$ %, Impellers 3-4, 7200 fps.

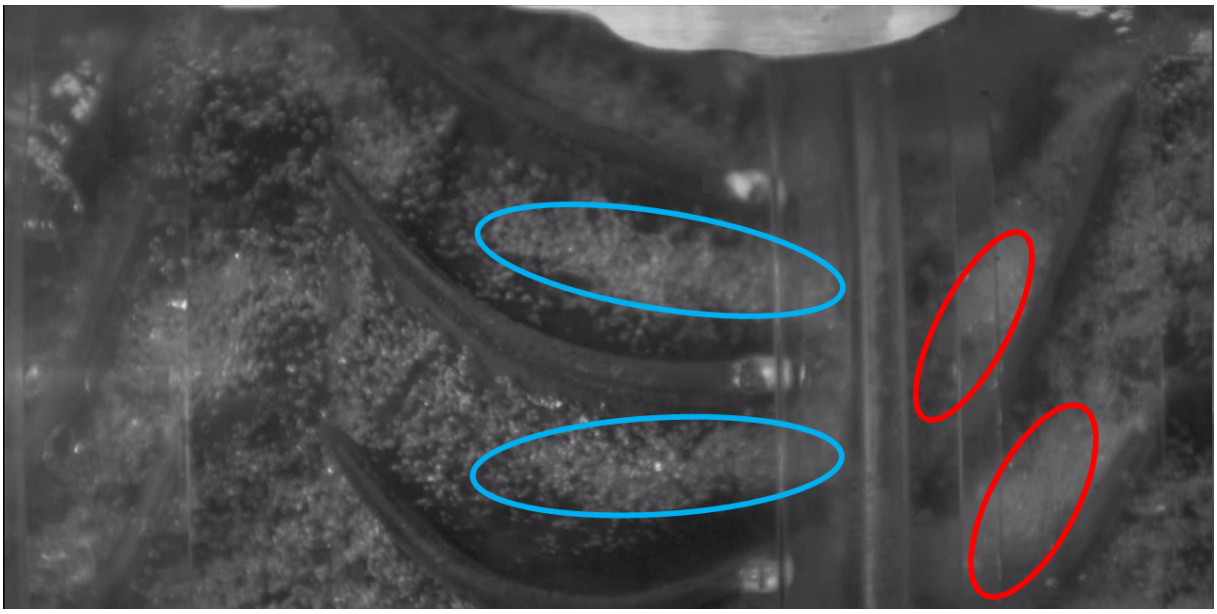

Figure F.4 Bubbly flow with gas accumulation in the impeller. $\Phi^* = 1$, $\lambda_0 = 2.5$ %, Impellers 3-4, 7200 fps.

Figure F.5 Bubbly flow with intermittent gas pocket in the impeller. $\Phi^* = 1$, $\lambda_0 = 5$ %, Impellers 3-4, 7200 fps.

F.4 High Flow Slugging (Video C1)

At high gas fraction and high flow rate, the flow patterns in the pump change rapidly. We can successively observe bubbly flows (Figures F.6 and F.7) or radially separated flow (Figure F.8). At that point, gas sometimes escapes to the non-passage cavity at the back of the impeller shroud. The large bubbles formed there (red circles) impair the flow visualisation in the flowing regions. The impeller flow can also be radially stratified. If looking closely, we can see wrinkles indicating surface waves in the impeller (blue ellipses in Figure F.7). The bubbles follow the secondary flow features, such as the horseshoe vortex at the diffuser leading edge (blue lines on Figure F.6)

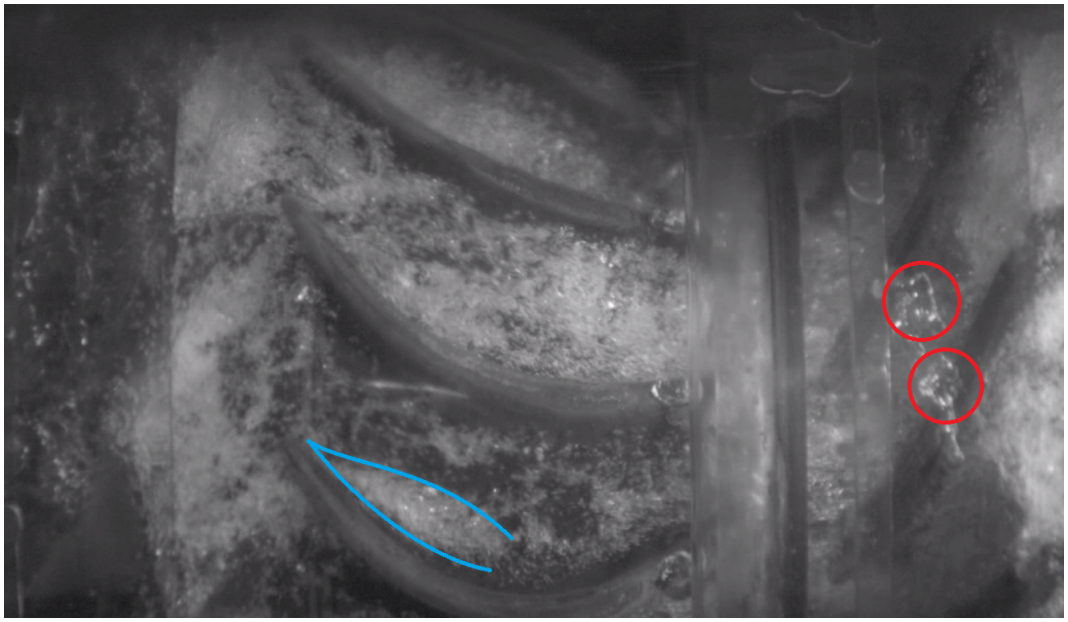

Figure F.6 Bubbly flow and horseshoe vortex. $\Phi^* = 1.54$, $\lambda_0 = 9.5$ %, Impellers 1-2, 7200 fps.

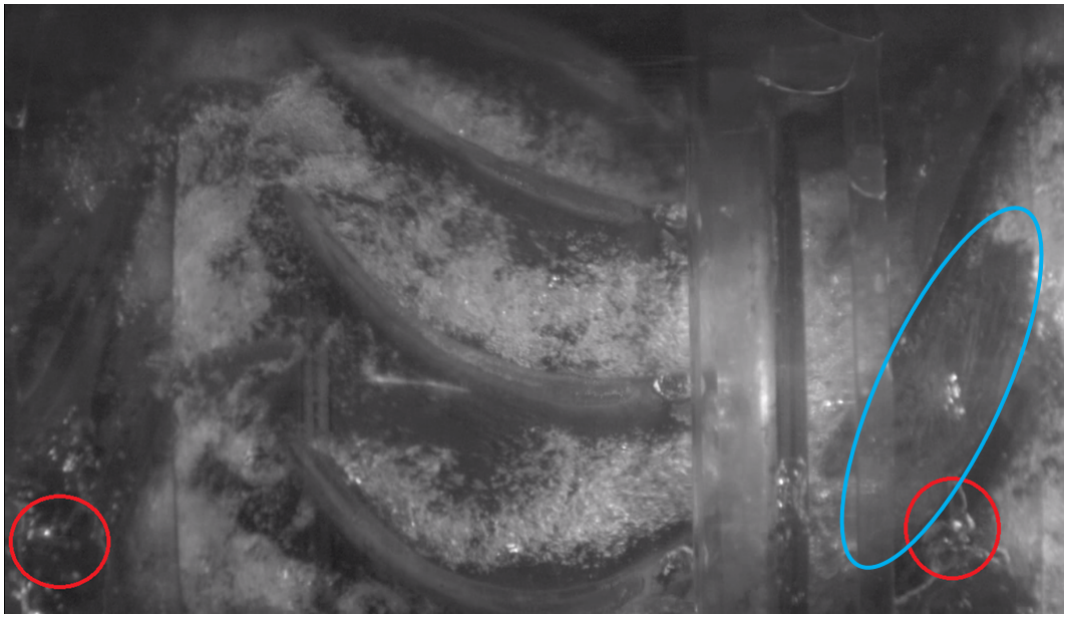

Figure F.7 Bubbly flow in the diffuser, phase separation in the impeller. $\Phi^* = 1.54$, $\lambda_0 = 9.5$ %, Impellers 1-2, 7200 fps.

Figure F.8 Radially separated flow in the impellers and diffusers. $\Phi^* = 1.54$, $\lambda_0 = 9.5$ %, Impellers 1-2, 7200 fps.

F.5 Low Flow, Low Gas Fraction (Video D1)

As we have seen in Chapter 3, recirculation cells are present in the diffuser at low flow rate in single phase flow. When the gas fraction is low ($\lambda_0 = 2.5$ %), this translates into recirculating bubbles, which tend to collide, coalesce and become larger, on average, at the diffuser outlet compared to the diffuser inlet (Figure F.9). Theses bubbles are travelling backwards on the diffuser blades suction side (red arrows) and forward on the pressure side (blue arrows).

We also notice that the flow in the first impeller is always radially separated, while this is not the case for the second impeller (bubbly flow). Finally, the disturbance created in the diffuser by the impeller blades passing through is more pronounced in this case than at design point.

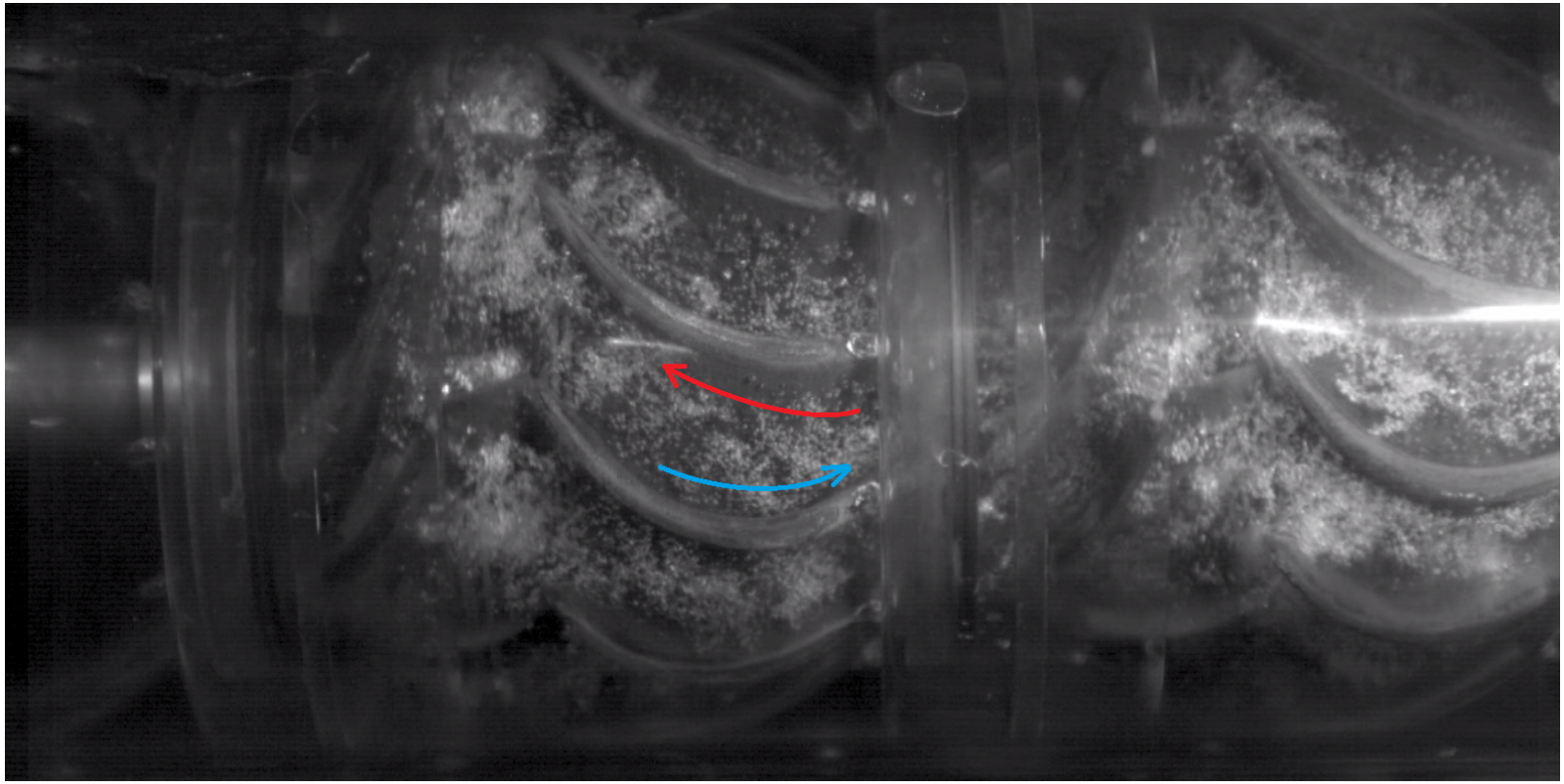

Figure F.9 Recirculation and large bubble in the diffuser at low flow $\Phi^* = 0.62$, $\lambda_0 = 2.5$ %, Inlet, Impellers 1-2, 6000 fps.

F.6 Low Flow, High Gas Fraction (Video D2)

At low flow rate ($\Phi^* = 0.58$), and medium gas fraction ($\lambda_0 = 15$ %), the flow is very unsteady, and a churn flow pattern sometimes appears in the diffuser, before it turns into a radially separated flow. The gas bubbles are very large (5 - 10 mm) and it becomes difficult to distinguish the two phases, especially at the impeller-diffuser interface.

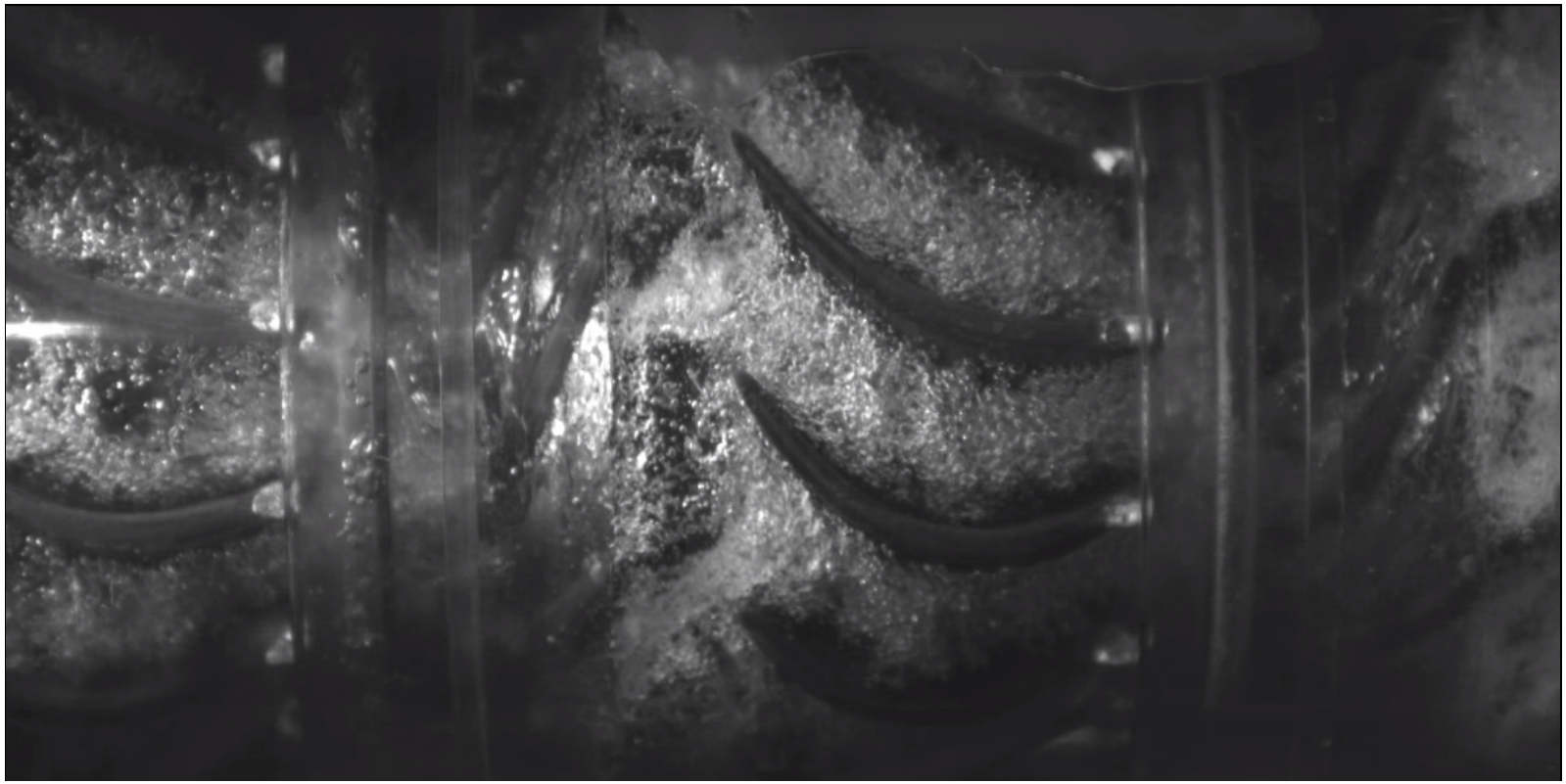

Figure F.10 Slugging churn flow in low flow with recirculation. $\Phi^* = 0.57$, $\lambda_0 = 15$ %, Impellers 3-4, 5400 fps.

Appendix G

List of all high speed videos

To make these tables more readable, the flow rate coefficient Φ^* is coloured with red for high flow rates and blue for low flow rate, while the inlet gas fraction λ_0 is coloured with green for low values, yellow for medium, and red for high values. The flow regimes were visually attributed and are marked with the following abbreviations:

- "b" for bubbly
- "b (iacc)" for bubbly with bubble accumulation (or gas pocket) in the impeller
- "ch" for churn
- "st" for stratified

Table G.1 Case B - Horizontal - $f = 20$ Hz - $P_{inlet} = 2.5$ bar

File name	Regime	fps	d [mm]	Φ_T^*	λ_0	Extent	Comment
E001	b	7200	0.6476	1.62	0.0	0I1232	Single phase
E002_a	b	7200	0.646	1.63	1.0	0I1233	
E002_b	b	500	0.6468	1.63	1.0	0I1234	With inlet, slugs
E002_c	b	7200	0.8272	1.63	1.0	I123	Swarms in D1, smoother in the res
E003	b (iacc)	7200	0.82	1.66	2.4	I123	Slugs, accumulation in I2, bubbles
E004	b	7200	0.8523	1.70	4.8	I1231	
E005	b (iacc)	500	0.8517	1.74	7.0	I1232	
E011	b	500	0.5678	1.43	1.0	I1233	
E012	b	500	0.8517	1.45	2.5	I1234	I1 different
E014	b / ch / st	7200	0.8584	1.54	7.9	I234	
E022_a	b (iacc)	7200	0.6328	1.36	5.0	0I1234	
E022_b	b (iacc)	7200	0.6435	1.36	5.0	I234	Acc. in I2, not in I3-4
E024	b (iacc)	500	0.79275	1.46	11.6	0I1234	Slugs, St. in D1 but not D2-4
E025	b / ch / st	7200	0.842	1.52	15.0	I234	Slugs
E032	b (iacc)	7200	1.05	1.23	10.0	I234	
E033	b / ch / st	7200	1.05	1.31	15.0	I234	
E035	b / ch / st	7200	0.8532	1.48	24.9	I34	
E038	b	7200	1.063	1.01	1.0	I34	E38 / E39 : good comparison
E039	b	7200	1.2756	1.03	2.5	I34	Focus on D3 outlet, start of acc.
E040	b	7200	1.512	1.05	5.0	I34	Focus on D3 outlet, start of acc.
E041	b	7200	1.296	1.11	10.0	I34	
E042	b (iacc)	7200	1.836	1.11	10.0	0I1	
E044	b (iacc)	7200	1.7816	1.25	20.0	0I1	Almost strt in diff
E047_a	b	7200	0.524	0.92	1.0	0I1	Break-ups, acc in I1
E047_b	b	7200	0.694	0.92	1.0	I12	Break-up and coalescence
E049	b (iacc)	7200	0.686	0.96	5.0	0I1	
E063_a	b / ch / st	7200	0.9185	1.15	30.0	0I12	Slugging
E063_b	b / ch / st	500	0.9185	1.21	33.3	0I12	Very nice slugging
E074	b	6000	0.7332	0.61	1.0	0I12	Acc. in I1
E075	b	6000	0.7332	0.62	2.5	0I12	Bubble size x2 if recirculation
E076	b (iacc)	6000	1.1064	0.64	5.0	I12	
E077	b (iacc)	6000	2.766	0.67	10.0	I12	Almost stratified in D1
E080	b / ch / st	4000	0.4905	0.87	30.0	0I1	Benjamin bubble at inlet
E083	b	5400	0.6256	0.49	1.0	0I1234	recirculation
E084	b	5400	0.6256	0.50	2.5	0I1234	
E085_a	b (iacc)	5400	0.817	0.51	5.0	0I12	
E085_b	b	5400	1.204	0.51	5.0	I34	no flow?
E086	b (iacc)	5400	2.31	0.54	10.0	I34	
E087	b (iacc)	5400	2.55	0.57	15.0	I34	looks like foam
E090	b / ch / st	4000	16.295	0.81	40.0		

Table G.2 Case C - Tilted (60 deg) - $f = 20$ Hz - $P_{inlet} = 1.6$ bar

File name	Regime	fps	d [mm]	Φ_T^*	λ_0	Extent	Comment
F02_a	b	5400	0.853	1.63	0.9	0I1234	
F02_b	b	5400	0.4682	1.63	0.9	0I12	up to 50mm bubble at inlet
F03_a	b	5400	0.702	1.66	2.4	0I12	large slugs
F03_b	b (iacc)	7200	0.686	1.66	2.4	0I1	accumulation when slug
F03_c	b	7200	0.6705	1.66	2.4	I3	stays bubbly through slug
F04	b	7200	0.648	1.70	4.7	0I1	horseshoe vortex + 2-3 mm bub
F05_a	b	7200	0.6705	1.74	7.1	0I1	
F05_b	b	7200	0.54	1.74	7.1	I3	
F10	b	7200	0.54	1.43	0.9	I3	
F15	b (iacc)	7200	0.54	1.65	14.2	I3	churn
F44_a	b (iacc)	5400	0.3768	1.02	2.3	0I1	almost single phase to churn
F44_b	b	5400	0.5568	1.02	2.3	I2	almost accumulation in I2
F44_c	b	5400	0.8456	1.02	2.3	I3	
F44_d	b (iacc)	5400	1.404	1.02	2.1	I2	accumulation when slug)
F072	b / ch / st	6000	0.6552	1.06	23.8	I2	D1 flooded then D2 then D1
F080	b (iacc)	6000	0.7496	0.78	9.5	I2	
F087	b	5400	1.1304	0.62	2.3	I2	recirculation, large bubbles
F088_a	b (iacc)	5400	1.2168	0.64	4.6	I2	Blockage + accumulation
F088_b	b (iacc)	7200	1.05	0.64	4.6	I12	Impeller fully stratified
F089	b (iacc)	7200	1.575	0.65	7.1	I12	
F099	b	7200	0.525	0.49	0.9	I12	Some larger bubbles (0.8)
F0100	b (iacc)	7200	1.05	0.50	2.3	I12	
F0101	b (iacc)	7200	1.05	0.51	4.7	I12	
F0102	b (iacc)	7200	1.785	0.52	7.0	I12	

Table G.3 Case D - Tilted (60 deg) - $f = 25$ Hz - $P_{inlet} = 1.6$ bar

File name	Regime	fps	d [mm]	Φ_T^*	λ_0	Extent	Comment
G02_a	b (iacc)	5000	0.515	1.23	2.3	0I1	Large bubbles at inlet
G02_b	b (iacc)	5000	0.618	1.26	4.7	0I1	
G02_c	b	5000	0.721	1.26	4.7	I2	
G02_d	b (iacc)	5000	0.618	1.33	9.4	I12	
G02_e	b	5000	0.424	1.43	2.4	I12	I acc during slug
G02_f	b	5000	0.424	1.47	4.7	I12	Short slugs (stratified) - 40 ms
G02_g	b	5000	0.63	1.54	9.5	I12	Short slugs (stratified) - 40 ms
G02_h	b (iacc)	5000	0.63	1.63	14.2	0I1	Large bubbles at inlet 3-4 mm
G02_i	b (iacc)	5000	0.42	1.63	14.2	I12	Short slugs (stratified) - 40 ms
G015	b	5000	0.824	0.99	2.4	I2	
G017_a	b (iacc)	5000	0.721	0.84	4.7	0I1	Churn in the inlet
G017_b	b	5000	0.927	0.84	4.7	I3	
G017_c	b (iacc)	5000	0.412	0.93	14.2	I2	
G017_d	b (iacc)	5000	0.618	1.07	9.4	I2	
G017_e	b / ch / st	5000	0.618	1.14	14.6	I2	
G017_f	b / ch / st	5000	0.618	1.28	24.4	0I1	Bubbly inlet
G017_g	b / ch / st	5000	1.03	1.28	24.4	I2	
G041_a	b	5000	0.515	0.51	2.4	I2	Recirculation
G041_b	b (iacc)	5000	0.721	0.53	4.7	I12	
G041_c	b (iacc)	5000	2.06	0.55	9.4	I12	Coalescence and break up

Table G.4 Case E - Tilted (60 deg) - $f = 30$ Hz - $P_{inlet} = 1.6$ bar

File name	Regime	fps	d [mm]	Φ_T^*	λ_0	Extent	Comment
H01	b (iacc)	5400	0.84	1.42	4.8	I12	
H08	b	5400	0.63	1.23	2.4	I12	some churn
H015_a	b	5400	0.63	1.02	2.4	0I1	
H015_b	b	5400	0.63	1.02	2.4	I12	
H017	b (iacc)	5400	0.735	1.16	14.2	0I1	Churn in D1
H023	b (iacc)	5400	0.63	0.81	2.4	0I1	
H024	b (iacc)	5400	0.525	0.84	5.0	0I1	
H028	b / ch / st	5400	0.84	1.04	23.9	0I1	
H032	b	5400	0.525	0.61	2.3	I23	
H038	b / ch / st	5400	0.84	0.79	23.9	I2	
H043	b (iacc)	5400	1.26	0.55	9.5	I2	recirculation, round bubbles

Table G.5 Case F - Vertical - $f = 20$ Hz - $P_{inlet} = 1.6$ bar

File name	Regime	fps	d [mm]	Φ_T^*	λ_0	Extent	Comment
J01_a	b	5400	0.7785	1.41	1.1	0I123	
J01_b	b	5400	0.636	1.43	2.3	0I1	
J01_c	b / st	5400	0.728	1.46	4.7	I12	Bubbly to stratified
J01_d	b	5400	0.7695	1.46	4.7	0I123	
J02	b	5400	0.7833	1.41	0.9	I1234	
J013_a	b / ch / st	5400	0.824	1.44	17.5	I12	
J013_b	b / ch / st	5400	1.321	1.44	17.5	0I123	Different I1 / I2, Inlet bubbles:
J013_c	b / ch / st	5400	1.321	1.44	17.5	I1234	
J16_a	b	5400	0.714	1.02	2.3	0I1	GVF change in different passage
J16_b	b	5400	0.728	1.02	2.3	I23	Accumulation in D2 outlet, rou
J16_c	b	5400	1.0448	1.02	2.3	I1234	
J17_a	b (iacc)	5400	0.816	1.05	4.7	0I1	
J17_b	b	5400	0.824	1.05	4.7	I23	sometimes bigger bubbles
J19_a	b / ch / st	5400	0.721	1.23	19.0	I23	
J19_b	b (iacc)	5400	0.7881	1.23	19.0	I1234	Slug strat in D1/D2 very churn
J19_c	b / ch / st	5400	0.7881	1.31	23.8	I1234	Slug
J34_1	b	1000	1.3	0.51	2.4	0I123	Good view of inlet
J34_2	b	5400	1.05	0.51	3.1	I23	Stationary bubbles in D2
J34_3	b (iacc)	1000	1.3	0.52	4.7	0I23	Sort of Taylor bb
J34_4	b (iacc)	5400	1.575	0.53	7.1	0I123	
J34_5	b (iacc)	1000	1.04	0.53	7.1	I23	
J34_6	b	5400	0.728	0.60	0.9	I1234	
J34_7	b	5400	0.78	0.60	0.9	I1234	
J34_8	b	5400	0.832	0.61	2.4	I23	
J34_9	b	5400	0.832	0.63	4.7	I23	
J34_10	b (iacc)	5400	0.832	0.64	7.1	I23	
J34_11	b (iacc)	5400	1.248	0.66	9.5	I23	Some big bubbles
J34_12	b (iacc)	5400	1.56	0.70	14.3	I23	Almost churn in D2
J34_13	b (iacc)	5400	3.9	0.74	19.1	I1234	Almost strat. in D2
J34_14	b / ch / st	5400	1.01	0.78	24.0	0I1	Bubbly inlet (Taylor?)
J34_15	b / ch / st	5400	1.3	0.78	24.0	0I23	Taylor bubble
J34_16	b / ch / st	5400	1.01	1.06	43.6	0I1	Taylor bubble
J34_17	b / ch / st	5400	1.3	1.06	43.6	0I123	Taylor bubble